

Two-dimensional Diffraction by Structures with Corners

Audrey Jeanette Markowski

B. App. Sc. (Hons) NSW Institute of Technology (1983)

B. Arts. (Hons) Macquarie University (2013)

Supervisor: Professor Paul D. Smith

A thesis presented for the degree of
Doctor of Philosophy



MACQUARIE
University

Department of Mathematics
Macquarie University
Sydney, Australia
12th December, 2018

Certification

This thesis entitled:

Two-dimensional Diffraction by Structures with Corners

written by: **Audrey Jeanette Markowskei**

has been approved by the Department of Mathematics at Macquarie University.



Paul Denis Smith

date: 12th December, 2018

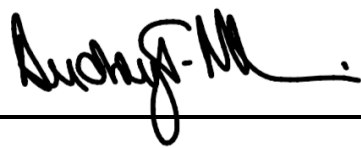
The final copy of this thesis has been examined by the signatory, and I find that both the content and the form meet acceptable presentation standards of scholarly work in the above mentioned discipline.

Declaration

I certify that the work in this thesis has not previously been submitted for a degree nor has it been submitted as part of the requirements for a degree to any other university or institution other than Macquarie University.

I also certify that this thesis is an original piece of research and has been written by me. Any help and assistance that I have received in my research work and the preparation of the thesis itself has been appropriately acknowledged.

In addition, I certify that all information sources and literature used are indicated in the thesis.

A handwritten signature in black ink, appearing to read 'Audrey-J.M.', is written over a solid black horizontal line.

Audrey Jeanette Markowskei

date: 12th December, 2018

Acknowledgements

I am deeply grateful to my supervisor and mentor Professor Paul Smith. Without his support and encouragement from the beginning of my days as a first-year undergraduate student and throughout all my studies, I would never have had the courage to undertake my PhD journey. I am eternally thankful for his infinite patience, advice and guidance over these last years without which this thesis would not have been possible.

I would like to express my thanks to the staff of the Mathematics Department at Macquarie University for their environment of learning and support and for all the kindness they have shown me during the course of my studies. I would like to especially thank my associate supervisor Dr Elena Vynogradova and those whose friendship and encouragement helped me stay the course. In particular: Frank Valckenborgh, Vladimir Gaitsgory, Carolyn Kennet, Dilshara Hill, Chris Gordon, Xuan Duong, Stuart Hawkins, Christine Hale and Garry Lawson. My thanks also go to all the PhD, masters and honours students that have crossed my path at Macquarie for their camaraderie and support. Especially my dear friends and colleagues Poon Leung, Joshua Peate, Geoff Edington-Cheater, Martin Sagradian, Turker Topal and Sherwin Bagheri. Special mention to fellow candidate (now Dr.) Leon Beale for his support, friendship and motivating pep talks, especially during the long final months of my thesis preparation - thank you.

I would also like to express my heartfelt gratitude to the A. F. Pillow Applied Mathematics Trust for their financial support during my PhD.

There are no words which can express adequately my love and gratitude to my husband Steven. Your immeasurable support and encouragement enabled me to undertake and complete this thesis. You are my rock and your love has kept me anchored throughout these long years of study and research. To our beautiful daughter Sarah - you have been a blessing in my life for which I am truly grateful. Your sunny disposition and positiveness

have helped me keep things in perspective, and the days we spent mastering the dark arts of baking were a wonderful, much needed, sanity restoring distraction. I dedicate this thesis to you both.

I also want to say thank you to my Mum for her gentle encouragement and for her joy in my achievements. Last but certainly not least, I would like to thank the rest my family and friends for supporting rather than abandoning me during the times I always seemed unavailable.

Summary

In studying acoustic or electromagnetic wave diffraction, the choice of an appropriate canonical structure to model the dominant features of a scattering scenario can be very illuminating. A common approach used when dealing with domains with corners is to round the corners, producing a smooth surface, eliminating the singularities introduced by the corners. This thesis examines and quantifies the effect of corner rounding both numerically and analytically. The diffraction from cylindrical scatterers which possess corners, that is, points at which the normal changes discontinuously is examined. We develop a numerical method for the scattering of a plane wave normally incident on such cylindrical structures with soft, hard or impedance loaded boundary conditions. We then examine the difference between various test structures with corners and with the corners rounded to assess the impact on near- and far-field scattering, as a function of the radius of curvature in the vicinity of the rounded corner point. We then examine the nature of the differences in the far-field between the cornered and rounded scatterers both in the frequency and the time domain. We obtain precise quantitative estimates for the rate of convergence of the maximum difference between the far-field solutions as the radius of curvature of the rounded scatterer approaches zero and verify them analytically. Having examined the near- and far-field solutions we confirm that the techniques employed also produce highly accurate solutions in close proximity to the surface of the scatterer especially in the vicinity of the corner. Our study of the effect of corner rounding is extended to arrays of scatterers using a classical but computationally intensive method for these calculations. To enable the study of larger scatterer arrays, we employ the recently available TMATROM an object-oriented T-matrix software package, with our own forward solvers.

Table of Contents

1	Introduction	1
1.1	Examination of Selected Literature	4
1.2	Thesis Outline	12
2	Problem Formulation	15
2.1	The Scatterers	16
2.1.1	Radius of Curvature	19
2.2	The Incident and Scattered Fields	20
2.3	The Boundary Conditions	21
2.4	Integral Representations	22
2.4.1	Single-layer and Double-layer Potentials	23
2.4.2	The Jump Relations	24
2.4.3	Integral Operators	25
2.4.4	Integral Representations of the Boundary Value Problems	26
2.5	Numerical Solution	28
2.5.1	Transformation into Line Integrals	29
2.5.2	Nyström Method	29
2.5.3	Surface Discretisation	30
2.5.4	Cornered Scatterers with Dirichlet Boundary Condition	32
3	Effect of Corner Rounding: Numerical Results	35
3.1	Verification of Numerical Results	36
3.2	Test Parameters	39

3.3	Graded Mesh is Essential for Smooth Scatterers with Small Radii of Curvature	40
3.4	Measuring the Effect of Rounding Corners on the Scattered Field	45
3.5	Different Interior Angles	47
3.6	The Nature of the Differences in the Far-field	51
3.7	Rate of Convergence of Far-field Solutions as the Radius of Curvature ρ Approaches Zero	54
3.8	Validation of Rawlins' Results on Diffraction by Absorbing Rectangular Cylinders	60
3.9	Conclusions	61
4	Bounds Analysis	63
4.1	Formulation	64
4.2	Integral Equations for the Difference in Surface Quantities	65
4.3	Approximate Integral Equation for the Difference in Surface Quantity	66
4.4	The Far-field Difference	81
4.5	Conclusion	83
5	The Total Field, the Normal Derivative and Surface Quantities Near the Vicinity of the Corner	85
5.1	The Total Field	86
5.2	The Derivative with Respect to the Normal on the Surface	88
5.3	Behaviour of the Surface Quantity, φ , in the Vicinity of the Corner	93
5.3.1	Dirichlet Boundary Condition	93
5.3.2	Neumann Boundary Condition	95
5.4	Analysis of the Neumann Result	98
5.5	Conclusions	103
6	The Nature of the Differences in the Far-field Measured in the Time Domain	105
6.1	Problem Formulation	105
6.2	The Discrete Fourier Transform	107
6.3	The Incident Pulses	108

6.4	Verification that Implementation is Correct	110
6.5	Results	113
7	Scatterer Arrays	117
7.1	The Geometries	117
7.1.1	Notation	118
7.2	Approach	119
7.2.1	The Dirichlet Case	120
7.2.2	The Neumann and Impedance Loaded Cases	123
7.3	Numerical Results	125
7.3.1	Test Parameters	125
7.3.2	Verification of Numerical Results	125
7.4	Convergence and Quadrature	125
7.5	Relative Differences	130
7.5.1	Dirichlet Boundary Condition	131
7.5.2	Neumann Boundary Condition	132
7.5.3	Impedance Loaded Boundary Condition	134
7.6	Far-field Differences	137
7.7	Conclusion	139
8	TMATROM	141
8.1	The TMATROM Package	142
8.2	Implementation of Single Scatterer Problems	143
8.2.1	Parameter Selection	144
8.2.2	MPSpack	146
8.3	Verification of Our Single Scatterer Results	151
8.4	Multiple Scatterer Configurations	155
8.5	The Advantages of Using TMATROM	164
8.6	Constraints	165
8.7	Acknowledgement	166
8.8	Conclusion	166

9	Large Arrays	169
9.1	The Geometries	169
9.2	Far-field behaviour	170
9.2.1	Limiting Behaviour	171
9.2.2	Diffraction Grating	174
9.3	Conclusion	179
10	Summary and Conclusions	181
	Appendices	187
	Appendix A Problem Formulation Details	189
A.1	Singularity of the Green's Function	189
A.2	The Nyström Method	191
A.2.1	The Nyström Method and the Kernel Singularities	192
A.2.2	The Martensen-Kussmaul Method	194
A.3	The Dirichlet Boundary Condition and Structures with Corners	198
A.3.1	Single Cornered Domains	198
	Appendix B Comparison to Rawlins' Results	201
	Appendix C Bounds Analysis Supporting Details	203
C.1	Lemmas used in Chapter 4	203
C.2	$\ \psi_\varepsilon - \psi_0\ _{\infty, J}$ and $\ \psi_\varepsilon - \psi_0\ _{1, J}$ are negligibly small	214
	Appendix D Surface Quantities Supporting Material	217
D.1	Convergence of Integral K_ν	217
D.2	Surface Quantity, φ , in the Vicinity of the Corner: Numerical Results . . .	219
	Appendix E Time Domain Supporting Material	223
E.1	Time Domain Incident Pulses	223
E.1.1	The Gaussian	223
E.1.2	The Derivative of the Gaussian	225
E.1.3	The Sine Packet	225

Appendix F Scatterer Arrays Numerical results	227
F.1 Relative Differences	227
F.2 Far-field Differences	235
Appendix G TMatROM Numerical Results	243
Appendix H Large Arrays Supporting Material	253
Bibliography	257

Chapter 1

Introduction

Diffraction of acoustic or electromagnetic waves by canonical shapes and structures of more general and arbitrary shape is of enduring interest. The choice of an appropriate canonical structure to model the dominant features of a scattering scenario can be very illuminating. Scattering by sharp edges and corners is informed by, for example, the diffraction from the half-plane and the wedge (of infinite extent). The nature of the singularities in the field and its derivatives is well described in [1]. There has been much work to develop analytical and numerical methods to account for these singularities which enable accurate modelling, however, these methods can be time consuming to implement and at times very specialised. When numerical methods are employed, a common approach used when dealing with domains with corners is to round the corners, producing a smooth surface. This eliminates the singularities introduced by the corners and allows for standard numerical quadratures to be used, though leaving the researcher with no clear estimate of the error or difference induced by the rounding.

The earliest study of scattering from a sharp object could be said to begin with Sommerfeld's solution to the half-plane problem [2, 3]. It was the first recognition that the dependencies of the scattered field differed to that of a smooth body. The next major development was the study of the wedge [4–6] where the dependence of the scattered field on the angle of the wedge was made explicit. These canonical problems admitted analytical solutions that demonstrated explicitly the dependence of field quantities on the corner angle. In more modern times, turning to finite dimensional bodies, there is a vast literature on numerical approaches to scattering calculations that may be classified

in terms of the diameter $2a$ of the scatterer in wavelengths. At long wavelengths, the scattered field may be regarded as a perturbation of a corresponding static problem and expansion in a series of powers of ka (k - wave number), whilst at short wavelengths ($ka \gg 1$), ray tracing techniques are often deployed.

In the intermediate or resonance regime, integral equation approaches provide the usual basis for numerical methods. Over the last couple of decades, the advantages of integral equation formulations - well-posed second kind equations, unknowns to be found only on the scattering surface (rather than the surrounding space) and automatic incorporation of the radiation condition obviating the need for terminating the volumetric grid characteristic of differential equation methods - have become well established for the reasons explained in [7, Ch 3], and provide the basis for an approach. The robustness and efficiency of such approaches are particularly important where a sequence of direct scattering problems is iteratively solved such as in some current inverse scattering algorithms: see for example [7, 8].

Although there is an extensive literature on scattering and diffraction from sharp cornered objects as well as those with smooth boundaries, there does not seem to be a systematic treatment of the transition from one to the other, in particular as the radius of curvature of the rounded corner points tends to zero. Two notable contributions are that of [9] who studied diffraction by slender bodies in the high-frequency regime and more recently [10] who develop a method to smooth corners of polygonal structures.

In order to clarify and quantify the effect of corner rounding this thesis examines the two-dimensional case of diffraction from cylindrical scatterers which possess corners, that is, points at which the normal changes discontinuously. Our approach provides a relatively simple yet efficient and accurate method for computing near- and far-fields scattered by sharp cornered objects of diameter up to several wavelengths in extent. Accuracy was of paramount importance in this study in assessing the effects of rounding a corner. The rounding used in this and earlier papers [11–14] replaces cornered scatterers (both curvilinear and polygonal) by a smooth object that is extremely close to the original except in the vicinity of the corners. The rounded curve is nearly a hyperbola with sides of the corner being its asymptotes, or similar. Recently [10] have developed a different method for rounding the corner of polygons and have considered the Dirichlet

and Neumann problem.

A more sophisticated approach to the scattering from soft cylindrical structures with sharp corners is given by [15]. It employs the so-called recursively compressed inverse preconditioning method, and in the survey of the two dimensional scattering literature, it alone addresses the problem of accurate near-field evaluation in scatterers with corners. Other approaches build in greater levels of complexity in modelling the surface distribution with attendant benefits. For example, the approach to scattering by convex polygons given by [16,17], where the choice of approximating basis functions involving plane waves propagating along the edges, produces a scheme where the degrees of freedom required to produce a prescribed level of accuracy grows only logarithmically with frequency of the incident wave. In [18] a collocation method is developed for convex polygons and high-frequency waves by adapting the approach used in [19] where a Galerkin method was used for similar problems. The MPSPack suite [20] is another (finite element) approach employing a more sophisticated basis of non-polynomial finite elements which is shown to be well adapted to scattering from polygonal structures. The methods listed and others will be further detailed in the examination of literature section.

Our calculations rigorously examined the acoustic resonance regime $ka \leq 16\pi$ corresponding to diameters less than 16 wavelengths. In this work we use a numerical method that is suitable for examining the scattering of acoustic or appropriately polarised electromagnetic plane waves by cylindrical structures possessing some points of small or zero radius of curvature (that is, having a sharp corner). Earlier work in [11–14, 21–25] is significantly extended. We examine three different boundary conditions: soft, hard and an impedance loaded boundary condition, enforced at all points on the cross-sectional boundary of the cylinder. We implement the Nyström method expounded by [7, 26] for the soft boundary condition for a scatterer with a single corner to obtain numerical solutions of this integral equation. We then develop other (similar) Nyström methods for the hard and impedance boundary conditions and adapt these methods for scatterers with two and four corners to obtain numerical solutions of the respective integral equations.

These numerical methods are first used to compare the convergence of solutions for different discretisations of the surfaces of the scatterers, and then to assess the impact on near- and far-field scattering, as a function of the radius of curvature in the vicin-

ity of the rounded corner point. The nature of the differences in the far-field between the cornered and rounded scatterers is examined as well as the effect on the differences as the frequency of the plane wave increases. We also examine the effect of rounding corners in the time domain. We quantify numerically the rate of convergence of the maximum difference between the far-field solutions as the radius of curvature of the rounded scatterer approaches zero and confirm this analytically. Having examined the near- and far-field solutions we confirm that the techniques employed also produce highly accurate solutions in close proximity to the surface of the scatterer especially in the vicinity of the corner. Our study of the effect of corner rounding is extended to arrays of scatterers using a classical but computationally intensive method for these calculations. To enable the study of larger scatterer arrays, we employ the recently available TROM [27], an object-oriented T-matrix software package, with our own forward solvers. We document the process required to employ this package and examine both the advantages and restrictions the use of this package provides. We then use our implementation of TROM to verify our earlier numerical results and to examine large (up to 256) scatterer arrays.

1.1 Examination of Selected Literature

The purpose of this work is to examine the effect of rounding corners on scatterers and as such we required a highly accurate method of evaluating the scattered field from both smooth scatterers and cornered ones. Our work is focussed on the acoustic resonance regime. In this region, differential and integral equation approaches are commonly used to solve the scattering problem. We have chosen to use an integral equation approach, specifically integral equations of the second kind and a boundary element method (BEM) for solving them. The main advantages over other methods such as the finite element method is the reduction of the problem dimension by reducing the scattering problem from a two-dimensional problem to a single-dimensional one governed by the boundary of the scatterer which automatically satisfies the radiation conditions. As such, there is no need for the imposition of an artificial domain boundary. We wish to present literature specific to these methods with some inclusions of other techniques being used for the solution of acoustic scattering problems for structures with corners. Although we have

attempted to provide a comprehensive survey, we apologise to any authors not mentioned in this section.

Much work was done in the 1980's and 1990's on boundary integral equation methods for the Laplace and Symm's equation problems for cornered scatterers which influenced the methods used for the time harmonic Helmholtz problem. Some of the papers of interest are [28–33]. The numerical methods used in these works are collocation, Galerkin's method and Nyström discretisation. Both analytical and numerical techniques such as employing a graded mesh are considered. A comprehensive review of the various techniques being employed at this time for the Laplace problem is provided in [34], the Galerkin method for boundary integral equations in [35] and the Galerkin, collocation and qualocation methods in [36].

In the acoustic regime, in 1982 Varadan et al. [37] use the T-matrix method to calculate the surface quantities and far-fields of rigid cylindrical objects with sharp corners. At this stage for the resonance regime problems, evaluation of these fields was only possible for a restricted number of cross-sectional shapes for which the differential operator is separable. Bowman et al. [1] present the separation of variable approach to these solvable problems. In 1993 Yan [38] developed a pre-conditioned Richardson iterative method suitable for circles and circular ellipses with Dirichlet boundary condition for wave numbers up to $ka = 100$. The method is as rapid as a trigonometric collocation method and does not suffer the loss of accuracy of the methods of [39–42]. In 1997 Yang takes a different approach and reformulates the integral equations governing the Helmholtz equations to be singularity free for the Dirichlet and Neumann problems and uses a Gauss-Legendre quadrature method. The work is designed to cater for higher frequency waves ka up to 20π but is for 3D scattering from smooth-surfaced scatterers, not cornered ones. Yang later extends this work to the 2D acoustic problem [43] but only for smooth-surfaced scatterers. At this time comprehensive code was provided in [44] which creates and refines triangulations on the surface of smooth and cornered objects which then solves the integral equations using different collocation methods depending on whether the surface is smooth or not. Kolm and Rohklin develop a method for designing high-order quadrature rules to enable evaluation of singular and hypersingular integral in [45]. In 2007 Engleder and Steinbach [46] reformulate the Helmholtz equa-

tions using modified regularised boundary integral equations for scatterer with Dirichlet or Neumann boundary condition which also cater for Lipschitz boundaries. Their method is suitable for a Galerkin discretisation. For high-frequency 3D problems for arbitrary shapes Nieminen et al. [47] use a modified Kirchhoff approach.

We adopted a Nyström method for scatterers with corners and a Dirichlet boundary condition developed by Rainer Kress. In 1990 Kress published [48] a convergence and error analysis for the numerical solution inside a plane domain with corners of the harmonic Dirichlet problem using a Nyström method using a double-layer boundary integral equation. In this work a graded mesh is used which results in high-order resolution of the weak singularities of the kernels of the integral operators as well as the stronger singularities of the derivatives of the unknowns in the vicinity of the corners. Similar graded meshes were also considered by [49, 50] and the superior rate of convergence exhibited when using a graded mesh rather than a uniform mesh for a finite crack in the half-plane is demonstrated numerically in [50]. Kress' approach is based on a global approximation which is easier to implement rather than the repeated rule used in [49, 50]. Yan and Sloane [51] demonstrate that for the harmonic Dirichlet problem using the single-layer potential and the Galerkin method with a graded mesh for polygonal domains (and open arcs) produces highly convergent solutions. In 1993 Kress and Sloane [52] present a solution to the Helmholtz Dirichlet problem using only the single-layer potential for smooth domains and suggest this method can be extended to cornered domains by the use of graded mesh. The collocation and Galerkin methods for numerical solutions in domains with corners were also considered by others [31, 53–55]. Kress chooses the Nyström method over others as it is computationally less costly.

In 1991 Kress published his seminal paper [26] where he examines the exterior boundary value problem in time-harmonic acoustic scattering for scatterers with a Dirichlet boundary condition. The theory on boundary integral equations for this problem in [56] is recapped, and the parameterisation of the integral equations governing this problem is presented. The solution uses the combined single- and double-layer potentials proposed by Burton and Miller [57] to ensure the uniqueness of the solution. The singularities present in the kernels of the integral equations are treated using the methods proposed by Martensen [58] and Kussmaul [59] which split the kernel into an analytic and non-

analytic part and employ trapezoidal polynomial interpolation quadrature, respectively to evaluate these kernels. Burton and Miller's [57] treatment of the hypersingular kernel (the derivative of the double-layer potential) is also employed. Kress then compares the Nyström, collocation and Galerkin methods and demonstrates that for smooth surfaced scatterers these methods demonstrate an exponential order of convergence. He concludes by detailing a method for cornered scatterers in which he modifies the integral equation used for smooth scatterers to accommodate the double-layer potential jump-relations in the corner and employs a graded mesh to deal with the singularities in the derivatives in the corner. This work is further detailed in [7] and is the method adopted for the smooth scatterers and single-cornered scatterers with Dirichlet boundary condition studied in this work. We developed our own graded mesh for two and four-cornered scatterers and extended Kress' methods to solve the Neumann and impedance boundary value problems. These methods produce a rapidly convergent solution.

Kress in 1995 [60] published the solution to the Neumann problem for smooth domains using a combined single- and double-layer potential, and describes a method to numerically solve the hypersingular operator that results from using this approach. Later in [61], Kress uses a the double-layer potential to solve the acoustic Helmholtz problem for smooth surfaced scatterers and uses a collocation method for the numerics. Our approach differs to that of Kress in that we only use the single-layer potential which eliminates the hypersingular operator. The integral equation has a unique solution at all except countably many wave numbers k . One of the advantages of using only the single-layer potential is that the solution to the integral equation gives the value of the derivative of the surface quantity directly, which represents the surface current in the electromagnetic case and the normal derivative of the acoustic wave potential in the acoustic case. We were able to reproduce the published numerical results [61] using our method. This is further described in Section 3.1.

In 2012 Anand et al. [62] present a high-order Nyström method for two-dimensional acoustic scattering problems with Neumann boundary conditions for scatterers with corners. Their approach is based on Direct Regularised Combined Field Integral Equation (DCFIE-R) formulations. This particular method does not require the evaluation of hypersingular operators typically occurring in DCFIE-R formulations. Their numerical

implementation follows Kress' to formulate the problem combined with the graded-mesh quadrature proposed by Kress [48], resulting in an efficient, high-order Nyström method which produces solutions to these scattering problems. Condition number estimates for the combined equation formulations and the upper and lower bounds on the single- and double-layer potential operators is provided in [63, 64].

Boubendir and Turc [65] also use a regularised CFIE approach with a Nyström method to solve the acoustic Neumann problem for smooth scatterers, and in [66] use a regularised CFIE with graded mesh and high-order Nyström discretisation to solve the Helmholtz impedance loaded problem for scatterers with corners.

In 2009 Bruno et al. [67] present a new algorithm for the Neumann Laplace problem for cornered scatterers, both concave and convex, which differs from the approach used by Kress [48] and others [49, 50]. The method isolates the leading singularity of the integral equation for special treatment and uses graded mesh for the regular remainder. Even though this method is used for the Laplace problem, the authors state that it can be applied to the Helmholtz and Maxwell problems.

Adkuman and Kress [68] solve the electromagnetic impedance problem for inhomogeneous boundary conditions, for both the direct and inverse problems. The aim is not to reconstruct the shape of the scatterer but to recover the impedance variable on the surface of the scatterer. Of particular interest is the method for the direct problem, which is based on an integral representation of the scattered field using Green's formula. Employing the jump relations of the single- and double-layer potentials a boundary integral equation is produced that is well posed and can be numerically solved using a Nyström method. This particular method eliminates the hypersingularity encountered when using the standard single- and double-layer potential approach used by Kress in [26, 60]. The effectiveness of these methods is demonstrated using an ellipse and a lemniscate as examples.

Other more recent work which has been considered is that of Chandler-Wilde and Langdon and their co-contributors. Their extensive work specialises in high-frequency acoustic problems. Earlier work was for the half-plane [69–74]. This was followed by works for sound-soft convex polygons using a Galerkin boundary element method [75, 76], and using a collocation method [18]. Later the method was extended to curvilinear

polygons in [77]. The more recent approach to high-frequency problems uses hybrid numerical-asymptotic methods for both smooth and cornered domains with Dirichlet, Neumann and impedance loaded boundary condition [78], convex polygons with impedance loaded boundary condition [16] and non-convex scatterers with Dirichlet boundary condition [79]. The same class of method is used for convex polygons in [17].

Other work considered was that of Rohklin et al. [42, 80–82] which employs fast multipole methods for solving the 2D and 3D Helmholtz problems. In 2013 Helsing and Karlsson [15] solve the Helmholtz (electromagnetic) problem for scatterers with corners, using the combined layer integral equations with a Nyström scheme and use the RCIP (recursively compressed inverse preconditioning) method to handle the corner singularities. They demonstrate the scheme’s effectiveness for high-frequency (large body) problems for both the Dirichlet and Neumann boundary conditions. As noted earlier, this work addresses the problem of accurate near-field evaluation in scatterers with corners.

More recently, Bremer, Rohklin et al. [83–85] developed an algorithm which constructs universal quadratures for the rapid and highly accurate solution to certain 2D Laplace and Helmholtz problems for domains with corners. One of the principal tools they use is charge bases, which are small finite orthonormal bases which span the restrictions of solution of the boundary integral equation to a small curve segment which is a subset of the main contour. A detailed algorithm is included on how to construct the charge bases as well as the algorithm of how to construct the quadrature formulae which employ them. In 2012, based on this work, Bremer [86] develops a modified Nyström scheme for the Neumann Laplace problem for domains with corners which is mathematically equivalent to a Galerkin discretisation. He describes a fast direct solver for the solution to scattering from planar curves with corners and demonstrates numerically the efficiency of this technique for convex and concave single-cornered scatterers as well as multi-cornered scatterers. The work concludes with the application of the technique to the combined layer potential solution of the Helmholtz problem with Dirichlet boundary condition for a multi-cornered scatterer (a starburst domain). This work is applicable to the Dirichlet and Neumann problems as well as acoustic scattering at the interface of two fluids. He specifically addresses the acoustic Neumann and Dirichlet problems in [87].

In 2012 Deckers et al. [88] use a wave based method based on Trefftz approach to solve

2D acoustic problems for domains with singularities such as those occurring in corners or at points where the boundary conditions change. They use special purpose enrichment functions to enhance the accuracy of more traditional wave based methods when encountering domains with singularities. In 2015 Sun et al. [89] present a boundary regularised integral equation formulation (BRIEF) solution to the 3D Laplace problem where singularities are removed analytically from the fundamental solution to produce a non-singular formulation of the problem. This removes the need for specialised quadrature resulting in coding effort savings. This method was extended to the acoustic Helmholtz equation in [90].

Of particular interest is a 2014 study performed by Hao et al. [91] comparing the Kapur-Rohklin [92], Kolm-Rohklin [45] and Alpert [93] quadrature rules which are fast multipole method compatible to that of Kress [26] for smooth surfaced scatterers. For the 2D acoustic Helmholtz problem it was demonstrated that the Kress' method solutions were of two to three digits better accuracy. The experiments were for scatterers of 0.5 to 50 wavelengths diameter.

There are software packages that offer different methods of solution to the wave scattering problem. In the early 90's Hamilton et al. [94,95] developed the FastScat program: an object-oriented software package for computing electromagnetic scattering and radiation. Using an object-oriented approach simplified the implementation of numerical techniques such as the fast multipole method. FastScat was used by Canino et al. [95] to implement a high-order Nyström scheme for the 2D and 3D time-harmonic scattering problem. For smooth-surfaced scatterers local corrections were used for discretisation in the vicinity of the kernel singularity. This employed the single-potential formulations for both the Dirichlet and Neumann problems rather than the combined field integral equations. An open source example of software employing boundary element methods is [96], and for multiple scattering problems by discs [97].

In this work, we made use of two software packages: MPSPack [98,99] and TMA-TROM [27,100]. MPSPack was developed by Barnett and Betcke and uses the method of fundamental solutions, choosing Trefftz-type basis functions in such a way as to eliminate the problem of ill-conditioned systems of equations that sometimes result [101]. The software allows modelling of 2D Laplace and Helmholtz boundary value problems

and eigenvalue problems for smooth and polygonal scatterers with Dirichlet, Neumann or impedance loaded boundary conditions [20]. TMATROM is a Matlab object-oriented T-matrix software package developed by Ganesh and Hawkins [102]. The package implements a numerically stable algorithm [103, 104], to compute the T-matrix of a two-dimensional scatterer. A discussion of relevant literature for the T-matrix method used for solving our scattering problems is detailed in Chapter 8.

Two specific works addressing corner rounding are those of Engineer et al. [9] and Epstein and O’Neil [10]. Engineer et al. examine diffraction of high-frequency sound waves from 2D curved slender bodies with Neumann boundary condition as the radius of curvature changes. For this high frequency study they used ray theory and identified additional creeping wave propagation features associated with high-frequency problems.

As is well recognised, rounding the corners of scatterers eliminates the need to deal with the singularities in the corners, and, in 2016 Epstein and O’Neil [10] develop a method to smooth corners of polygonal structures using a rounding algorithm such that the difference in the structures is localised in a small neighbourhood of the corner. To discretise the smoothing, they first use polynomial panels with Gauss-Legendre interpolation nodes, followed by a weighted Nyström method. For the Dirichlet case, the use of a combined single- and double-layer approach and for the Neumann case the single-layer potential. They demonstrate numerically that in both cases, as the size of the region that is rounded near the corners reduces to sub-wavelength, the convergence of the bi-static cross sections is approximately first order. They report for wavelengths approximately 2π and 50π , at distances ranging from 20λ up to 8333λ . Their work concludes with an extension to piecewise smooth boundaries which is used to smooth the corners of 3D polyhedra. The approach used by Epstein and O’Neil differs from ours but the numerical results are consistent with our own. The reported relative errors are of a similar order to our earlier 2015 results [12–14], and they too demonstrate numerically that the difference in the scattered potentials converges as the radius of curvature decreases and that the rate of convergence is dependent on the radius of curvature. For the two examples used in their paper - a structure with interior right-angles and one with interior angles of $\pi/3$ - the rates of convergence correspond to ours. In our work we have made the precise dependence of the rate of convergence on the interior angle of the corner as well as the

radius of curvature, incident wave number and boundary conditions. We have quantified this both numerically and analytically.

An example of current work employing and examining the effect of rounding corners is that of Tzarouchis and his work on plasmonic resonances when the corners of polyhedra are rounded [105, 106]. We also note that the method we use for rounding the corners of our four-cornered polygonal (square) scatterer is similar to that used by Onaka [107], where an equation to round the corners of N -sided polygons with different radii of curvature is presented. Onaka uses it to model precipitates of alloys which naturally have polyhedral shapes with rounded corners. Our method of rounding the lemniscate and two-cornered scatterers studied are our own.

We adopted and then extended the method used in [26] as it produced highly accurate solutions and was not overly complex to implement. The aim of this work is to rigorously examine the effect of corner rounding on the acoustic near- and far-fields and, as such, more complex solutions were not warranted. When we extended our study to arrays of scatterers, we used the TMatROM package with our own forward-solvers to reduce computational load, again allowing us to generate highly accurate solutions. We acknowledge that there has been much work, some of which is mentioned above, addressing the method of handling the corner singularities and computational efficiency which allows for more efficient solutions, as well as methods suitable for high-frequency problems. For readers seeking such methods we refer them to the works mentioned above.

1.2 Thesis Outline

In this thesis we rigorously examine the effect on the resulting scattered field when the corners of scatterers are rounded. In Chapter 2, we describe the various single scatterer problems studied. We examine the geometry of the scatterers, establish the differential equations governing the wave motion of the scattered and incident fields, and describe the boundary conditions encountered in this project. We reformulate the various scattering problems in the form of integral equations and introduce the numerical method that is used in the project: the Nyström method for discretising and solving an integral equation. We detail adaptations of the Nyström method in treating the singular kernels for smooth scatterers as well as the additional techniques required for the singularities in the corners

of the cornered structures. Our work is based on [7, 26] for single-cornered scatterers with Dirichlet boundary condition. We introduce our extension of this technique to scatterers of two and four corners and scatterers with Neumann and impedance loaded boundary conditions.

In Chapter 3, we present the numerical results for the different single-scatterer problems studied and discuss the methods used to determine the accuracy and convergence of our solutions. We establish that graded mesh is essential for discretising smooth surfaced scatterers with small radii of curvature. We examine the deviation of solution and the nature of the differences when corners are rounded when compared to the cornered solution. This is done for both the frequency and the time domain. Most significantly we demonstrate numerically the dependence of the maximum differences in the far-field of a cornered scatterer and its rounded counterpart on the radius of curvature in the rounded corner and the wave number and direction of travel of the illuminating incident plane wave. We establish a set of approximations or bounds for these differences for each of the three boundary conditions studied.

In Chapter 4 we prove analytically the approximations for the maximum differences in the far-fields that were numerically established in Chapter 3. This is achieved by introducing suitable surface parameterisations for the rounded and unrounded scatterers and then analysing the underlying integral equations. This leads to an approximate integral equation for the difference in the surface density, in terms of the difference in the illuminating incident field at corresponding points on each scatterer and of the surface quantity on the sharp cornered object. We take the lemniscate scatterer with right-angled corner and Dirichlet boundary condition studied in Chapter 3 as a test case.

In Chapter 5 the behaviour of three quantities at close proximity to the corner of a scatterer are examined: the total field u^{tot} external to the scatterer, the derivative with respect to the normal $\frac{\partial u^{\text{tot}}}{\partial n}$ measured on the surface of the scatterer and the surface quantity φ . We verify that the numerical schemes described in Chapter 2 produce a valid solution at points very near the scatterer surface, especially in the vicinity of a corner. We conclude this chapter with a numerical examination of the behaviour of the surface quantity φ near the vicinity of the corner for scatterers with Dirichlet and Neumann boundary condition and establish numerically that it can be approximated based on the

wave number k and the distance from the corner along the surface of the scatterer. We then establish the analytical basis for the Neumann result.

Previous chapters measured the impact on near- and far-field scattering, as a function of the radius of curvature in the frequency domain. In Chapter 6 we examine the effect of corner rounding on the far-field in the time domain. For this analysis discrete Fourier transforms are used to shift the previously collected frequency domain data to the time domain.

In Chapter 7 we undertake an analysis of the effect of rounding the corners of scatterers on the near- and far-fields, when the scattering problems studied in Chapter 3 are extended to arrays of two and four scatterers. We demonstrate that the number of quadrature points required on each scatterer for a desired degree of accuracy is nearly the same, whether we are solving a single or multiple scatterer problem. We examine the relative differences of the far-field solutions produced by arrays of two and four scatterers and compare them to the single scatterer results. We conclude by examining the bounds of the far-field differences and determine the relationship to those established in Section 3.7 for single scatterers. The classical coupling method used for the work in this chapter, combined with the Nyström scheme using graded mesh produces highly accurate solutions but is computationally demanding as the number of scatterers increases. For investigations into larger scatterer arrays alternative methods were considered.

One such method is to use a software package. In Chapter 8 we examine the TMA-TROM package [27, 100] - a Matlab object-oriented T-matrix software package, the advantages that its use provides as well as some limitations. We outline our implementation which includes incorporating our own forward solvers for cornered scatterers and conclude with a detailed verification of the results of earlier work. As part of the verification process we also employ the MPSPack software [98, 99].

In Chapter 9 we use the TMA-TROM package with our own forward solvers to examine larger scatterer arrangements of up to 256 scatterers.

Chapter 2

Problem Formulation

In this chapter we describe the various direct scattering problems studied. We examine the geometries of the scatterers, establish the differential equations governing the wave motion of the scattered and incident fields, and describe the three boundary conditions, Dirichlet, Neumann and impedance loaded, that characterise the scatterers encountered in this work.

With few exceptions, analytical expressions for the scattered field from non-circular scatterers cannot be obtained. A selection of various canonical scattering problems and their analytical solutions is collected in [1]. We reformulate the various scattering problems in the form of integral equations that are the basis for the development of numerical methods for the scattering from a rather general class of closed (non-circular) scatterers. The integral equation form uses a Green's function which has a singularity that is of logarithmic order.

We transform the integral equation formulations into one-dimensional line integral format. This enables the application of numerical methods to solve the relevant integral equation and subsequently compute the scattered field. Next, we introduce the numerical method, based on [7, 26], that is used in this thesis: the Nyström method for discretising and solving an integral equation. It should also be noted that the standard Gaussian elimination method is also frequently employed in our calculations as a means of solving a system of linear equations, resulting from discretisation.

The kernels of the integral equation form of our solution have an integrable logarithmic singularity. We detail an adaptation of the Nyström method in treating these

singular kernels. This works well for objects with smooth boundaries, but as is well understood, these methods are not adequate for producing convergent solutions for domains with corners. The adaptation [26] of the approach for a scatterer with a single corner and Dirichlet boundary condition introduces a graded mesh and subtracts a vanishing term to compensate for the strong singularity in the corner. The solutions employing this method exhibit super-algebraic convergence. We extend this technique to scatterers of two and four corners by employing our own graded mesh and developing a method of distributing the effect of subtracting the vanishing term from each corner.

The works [7, 26] concern smooth and single-cornered scatterers with a Dirichlet boundary condition. We used this as a basis to develop methods for scatterers with Neumann and impedance loaded boundary conditions using a single-layer potential as the solution to these problems. This approach was also used for the Neumann problem by [10] subsequent to our earlier work [13]. To the best of our knowledge it has not been used as a solution to the impedance loaded problem to date. For smooth scatterers with Neumann boundary condition, Kress [60] uses the combined potentials, and later in [61] uses the double-layer potential. For cornered scatterers with Neumann boundary condition the works [15, 15, 62, 86] use the combined potentials or other techniques. For the impedance loaded problem the paper [68] uses the combined potentials for smooth scatterers, as does [16] in the case of cornered scatterers.

2.1 The Scatterers

Consider an infinitely long cylinder with uniform cross-section. Without loss of generality we assume that the axis of the cylinder is parallel to the z -axis. The cylinder is illuminated by an incident plane wave propagating with direction parallel to the x - y plane. The cross-section D lying in the x - y plane has a closed boundary ∂D parameterised in the form

$$\mathbf{x}(t) = (x_1(t), x_2(t)), \quad t \in [0, 2\pi]. \quad (2.1)$$

In this work, we consider three classes of scatterers with one, two or four corners, respectively, and the scatterers that result after the corners have been rounded (see Figure 2.1). They have been chosen to give some flexibility and diversity in the number

of corners and size of the angle in the corner.

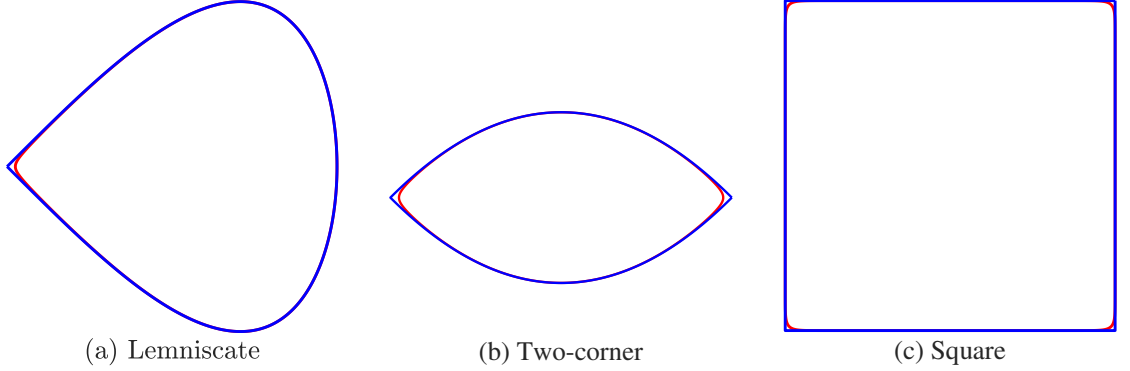


Figure 2.1: The different scatterers considered in this work. Those with sharp corners are shown in blue. The rounded scatterers with radius of curvature $\rho \approx 0.05$ are shown in red.

First, the single-cornered scatterer (lemniscate) has parametric representation

$$\mathbf{x} = \mathbf{x}(t) = a(2 \sin(t/2), -\sin t), \quad t \in [0, 2\pi], \quad (2.2)$$

where a is a parameter, henceforth set equal to 1 length unit. The right-angled corner occurs at $t = 0$. The families of curves in which the corners have been rounded are parameterised by the quantity ε ($0 \leq \varepsilon \leq 1$). The rounded lemniscate has representation

$$\mathbf{x} = \mathbf{x}(t) = a \left(2\sqrt{\varepsilon^2 + (1 - \varepsilon^2) \sin^2(t/2)}, -\sin t \right), \quad t \in [0, 2\pi]. \quad (2.3)$$

The two-cornered scatterer is described by the parametric representation

$$\mathbf{x} = \mathbf{x}(t) = a(\cos t, \sin t) / (1 + |\sin t|), \quad t \in [0, 2\pi], \quad (2.4)$$

where a is a parameter, henceforth set equal to 1 length unit, with corners at $t = 0$ and $t = \pi$. The rounding is achieved using the representation

$$\mathbf{x} = \mathbf{x}(t) = a \left(\frac{\cos t}{1 + \sqrt{\varepsilon^2 + \sin^2 t}}, \frac{\sin t}{1 + \sqrt{\varepsilon^2 + \sin^2 t}} \right), \quad t \in [0, 2\pi]. \quad (2.5)$$

The four-cornered scatterer has parametric representation

$$\mathbf{x} = \mathbf{x}(t) = (a(\cos t - \sin t), b(\cos t + \sin t)) / \hat{R}, \quad (2.6)$$

where $\hat{R} = (|\cos t| + |\sin t|)$, so that corners occur at $t = 0, \pi/2, \pi$ and $3\pi/2$ respectively. Henceforth the parameters a and b are set equal to 1 length unit, so that the resultant shape is a square. The corners are rounded using the representation

$$\mathbf{x}(t) = (\cos \hat{t}, \sin \hat{t}) / R, \quad (2.7)$$

where $\hat{t} = t + \pi/4$ and

$$R = \begin{cases} |\sin \hat{t}| \left(1 + (\cot \hat{t})^{1/\varepsilon}\right)^\varepsilon & \text{for } \hat{t} \in I = [\frac{\pi}{4}, \frac{3\pi}{4}] \cup [\frac{5\pi}{4}, \frac{7\pi}{4}], \\ |\cos \hat{t}| \left(1 + (\tan \hat{t})^{1/\varepsilon}\right)^\varepsilon & \text{for } \hat{t} \in [0, 2\pi] \setminus I, \end{cases} \quad (2.8)$$

and ε is restricted to $0 < \varepsilon \leq 1$.

The corners of the above scatterers all have an interior right angle. We also consider scattering structures with corners that are not right-angles: convex structures with acute and obtuse interior angles as well as concave structures.

The following modification made to the lemniscate (2.2) allows for different acute interior angles β ,

$$\mathbf{x} = \mathbf{x}(t) = a \left(2 \sin \left(\frac{t}{2} \right), -\tan \left(\frac{\beta}{2} \right) \sin t \right), \quad t \in [0, 2\pi], \quad (2.9)$$

where $0 < \beta < \pi/2$.

The following modification made to (2.2) models single-cornered scatterers with an obtuse interior angle β ,

$$\mathbf{x} = \mathbf{x}(t) = a \left(2 \tan \left(\frac{\pi - \beta}{2} \right) \sin \left(\frac{t}{2} \right), -\sin t \right), \quad t \in [0, 2\pi], \quad (2.10)$$

where $\pi/2 < \beta < \pi$.

The parametric representation

$$\mathbf{x} = \mathbf{x}(t) = a \left(-\sin \left(\frac{3t}{2} \right), -\tan \left(\pi - \frac{\beta}{2} \right) \sin t \right), \quad t \in [0, 2\pi], \quad (2.11)$$

models a single-cornered concave scatterer with an interior (reflex) angle $3\pi/2 \leq \beta < 2\pi$,

and the representation

$$\mathbf{x} = \mathbf{x}(t) = a \left(\tan \left(\frac{\pi - \beta}{2} \right) \sin \left(\frac{3t}{2} \right), -\sin t \right), \quad t \in [0, 2\pi], \quad (2.12)$$

models single-cornered concave scatterers with shallower reflex angles, $\pi \leq \beta < 3\pi/2$. The corner occurs at $t = 0$ for all the described non-right angled scatterers. Figure 2.2 illustrates these shapes with differing interior angles.

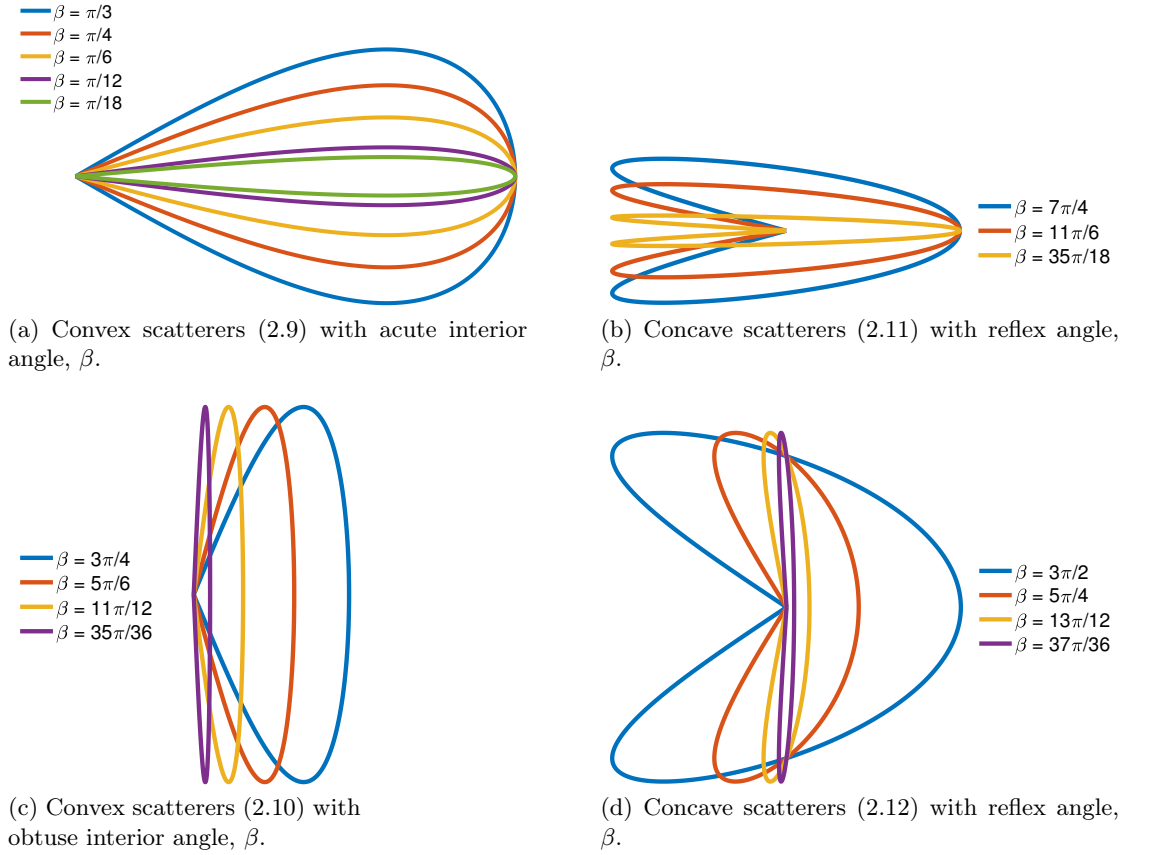


Figure 2.2: Single-cornered scatterers with different interior angles, β .

2.1.1 Radius of Curvature

The radius of curvature ρ at the point $(x_1(t), x_2(t))$ is calculated from the standard formula

$$\rho(t) = \left| \frac{(x_1'(t)^2 + x_2'(t)^2)^{3/2}}{x_1'(t)x_2''(t) - x_2'(t)x_1''(t)} \right|, \quad t \in [0, 2\pi]. \quad (2.13)$$

Table 2.1 lists approximate radius of curvature ρ at the corner point and the corresponding value of the rounding parameter ε that is required in the parametric representations

(2.3), (2.5), (2.7) for the three different cornered scatterers.

$\sim \rho$	Rounding parameter, ε		
	Lemniscate	Two-corner	Square
0.05	0.025	0.053	0.036
0.04	0.02	0.042	0.028
0.03	0.015	0.031	0.021
0.02	0.01	0.021	0.014
0.01	0.005	0.01	0.008

Table 2.1: Radii of curvature corresponding to rounding parameter ε used in the parameterisations of different scatterers.

2.2 The Incident and Scattered Fields

The incident field illuminating the scatterer induces a scattered field. We assume that the incident and scattered fields are time harmonic with a temporal factor $e^{-i\omega t}$. The spatial component $u^{\text{inc}}(x, y)$ of the incident wave travelling in the direction of the unit vector $\mathbf{d} = (\cos \theta_0, \sin \theta_0)$ takes the form

$$u^{\text{inc}}(x, y) = e^{ik\mathbf{x} \cdot \mathbf{d}}, \quad (2.14)$$

and satisfies the Helmholtz equation

$$\Delta u(x, y) + k^2 u(x, y) = 0, \quad (x, y) \in \mathbb{R}^2, \quad (2.15)$$

where $k = \omega/c$ is the wave number and c is the speed of waves in the medium or of light in free space.

The spatial component $u^{\text{sc}}(x, y)$ of the scattered field obeys the Helmholtz equation (2.15) at all points (x, y) exterior to the body; moreover it obeys the two-dimensional form of the Sommerfeld radiation condition

$$\lim_{|\mathbf{x}| \rightarrow \infty} \sqrt{|\mathbf{x}|} \left(\frac{\partial u^{\text{sc}}(\mathbf{x})}{\partial \mathbf{x}} - ik u^{\text{sc}}(\mathbf{x}) \right) = 0, \quad \mathbf{x} \in \mathbb{R}^2 \setminus D, \quad (2.16)$$

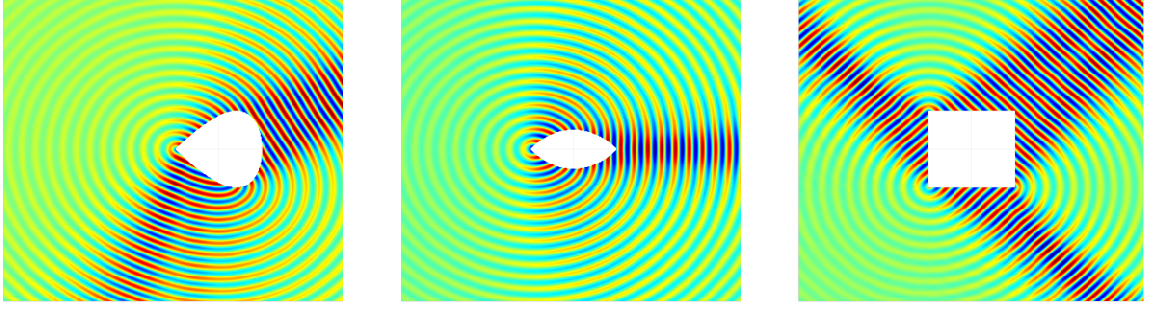


Figure 2.3: The scattered field, $\text{Re}(u^{\text{sc}})$, for the three scatterers with Dirichlet boundary condition. Direction of the incident wave $\theta_0 = \pi/6, 0$ and $\pi/4$, respectively.

as well as the finiteness of energy condition

$$\int_V \left(k^2 |u^{\text{sc}}|^2 + |\nabla u^{\text{sc}}|^2 \right) dV < \infty, \quad (2.17)$$

where V denotes any bounded volume containing the scatterer D .

2.3 The Boundary Conditions

The nature of the scatterer imposes certain conditions that must be satisfied by the total field

$$u^{\text{tot}} = u^{\text{inc}} + u^{\text{sc}}, \quad (2.18)$$

on the boundary of the scatterer ∂D . This work considers three different boundary conditions:

$$u^{\text{tot}}(\mathbf{x}) = 0, \quad \mathbf{x} \in \partial D, \quad (\text{sound-soft, E-polarised, Dirichlet}) \quad (2.19)$$

$$\frac{\partial u^{\text{tot}}}{\partial \mathbf{n}}(\mathbf{x}) = 0, \quad \mathbf{x} \in \partial D, \quad (\text{sound-hard, H-polarised, Neumann}) \quad (2.20)$$

$$\frac{\partial u^{\text{tot}}}{\partial \mathbf{n}}(\mathbf{x}) + ikZu^{\text{tot}}(\mathbf{x}) = 0, \quad \mathbf{x} \in \partial D, \quad (\text{impedance loaded}) \quad (2.21)$$

where $\mathbf{n}(x)$ is the unit outward normal to the boundary ∂D at the point \mathbf{x} and $Z = Z(\mathbf{x})$ is a continuous function of position. To ensure uniqueness $\text{Re}(Z)$ must be positive on the boundary ∂D . Throughout, we restrict Z to be a complex constant.

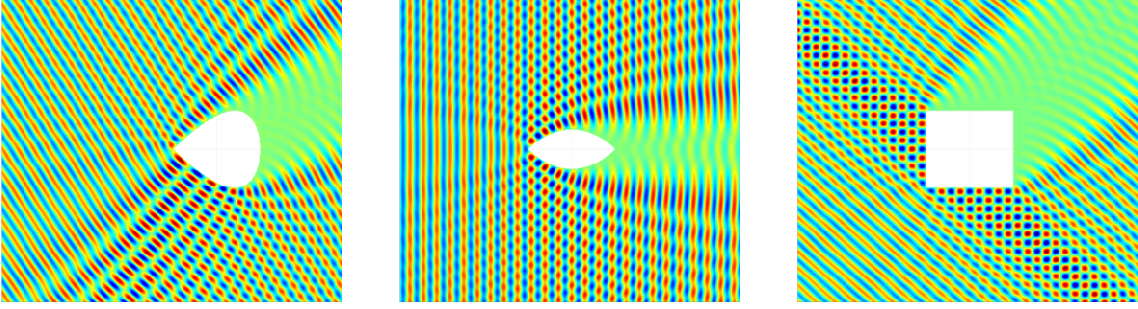


Figure 2.4: The total field, $\text{Re}(u^{\text{tot}})$, for the three scatterers with Dirichlet boundary condition. Direction of the incident wave $\theta_0 = \pi/6, 0$ and $\pi/4$, respectively.

2.4 Integral Representations

In this section we introduce various concepts and results that we will draw upon in future sections.

Classical domain methods, such as the finite-difference method or finite-element method, which are used for numerically solving partial differential equations, require the division of the domain into a finite number of grid points or sub-domains. Typically, a minimum of $5/\lambda$ to $10/\lambda$ grid points per linear dimension is needed for solutions of acceptable accuracy, where λ is the wavelength. Thus the number of grid points in a two dimensional domain is proportional to $1/\lambda^2$. This results in a linear system of order $O(1/\lambda^2)$ equations to be solved. By reformulating the scattering problem as integral equations, we are able to reduce the problem to one that solves for an unknown function on the boundary of the scatterer ∂D rather than in space. After discretisation, the problem is reduced to one of order $O(1/\lambda)$ linear equations.

A further consideration is that the scattering problem is set in unbounded space. Using one of the classical domain methods will require the imposition of an artificial boundary with suitable boundary conditions to approximate the Sommerfeld radiation condition (2.16). The reformulation of the problem as a boundary value problem auto-

matically incorporates exactly the Sommerfeld radiation condition.

In this section we define the acoustic single- and double-layer potentials and explore certain properties of these potentials on the boundary of the scatterer. We then use these potentials to reformulate the boundary value problems described in Section 2.3 into integral equation form. Our integral equation form uses the free space Green's function, which has a logarithmic singularity on the surface of the scatterer; it is thus integrable.

2.4.1 Single-layer and Double-layer Potentials

Two integral representations of solutions to the Helmholtz equation (2.15) are the acoustic single-layer potential and the acoustic double-layer potential.

Definition 2.4.1 The acoustic single-layer potential u with integrable density φ is

$$u(\mathbf{x}) = \int_{\partial D} G(\mathbf{x}, \mathbf{y}) \varphi(\mathbf{y}) \, ds(\mathbf{y}), \quad \mathbf{x} \in \mathbb{R}^2 \setminus \partial D, \quad (2.22)$$

where G is the the two-dimensional free-space Green's function

$$G(\mathbf{x}, \mathbf{y}) = \frac{i}{4} H_0^{(1)}(k |\mathbf{x} - \mathbf{y}|), \quad (2.23)$$

and $H_0^{(1)}$ denotes the Hankel function of first kind and order zero. The Green's function satisfies the Helmholtz equation (2.15) everywhere except at $\mathbf{x} = \mathbf{y}$, and satisfies the Sommerfeld radiation condition (2.16). The acoustic single-layer potential is continuous and bounded throughout $\mathbb{R}^2 \setminus \partial D$.

Definition 2.4.2 The acoustic double-layer potential v with integrable density φ is

$$v(\mathbf{x}) = \int_{\partial D} \frac{\partial G(\mathbf{x}, \mathbf{y})}{\partial \mathbf{n}(\mathbf{y})} \varphi(\mathbf{y}) \, ds(\mathbf{y}), \quad \mathbf{x} \in \mathbb{R}^2 \setminus \partial D, \quad (2.24)$$

where

$$\frac{\partial G(\mathbf{x}, \mathbf{y})}{\partial \mathbf{n}(\mathbf{y})} = \nabla_{\mathbf{y}} G(\mathbf{x}, \mathbf{y}) \cdot \mathbf{n}(\mathbf{y}), \quad (2.25)$$

is the normal derivative of the Green's function with respect to the outward unit normal $\mathbf{n}(\mathbf{y})$ at \mathbf{y} . Both the single- and double-layer potentials are solutions to the Helmholtz

equation in D and satisfy the Sommerfeld radiation condition (2.16) in $\mathbb{R}^2 \setminus \bar{D}$. Any solution of the Helmholtz equation can be represented as a combination of these two potentials [7, p.40].

The Green's function (2.23) has a singularity when $\mathbf{x} = \mathbf{y}$. In Appendix A.1 we show that this singularity is logarithmic and as such integrable.

The single- and double-layer potentials are defined on $\mathbb{R}^2 \setminus \partial D$. To enforce the boundary conditions on ∂D , we continuously extend these functions to the boundary of the scatterer ∂D . The behaviour of these potentials as \mathbf{x} approaches a point on ∂D , where the integrals become singular, is given by the jump relations.

2.4.2 The Jump Relations

Theorem 2.4.1 [7, p.40] *Let ∂D be of class C^2 and let φ be continuous on ∂D . The single-layer potential u with density φ is continuous throughout \mathbb{R}^2 and on the boundary is defined by the convergent integral*

$$u(\mathbf{x}) = \int_{\partial D} G(\mathbf{x}, \mathbf{y}) \varphi(\mathbf{y}) \, ds(\mathbf{y}), \quad \mathbf{x} \in \partial D. \quad (2.26)$$

Also

$$\frac{\partial u_{\pm}}{\partial \mathbf{n}}(\mathbf{x}) = \int_{\partial D} \frac{\partial G(\mathbf{x}, \mathbf{y})}{\partial \mathbf{n}(\mathbf{x})} \varphi(\mathbf{y}) \, ds(\mathbf{y}) \mp \frac{\varphi(\mathbf{x})}{2}, \quad \mathbf{x} \in \partial D, \quad (2.27)$$

where

$$\frac{\partial u_{\pm}}{\partial \mathbf{n}}(\mathbf{x}) = \lim_{h \rightarrow 0^+} \mathbf{n}(\mathbf{x}) \cdot \text{grad } u(\mathbf{x} \pm h \mathbf{n}(\mathbf{x})), \quad (2.28)$$

is to be understood in the sense of uniform convergence on ∂D and where the integrals exist as improper integrals.

The double-layer potential v with density φ can be continuously extended from D to \bar{D} and from $\mathbb{R}^2 \setminus \partial \bar{D}$ to $\mathbb{R}^2 \setminus \partial D$ with limiting values

$$v_{\pm}(\mathbf{x}) = \int_{\partial D} \frac{\partial G(\mathbf{x}, \mathbf{y})}{\partial \mathbf{n}(\mathbf{y})} \varphi(\mathbf{y}) \, ds(\mathbf{y}) \pm \frac{\varphi(\mathbf{x})}{2}, \quad \mathbf{x} \in \partial D, \quad (2.29)$$

where

$$v_{\pm}(\mathbf{x}) = \lim_{h \rightarrow +0} v(\mathbf{x} \pm h \mathbf{n}(\mathbf{x})), \quad (2.30)$$

and where the integral exists as an improper integral. Furthermore,

$$\lim_{h \rightarrow 0} \left\{ \frac{\partial v}{\partial \mathbf{n}}(x + h\mathbf{n}(\mathbf{x})) - \frac{\partial v}{\partial \mathbf{n}}(x - h\mathbf{n}(\mathbf{x})) \right\} = 0, \quad \mathbf{x} \in \partial D, \quad (2.31)$$

uniformly on ∂D .

2.4.3 Integral Operators

We define two operators associated with the single- and double-layer potentials of a continuous density $\varphi(\mathbf{y})$ defined on the boundary ∂D ,

$$(\mathcal{S}\varphi)(\mathbf{x}) = 2 \int_{\partial D} G(\mathbf{x}, \mathbf{y}) \varphi(\mathbf{y}) \, ds(\mathbf{y}), \quad \mathbf{x} \in \mathbb{R}^2, \quad (2.32)$$

$$(\mathcal{K}\varphi)(\mathbf{x}) = 2 \int_{\partial D} \frac{\partial G(\mathbf{x}, \mathbf{y})}{\partial \mathbf{n}(\mathbf{y})} \varphi(\mathbf{y}) \, ds(\mathbf{y}), \quad \mathbf{x} \in \mathbb{R}^2; \quad (2.33)$$

their normal derivatives are, respectively

$$(\mathcal{K}'\varphi)(\mathbf{x}) = 2 \int_{\partial D} \frac{\partial G(\mathbf{x}, \mathbf{y})}{\partial \mathbf{n}(\mathbf{x})} \varphi(\mathbf{y}) \, ds(\mathbf{y}), \quad \mathbf{x} \in \partial D, \quad (2.34)$$

$$(\mathcal{T}\varphi)(\mathbf{x}) = 2 \frac{\partial}{\partial \mathbf{n}(\mathbf{x})} \int_{\partial D} \frac{\partial G(\mathbf{x}, \mathbf{y})}{\partial \mathbf{n}(\mathbf{y})} \varphi(\mathbf{y}) \, ds(\mathbf{y}), \quad \mathbf{x} \in \partial D. \quad (2.35)$$

For $\mathbf{x} \in \partial D$ the limiting values of the integral operators (2.32) and (2.33) are

$$\lim_{\mathbf{x}' \rightarrow \mathbf{x}} (\mathcal{S}\varphi)(\mathbf{x}') = 2 \int_{\partial D} G(\mathbf{x}, \mathbf{y}) \varphi(\mathbf{y}) \, ds(\mathbf{y}), \quad (2.36)$$

$$\lim_{h \rightarrow 0^+} (\mathcal{K}\varphi)(\mathbf{x} \pm h\mathbf{n}) = 2 \int_{\partial D} \frac{\partial G(\mathbf{x}, \mathbf{y})}{\partial \mathbf{n}(\mathbf{y})} \varphi(\mathbf{y}) \, ds(\mathbf{y}) \pm \varphi(\mathbf{x}), \quad (2.37)$$

and we apply (2.27) and (2.28) to (2.32), so that for $\mathbf{x} \in \partial D$

$$\frac{\partial (\mathcal{S}\varphi)_{\pm}}{\partial \mathbf{n}(\mathbf{x})}(\mathbf{x}) = 2 \int_{\partial D} \frac{\partial G(\mathbf{x}, \mathbf{y})}{\partial \mathbf{n}(\mathbf{x})} \varphi(\mathbf{y}) \, ds(\mathbf{y}) \mp \varphi(\mathbf{x}). \quad (2.38)$$

We note that the integral operators (2.32), (2.33), (2.34) and (2.35) are compact [56, p.61] when the boundary ∂D is smooth.

2.4.4 Integral Representations of the Boundary Value Problems

We reformulate the boundary value problems described in Section 2.3 into integral equation form.

2.4.4.1 The Exterior Dirichlet Problem

The solution to the exterior Dirichlet problem for all $\mathbf{x} \in \mathbb{R}^2 \setminus \bar{D}$, is based on representing the scattered field as a combination of the single- and double-layer potentials

$$u^{\text{sc}}(\mathbf{x}) = \int_{\partial D} \left\{ \frac{\partial G(\mathbf{x}, \mathbf{y})}{\partial \mathbf{n}(\mathbf{y})} - i\eta G(\mathbf{x}, \mathbf{y}) \right\} \varphi(\mathbf{y}) \, ds(\mathbf{y}), \quad \mathbf{x} \in \mathbb{R}^2 \setminus \bar{D}, \quad (2.39)$$

where η is a coupling parameter. We use the Dirichlet boundary condition (2.19) and the jump relations for the single- and double-layer potentials, (2.26) and (2.29), to obtain the integral equation

$$\frac{\varphi(\mathbf{x})}{2} + \int_{\partial D} \left\{ \frac{\partial G(\mathbf{x}, \mathbf{y})}{\partial \mathbf{n}(\mathbf{y})} - i\eta G(\mathbf{x}, \mathbf{y}) \right\} \varphi(\mathbf{y}) \, ds(\mathbf{y}) = -u^{\text{inc}}(\mathbf{x}), \quad \mathbf{x} \in \partial D, \quad (2.40)$$

for which the unknown continuous density φ is a solution. In operator form we write

$$I\varphi + \mathcal{K}\varphi - i\eta \mathcal{S}\varphi = g, \quad (2.41)$$

where $g = -2u^{\text{inc}}$. This integral equation is uniquely solvable for all wave numbers satisfying $\text{Im } k \geq 0$ [56, p.91] when η is positive. To minimise the condition number of (2.41) we set the coupling parameter η to the value k as recommended in [108].

2.4.4.2 The Exterior Neumann Problem

The single-layer potential

$$u^{\text{sc}}(\mathbf{x}) = \int_{\partial D} G(\mathbf{x}, \mathbf{y}) \varphi(\mathbf{y}) \, ds(\mathbf{y}), \quad \mathbf{x} \in \mathbb{R}^2 \setminus \bar{D}, \quad (2.42)$$

with continuous density φ is a solution to the exterior Neumann problem for all $\mathbf{x} \in \mathbb{R}^2 \setminus \bar{D}$ [109, p.95], provided φ is a solution of

$$-\frac{\varphi(\mathbf{x})}{2} + \int_{\partial D} \frac{\partial G(\mathbf{x}, \mathbf{y})}{\partial \mathbf{n}(\mathbf{x})} \varphi(\mathbf{y}) \, ds(\mathbf{y}) = -\frac{\partial u^{\text{inc}}}{\partial \mathbf{n}(\mathbf{x})}, \quad \mathbf{x} \in \partial D. \quad (2.43)$$

We use the Neumann boundary condition (2.20) and the jump relation for the normal derivative of the single-layer potential (2.27) to derive this equation. In operator form we write

$$-\varphi + \mathcal{K}'\varphi = h, \quad (2.44)$$

where

$$h(\mathbf{x}) = -2 \frac{\partial u^{\text{inc}}}{\partial \mathbf{n}}(\mathbf{x}), \quad \mathbf{x} \in \partial D \quad (2.45)$$

and $\varphi(x)$ satisfies

$$\int_{\partial D} \varphi \, ds = 0, \quad (2.46)$$

when $D \in \mathbb{R}^2$. Further, in \mathbb{R}^2 , the exterior Neumann problem is uniquely solvable if and only if

$$\int_{\partial D} h \, ds = 0, \quad (2.47)$$

is satisfied [109, p.95] and that k is not an interior Dirichlet eigenvalue [56, p.98].

2.4.4.3 The Exterior Impedance Problem

The single-layer potential

$$u^{\text{sc}}(\mathbf{x}) = \int_{\partial D} G(\mathbf{x}, \mathbf{y}) \varphi(\mathbf{y}) \, ds(\mathbf{y}), \quad \mathbf{x} \in \mathbb{R}^2 \setminus \bar{D}, \quad (2.48)$$

is a solution to the exterior impedance problem for all $\mathbf{x} \in \mathbb{R}^2 \setminus \bar{D}$ [56, p.98]. We use the impedance boundary condition (2.21) and the jump relation for the normal derivative of the single-layer potential (2.27), thus obtaining the integral equation

$$-\frac{\varphi(\mathbf{x})}{2} + \int_{\partial D} \frac{\partial G(\mathbf{x}, \mathbf{y})}{\partial \mathbf{n}(\mathbf{x})} \varphi(\mathbf{y}) \, ds(\mathbf{y}) + ikZ \int_{\partial D} G(\mathbf{x}, \mathbf{y}) \varphi(\mathbf{y}) \, ds(\mathbf{y}) = -\frac{\partial u^{\text{inc}}}{\partial \mathbf{n}}(\mathbf{x}) - ikZ u^{\text{inc}}(\mathbf{x}),$$

$$\mathbf{x} \in \partial D, \quad (2.49)$$

for which the unknown continuous density φ is a solution. In operator form we write

$$-\varphi + \mathcal{K}'\varphi + ikZ\mathcal{S}\varphi = m, \quad (2.50)$$

where

$$m(\mathbf{x}) = -2 \left(\frac{\partial u^{\text{inc}}}{\partial \mathbf{n}}(\mathbf{x}) + ikZ u^{\text{inc}}(\mathbf{x}) \right), \quad \mathbf{x} \in \partial D. \quad (2.51)$$

This solution is unique provided that k is not an interior Dirichlet eigenvalue [56, p.98].

Uniqueness is guaranteed by considering a suitable combination of single- and double-layer potentials, ie the combined potential

$$u^{\text{sc}}(\mathbf{x}) = \int_{\partial D} \left\{ \frac{\partial G(\mathbf{x}, \mathbf{y})}{\partial \mathbf{n}(\mathbf{y})} - i\eta G(\mathbf{x}, \mathbf{y}) \right\} \varphi(\mathbf{y}) \, ds(\mathbf{y}), \quad \mathbf{x} \in \mathbb{R}^2 \setminus \bar{D}, \quad (2.52)$$

where $\eta \neq 0$ solves the exterior impedance problem uniquely provided that the density $\varphi(\mathbf{x}) \in \partial D$ is a solution of

$$(1 - i\eta Z) \varphi - (\mathcal{K}' + i\eta \mathcal{T} + i\eta Z\mathcal{K} + Z\mathcal{S}) \varphi = -m, \quad (2.53)$$

for all wave numbers $\text{Im } k \geq 0$ [56, p.98].

2.5 Numerical Solution

In this section we outline the numerical method used to solve the boundary value problem representations defined in the previous section.

2.5.1 Transformation into Line Integrals

Using the boundary parametrisation (2.1), the operator $\mathcal{S}\varphi$ (2.32) may be expressed as

$$(\mathcal{S}\varphi)(\mathbf{x}(t)) = \int_0^{2\pi} S_0(t, \tau) \varphi(\tau) |\mathbf{x}'(\tau)| d\tau, \quad (2.54)$$

where the kernel $S_0(t, \tau) = 2G(\mathbf{x}(t), \mathbf{x}(\tau))$ and

$$|\mathbf{x}'(\tau)| = \sqrt{(x'_1(\tau))^2 + (x'_2(\tau))^2}. \quad (2.55)$$

Similarly, the operators $\mathcal{K}\varphi$ (2.33) and $\mathcal{K}'\varphi$ (2.34) generate associated kernels $K_0(t, \tau)$, $K'_0(t, \tau)$.

Thus the integral equation formulation (2.41) of the exterior Dirichlet problem is transformed into the parametric operator form

$$\varphi(t) + \int_0^{2\pi} \{K_0(t, \tau) - i\eta S_0(t, \tau)\} \varphi(\tau) |\mathbf{x}'(\tau)| d\tau = 2g(t), \quad 0 \leq t \leq 2\pi; \quad (2.56)$$

the formulation (2.44) of the exterior Neumann problem takes the parametric form

$$-\varphi(t) + \int_0^{2\pi} K'_0(t, \tau) \varphi(\tau) |\mathbf{x}'(\tau)| d\tau = 2h(t), \quad 0 \leq t \leq 2\pi; \quad (2.57)$$

and the formulation (2.50) of the exterior impedance problem takes the parametric form

$$-\varphi(t) + \int_0^{2\pi} \{K'_0(t, \tau) + ikZS_0(t, \tau)\} \varphi(\tau) |\mathbf{x}'(\tau)| d\tau = 2m(t), \quad 0 \leq t \leq 2\pi. \quad (2.58)$$

2.5.2 Nyström Method

The Nyström method outlined in [7, 26] is used to numerically approximate the solution to the integral equations (2.56), (2.57) and (2.58).

A method developed by Martensen [58] and Kussmaul [59] and outlined in [26] for the logarithmic singularities arising in (2.56), (2.57) and (2.58) was employed: the singular parts of the kernels $S_0(t, \tau)$, $K_0(t, \tau)$ and $K'_0(t, \tau)$ are isolated in the following manner so that

$$\hat{K}_0(t, \tau) = \hat{K}_1(t, \tau) \ln \left(4 \sin^2 \frac{t - \tau}{2} \right) + \hat{K}_2(t, \tau), \quad (2.59)$$

where \hat{K}_1, \hat{K}_2 are analytic. The smooth components of the kernels are approximated using the trapezoidal rule and the logarithmically singular kernels are approximated using a weighted trigonometric interpolation quadrature. The resulting system of $2n$ linear equations is a discretisation of the integral equations (2.41), (2.44) and (2.50). Fuller details of the Nyström and Martensen/Kusmaul methods used are provided in Appendix A.2.

2.5.3 Surface Discretisation

Four different spacings of the $2n$ mesh points were used. For smooth scatterers we began by using a mesh of $2n$ uniformly spaced points $t_j = \pi j/n$, for $j = 0, 1, \dots, 2n - 1$, in the parametrisation (2.1). However, for domains with corners, the solutions to (2.41), (2.44) and (2.50) have singularities in the derivatives in the corners. To deal with these singularities, the uniform mesh is replaced by a non-uniform graded mesh [7, 26]. This is achieved by substituting a new variable such that the derivatives of the transformed integrand vanish up to a certain order at the corners and following [7, 26] approximately half of the quadrature points are uniformly distributed around the surface of the scatterer between the corners and the other half are concentrated at the corners. Thus for any function $f(t)$, its definite integral over $[0, 2\pi]$ is evaluated by the trapezoidal quadrature rule after the substitution $t = w(s)$ by the appropriately chosen function $w(s)$:

$$\int_0^{2\pi} f(t) dt = \int_0^{2\pi} f(w(s)) w'(s) ds \approx \frac{\pi}{n} \sum_{j=1}^{2n-1} a_j f(s_j), \quad (2.60)$$

with weights $a_j = w'(t_j)$ and mesh points $s_j = w(t_j)$.

For domains with corners, the corners are assumed to be located at the points \mathbf{x}_i on the scatterer boundary ∂D , and $\partial D \setminus \bigcup \{\mathbf{x}_i\}$ is assumed to be C^2 and piecewise analytic. The angle γ_i at the corners is assumed to lie in the interval $0 < \gamma_i < 2\pi$. The function $w(s)$ must be strictly monotonically increasing between the corners and the derivatives at the corners must vanish up to some order p .

For a domain with a single corner, the function $w(s)$ recommended by [7, 26] is

$$w(s) = 2\pi \frac{[v(s)]^p}{[v(s)]^p + [v(2\pi - s)]^p}, \quad 0 \leq s \leq 2\pi, \quad (2.61)$$

where

$$v(s) = \left(\frac{1}{p} - \frac{1}{2}\right) \left(\frac{\pi - s}{\pi}\right)^3 + \frac{1}{p} \frac{s - \pi}{\pi} + \frac{1}{2}, \quad (2.62)$$

for some integer $p \geq 2$. In this study we use the value $p = 8$ following the recommendation of [7, 26].

The required substitution is applied to the discretisation of (2.54) by setting $t = w(s)$ and $\tau = w(\sigma)$ to obtain

$$\int_0^{2\pi} S_0(t, \tau) \varphi(\tau) d\tau = \int_0^{2\pi} S_0(w(s), w(\sigma)) \varphi(w(\sigma)) w'(\sigma) d\sigma. \quad (2.63)$$

and (2.59) such that

$$\hat{K}_0(w(s), w(\sigma)) = \hat{K}_1(s, \sigma) \ln \left(4 \sin^2 \frac{s - \sigma}{2} \right) + \hat{K}_2(s, \sigma). \quad (2.64)$$

The kernels $\hat{K}_1(s, \sigma)$ and $\hat{K}_2(s, \sigma)$ are analytic. The operator is now discretised using the points $s_j = w(t_j)$ and weights $a_j = w'(t_j)$. Fuller details are in [7].

To create a graded mesh for the two and four-cornered scatterers we require functions which are strictly monotonically increasing between each corner point with derivatives that vanish at the corners up to some order p , and that ensure that the quadrature points are densely clustered around each corner. In this case we choose $p = 6$. For a domain with two corners, our choice of the function $w(s)$ is

$$w(s) = s - \frac{3}{4} \sin 2s + \frac{3}{20} \sin 4s - \frac{1}{60} \sin 6s, \quad 0 \leq s \leq 2\pi, \quad (2.65)$$

and for a domain with four corners

$$w(s) = s - \frac{3}{8} \sin 4s + \frac{3}{40} \sin 8s - \frac{1}{120} \sin 12s. \quad (2.66)$$

The appropriate substitution is applied to the kernels S_0 , K_0 or K'_0 and is then discretised as before. Fuller details are in [7, 13, 26].

The application of the quadrature rule (2.60) with the use of (2.61), (2.65) or (2.66) as appropriate, evaluated at the $2n$ points t_j , produces a system of $2n$ linear equations. The solutions are obtained by the usual Gaussian elimination procedure.

2.5.4 Cornered Scatterers with Dirichlet Boundary Condition

Implementation of the graded mesh ensures a rapid convergence rate (as a function of n) for scatterers with corners and the Neumann and impedance boundary conditions. In the case where these scatterers have a Dirichlet boundary condition further modifications are necessary to achieve comparable convergence rates. For these domains the kernel of (2.39) is no longer weakly singular at the corner, and the corresponding operator loses compactness.

2.5.4.1 Single-cornered Scatterers

For domains with a single corner at \mathbf{x}_0 and the Dirichlet boundary condition we follow the technique proposed by [7, 26] which uses the fundamental solution (the static Green's function)

$$G_0(\mathbf{x}, \mathbf{y}) = \frac{1}{2\pi} \ln \frac{1}{|\mathbf{x} - \mathbf{y}|}, \quad \mathbf{x} \neq \mathbf{y}, \quad (2.67)$$

to the Laplace equation in \mathbb{R}^2 to subtract a vanishing term. This transforms (2.39) into

$$u^{\text{sc}}(\mathbf{x}) = \int_{\partial D} \left\{ \left\{ \frac{\partial G(\mathbf{x}, \mathbf{y})}{\partial \mathbf{n}(\mathbf{y})} - i\eta G(\mathbf{x}, \mathbf{y}) \right\} \varphi(\mathbf{y}) - \frac{\partial G_0(\mathbf{x}, \mathbf{y})}{\partial \mathbf{n}(\mathbf{y})} \varphi(\mathbf{x}_0) \right\} ds(\mathbf{y}),$$

$$\mathbf{x} \in \mathbb{R}^2 \setminus \bar{D}, \quad (2.68)$$

and the associated boundary equation (2.40) is reformulated as

$$\varphi(\mathbf{x}) - \varphi(\mathbf{x}_0) + 2 \int_{\partial D} \left\{ \frac{\partial G(\mathbf{x}, \mathbf{y})}{\partial \mathbf{n}(\mathbf{y})} - i\eta G(\mathbf{x}, \mathbf{y}) \right\} \varphi(\mathbf{y}) ds(\mathbf{y})$$

$$- 2 \int_{\partial D} \frac{\partial G_0(\mathbf{x}, \mathbf{y})}{\partial \mathbf{n}(\mathbf{y})} \varphi(\mathbf{x}_0) ds(\mathbf{y}) = -2u^{\text{inc}}(\mathbf{x}), \quad \mathbf{x} \in \partial D. \quad (2.69)$$

An analysis showing the existence of a solution to (2.69) is provided in [7]. Fuller details of the numerical method changes required to implement this reformulation are available in Appendix A.3.

2.5.4.2 Two-cornered Scatterers

This modification needs to be extended when the scatterer has two corners on ∂D . There are now two points in the domain with singularities in the derivatives: at $t = 0$ and $t = \pi$. Each of these singularities have a contributing effect to be accounted for. Again, we use the fundamental solution to the Laplace equation in \mathbb{R}^2 (2.67) to subtract vanishing terms. To reflect these combined contributions (2.39) is reformulated for the domain with two-corners as

$$u^{\text{sc}}(\mathbf{x}) = \int_{\partial D} \left\{ \left\{ \frac{\partial G(\mathbf{x}, \mathbf{y})}{\partial \mathbf{n}(\mathbf{y})} - i\eta G(\mathbf{x}, \mathbf{y}) \right\} \varphi(\mathbf{y}) - \cos^2 \frac{t(\mathbf{x})}{2} \frac{\partial G_0(\mathbf{x}, \mathbf{y})}{\partial \mathbf{n}(\mathbf{y})} \varphi(\mathbf{x}_0) - \sin^2 \frac{t(\mathbf{x})}{2} \frac{\partial G_0(\mathbf{x}, \mathbf{y})}{\partial \mathbf{n}(\mathbf{y})} \varphi(\mathbf{x}_\pi) \right\} ds(\mathbf{y}),$$

$$\mathbf{x} \in \mathbb{R}^2 \setminus \bar{D}, \quad (2.70)$$

where \mathbf{x}_0 and \mathbf{x}_π are the two corner points and $t(\mathbf{x})$ denotes the parameter value of point \mathbf{x} . The associated boundary equation (2.40) is now

$$\begin{aligned} \varphi(\mathbf{x}) - \left(\cos^2 \frac{t(\mathbf{x})}{2} \varphi(\mathbf{x}_0) + \sin^2 \frac{t(\mathbf{x})}{2} \varphi(\mathbf{x}_\pi) \right) \\ + 2 \int_{\partial D} \left\{ \frac{\partial G(\mathbf{x}, \mathbf{y})}{\partial \mathbf{n}(\mathbf{y})} - i\eta G(\mathbf{x}, \mathbf{y}) \right\} \varphi(\mathbf{y}) ds(\mathbf{y}) \\ - 2 \int_{\partial D} \left(\cos^2 \frac{t(\mathbf{x})}{2} \frac{\partial G_0(\mathbf{x}, \mathbf{y})}{\partial \mathbf{n}(\mathbf{y})} \varphi(\mathbf{x}_0) + \sin^2 \frac{t(\mathbf{x})}{2} \frac{\partial G_0(\mathbf{x}, \mathbf{y})}{\partial \mathbf{n}(\mathbf{y})} \varphi(\mathbf{x}_\pi) \right) ds(\mathbf{y}) \\ = -2u^{\text{inc}}(\mathbf{x}), \quad \mathbf{x} \in \partial D. \end{aligned} \quad (2.71)$$

2.5.4.3 Four-cornered Scatterers

A different modification is needed when the scatterer has four corners on ∂D . There are now four points in the domain with singularities in the derivatives: at $t = 0, \frac{\pi}{2}, \pi$ and $\frac{3\pi}{2}$. Each of these singularities have a contributing effect that needs to be accounted for. For scatterers with four corner points, equation (2.39) is reformulated as

$$u^{\text{sc}}(\mathbf{x}) = \int_{\partial D} \left\{ \frac{\partial G(\mathbf{x}, \mathbf{y})}{\partial \mathbf{n}(\mathbf{y})} - i\eta G(\mathbf{x}, \mathbf{y}) \right\} \varphi(\mathbf{y}) -$$

$$\int_{\partial D} \left\{ f_1(\mathbf{x}) \frac{\partial G_0(\mathbf{x}, \mathbf{y})}{\partial \mathbf{n}(\mathbf{y})} \varphi(\mathbf{x}_0) + f_2(\mathbf{x}) \frac{\partial G_0(\mathbf{x}, \mathbf{y})}{\partial \mathbf{n}(\mathbf{y})} \varphi(\mathbf{x}_{\pi/2}) \right. \\ \left. + f_3(\mathbf{x}) \frac{\partial G_0(\mathbf{x}, \mathbf{y})}{\partial \mathbf{n}(\mathbf{y})} \varphi(\mathbf{x}_\pi) + f_4(\mathbf{x}) \frac{\partial G_0(\mathbf{x}, \mathbf{y})}{\partial \mathbf{n}(\mathbf{y})} \varphi(\mathbf{x}_{3\pi/2}) \right\} ds(\mathbf{y}), \quad \mathbf{x} \in \mathbb{R}^2 \setminus \bar{D}, \quad (2.72)$$

where \mathbf{x}_0 , $\mathbf{x}_{\pi/2}$, \mathbf{x}_π and $\mathbf{x}_{3\pi/2}$ are the four corner points and

$$f_1(\mathbf{x}) = \frac{1}{2} \cos^2 \left(\frac{t(\mathbf{x})}{2} \right), \quad f_2(\mathbf{x}) = \frac{1}{2} \sin^2 \left(\frac{t(\mathbf{x})}{2} + \frac{\pi}{4} \right), \quad (2.73)$$

$$f_3(\mathbf{x}) = \frac{1}{2} \cos^2 \left(\frac{t(\mathbf{x})}{2} + \frac{\pi}{2} \right), \quad f_4(\mathbf{x}) = \frac{1}{2} \sin^2 \left(\frac{t(\mathbf{x})}{2} + \frac{3\pi}{4} \right). \quad (2.74)$$

The associated boundary equation (2.40) is now

$$\varphi(\mathbf{x}) - (f_1(\mathbf{x})\varphi(\mathbf{x}_0) + f_2(\mathbf{x})\varphi(\mathbf{x}_{\pi/2}) + f_3(\mathbf{x})\varphi(\mathbf{x}_\pi) + f_4(\mathbf{x})\varphi(\mathbf{x}_{3\pi/2})) \\ + 2 \int_{\partial D} \left\{ \frac{\partial G(\mathbf{x}, \mathbf{y})}{\partial \mathbf{n}(\mathbf{y})} - i\eta G(\mathbf{x}, \mathbf{y}) \right\} \varphi(\mathbf{y}) ds(\mathbf{y}) \\ - 2 \int_{\partial D} \left\{ f_1(\mathbf{x}) \frac{\partial G_0(\mathbf{x}, \mathbf{y})}{\partial \mathbf{n}(\mathbf{y})} \varphi(\mathbf{x}_0) + f_2(\mathbf{x}) \frac{\partial G_0(\mathbf{x}, \mathbf{y})}{\partial \mathbf{n}(\mathbf{y})} \varphi(\mathbf{x}_{\pi/2}) \right. \\ \left. + f_3(\mathbf{x}) \frac{\partial G_0(\mathbf{x}, \mathbf{y})}{\partial \mathbf{n}(\mathbf{y})} \varphi(\mathbf{x}_\pi) + f_4(\mathbf{x}) \frac{\partial G_0(\mathbf{x}, \mathbf{y})}{\partial \mathbf{n}(\mathbf{y})} \varphi(\mathbf{x}_{3\pi/2}) \right\} ds(\mathbf{y}) \\ = -2u^{\text{inc}}(\mathbf{x}), \quad \mathbf{x} \in \partial D. \quad (2.75)$$

In all of the above cases we apply the substitution (2.60) with graded mesh (2.61), (2.65) or (2.66) as appropriate, discretise and solve as previously described. The described modifications applied to (2.39) and (2.40) ensure that rapid convergence is achieved for scatterers with corners and the Dirichlet boundary condition on ∂D .

Chapter 3

Effect of Corner Rounding: Numerical Results

In this chapter we present the numerical results after implementation of the methods presented in the previous chapter to solve the various boundary value problems for a variety of scatterers.

We begin by outlining the methods used to verify the correctness of our solutions and examine the difference on the rate of convergence between the two quadrature schemes: uniform versus graded mesh. We then measure the deviation from the solution produced by a cornered scatterer to that produced when the corners are rounded as a function of the radius of curvature, ρ . We also report on the effectiveness of the numerical schemes when used on structures with corners that are not right-angled. We next report on the nature of the differences between the far-fields of cornered scatterers and their rounded counterparts to answer the questions: at which observation points are the fields most noticeably different? Are the magnitude of the differences dependent on the incident field wave number, ka , or angle, θ_0 ?

We also undertake a numerical investigation of the rate of convergence of the differences of the far-fields of the cornered scatterer u_0^∞ and its rounded counterpart u_ρ^∞ as the radius of curvature, ρ , approaches 0.

We conclude this chapter with a summary of some earlier work where the numerical methods developed in Chapter 2 were used to validate a model developed by Rawlins [110] to approximate the diffraction of an E-polarised wave by an absorbing rect-

angular cylinder. It employed Keller's method of GTD and its extensions to deal with multiple diffraction, utilising the diffraction coefficient derived for the canonical problem of diffraction by an impedance corner. Since the original report [111] the numerical validation experiments have been re-run employing graded mesh and an identical scatterer geometry.

To the best of our knowledge, this work is the most comprehensive exploration for the 2D Helmholtz problem of the effect on the near- and far-fields of rounding corners of scatterers. The only other work we have identified where the effect of corner rounding has been quantified for this class of problem is that of [10]. Though the use of graded mesh for cornered structures is well known, we establish the superiority of using a graded mesh for obtaining the scattered field for smooth surfaced scatterers with small radii of curvature at some point on their surface. Most significantly, we quantify the rate of convergence of the differences in the far-fields between the cornered scatterers and their rounded counterparts, as the radius of curvature tends to zero. This is established for each of the three boundary conditions and we demonstrate numerically the relationship of these differences to the wave number and radius of curvature is such that the differences are either approximated or bounded by $C(k\rho)^m$, where the constant C is dependent on the angle of incidence of the plane wave, and the power m is dependent on the interior angle of the corner and the boundary condition being studied.

3.1 Verification of Numerical Results

The numerical results discussed in this work were obtained after implementation of the schemes developed in Chapter 2 in a MATLAB code.

A number of tests were applied to verify its correctness. Analytical solutions were derived for a circular scatterer for the three boundary conditions and the resultant Mie-type¹ series were used to compute an actual solution. This enabled comparison with the scattered field computed by the methods described in Chapter 2 for a circular scatterer. For all three boundary conditions the relative error was in the order of 10^{-15} which was

¹The term Mie series is commonly used for the scattering of an electromagnetic plane wave by a spherical scatterer. However, papers by Clebsch [112] and Lorenz [113] addressing similar scattering problems pre-date Mie's work. For an historical overview see Logan [114,115] and Kerker [116,117]. We refer to the corresponding series for scattering by a cylindrical scatterer as a Mie-type series.

considered a suitable tolerance. Also, the condition number of the systems was checked to ensure that uniqueness problems arising for wave numbers ka near an interior Dirichlet eigenvalue of the scatterer were avoided.

However, there is no analytical expression for the scattered field from the non-circular scatterers described in Section 2.1 and as such, there is no true solution to which we can compare results. For this study, we use a significant digit measurement to determine the convergence of the solution.

We choose a point \mathbf{x} in the domain external to the scatterer and compute the field. As the number of quadrature points increases, if the solution is convergent, the number of significant digits in agreement increases. Thus we measure the number of unchanging digits in the approximate solution as the number of quadrature points N increases, and terminate the calculation when the truncation of the computed value to a pre-specified number of significant digits does not change as N increases.

Two measures were used to determine the convergence of the solutions. Firstly, a near-field² measure of the real and imaginary parts of the scattered field u^{sc} . This measurement was taken at a radius $r = 10$ from the origin in the direction $\mathbf{x} = (-1, 1)$.

The second measure employs the far-field. It is measured in a specified direction $\hat{\mathbf{x}} = \hat{\mathbf{x}}(\hat{\theta}) = (\cos \hat{\theta}, \sin \hat{\theta})$, with $\hat{\theta}$ being the angle of observation of the far-field, where $|\hat{\mathbf{x}}| = 1$. For the Dirichlet boundary condition, the far field pattern is calculated as

$$u^\infty(\hat{\mathbf{x}}) = \frac{e^{-i\frac{\pi}{4}}}{\sqrt{8\pi k}} \int_{\partial D} \{k\mathbf{n}(y) \cdot \hat{\mathbf{x}} + \eta\} e^{-ik\hat{\mathbf{x}} \cdot \mathbf{y}} \varphi(\mathbf{y}) \, ds(\mathbf{y}), \quad (3.1)$$

and for Neumann and impedance boundary conditions the calculation is

$$u^\infty(\hat{\mathbf{x}}) = \frac{ie^{-i\frac{\pi}{4}}}{\sqrt{8\pi k}} \int_{\partial D} e^{-ik\hat{\mathbf{x}} \cdot \mathbf{y}} \varphi(\mathbf{y}) \, ds(\mathbf{y}). \quad (3.2)$$

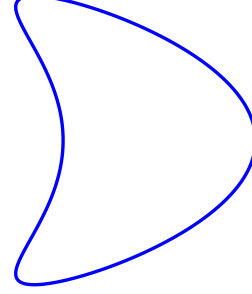
Using the significant digit method enables measurement of convergence, but of course does not fully guarantee the accuracy of our results. We were able to find some published

²In antenna studies, the near-field to far-field transition is associated with the Fraunhofer distance $d_f = 2D^2/\lambda$, where D is the maximum dimension of the radiator, and λ is the wavelength. The points on a circle of radius 10 are not necessarily in the near-field of a scatterer of diameter $2a = 2$, especially at larger wave numbers. In this thesis we use the term near-field to describe any measurement of the scattered field up to a distance of 10 units from the centre of the scatterer, irrespective of wave number. In Chapter 5 we specifically examine the scattered field at close proximity to the scattered surface.

results which allowed a direct comparison to those produced by the implementation of our schemes.

Kress [26] has published a set of results for a smooth kite shaped scatterer

$$\mathbf{x} = \mathbf{x}(t) = (\cos t + 0.65 \cos 2t - 0.65, 1.5 \sin t), \quad t \in [0, 2\pi], \quad (3.3)$$



with Dirichlet boundary condition, and in [61] for the Neumann boundary condition. Our codes reproduced these results exactly.

Figure 3.1: Kite shaped scatterer.

Kress [26] has also published some results for the lemniscate (2.2)

with Dirichlet boundary condition. We were able to reproduce these results exactly.

For the square (2.6) with Dirichlet or Neumann boundary conditions, we were able to compare our results to those produced by Barnett and Betcke's MPSPack software [98]. The difference between the MPSPack far-field u_M^∞ and that produced by our code u_0^∞ was measured using the L^∞ norm

$$\sqrt{k} \|u_0^\infty - u_M^\infty\|_\infty = \max_{\hat{\mathbf{x}} \in [0, 2\pi]} |u_0^\infty(\hat{\mathbf{x}}) - u_M^\infty(\hat{\mathbf{x}})|, \quad (3.4)$$

and the L^2 norm

$$\sqrt{k} \|u_0^\infty - u_M^\infty\|_2 = \left(\int_0^{2\pi} |u_0^\infty(\hat{\mathbf{x}}) - u_M^\infty(\hat{\mathbf{x}})|^2 d\hat{\mathbf{x}} \right)^{\frac{1}{2}}. \quad (3.5)$$

For the Dirichlet boundary condition the L^∞ difference was of the order of 10^{-11} and the L^2 difference of the order of 10^{-10} . For the Neumann case the respective differences were in the order 10^{-10} and 10^{-9} . These calculations were performed for wave number $ka = 2\pi$ with plane wave angle of incidence $\theta_0 = 0$. Changing the angle of incidence to $\theta_0 = \pi/4$ produced the same results. The same results were observed for a variety of wave numbers and angles of incidence.

Another verification method used, was to approximate the far-field $u^\infty(\hat{\mathbf{x}})$ from the near-field $u^{\text{sc}}(\mathbf{x})$. From the definition [7] of the far-field pattern,

$$u^{\text{sc}}(\mathbf{x}) = \frac{e^{ik|\mathbf{x}|}}{\sqrt{|\mathbf{x}|}} \left(u^\infty(\hat{\mathbf{x}}) + \mathcal{O}\left(\frac{1}{|\mathbf{x}|}\right) \right), \quad |\mathbf{x}| \rightarrow \infty, \quad (3.6)$$

where $\hat{\mathbf{x}} = \frac{\mathbf{x}}{|\mathbf{x}|}$, we may thus approximate it by

$$u^\infty(\hat{\mathbf{x}}) \approx u^{\text{sc}}(\mathbf{x}) \frac{\sqrt{|\mathbf{x}|}}{e^{ik|\mathbf{x}|}}. \quad (3.7)$$

This was particularly helpful when working with scatterers for which published results were not readily available. Figure 3.2 illustrates two typical examples. The actual far-field, $u^\infty(\hat{\mathbf{x}})$, is shown in red and the approximated far-field calculated at the same points $\hat{\mathbf{x}}$ in blue. Although there are discrepancies they are relatively small and offer additional validation that the calculated far-field is correct.

In October 2017, Ganesh and Hawkins [27] released TMatROM - a Matlab object oriented T-matrix software package [118]. We made use of this package to verify the numerical results of some completed work, where applicable. Full details are presented in Section 8.3. We also used the package when modelling larger scatterer arrays in Chapter 9.

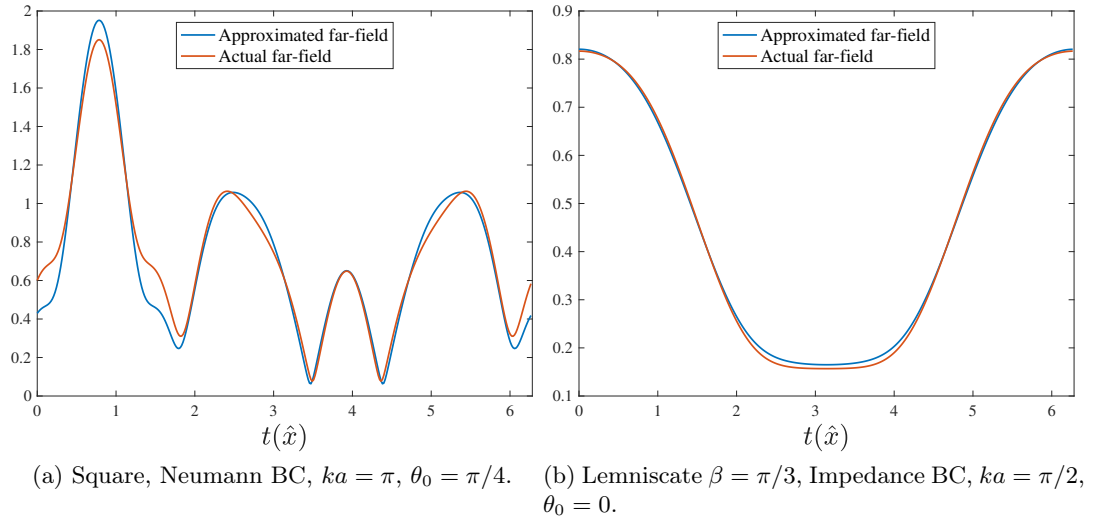


Figure 3.2: Showing the far-field $|u^\infty(\hat{\mathbf{x}})|$ and the approximated far-field (3.7).

3.2 Test Parameters

For all scenarios presented in this work a variety of angles of incidence, θ_0 , were tested. However, unless otherwise specified, the results reported in this work typically use an incident plane wave propagating in a direction incident to a corner on the scatterer; that is, the direction of propagation bisects the angle at the impacted corner. As such,

$\theta_0 = 0$ for the lemniscate and two-cornered scatterer and $\theta_0 = \pi/4$ for the square. Also, a number of impedance parameters were tried; all produced similar results. In this work we report on the results for impedance parameter $Z = 1 + i$. The choice of impedance parameter was chosen to explore a scenario with significant resistance and significant phase shift. All tests were performed for a variety of wave numbers: $ka = 1, \pi/2, \pi, 5, 2\pi, 10, 4\pi, 8\pi$ and 16π . The results reported in this work are for the far-field. In all cases, similar results were observed when measuring the near-field. All rates of convergence and significant digits in agreement for the far-field reported in this chapter are measured in the back-scatter region, unless stated otherwise.

3.3 Graded Mesh is Essential for Smooth Scatterers with Small Radii of Curvature

The near- and far-fields were computed for each of the three boundary conditions for the lemniscate (2.2), two-cornered scatterer (2.4) and the square (2.6) as well as the non right-angled scatterers (2.9), (2.10), (2.11), (2.12) using the appropriate graded mesh, (2.61), (2.65) and (2.66), respectively. Figure 3.3 provides a graphical representation of the near- and far-fields induced by a lemniscate with Dirichlet boundary condition.

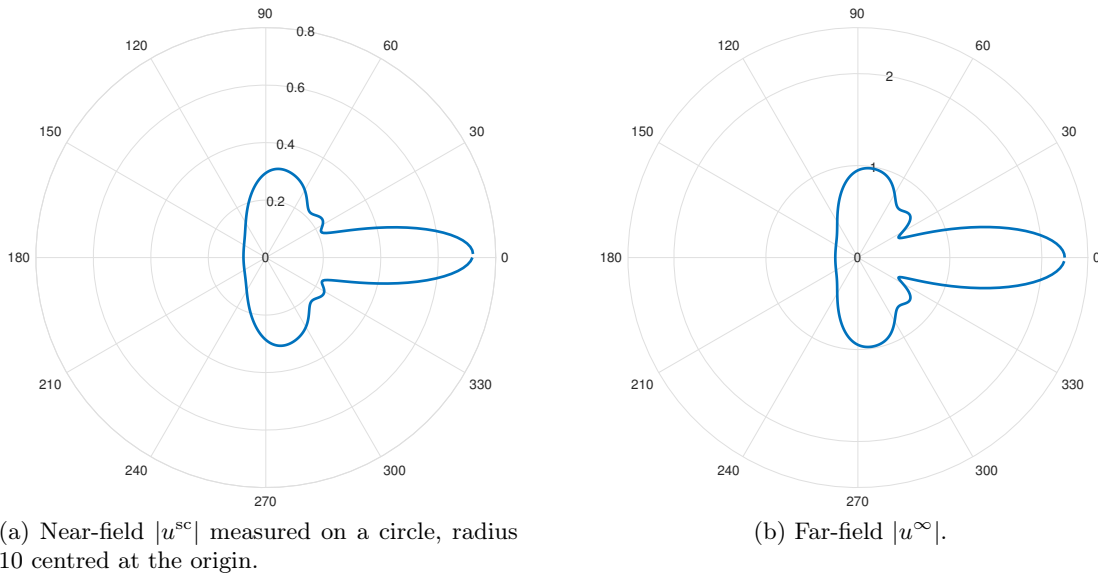


Figure 3.3: Near- and far-fields induced by a lemniscate with Dirichlet boundary condition. Wave number $ka = 2\pi$, incidence angle $\theta_0 = 0$.

Figure 3.4 illustrates the convergence rates using graded mesh to discretise each of the three scatterers for the different boundary conditions. It shows the change in the number of significant digits in agreement of the far-field measurement as the number of quadrature points increases and illustrates the high convergence rates achieved when using graded mesh. The number of corners on each scatterer affects the number of quadrature points required for a desired accuracy. Using 64 quadrature points achieves at least 10 significant digits accuracy for the lemniscate, 9 for the two-cornered scatterer and 5 to 6 for the square. Conversely, to achieve at least 10 significant digits accuracy requires 64 quadrature points for the lemniscate, 128 for the two-cornered scatterer and 512 for the square. Note that for the Dirichlet case, the square scatterer does not achieve the same degree of accuracy in the solution as for the Neumann and impedance boundary conditions. This seems to be attributable to the treatment of the singularities in the four corners in (2.72). Further refinement of this approach should improve the accuracy achieved.

The rates of convergence achieved for each cornered scatterer with an impedance boundary condition and wave number $ka = 2\pi$, measured as

$$-\log_2 [|u_{2N}^\infty(\hat{\mathbf{x}}) - u_{256}^\infty(\hat{\mathbf{x}})| / |u_N^\infty(\hat{\mathbf{x}}) - u_{256}^\infty(\hat{\mathbf{x}})|], \quad (3.8)$$

are listed in Table 3.1. This is demonstrative of the typical rates of convergence achieved. In the case of the lemniscate a convergence rate consistent with super-algebraic convergence is observed. The apparent slowing of the rate shown for $N \geq 64$ is a result of limited accuracy attainable from the measure of only 15 significant digits. The two-cornered and square scatterers also exhibit very rapid convergence, and we anticipate that improvements to the graded mesh employed will match the rate of convergence demonstrated for the lemniscate.

We then computed the near- and far-fields for each of the cornered scatterers and the rounded scatterers (2.3), (2.5) and (2.7) for each of the boundary conditions using a uniform mesh $t_j = \pi j/n$, for $j = 0, 1, \dots, 2n - 1$, in the parameterisation (2.1) of the scatterer. For the rounded scatterers we tested radii of curvature $\rho = 0.1, 0.09, \dots, 0.01, 0.005, 0.0025, 0.00125$ in the corners. The results for the scatterers with corners,

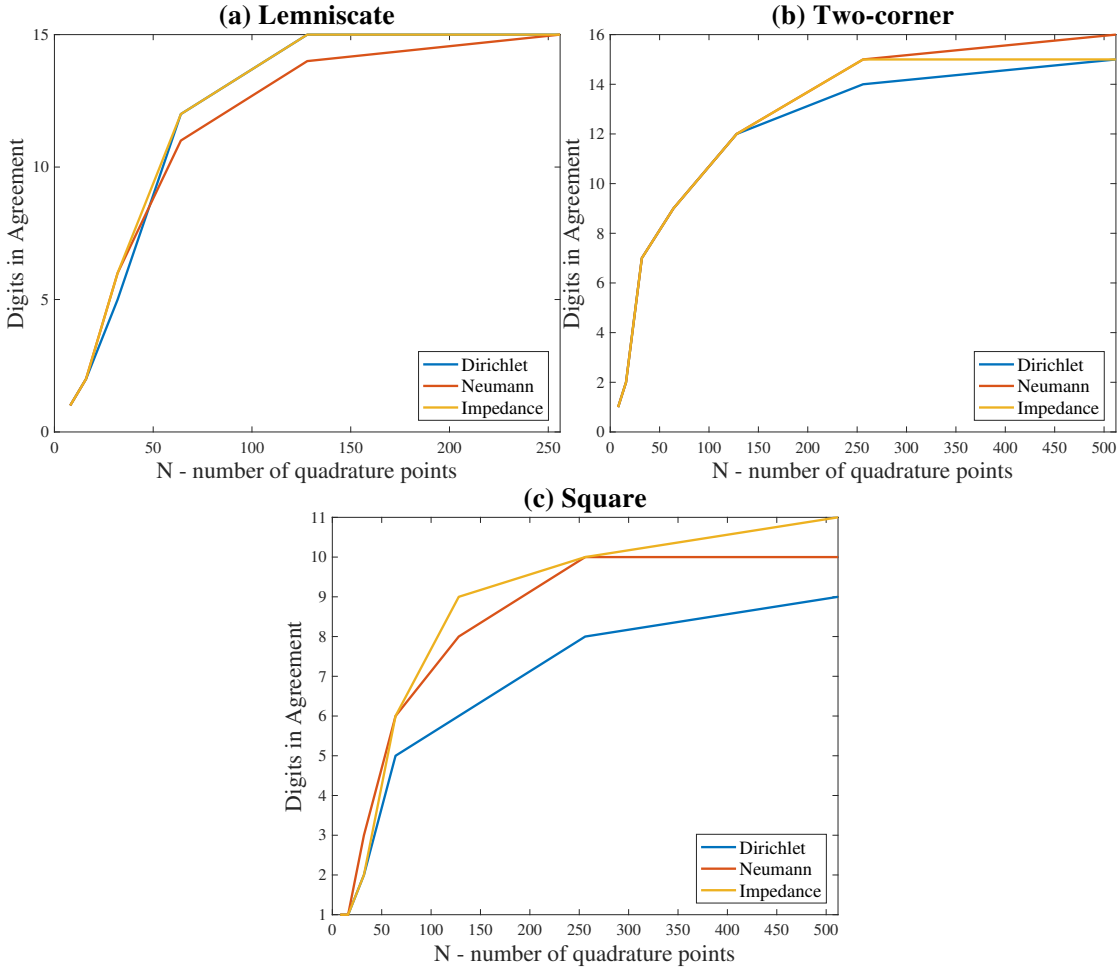


Figure 3.4: Significant digits in agreement of the far-field of the three sharp-cornered scatterers, employing a graded mesh to discretise the surface. Results shown are for $ka = 2\pi$, impedance boundary condition, $Z = 1 + i$. Incidence angle: $\theta_0 = 0$ for lemniscate (a) and two-corner (b); $\theta_0 = \pi/4$ for the square (c).

as expected, exhibit non-convergence when using a uniform mesh. Figures 3.5a, 3.5c and 3.5e illustrate the effect on convergence when using a uniform mesh for the three rounded scatterers with an impedance boundary condition for $ka = 2\pi$. In short, the number of uniformly spaced quadrature points required to achieve convergence - or at least a specified level of accuracy - grows sharply as the radius of curvature decreases. Similar results were obtained for the Dirichlet and Neumann boundary conditions.

The same series of experiments were then re-run using instead the appropriate graded mesh (2.61), (2.65) and (2.66) for the scatterers with rounded corners. In all cases this discretisation method exhibits superior results. In all cases at least 14 significant digit convergence was achieved. In particular, the use of a graded mesh is essential in obtaining convergent results for small radii of curvature. Figures 3.5b, 3.5d and 3.5f illustrate the

effect on convergence when using a graded mesh for the three scatterers with rounded corners for each of the boundary conditions as the radius of curvature decreases. Similar results were obtained when measuring the significant digits in agreement of the near-field data and for different values of ka .

N	Lemniscate	Two-corner	Square
8	4.6	4.4	1.0
16	11.3	13.9	6.0
32	21.5	8.0	13.6
64	11.1	8.9	9.1
128	-	9.1	4.5

Table 3.1: Rate of convergence (3.8) using a graded mesh. Impedance boundary condition, $Z = 1 + i$, wave number $ka = 2\pi$. Incidence angle: $\theta_0 = 0$ for lemniscate and two-corner, $\theta_0 = \pi/4$ for the square.

N	$\rho = 0.05$		$\rho = 0.02$		$\rho = 0.01$	
	Uniform	Graded	Uniform	Graded	Uniform	Graded
8	5.2	4.6	4.3	4.7	3.7	4.6
16	2.7	11.3	2.1	11.3	1.9	11.3
32	4.3	32.5	2.3	33.6	1.9	31.7
64	8.0	-	3.5	-	2.3	-
128	14.9	-	6.5	-		

Table 3.2: Rate of convergence (3.8): comparing uniform vs. graded mesh for a rounded lemniscate with an impedance boundary condition, $Z = 1 + i$, where ρ is the radius of curvature in the corner. Wave number $ka = 2\pi$, incidence angle $\theta_0 = 0$.

We conclude that even though the rounded scatterers have a smooth boundary ∂D , as the radius of curvature decreases use of the uniform mesh for discretisation fails to produce a numerically convergent solution. Use of a graded mesh to discretise the surface is thus recommended once the radius of curvature is small. As an example, for $ka = 2\pi$, when $\rho < 0.04$ for the lemniscate and two-cornered scatterer and $\rho < 0.03$ for the square, use of the graded mesh is essential to achieve a rapidly convergent solution.

We also note the rate of convergence is superior when using graded mesh even for scatterers where the radius of curvature is relatively large. For example, in the case of the lemniscate with radius of curvature $\rho = 0.05$, using a uniform mesh achieves 12 digits agreement with $N = 256$, whereas using a graded mesh achieves 15 digits agreement for $N = 64$. For all cases a convergence rate consistent with super-algebraic convergence was observed. This is further illustrated in Table 3.2, which shows the rates of convergence for the lemniscate with an impedance boundary condition, for $ka = 2\pi$, when a uniform

versus a graded mesh is used. This suggests that the type of discretisation method chosen should be decided on a more sophisticated approach rather than a simplistic smooth versus not smooth criterion.

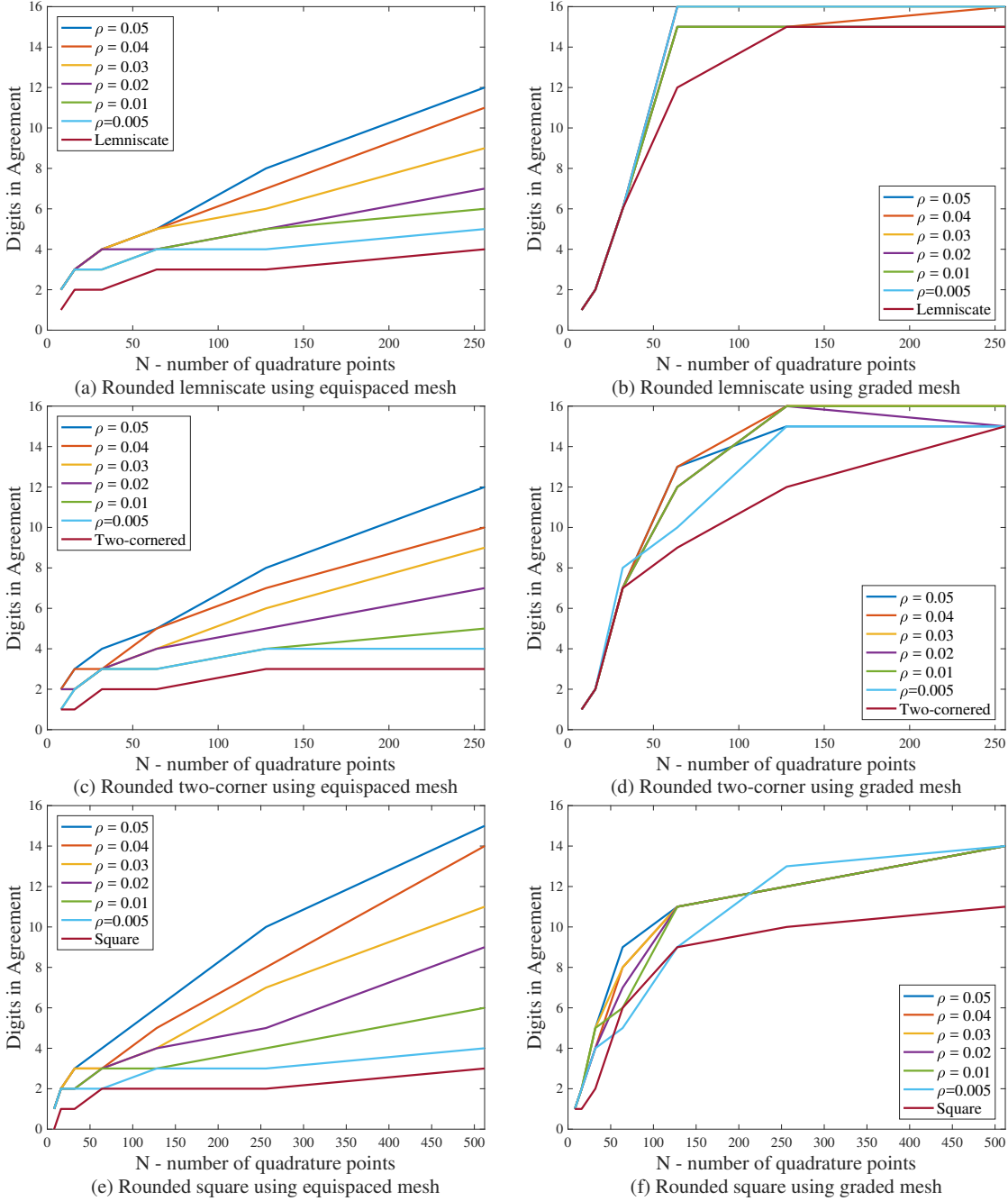


Figure 3.5: Illustrating the effect of using graded mesh for discretisation. Significant digits in agreement of the far-field for impedance boundary condition, $Z = 1 + i$, for wave number $ka = 2\pi$. Incidence angle: $\theta_0 = 0$ for lemniscate and two-corner, $\theta_0 = \pi/4$ for the square.

3.4 Measuring the Effect of Rounding Corners on the Scattered Field

A common approach used when dealing with domains with corners is to round the corners, producing a smooth surface and thus eliminating the singularities introduced by the corners. This is done in the expectation that the difference in the scattered field quantities are ‘small’ and tend to zero as the radius of curvature of the rounded corners is reduced to zero.

This section examines the differences in the solution such rounding elicits. Having established that the graded mesh gives superior results for the rounded scatterers, we now measure the deviation from the solution produced by a cornered scatterer to that produced when the corners are rounded. For all experiments the appropriate graded mesh was used on both the cornered scatterers and those where the corners were rounded. The difference between the solution produced by a cornered scatterer, $u_0^\infty(\hat{\mathbf{x}})$, and that produced by rounding $u_\rho^\infty(\hat{\mathbf{x}})$, with associated radius of curvature ρ , is measured using the L^2 norm

$$\|u_0^\infty - u_\rho^\infty\|_2 = \left(\int_0^{2\pi} |u_0^\infty(\hat{\mathbf{x}}) - u_\rho^\infty(\hat{\mathbf{x}})|^2 d\hat{\mathbf{x}} \right)^{\frac{1}{2}}, \quad (3.9)$$

and L^∞ norm

$$\|u_0^\infty - u_\rho^\infty\|_\infty = \max_{\hat{\mathbf{x}} \in [0, 2\pi]} |u_0^\infty(\hat{\mathbf{x}}) - u_\rho^\infty(\hat{\mathbf{x}})|. \quad (3.10)$$

These tests were run for all three scatterers and each of the three boundary conditions for the ka values and radii of curvature specified in the previous section. The smaller the radius of curvature used for the rounding, the smaller the measured difference. Both the absolute and relative difference were measured. The relative difference is expressed as a percentage of the same norm of the scatterer’s far-field. Table 3.3 presents a selection of results for the far-field relative differences for $ka = 2\pi$.

Typical results when comparing rounded structures to sharp-cornered ones with $\rho = 0.02$ are as follows. For the lemniscate, the differences in the L^2 norm are 2.4%, 0.9% and 1.7% in the Dirichlet, Neumann and impedance cases, respectively. Similarly, the L^∞ norm measures a difference of 1.4% in the Dirichlet case, 0.5% in the Neumann case and 0.8% for the impedance boundary condition. For the two corner scatterer, the respective

differences in the L^2 norm are 3.2%, 1.6% and 2.4% and for the square scatterer, the respective differences are all 1.3%. As Table 3.3 indicates, these differences increase as ρ increases. We also note that for a given ρ the two-cornered scatterer has higher percentage differences for the norms compared to those of the lemniscate or the square. This is attributable to two factors: the choice of function for the graded mesh and the smaller cross-sectional area of the two-cornered scatterer. In the case of the lemniscate and square, the derivatives vanish up to order $p = 8$, whereas for the two-cornered scatterer the choice of function has $p = 6$. Choosing a function with a higher-order p is expected to reduce this difference.

Changes to the wave number ka also affect the magnitude of the differences. Decreasing the wave number decreases the differences and increasing the wave number increases the differences. As an example, for scatterers with the Dirichlet boundary condition and $\rho = 0.02$, the differences in the L^∞ norm are 0.73%, 1.85% and 2.63% for $ka = \pi/2$, 4π and 16π , respectively. Similarly, the differences in the L^2 norm are 0.71%, 4.34% and 13.3%. Similar variations were observed for the Neumann and impedance loaded cases. As ka increases, the wavelength of the illuminating field becomes smaller so that the amount of corner removed by rounding and the impact on the scattered far-field becomes more significant. In Section 3.6 the nature of the differences between the fields when the wave number is changed is discussed as is the effect of changing the direction of the incident field, θ_0 .

ρ	Lemniscate		Two-corner		Square	
	L^2	L^∞	L^2	L^∞	L^2	L^∞
Dirichlet						
0.05	8.1	4.7	10.3	7.5	4.5	2.3
0.04	6.0	3.6	7.7	5.6	3.2	2.1
0.03	4.1	2.5	5.3	3.9	2.2	1.5
0.02	2.4	1.4	3.2	2.4	1.3	0.9
0.01	1.0	0.6	1.2	0.9	0.6	0.4
0.005	0.4	0.2	0.5	0.4	0.2	0.1
Neumann						
0.05	4.1	2.2	7	6.6	4.1	3.2
0.04	2.8	1.5	4.9	4.6	2.9	2.2
0.03	1.7	0.9	3.0	2.8	2.0	1.5
0.02	0.9	0.5	1.6	1.5	1.3	0.9
0.01	0.3	0.1	0.5	0.4	0.5	0.4
0.005	0.06	0.03	0.1	0.1	0.2	0.1
Impedance $Z = 1 + i$						
0.05	5.2	2.4	6.9	4.0	3.6	1.8
0.04	4.0	1.8	5.3	3.1	2.7	1.3
0.03	2.8	1.3	3.7	2.2	1.9	1.0
0.02	1.7	0.8	2.4	1.4	1.3	0.6
0.01	0.8	0.4	1.0	0.6	0.6	0.3
0.005	0.4	0.2	0.5	0.3	0.3	0.1

Table 3.3: Measuring the effect of rounding on the far-field. Relative difference of norms expressed as a percentage. Wave number $ka = 2\pi$, incidence angle: $\theta_0 = 0$ for the lemniscate and two-corner, $\theta_0 = \pi/4$ for the square.

3.5 Different Interior Angles

In this section we examine the effectiveness of the quadrature schemes developed for structures with non right-angled corners, that is, those with acute, obtuse and reflex interior angles. The near- and far-fields were computed for a variety of angles of incidence $0 \leq \theta_0 < 2\pi$ and wave numbers $1 \leq ka \leq 16\pi$ for each type of single-cornered scatterer, that is, convex with acute interior angle (2.9) and obtuse interior angle (2.10); and concave structures with reflex interior angles (2.11) and (2.12). A variety of internal angles β were chosen. All results reported in this section are for scatterers with a Dirichlet boundary condition (2.19) with incident wave number $ka = 2\pi$ and angle of incidence $\theta_0 = 0$. Similar results were obtained for the other angles of incidence and wave numbers as well as the other two boundary conditions..

Figures 3.6a, 3.6b, 3.6c and 3.6d illustrate the convergence rates using the graded

mesh to discretise the scatterers (2.9), (2.10), (2.11) and (2.12) respectively, for a selection of wave numbers, ka . They show the change in the number of significant digits in agreement of the far-field measurement as the number of quadrature points increases. Similar results were obtained for all wave numbers and when measuring the near-field data. Rapid convergence is achieved for all interior angles $\pi/12 < \beta < 35\pi/36$. We note that for interior angles β outside this range a large number of quadrature points (1024) is required to achieve a highly accurate solution. In the case of very acute angles, eg, $\beta = \pi/36$, using 1024 quadrature points only achieves 8 significant digits of agreement. This is attributable to the proximity of the mesh points on one side of the corner to those on the other side. As the interior angle is reduced the associated matrix almost becomes singular, that is, approaches a singular matrix.

A series of experiments was run to examine whether rounding the corners of the scatterers with small acute internal angles would improve the rate of convergence. The family of curves in which the corner has been rounded and parameterised by the quantity ε ($0 \leq \varepsilon \leq 1$) corresponding to the convex scatterers with acute interior angles (2.2) is

$$\mathbf{x}(t) = a \left(2\sqrt{\varepsilon^2 + (1 - \varepsilon^2) \sin^2 \frac{1}{2}t}, -\tan\left(\frac{\beta}{2}\right) \sin t \right).$$

The radius of curvature ρ at the rounded corner is readily calculated.

Figure 3.7 illustrates the changes to the rates of convergence when the corner of the scatterer is rounded using $\varepsilon = 0.01$ ($\rho \sim 0.0001$) for these angles. For interior angle of $\pi/12$, to achieve 13 digits agreement requires 1024 quadrature points, but 14 digits can be achieved with 256 points when the corner is slightly rounded. An interior angle of $\pi/18$ requires 1024 points to achieve 11 digit agreement, whereas the rounded structure requires 256 points for 10 digit agreement and 512 points for 15. For interior angle $\pi/36$ using 1024 points achieves 8 digit agreement and the rounded structure requires 512 points to achieve 9 digit agreement, and using 1024 points will achieve 15.

Rounding the corner of these almost wedge-like scatterers with this small radius of curvature, improves the convergence rate but has a greater effect on the differences in the far-fields induced by the rounding than say, a scatterer with interior angle $\beta = \pi/2$. The difference between the actual far-field solution, $u_0^\infty(\hat{\mathbf{x}})$, as a function of observation

direction $\hat{\mathbf{x}}$ and that produced by rounding, $u_\rho^\infty(\hat{\mathbf{x}})$, was measured using the L^2 and the L^∞ norms, (3.9), (3.10), respectively. The relative difference is expressed as a percentage of the same norm of the unrounded scatterer. The relative L^∞ norm differences for $\varepsilon = 0.01$ ($\rho \sim 0.0001$) and interior angles $\beta = \pi/12, \pi/18$ and $\pi/36$, are 3.7%, 4.0% and 4.1%, respectively, for wave number $ka = 2\pi$ whereas for a lemniscate with interior angle $\pi/2$ and $\rho = 0.02$ the relative difference is 1.4%. Table 3.4 shows the relative L^2 and L^∞ norm differences for differing wave numbers for the three scatterers of interest with $\rho \sim 0.0001$ as well as the results for the lemniscate with interior angle $\pi/2$ and $\rho = 0.02$.

We conclude that for interior angles $\pi/12 < \beta < 35\pi/36$ the quadrature schemes achieve rapid convergence. Outside this range, the number of quadrature points required to achieve a highly accurate solution increases noticeably for extremely acute angles. The number of quadrature points in this circumstance can be decreased for these structures if the corner is rounded slightly and the resultant maximum difference in the far-field is 1.7% or less for wave number $ka = 1$, and $\leq 4.1\%$, $\leq 9.6\%$ for $ka = 2\pi$ and 16π , respectively. Methods for slender bodies such as those used in [9] should be considered for these cases.

β	$ka = 1$		$ka = 2\pi$		$ka = 16\pi$	
	L^2	L^∞	L^2	L^∞	L^2	L^∞
$\rho \approx 0.0001$						
$\pi/12$	1.3	1.5	5.2	3.7	20.9	7.9
$\pi/18$	1.4	1.6	5.5	4.0	22.6	8.8
$\pi/36$	1.5	1.7	5.9	4.1	24.5	9.6
$\rho = 0.02$						
$\pi/2$	0.4	0.5	2.4	1.4	13.2	2.6

Table 3.4: Relative difference between far-fields expressed as a percentage. Lemniscates with Dirichlet boundary condition, interior angle β and radius of curvature ρ . Direction of plane wave $\theta_0 = 0$.

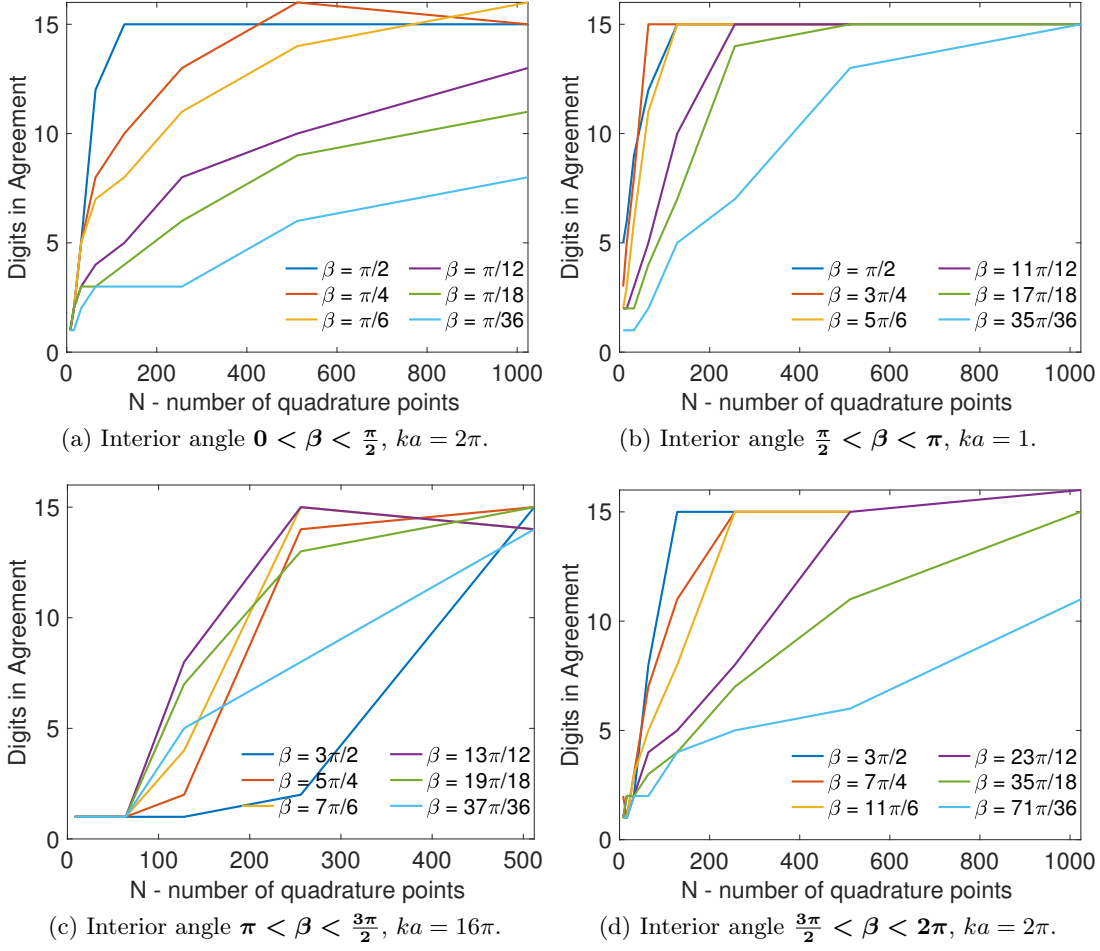


Figure 3.6: Significant digits in agreement of the far-field $|u^\infty(\hat{\mathbf{x}})|$ for a single-cornered scatterer with interior angle β . Direction of incident plane wave $\theta_0 = 0$.

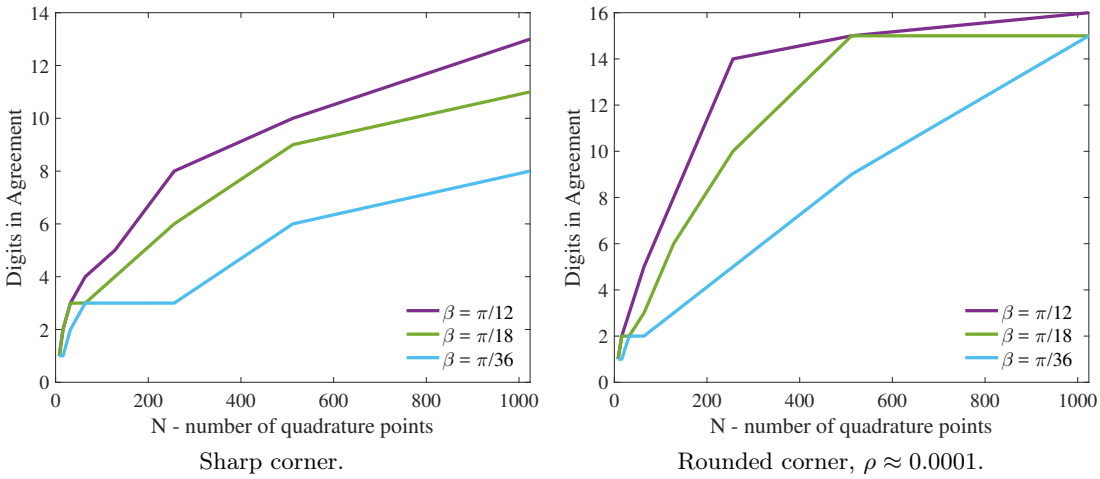


Figure 3.7: Significant digits in agreement of the far-field $|u^\infty(\hat{\mathbf{x}})|$ for a single-cornered scatterer with interior angle β . Direction of incident plane wave $\theta_0 = 0$.

3.6 The Nature of the Differences in the Far-field

When examining the differences in the far-field generated by a cornered scatterer and that generated when the corners are rounded, interest naturally focusses on those observation points at which the fields most noticeably differ. Figure 3.8 illustrates the differences in the far-field for each of the three scatterers, using a Dirichlet boundary condition. The figures show the far-field measured over all observation angles θ ($0 \leq \theta \leq 2\pi$) encircling the scatterer. To emphasise at which points the fields differ most, a logarithmic decibel scale $10 \log_{10}(2\pi|u^\infty|^2)$ is used to plot the fields. The reported results are comparable to those using the Neumann and impedance loaded boundary conditions.

In all cases, the greatest differences in the far-fields of the rounded and unrounded scatterers occur in the back-scatter region. Physically this is attributable to the difference in the scattering mechanisms in the locality of the corner. Figures 3.8a, 3.8b and 3.8c show the differences resulting when the radius of curvature $\rho = 0.05$. At the same wave number (with $ka = 2\pi$) figures 3.8d, 3.8e and 3.8f demonstrate the decrease in the difference when the radius of curvature is reduced to $\rho = 0.02$. As expected, as the radius of curvature decreases, the difference between the fields is minimised.

We also examined the differences of the solutions produced by a cornered scatterer and its rounded counterparts for higher frequency waves, that is, as the wave number relative to the size of the scatterer, ka , increases. The differences increase as the wave number increases and are again most noticeable in the back-scatter region. This is, of course, not unexpected. As ka increases, the wavelength of the illuminating field becomes smaller so that the amount of corner removed by rounding and the impact on the scattered far-field becomes more significant. Figures 3.8g, 3.8h and 3.8i show the effect on the far-field of corner rounding for the three scatterers for $\rho = 0.02$ and $ka = 16\pi$.

We conclude this section with an examination of the effect on the far-field differences as the angle of the incident plane wave θ_0 changes relative to the corner. The results illustrated in Figure 3.9 are, again, for scatterers with a Dirichlet boundary condition and $ka = 2\pi$. The magnitude of the differences is dependent on the direction of the incident plane wave in relation to the corner. Of particular interest is Figure 3.9l, which shows that when the incident wave is travelling in the direction that first makes contact with the broad end of the lemniscate, even with a radius of curvature $\rho = 0.05$ the two

fields are nearly identical. The actual maximum difference between the fields (3.10) is 4×10^{-3} : a relative difference of 0.2%.

In summary, the maximum differences between the far-fields of the cornered and rounded scatterers occur in the back-scatter region and the magnitude of these differences is dependent in the radius of curvature, ρ , used for the rounding, the wave number, ka , and the angle of the incident plane wave, θ_0 .

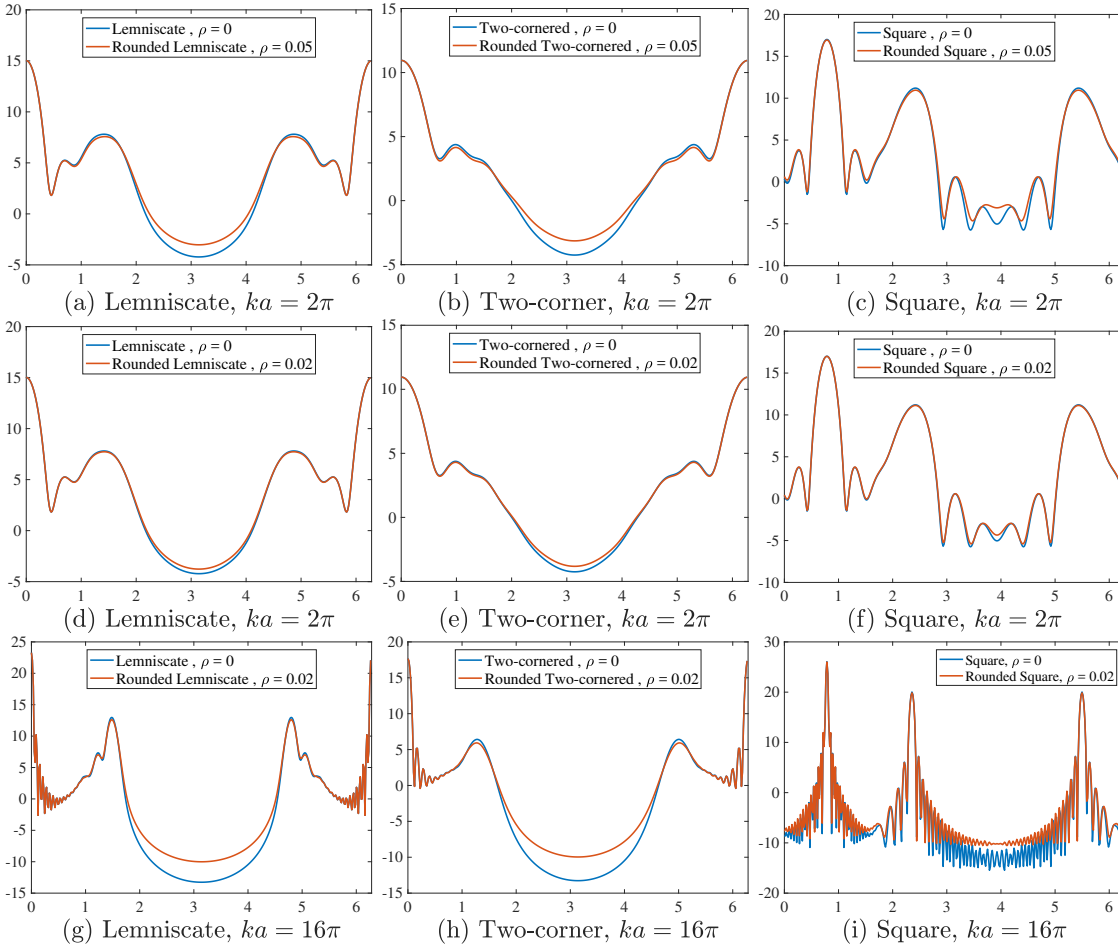


Figure 3.8: $x = \text{observation point } \hat{\theta} \text{ for } 0 \leq \hat{\theta} \leq 2\pi$; $y = 10 \log_{10}(2\pi|u^\infty|^2)$.

Decibel plot of the far-field of the sharp-cornered scatterer and that of the rounded one from different observation points for the each three different scatterers with a Dirichlet boundary condition. Figures (a), (b) and (c) show the differences for a radius of curvature $\rho = 0.05$. Figures (d), (e), and (f), the differences when $\rho = 0.02$. Figures (g), (h) and (i) demonstrate the effect between the fields of reducing the wavelength when $\rho = 0.02$.

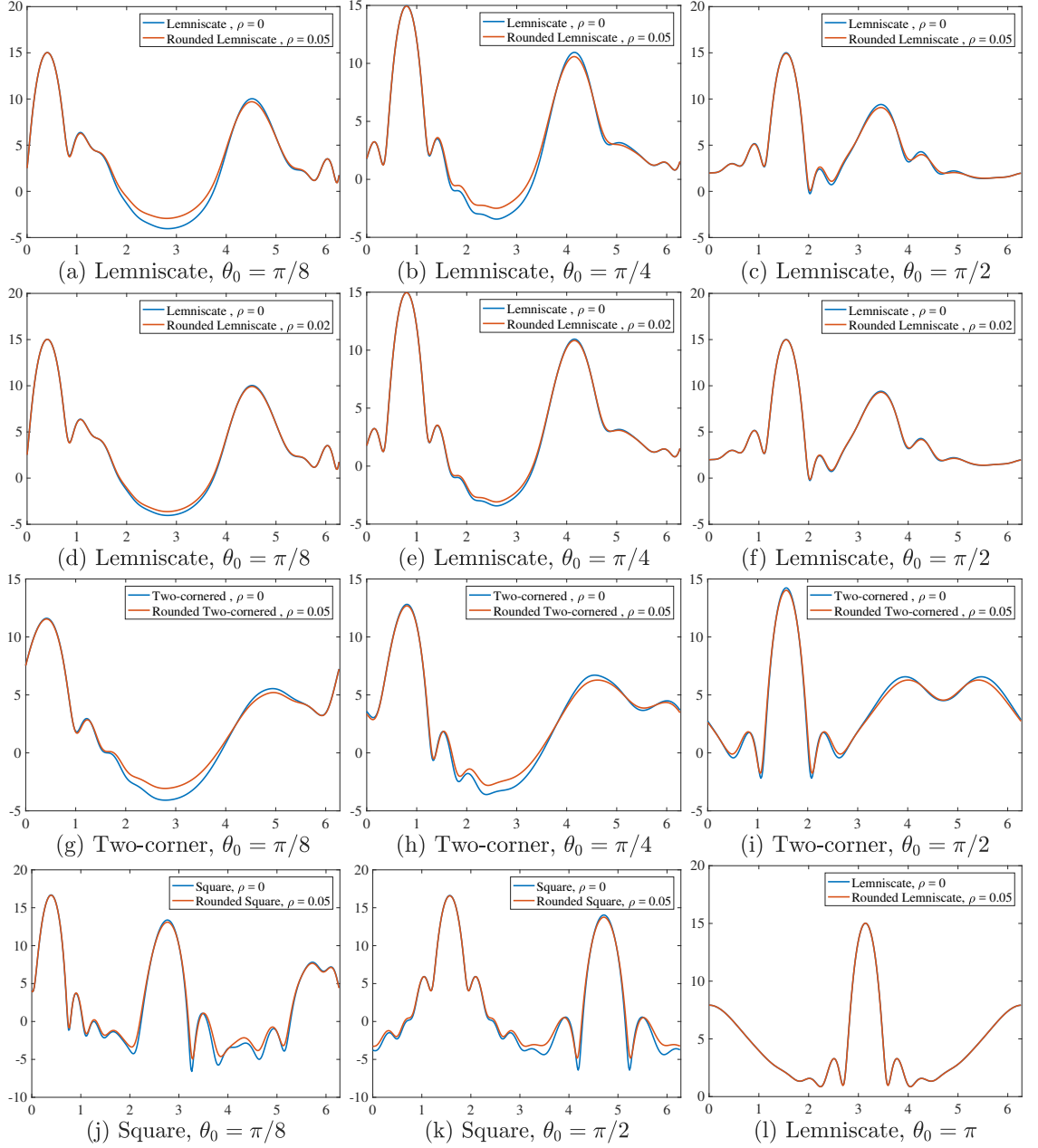


Figure 3.9: $x = \text{observation point } \hat{\theta} \text{ for } 0 \leq \hat{\theta} \leq 2\pi$; $y = 10 \log_{10}(2\pi|u^\infty|^2)$.

Decibel plot of the far-field of the sharp-cornered scatterer and that of the rounded one from different observation points for the each three different scatterers with a Dirichlet boundary condition. Highlights the effect of changing the angle of incidence of the plane wave. Figures (a), (b) and (c) are for the lemniscate with difference incidence angles and a radius of curvature $\rho = 0.05$. Figures (d), (e), and (f), the difference when $\rho = 0.02$. Figures (g), (h) and (i) are for the two-cornered scatterer with $\rho = 0.05$ and figures (j) and (k) are for the square. Figure (l) shows that for a lemniscate when the angle of incidence makes first contact with the broad end, the differences in the two-fields is imperceptible.

3.7 Rate of Convergence of Far-field Solutions as the Radius of Curvature ρ Approaches Zero

Based on the observations of the preceding section we examine the quantity

$$\sqrt{k} \|u_0^\infty - u_\rho^\infty\|_\infty, \quad (3.11)$$

where u_0^∞ is the far-field of the cornered object and u_ρ^∞ is the far-field of the rounded scatterer with radius of curvature ρ , as the radius of curvature ρ approaches 0. The \sqrt{k} factor correctly non-dimensionalises the far-field quantities. We seek an approximation of the form

$$\sqrt{k} \|u_0^\infty - u_\rho^\infty\|_\infty \approx C(\theta_0) (k\rho)^m, \quad (3.12)$$

for some constant C dependent on the direction of the plane wave, θ_0 , and some constant m .

Data was collected for all the described cornered scatterers (Section 2.1), for all three boundary conditions for various wave numbers ka using different incident angles, θ_0 . The same data was collected for their rounded counterparts, using many different radii of curvature. A least squares fit to the logarithms of the data (see Figures 3.10 and 3.11), was used for $k\rho \leq 0.25$ to determine the constants C and m , and the results for the Dirichlet, Neumann and impedance loaded (with $Z = 1 + i$) boundary conditions are presented in Tables 3.6, 3.7 and 3.8, respectively.

For scatterers with the impedance loaded boundary condition, the results show that

$$\sqrt{k} \|u_0^\infty - u_\rho^\infty\|_\infty \approx C(\theta_0) (k\rho)^1, \quad (3.13)$$

for some constant C dependent on the direction of the plane wave, θ_0 , for interior angles $\pi/36 \leq \beta \leq \pi/2$ of the corner of the scatterer³.

For scatterers with the Dirichlet boundary condition

$$\sqrt{k} \|u_0^\infty - u_\rho^\infty\|_\infty \approx C(\theta_0) (k\rho)^m, \quad (3.14)$$

³On the other hand, Ilyinski et al. [119] state that the impedance boundary conditions break down for strips of infinitesimal thickness. Thus (3.13) is expected to break down as $\beta \rightarrow 0$

for some constant C dependent on the direction of the plane wave, θ_0 , and some constant m . We introduce a quantity ν , which is encountered when studying the infinite wedge problem [1] where

$$\nu = \frac{2\pi - \beta}{\pi}. \quad (3.15)$$

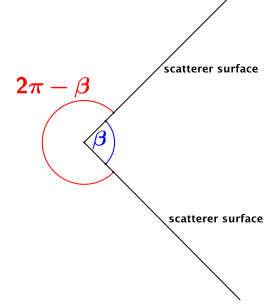


Table 3.5 shows for various interior angles, β , the relationship between the power m and the quantity $2/\nu$. It is clear that there is a correlation between the power m and the quantity $2/\nu$

for scatterers with a Dirichlet boundary condition with interior angle β . Our numerical results demonstrate that for scatterers with Dirichlet boundary condition,

$$\sqrt{k} \|u_0^\infty - u_\rho^\infty\|_\infty \approx C(\theta_0)(k\rho)^{2/\nu}, \quad (3.16)$$

for some constant C dependent on the incident field angle θ_0 . We note the the constant C is greatest when $\theta_0 = 0$ and decreases as θ_0 increases. We observe, that a rule of type (3.12) does not hold for the Neumann boundary condition for the curvilinear scatterers. The value of m is dependent on the direction of the incident plane wave. In these cases the far-field difference tend to zero faster than $(k\rho)^{2/\nu}$, that is

$$\sqrt{k} \|u_0^\infty - u_\rho^\infty\|_\infty \leq C(\theta_0)(k\rho)^{2/\nu}. \quad (3.17)$$

for some constant C dependent on the direction of the plane wave, θ_0 . For all the scatterers the order of m is greatest when the incident plane wave is propagating in a direction incident to a corner on the scatterer, that is, $\theta_0 = 0$ for the curvilinear scatterers and $\theta_0 = \pi/4$ for the square. The effect of the incident plane wave direction is most marked in the case of the curvilinear scatterers, where $1.7 \leq m \leq 1.9$ for $\theta_0 = 0$, with m rapidly approaching $2/\nu$ as the incidence angle deviates from 0. We highlight that the results for the lemniscate with interior angle $\beta = \pi/36$ are not as consistent as for the other interior angles. This is not unexpected as the size of the region that is rounded near the corner is a larger percentage of the scatterer body. We note that some of these results are also demonstrated in [10], where for the Dirichlet case they show the

differences in the scattered potential of $O((k\rho)^{1.34})$ and $O((k\rho)^{1.2})$ for scatterers with interior angles of $\pi/2$ and $\pi/6$ respectively. In the Neumann case they too exhibit the demonstrated bound (3.17).

In Chapter 4 we examine the Dirichlet result analytically, and establish a bound of the form (3.16).

β	m	$2/\nu$	β	m	$2/\nu$
$\pi/2$	1.33	1.33	$\pi/12$	1.04	1.04
$\pi/3$	1.20	1.20	$\pi/18$	1.03	1.03
$\pi/4$	1.14	1.14	$\pi/36$	1.01	1.01
$\pi/6$	1.09	1.09			

Table 3.5: Illustrating the relationship between m and 2ν in $\sqrt{k}\|u_0^\infty - u_\rho^\infty\|_\infty \approx C(\theta_0)(k\rho)^m$ for different interior angles β .

θ_0	C	m	C	m	C	m
	Lemniscate, $\beta = \pi/2$		Lemniscate, $\beta = \pi/3$		Lemniscate, $\beta = \pi/12$	
0	1.32	1.33	3.73	1.20	56.11	1.04
$\pi/32$	1.32	1.33	3.73	1.20	56.03	1.04
$\pi/16$	1.31	1.33	3.71	1.20	55.80	1.04
$\pi/8$	1.28	1.33	3.64	1.20	54.87	1.04
$\pi/4$	1.16	1.33	3.35	1.20	51.41	1.04
$\pi/2$	0.68	1.33	2.27	1.20	40.58	1.05
	Two-corner		Lemniscate, $\beta = \pi/4$		Lemniscate, $\beta = \pi/18$	
0	1.30	1.33	6.88	1.14	120.85	1.03
$\pi/32$	1.30	1.33	6.87	1.14	120.68	1.03
$\pi/16$	1.29	1.33	6.84	1.14	120.19	1.03
$\pi/8$	1.26	1.33	6.71	1.14	118.26	1.03
$\pi/4$	1.14	1.33	6.22	1.14	111.01	1.03
$\pi/2$	0.69	1.33	4.33	1.14	87.73	1.03
	Square		Lemniscate, $\beta = \pi/6$		Lemniscate, $\beta = \pi/36$	
0	0.93	1.33	15.23	1.09	452.96	1.01
$\pi/32$	0.93	1.33	15.21	1.09	452.33	1.01
$\pi/16$	0.93	1.33	15.14	1.09	450.47	1.01
$\pi/8$	0.93	1.34	14.89	1.09	443.20	1.01
$\pi/4$	0.89	1.35	13.89	1.09	416.52	1.01
$\pi/2$	-	-	10.05	1.09	342.59	1.02

Table 3.6: Showing the constants C and m derived using least squares fit for $\sqrt{k}\|u_0^\infty - u_\rho^\infty\|_\infty = C(k\rho)^m$ for different directions of the incident plane wave for cornered scatterers with Dirichlet boundary condition and different interior angles, β .

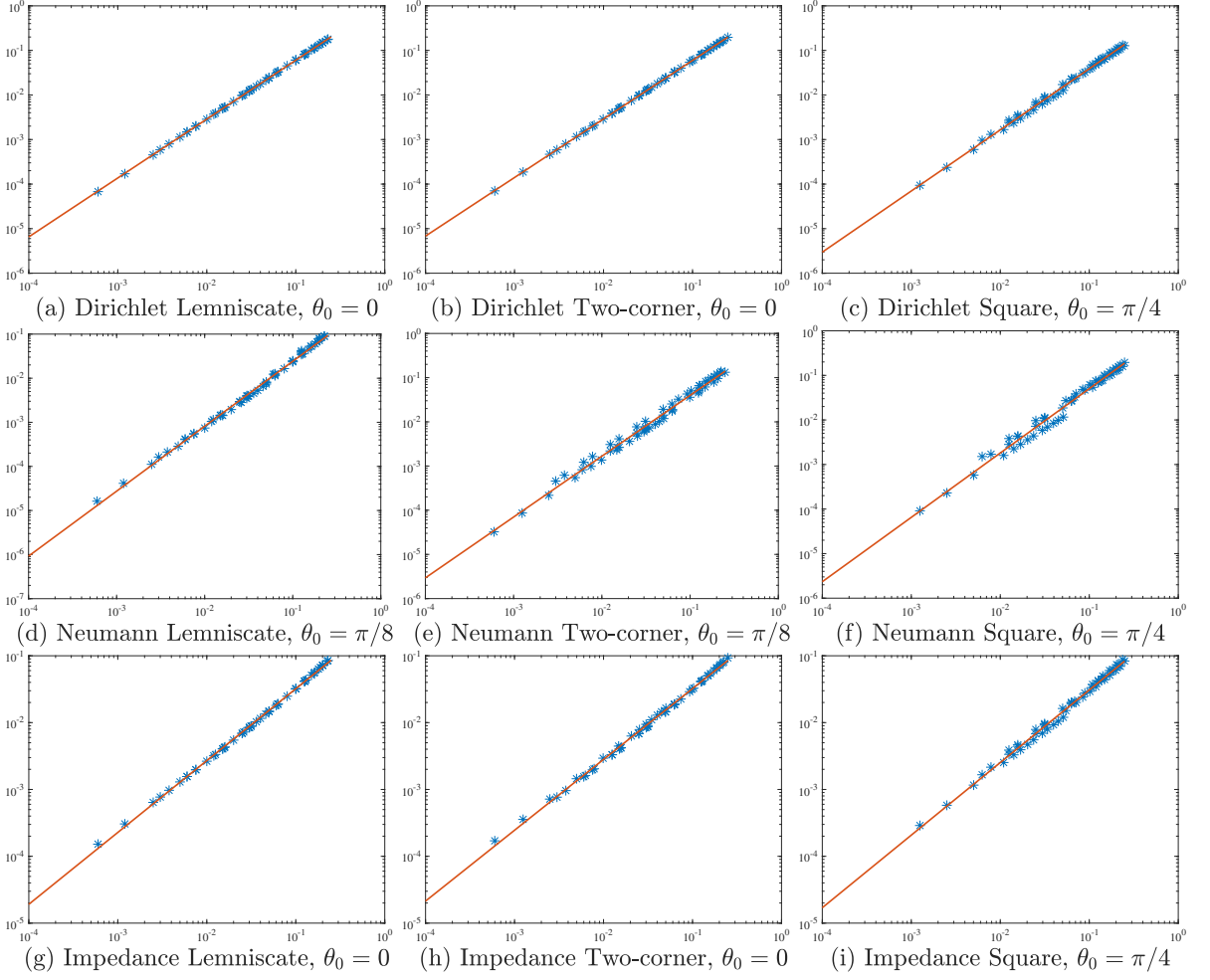


Figure 3.10: Logarithmic plot: $x = k\rho$, $y = \sqrt{k} \|u_0^\infty - u_\rho^\infty\|_\infty$.

The data points used are represented by the blue asterisks, the least squares line of fit is shown in red.

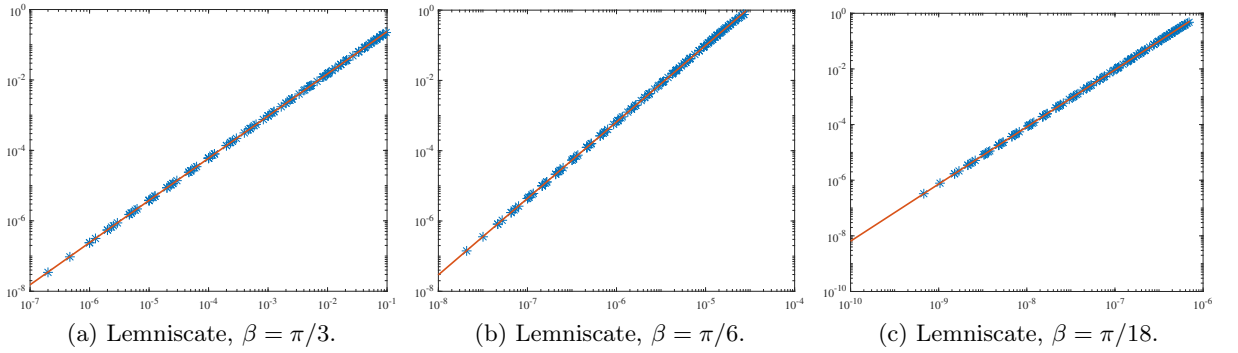


Figure 3.11: Logarithmic plot: $x = k\rho$, $y = \sqrt{k} \|u_0^\infty - u_\rho^\infty\|_\infty$.

Dirichlet boundary condition, with incident direction $\theta_0 = 0$. The data points used are represented by the blue asterisks, the least squares line of fit is shown in red.

θ_0	C	m	C	m	C	m
	Lemniscate, $\beta = \pi/2$		Lemniscate, $\beta = \pi/3$		Lemniscate, $\beta = \pi/12$	
0	1.44	1.89	4.51	1.88	158.45	1.82
$\pi/32$	0.24	1.41	0.50	1.27	3.69	1.05
$\pi/16$	0.29	1.37	0.67	1.23	6.96	1.04
$\pi/8$	0.40	1.35	1.03	1.21	12.62	1.04
$\pi/4$	0.63	1.33	1.68	1.19	26.01	1.04
$\pi/2$	1.01	1.32	2.82	1.19	48.76	1.04
	Two-corner		Lemniscate, $\beta = \pi/4$		Lemniscate, $\beta = \pi/18$	
0	1.21	1.87	13.88	1.90	206.67	1.73
$\pi/32$	0.46	1.37	0.49	1.16	7.11	1.02
$\pi/16$	0.60	1.35	0.89	1.15	13.22	1.02
$\pi/8$	0.81	1.34	1.69	1.14	25.58	1.02
$\pi/4$	1.15	1.32	3.22	1.14	56.13	1.02
$\pi/2$	1.65	1.32	5.78	1.14	101.25	1.02
	Square		Lemniscate, $\beta = \pi/6$		Lemniscate, $\beta = \pi/36$	
0	0.64	1.30	38.39	1.88	756.16	1.68
$\pi/32$	0.77	1.32	1.04	1.10	15.32	0.96
$\pi/16$	0.87	1.32	1.91	1.09	36.10	0.98
$\pi/8$	1.04	1.34	3.64	1.09	95.07	1.00
$\pi/4$	1.21	1.37	6.74	1.09	182.47	0.98
$\pi/2$	-	-	12.54	1.09	278.92	0.97

Table 3.7: Showing the constants C and m derived using least squares fit for $\sqrt{k} \|u_0^\infty - u_\rho^\infty\|_\infty = C(k\rho)^m$ for different directions of the incident plane wave for cornered scatterers with Neumann boundary condition and different interior angles, β .

θ_0	C	m	C	m	C	m
	Lemniscate, $\beta = \pi/2$		Lemniscate, $\beta = \pi/3$		Lemniscate, $\beta = \pi/12$	
0	0.28	1.01	1.01	1.01	19.57	1.00
$\pi/32$	0.28	1.01	1.01	1.01	19.63	1.00
$\pi/16$	0.28	1.01	1.01	1.01	19.81	1.00
$\pi/8$	0.28	1.01	1.01	1.01	20.43	1.00
$\pi/4$	0.26	1.01	1.01	1.01	22.04	1.01
$\pi/2$	0.20	1.01	0.90	1.02	23.67	1.01
	Two-corner		Lemniscate, $\beta = \pi/4$		Lemniscate, $\beta = \pi/18$	
0	0.31	1.02	1.94	1.00	43.18	1.00
$\pi/32$	0.31	1.02	1.94	1.00	43.38	1.00
$\pi/16$	0.31	1.02	1.94	1.00	43.94	1.00
$\pi/8$	0.31	1.02	1.95	1.00	45.50	1.00
$\pi/4$	0.31	1.02	1.98	1.01	49.49	1.00
$\pi/2$	0.37	1.04	1.84	1.01	53.77	1.01
	Square		Lemniscate, $\beta = \pi/6$		Lemniscate, $\beta = \pi/36$	
0	0.30	1.01	4.76	1.00	165.58	0.99
$\pi/32$	0.30	1.01	4.77	1.00	166.71	0.99
$\pi/16$	0.30	1.01	4.80	1.00	170.14	1.00
$\pi/8$	0.31	1.01	4.89	1.00	176.80	1.00
$\pi/4$	0.33	1.03	5.15	1.01	194.21	1.00
$\pi/2$	-	-	5.27	1.02	213.60	1.00

Table 3.8: Showing the constants C and m derived using least squares fit for $\sqrt{k} \|u_0^\infty - u_\rho^\infty\|_\infty = C(k\rho)^m$ for different directions of the incident plane wave for cornered scatterers with impedance loaded boundary condition, $Z = 1 + i$, and different interior angles, β .

3.8 Validation of Rawlins' Results on Diffraction by Absorbing Rectangular Cylinders

A recent publication by Rawlins [110] developed a model to approximate the diffraction of an E-polarised wave by an absorbing rectangular cylinder. It employed Keller's method of GTD and its extensions to deal with multiple diffraction, utilising the diffraction coefficient derived for the canonical problem of diffraction by an impedance wedge. In this way, relatively simple high frequency approximate expressions for the scattered far-field resulting from a plane wave obliquely incident on an imperfectly conducting rectangle were obtained. In [111] the results of [110] were validated and reported on using some of the methods developed in Chapter 2, by comparing them to the scattering of an E-polarised plane wave by an infinite cylindrical structure with an impedance boundary condition. The impedance problem solution (2.49) was used with parametrisation for the rounded square (2.5) and a mesh of $2n$ uniformly spaced points $t_j = \pi j/n$, for $j = 0, 1, \dots, 2n - 1$, in the parameterisation (2.1) was employed. The scattered field $u^{\text{sc}}(\mathbf{x})$ was captured on a circle radius 10 encapsulating the scatterer and plotted. This was used for visual comparison to the results reported by Rawlins [110]. This led to the conclusion that the approximations developed in [110] provide accurate scattered field patterns for rectangular structures for the range of wave numbers and dimensions examined. The back-scatter and forward-scatter were of a similar magnitude. The primary difference being the magnitude of the scattered field orthogonal to the forward- and back-scatter. Subsequent to the development of the graded mesh for four-cornered scatterers (2.66) as described in Section 2.5.3, the experiments were re-run employing graded mesh. The first set of experiments used a rounded corner as per parameterisation (2.5), with rounding parameter $\varepsilon = 0.01$ which produces a radius of curvature $\rho = 0.0142$ in the corner. The second set of experiments used an actual square (2.3), rather than a rounded one. A sample of these graphical results is provided in Appendix B. They show that the difference between the solutions of the square and rounded square scatterer is not perceptible, but that the differences between the Rawlins results and those produced using the methods described in Chapter 2 are similar to those reported in [111]: the back-scatter and forward-scatter were of a similar magnitude but that the Rawlins method magnifies

the scattered field orthogonal to the forward- and back-scatter, that is, the side scatter.

It should be noted that it is only relevant to compare the GTD based results with appropriate near-field results computed by our approach. With that in mind, our results provide a validation of Rawlins' result.

3.9 Conclusions

In this chapter we have presented the numerical results from implementing numerical schemes described in Chapter 2 for the solution of the scattering of a plane wave by different cylindrical structures possessing corners, on the surface of which we imposed three different boundary conditions - soft, hard and an impedance boundary condition. A number of conclusions may be drawn.

First, we have numerically demonstrated that the field scattered by the rounded structure converges, in both the L^2 and L^∞ norm, to that scattered by the corresponding sharp cornered object as the radius of curvature in the vicinity of the corner tends to zero.

Secondly, when the scatterer possesses sharp corners or rounded corners of small radii of curvature, it is essential to use an appropriate quadrature scheme - a graded mesh - in order to obtain numerical results efficiently. Use of a uniform mesh is at best grossly inefficient and at worst produces non-convergence of the numerical process.

Thirdly, some useful rules of thumb are as follows. For the soft boundary condition, the L^∞ norm difference between the far-scattered field of the single-cornered scatterer and that of the rounded scatterer is less than 3% when the radius of curvature is restricted so that $k\rho \leq 3\pi/50$. This percentage reduces to 1% or 2% respectively, when the boundary condition is replaced by the Neumann boundary condition or the impedance boundary condition (with $Z = 1 + i$), respectively. More precise measures of the difference are given in Table 3.3. Similar results were obtained for the two-cornered and four-cornered objects, and are also displayed in Table 3.3. We also demonstrated that the maximum differences between the far-fields of the cornered and rounded scatterers occur in the back-scatter region and the magnitude of these differences is dependent on the radius of curvature, ρ , used for the rounding, the wave number, ka , and the angle of the incident plane wave, θ_0 .

Fourthly, we have shown that the described quadrature schemes are valid for structures with non right-angled corners, that is, for structures with interior angles $\pi/12 < \beta < 35\pi/36$, and achieve rapid convergence. Outside this range, the number of quadrature points required to achieve a highly accurate solution increases noticeably for extremely acute angles. The number of quadrature points in this circumstance can be decreased for these structures if the corner is rounded slightly and the resultant maximum difference in the far-field is 1.7% or less for wave number $ka = 1$, and $\leq 4.1\%$, $\leq 9.6\%$ for $ka = 2\pi$ and $ka = 16\pi$, respectively.

We have also examined the nature of the differences in the far-fields of the cornered structure and its rounded counterpart. We observed that the maximum differences between the far-fields of the cornered and rounded scatterers occur in the back-scatter region and the magnitude of these differences is dependent on the radius of curvature, ρ , used for the rounding, the wave number, ka , and the angle of the incident plane wave, θ_0 .

Finally, we have demonstrated the dependence on the maximum differences in the far-field of a cornered scatterer and its rounded counterpart on the radius of curvature in the rounded corner and the wave number and direction of travel of the illuminating incident plane wave. In the Dirichlet case, the non-dimensionalised maximum difference in the far-fields has the form $C(\theta_0)(k\rho)^{2/\nu}$, for some constant $C(\theta_0)$ dependent on the angle of illumination, as $k\rho \rightarrow 0$. For the impedance loaded case with $Z = 1 + i$, the exponent $2/\nu$ is replaced by 1. For the Neumann case, the exponent is dependent on the angle of illumination, but the maximum difference is bounded by $C(\theta_0)(k\rho)^{2/\nu}$.

To summarise, we have produced strong numerical evidence that supports the expectation that the differences in the scattered field quantities are small and tend to zero as the radius of curvature of the rounded corners is reduced to zero. In the next chapter we will prove that this is indeed the case and establish the validity of the power law dependence on $k\rho$.

Chapter 4

Bounds Analysis

When a two-dimensional scatterer with Dirichlet boundary condition, which is smooth except at finitely many sharp corner points, is illuminated by a time-harmonic acoustic plane wave, the physical surface quantity (equal to the normal derivative of the acoustic velocity potential) exhibits singularities at those corner points. In the Neumann case the corresponding physical quantity (equal to the acoustic velocity potential itself) exhibits singularities in its derivative at those points. Once the corners are rounded, these surface quantities become non-singular.

In Chapters 2 and 3, a numerical scheme and its implementation for the solution of scattering of a plane wave by structures with corners for three different boundary conditions (Dirichlet, Neumann and impedance loaded) were examined. The maximum difference in the far-field patterns generated by the cornered structure u_0^∞ and the corresponding quantity u_ρ^∞ when the corners are rounded, were computed for a range of wave numbers k ; in particular it was demonstrated numerically that as the radius of curvature ρ of the rounded corner decreases, that is, as $k\rho \rightarrow 0$, the non-dimensionalised difference $\sqrt{k} \|u_0^\infty - u_\rho^\infty\|_\infty$ is $O((k\rho)^m)$, where $m = 4/3$ for the Dirichlet case for structures with right-angled corners.

An integral equation formulation was used for these numerical studies of the scattering of plane waves by a soft obstacle; its solution provides a continuous surface density from which all physical quantities such as far-field pattern can be calculated. This surface density is different from the physical surface quantities described above and has

no simple physical interpretation¹. In this chapter, after introducing suitable surface parameterisations for the rounded and unrounded scatterers, we analyse the underlying integral equations for each scatterer, and deduce an approximate integral equation for the difference in the surface density at corresponding points, in terms of the difference in the illuminating incident field on each scatterer and of the surface quantity on the sharp cornered object. We take the lemniscate scatterer with right-angled corner studied in Chapter 3 as a test case. The approximate solution of the integral equation is shown to be $O((k\rho)^{2/3})$, from which it is deduced that $\sqrt{k} \|u_0^\infty - u_\rho^\infty\|_\infty = O((k\rho)^{4/3})$, as $k\rho \rightarrow 0$.

4.1 Formulation

We consider an infinitely long cylinder with uniform cross-section and Dirichlet boundary condition (2.19), with axis parallel to the z -axis, and illuminated by a time-harmonic incident plane wave $u^{\text{inc}}(\mathbf{x})$ propagating with direction parallel to the x - y plane; the cross-section D lying in the x - y plane has a closed boundary ∂D parameterised by

$$\mathbf{x}(t) = (x_1(t), x_2(t)), \quad t \in [-\pi, \pi]. \quad (4.1)$$

We assume the properties regarding the incident and scattered fields described in Section 2.2.

As shown in [7, 56], the combined single-layer $\frac{1}{2}\mathcal{S}\varphi(\mathbf{x})$ (2.32) and double-layer $\frac{1}{2}\mathcal{K}\varphi(\mathbf{x})$ (2.32) potentials provide a solution, at all points \mathbf{x} exterior to the body D , to the exterior Dirichlet problem (2.39) provided $\varphi(\mathbf{x})$ is a solution to the following integral equation on ∂D :

$$\varphi + \mathcal{K}\varphi - i\eta\mathcal{S}\varphi = -2g, \quad (4.2)$$

where $g = u^{\text{inc}}$, the real constant $\eta \neq 0$ and

$$(\mathcal{S}\varphi)(\mathbf{x}) = 2 \int_{\partial D} G(\mathbf{x}, \mathbf{y}) \varphi(\mathbf{y}) \, ds(\mathbf{y}), \quad (4.3)$$

¹We tentatively suggest the name *soft surface distribution*. The relevant physical surface distribution is of course zero (corresponding to the Dirichlet boundary condition); the other relevant physical quantity is its normal derivative which is non-zero.

and

$$(\mathcal{K}\varphi)(\mathbf{x}) = 2 \int_{\partial D} \frac{\partial G(\mathbf{x}, \mathbf{y})}{\partial \mathbf{n}(\mathbf{y})} \varphi(\mathbf{y}) \, ds(\mathbf{y}). \quad (4.4)$$

For simplicity of presentation we will suppose that $\eta = 0$; then the integral equation has a unique solution at all except countably many wave numbers k .

4.2 Integral Equations for the Difference in Surface Quantities

We examine the lemniscate, shown in Fig. 4.1, as a test case.

We use the following parameterisations,

$$\mathbf{x}_0(t) = (x_{0,1}(t), x_{0,2}(t)) = (2 \sin(|t|/2), -\sin t), \quad (4.5)$$

and the corresponding rounded object depending upon a (small) positive parameter ε ,

$$\mathbf{x}_\varepsilon(t) = (x_{\varepsilon,1}(t), x_{\varepsilon,2}(t)) = (2\sqrt{\varepsilon^2 + (1 - \varepsilon^2) \sin^2(t/2)}, -\sin t), \quad (4.6)$$

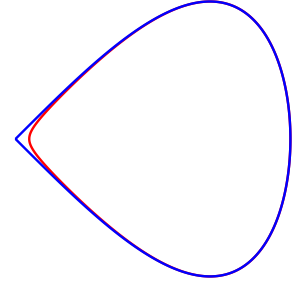


Figure 4.1: The lemniscate (blue) and the rounded scatterer (red) with a radius of curvature $\rho \approx 0.1$.

for $t \in [-\pi, \pi]$. The radius of curvature ρ at the rounded corner point (corresponding to $t = 0$) is very close to 2ε , for small ε (Lemma C.1.1).

The outward pointing unit normal at the point $\mathbf{x}_0(t)$ on the lemniscate is

$$\mathbf{n}(\mathbf{x}_0(t)) = (x'_{0,2}(t), -x'_{0,1}(t)) / \sqrt{(x'_{0,1}(t))^2 + (x'_{0,2}(t))^2}; \quad (4.7)$$

the outward pointing unit normal at the point $\mathbf{x}_\varepsilon(\tau)$ on the rounded object is similarly defined.

Inserting these parameterisations in (4.4) determines double-layer potentials \mathcal{K}_0 and \mathcal{K}_ε . The integral equations governing the surface quantities $\varphi_0 = \varphi(\mathbf{x}_0)$ and $\varphi_\varepsilon = \varphi(\mathbf{x}_\varepsilon)$ are

$$\varphi(\mathbf{x}_0) + \mathcal{K}_0 \varphi(\mathbf{x}_0) = -2u^{\text{inc}}(\mathbf{x}_0), \quad (4.8)$$

and

$$\varphi(\mathbf{x}_\varepsilon) + \mathcal{K}_\varepsilon \varphi(\mathbf{x}_\varepsilon) = -2u^{\text{inc}}(\mathbf{x}_\varepsilon). \quad (4.9)$$

More concretely, if we set $\varphi_0(t) = \varphi_0(\mathbf{x}_0(t))$ and $\varphi_\varepsilon(t) = \varphi_\varepsilon(\mathbf{x}_\varepsilon(t))$, then with $t \in [-\pi, \pi]$,

$$\varphi_\varepsilon(t) - \int_{-\pi}^{\pi} H_\varepsilon(t, \tau) \varphi_\varepsilon(\tau) d\tau = g_\varepsilon(t), \quad (4.10)$$

and

$$\varphi_0(t) - \int_{-\pi}^{\pi} H_0(t, \tau) \varphi_0(\tau) d\tau = g_0(t), \quad (4.11)$$

where (see [7])

$$H_0(t, \tau) = \frac{1}{2}ik \frac{H_1^{(1)}(k|\mathbf{x}_0(t) - \mathbf{x}_0(\tau)|)}{|\mathbf{x}_0(t) - \mathbf{x}_0(\tau)|} \mathbf{n}(\mathbf{x}_0(\tau)) \cdot (\mathbf{x}_0(t) - \mathbf{x}_0(\tau)) |\mathbf{x}_0'(\tau)|, \quad (4.12)$$

and $H_\varepsilon(t, \tau)$ is similarly defined.

Thus, setting $\Delta(t) = \varphi_\varepsilon(t) - \varphi_0(t)$, we obtain

$$\Delta(t) - \int_{-\pi}^{\pi} H_\varepsilon(t, \tau) \Delta(\tau) d\tau = \int_{-\pi}^{\pi} (H_\varepsilon(t, \tau) - H_0(t, \tau)) \varphi_0(\tau) d\tau + g_\varepsilon(t) - g_0(t). \quad (4.13)$$

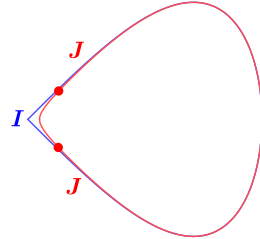
Thus if we regard $\varphi_0(\tau)$ as known, then this is an integral equation for the unknown difference to be determined.

4.3 Approximate Integral Equation for the Difference in Surface Quantity

Now let I be a symmetrical subinterval of $[-\pi, \pi]$ containing 0, and set $J = [-\pi, \pi] \setminus I$. The intervals I and J will be fully specified later (in fact $I = [-\varepsilon^{2/3}, \varepsilon^{2/3}]$), but the requirements are:

- (a) on the set J , the difference in the parameterisations (4.5) and (4.6), and in their derivatives, are negligibly small. In fact,

$$\|\mathbf{x}_0 - \mathbf{x}_\rho\|_{\infty, J} = \max_{t \in J} |\mathbf{x}_0(t) - \mathbf{x}_\rho(t)| \leq 4\varepsilon^{4/3}, \quad (4.14)$$



from Lemma C.1.2, and similarly

$$\|\mathbf{x}'_0 - \mathbf{x}'_\rho\|_{\infty, J} = \max_{t \in J} |\mathbf{x}'_0(t) - \mathbf{x}'_\rho(t)| \leq 2\varepsilon^{2/3}, \quad (4.15)$$

from Lemma C.1.3;

- (b) on the set J , the difference in the surface currents on either object, $\|\varphi_\varepsilon - \varphi_0\|_{\infty, J}$, are negligibly small. We make this analytic assumption which is numerically justified in Appendix C.2;
- (c) the interval I is small, that is, $k|I|$ is small, so that we may use small argument approximations for the Hankel function $H_1^{(1)}$. This is equivalent to approximating the Green's function $G(\mathbf{x}, \mathbf{y})$ at points \mathbf{x}, \mathbf{y} , parameterised by I , by the corresponding values of static Green's function $G_0(\mathbf{x}, \mathbf{y})$.

Thus we make the approximation $\Delta(t) = 0$ for $t \in J$. Inserting this in (4.13) produces, when $t \in I$,

$$\begin{aligned} \Delta(t) - \int_I H_\varepsilon(t, \tau) \Delta(\tau) d\tau &= \int_I (H_\varepsilon(t, \tau) - H_0(t, \tau)) \varphi_0(\tau) d\tau \\ &\quad + \int_J (H_\varepsilon(t, \tau) - H_0(t, \tau)) \varphi_0(\tau) d\tau + g_\varepsilon(t) - g_0(t). \end{aligned} \quad (4.16)$$

Define the operator L by

$$L\varphi(t) = \int_I H_\varepsilon(t, \tau) \varphi(\tau) d\tau, \quad (4.17)$$

for $t \in I$, and for each $\varphi \in C[-\pi, \pi]$. Then denoting the right hand side of (4.16) by $h(t)$, we obtain

$$(I - L)\Delta(t) = h(t). \quad (4.18)$$

We will proceed to obtain an estimate for $\Delta(t)$ by obtaining bounds on the operator L and on the function $h(t)$. First we establish

Lemma 4.3.1 *The operator L has the property $\|L\|_\infty < 1$.*

Proof. Without loss of generality, we fix $t \in I$ for some $t > 0$. Consider

$$\begin{aligned}
|L\varphi(t)| &= \left| \int_I H_\varepsilon(t, \tau) \varphi(\tau) d\tau \right| \\
&\leq \int_I |H_\varepsilon(t, \tau) \varphi(\tau)| d\tau \\
&\leq \int_I |H_\varepsilon(t, \tau)| d\tau \|\varphi\|_\infty, \quad \text{where } \|\varphi\|_\infty = \sup_{t \in I} |\varphi(t)|, \\
&= \left(\int_{I, \tau > 0} |H_\varepsilon(t, \tau)| d\tau + \int_{I, \tau < 0} |H_\varepsilon(t, \tau)| d\tau \right) \|\varphi\|_\infty, \tag{4.19}
\end{aligned}$$

where the first integral is taken over the interval $\{\tau \in I \mid \tau > 0\}$ and the second integral similarly. We will evaluate each of the integral contributions separately.

Contribution when $\tau > 0$:

We use the small argument approximation for $H_1^{(1)}$ [120], thus

$$\begin{aligned}
&\int_{I, \tau > 0} |H_\varepsilon(t, \tau)| d\tau \\
&= \int_0^{\varepsilon^{2/3}} \left| \frac{ik H_1^{(1)}(k|\mathbf{x}_\varepsilon(t) - \mathbf{x}_\varepsilon(\tau)|)}{2} \frac{\mathbf{n}(\mathbf{x}_\varepsilon(\tau)) \cdot (\mathbf{x}_\varepsilon(t) - \mathbf{x}_\varepsilon(\tau))}{|\mathbf{x}_\varepsilon(t) - \mathbf{x}_\varepsilon(\tau)|} |\mathbf{x}'_\varepsilon(\tau)| \right| d\tau \\
&= \int_0^{\varepsilon^{2/3}} \left| \frac{ik}{2} \left(\frac{-2i}{\pi} \right) \frac{\mathbf{n}(\mathbf{x}_\varepsilon(\tau)) \cdot (\mathbf{x}_\varepsilon(t) - \mathbf{x}_\varepsilon(\tau))}{k|\mathbf{x}_\varepsilon(t) - \mathbf{x}_\varepsilon(\tau)|^2} |\mathbf{x}'_\varepsilon(\tau)| \right| d\tau \\
&= \frac{1}{\pi} \int_0^{\varepsilon^{2/3}} |\mathbf{x}'_\varepsilon(\tau)| \frac{|\mathbf{n}(\mathbf{x}_\varepsilon(\tau)) \cdot (\mathbf{x}_\varepsilon(t) - \mathbf{x}_\varepsilon(\tau))|}{|\mathbf{x}_\varepsilon(t) - \mathbf{x}_\varepsilon(\tau)|^2} d\tau. \tag{4.20}
\end{aligned}$$

Note that $|\mathbf{x}'_\varepsilon(\tau)| \leq \sqrt{2}$ (see Lemma C.1.4 for details); also $\mathbf{n}(\mathbf{x}_\varepsilon(\tau)) \cdot \mathbf{x}'_\varepsilon(\tau) = 0$ for all τ . Thus the integral (4.20) is bounded by

$$\frac{\sqrt{2}}{\pi} \int_0^{\varepsilon^{2/3}} \frac{|\mathbf{n}(\mathbf{x}_\varepsilon(\tau)) \cdot (\mathbf{x}_\varepsilon(t) - \mathbf{x}_\varepsilon(\tau) - (t - \tau)\mathbf{x}'_\varepsilon(\tau))|}{|\mathbf{x}_\varepsilon(t) - \mathbf{x}_\varepsilon(\tau)|^2} d\tau. \tag{4.21}$$

We apply the Mean Value Theorem to the denominator, where

$$|\mathbf{x}_\varepsilon(t) - \mathbf{x}_\varepsilon(\tau)| \doteq |(t - \tau)| |\mathbf{x}'_\varepsilon(\tau^*)|, \tag{4.22}$$

for some $\tau^* \in (t, \tau)$. We make the standard central finite difference choice $\tau^* = \frac{t+\tau}{2}$ and approximate the numerator with the second order Taylor series expansion with the same

choice of τ^* ,

$$\mathbf{x}_\varepsilon(t) = \mathbf{x}_\varepsilon(\tau) + (t - \tau)\mathbf{x}'_\varepsilon(\tau) + \frac{1}{2}(t - \tau)^2\mathbf{x}''_\varepsilon(\tau^*), \quad (4.23)$$

so that (4.21) is approximated by

$$\begin{aligned} & \frac{1}{\sqrt{2\pi}} \int_0^{\varepsilon^{2/3}} \frac{|\mathbf{n}(\mathbf{x}_\varepsilon(\tau)) \cdot ((t - \tau)^2 \mathbf{x}''_\varepsilon(\tau^*))|}{|(t - \tau)|^2 |\mathbf{x}'_\varepsilon(\tau^*)|^2} d\tau \\ &= \frac{1}{\sqrt{2\pi}} \int_0^{\varepsilon^{2/3}} \frac{|(t - \tau)|^2 |\mathbf{n}(\mathbf{x}_\varepsilon(\tau)) \cdot \mathbf{x}''_\varepsilon(\frac{t+\tau}{2})|}{|(t - \tau)|^2 |\mathbf{x}'_\varepsilon(\frac{t+\tau}{2})|^2} d\tau \\ &= \frac{1}{\sqrt{2\pi}} \int_0^{\varepsilon^{2/3}} \frac{|\mathbf{n}(\mathbf{x}_\varepsilon(\tau)) \cdot \mathbf{x}''_\varepsilon(\frac{t+\tau}{2})|}{|\mathbf{x}'_\varepsilon(\frac{t+\tau}{2})|^2} d\tau. \end{aligned} \quad (4.24)$$

The integrand in (4.24) is correct to order $O(t - \tau)$, so that the approximation is overall correct to $O(\varepsilon^{2/3})$. Note that $\mathbf{x}_\varepsilon(\tau) = (x_{\varepsilon,1}(\tau), -\sin \tau) \sim (x_{\varepsilon,1}(\tau), -\tau)$ when τ is small.

As such,

$$\begin{aligned} \mathbf{x}'_\varepsilon(\tau) &\sim (x'_{\varepsilon,1}(\tau), -1) \\ |\mathbf{x}'_\varepsilon(\tau)| &\sim (1 + (x'_{\varepsilon,1}(\tau))^2)^{1/2} \\ \mathbf{x}''_\varepsilon(\tau) &\sim (x''_{\varepsilon,1}(\tau), 0). \end{aligned} \quad (4.25)$$

Applying these results for t and τ small enough, the integral (4.24) is approximated by

$$\begin{aligned} & \frac{1}{\sqrt{2\pi}} \int_0^{\varepsilon^{2/3}} \frac{|-x''_{\varepsilon,1}(\frac{t+\tau}{2})|}{|1 + (x'_{\varepsilon,1}(\frac{t+\tau}{2}))^2|} d\tau \\ &= \frac{1}{\sqrt{2\pi}} \int_0^{\varepsilon^{2/3}} \frac{x''_{\varepsilon,1}(\frac{t+\tau}{2})}{1 + (x'_{\varepsilon,1}(\frac{t+\tau}{2}))^2} d\tau \\ &= \frac{1}{\sqrt{2\pi}} [2 \arctan(x'_{\varepsilon,1}(\frac{t+\tau}{2}))]_0^{\varepsilon^{2/3}} \\ &\leq \frac{\sqrt{2}}{\pi} \arctan\left(x'_{\varepsilon,1}(\frac{t+\varepsilon^{2/3}}{2})\right) \\ &\leq \frac{\sqrt{2}}{\pi} \arctan(1), \end{aligned} \quad (4.26)$$

since $|x'_{\varepsilon,1}(t^*)| < 1$ for all t^* , which can readily be deduced from (C.2). Thus

$$\int_{I, \tau > 0} |H_\varepsilon(t, \tau)| d\tau \leq \frac{1}{2\sqrt{2}}. \quad (4.27)$$

Contribution when $\tau < 0$:

In this case, the argument applied above may be employed to show

$$\int_{I, \tau < 0} |H_\varepsilon(t, \tau)| d\tau \leq \frac{1}{2\sqrt{2}}. \quad (4.28)$$

However, it might be considered that the Taylor series substitution is not suitable for this case because with $t > 0$ and $\tau < 0$ in (4.23), the term $\mathbf{x}_\varepsilon''(\tau^*)$ may be very large; indeed $\mathbf{x}_\varepsilon''(0) \sim 1/\varepsilon$. Instead we approximate $H_\varepsilon(t, \tau)$ using $H_0(t, \tau)$. Thus $\mathbf{x}_0(t) = (t, t)$, $\mathbf{x}_0(\tau) = (\tau, -\tau)$, $\mathbf{n}(\mathbf{x}_0(\tau)) \cdot \mathbf{x}_0(\tau) = 0$ for all τ , and $\mathbf{n}(\mathbf{x}_0(\tau)) \cdot \mathbf{x}_0(t) = -|\mathbf{x}_0(t)|$.

Using the small argument approximation for $H_1^{(1)}$ [120],

$$\begin{aligned} & \int_{I, \tau < 0} |H_\varepsilon(t, \tau)| d\tau \\ & \approx \int_{I, \tau < 0} |H_0(t, \tau)| d\tau \\ & = \int_{-\varepsilon^{2/3}}^0 \left| \frac{ik H_1^{(1)}(k|\mathbf{x}_0(t) - \mathbf{x}_0(\tau)|)}{2} \frac{\mathbf{n}(\mathbf{x}_0(\tau)) \cdot (\mathbf{x}_0(t) - \mathbf{x}_0(\tau))}{|\mathbf{x}_0(t) - \mathbf{x}_0(\tau)|} |\mathbf{x}_0'(\tau)| \right| d\tau \\ & \simeq \int_{-\varepsilon^{2/3}}^0 \left| \frac{ik}{2} \left(\frac{-2i}{\pi} \right) \frac{\mathbf{n}(\mathbf{x}_0(\tau)) \cdot (\mathbf{x}_0(t) - \mathbf{x}_0(\tau))}{k|\mathbf{x}_0(t) - \mathbf{x}_0(\tau)|^2} |\mathbf{x}_0'(\tau)| \right| d\tau \\ & = \frac{\sqrt{2}}{\pi} \int_{-\varepsilon^{2/3}}^0 \frac{|\mathbf{x}_0(t)|}{|\mathbf{x}_0(t) - \mathbf{x}_0(\tau)|^2} d\tau \\ & = \frac{1}{\pi} \int_0^{\varepsilon^{2/3}} \frac{t}{t^2 + \tau^2} d\tau \\ & = \frac{1}{\pi} \arctan \frac{\varepsilon^{2/3}}{t} \leq \frac{1}{2}. \end{aligned} \quad (4.29)$$

Thus

$$\begin{aligned} |L\varphi(t)| & \leq \left(\int_{I, \tau > 0} |H_\varepsilon(t, \tau)| d\tau + \int_{I, \tau < 0} |H_\varepsilon(t, \tau)| d\tau \right) \|\varphi\|_\infty \\ & \leq \left(\frac{1}{2\sqrt{2}} + \frac{1}{2} \right) \|\varphi\|_\infty \\ & < \|\varphi\|_\infty. \end{aligned} \quad (4.30)$$

Thus

$$\|L\|_\infty < 1. \quad (4.31)$$

■

Applying Lemma 4.3.1, $\Delta(t)$ may be recovered from the convergent Neumann series

$$\Delta(t) = (I - L)^{-1}h(t) = \sum_{n=0}^{\infty} L^n h(t). \quad (4.32)$$

Moreover,

$$|\Delta(t)| \leq \|(I - L)^{-1}\|_{\infty} \|h\|_{\infty}, \quad (4.33)$$

for all t ; also

$$\|(I - L)^{-1}\|_{\infty} \leq (1 - \|L\|_{\infty})^{-1}. \quad (4.34)$$

We now consider estimates for $h(t)$. First an estimate for the function $\varphi_0(t)$ for $t \in I$ is needed.

Lemma 4.3.2

$$\varphi_0(r) = A + B(kr)^{2/3} + O(kr),$$

where A and B are suitable constants, as $kr \rightarrow 0$.

Proof. We approximate this by the surface current induced by the same illuminating field on the infinite wedge whose edges are tangent to the corner point (corresponding to parameter value $t = 0$). We use the results of [1] concerning infinite wedges of internal angle 2Ω (and specialise later to the case $2\Omega = \pi/2$).

Employ cylindrical polars (r, θ) with centre at the tip of the wedge of internal angle 2Ω whose sides are defined by $\theta = \pm\Omega$. Suppose the wedge is illuminated by a unit strength field incident from direction θ_0 , so that

$$u^{\text{inc}} = \exp(-ikr \cos(\theta - \theta_0)). \quad (4.35)$$

Set $\nu = (2\pi - 2\Omega)/\pi$.

Then in the vicinity of the tip [1], the total field is

$$u_0^{\text{tot}}(r, \theta) = \frac{4}{\Gamma(1/\nu)} \left(\frac{1}{2}kr\right)^{1/\nu} e^{-i\pi/\nu} \sin\left(\frac{\theta - \Omega}{\nu}\right) \sin\left(\frac{\theta_0 - \Omega}{\nu}\right) + O((kr)^{\min(2/\nu, 1)}), \quad (4.36)$$

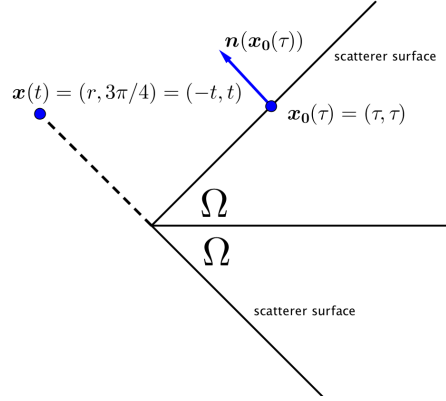
as $kr \rightarrow 0$. Thus the scattered field has the form

$$u_0^{\text{sc}}(r, \theta) = u_0^{\text{tot}}(r, \theta) - u_0^{\text{inc}}(r, \theta) = C_\nu \left(\frac{1}{2}kr\right)^{1/\nu} - 1 + O((kr)^{\min(2/\nu, 1)}), \quad (4.37)$$

as $kr \rightarrow 0$, for a suitable constant C_ν .

The scattered field at an off-body point \mathbf{x} is related to the corresponding surface distribution φ_0^w on the wedge ∂D by

$$u_0^{\text{sc}}(\mathbf{x}) = \int_{\partial D} \frac{\partial G(\mathbf{x}, \mathbf{y})}{\partial \mathbf{n}(\mathbf{y})} \varphi_0^w(\mathbf{y}) \, ds(\mathbf{y}). \quad (4.38)$$



We use the parameterisation $\mathbf{x}_0(\tau) = (|\tau|, \tau \tan \Omega)$ for the wedge, so that the unit outward normal is $\mathbf{n}(\mathbf{x}_0(\tau)) = (-\sin \Omega, (\text{sgn} \tau) \cos \Omega,)$. Now specialise to the case $\Omega = \pi/4$. Notice that

$$\mathbf{n}(\mathbf{x}_0(\tau)) \cdot \mathbf{x}_0(\tau) = 0, \quad (4.39)$$

for all τ , and for an off body point with polar coordinates $(r, 3\pi/4)$,

$$\mathbf{n}(\mathbf{x}_0(\tau)) \cdot \mathbf{x}(t) = 0, \quad (4.40)$$

when $\tau < 0$. Thus, for the right-angled wedge, the scattered field representation at that off-body point may be written as

$$\begin{aligned} & \frac{ik}{2} \int_{\partial D} \frac{H_1^{(1)}(k|\mathbf{x}_0(t) - \mathbf{x}_0(\tau)|)}{|\mathbf{x}_0(t) - \mathbf{x}_0(\tau)|} \mathbf{n}(\mathbf{x}_0(\tau)) \cdot (\mathbf{x}_0(t) - \mathbf{x}_0(\tau)) |\mathbf{x}'_0(\tau)| \varphi_0(\tau) \, d\tau \\ &= \frac{ik}{2} \int_0^\infty \frac{H_1^{(1)}(k|\mathbf{x}_0(t) - \mathbf{x}_0(\tau)|)}{|\mathbf{x}_0(t) - \mathbf{x}_0(\tau)|} \mathbf{n}(\mathbf{x}_0(\tau)) \cdot (\mathbf{x}_0(t) - \mathbf{x}_0(\tau)) |\mathbf{x}'_0(\tau)| \varphi_0(\tau) \, d\tau \quad (\text{see 4.40}) \\ &= \frac{ikr}{\sqrt{2}} \int_0^\infty \frac{H_1^{(1)}(k\sqrt{2}(r^2 + \tau^2)^{1/2})}{(r^2 + \tau^2)^{1/2}} \varphi_0(\tau) \, d\tau, \end{aligned} \quad (4.41)$$

and setting $\tau = ru$ yields,

$$\frac{ikr}{\sqrt{2}} \int_0^\infty \frac{H_1^{(1)}(\sqrt{2}kr(u^2 + 1)^{1/2})}{(u^2 + 1)^{1/2}} \varphi_0(ru) \, du. \quad (4.42)$$

This must equal (4.37), upon setting $2\Omega = \pi/2$. We note that this integral is convergent, since, using the limiting values of the Hankel function [120],

$$\frac{H_1^{(1)}(\sqrt{2}kr(u^2 + 1)^{1/2})}{(u^2 + 1)^{1/2}} \sim \sqrt{\frac{2}{\pi}} e^{i3\pi/4} \frac{e^{-i\sqrt{2}kr(u^2 + 1)^{1/2}}}{(\sqrt{2}kr)^{1/2}(u^2 + 1)^{3/4}} = O\left(\frac{1}{u^{3/4}}\right), \quad (4.43)$$

as $u \rightarrow \infty$.

We split the contribution to the integral as the sum over into the two intervals $[0, 1/(kr)]$ and $[1/(kr), \infty)$. When $\varphi_0(r)$ has the form $(kr)^\alpha$ for some α (restricted to $0 \leq \alpha < 1$), we can show that the integral takes the values $K_\alpha(kr) + O(kr)$ as $kr \rightarrow 0$, where

$$K_\alpha = \frac{1}{\pi} \int_0^\infty \frac{u^\alpha}{u^2 + 1} \, du. \quad (4.44)$$

The details are as follows.

$$\begin{aligned} & \frac{ikr}{\sqrt{2}} \int_0^{1/kr} \frac{H_1^{(1)}(\sqrt{2}kr(u^2 + 1)^{1/2})}{(u^2 + 1)^{1/2}} \varphi_0(ru) \, du \\ &= \frac{ikr}{\sqrt{2}} \int_0^{1/kr} \frac{H_1^{(1)}(\sqrt{2}kr(u^2 + 1)^{1/2})}{(u^2 + 1)^{1/2}} (kru)^\alpha \, du, \end{aligned} \quad (4.45)$$

and using the small argument approximation for $H_1^{(1)}$ [120],

$$\begin{aligned} & \sim \frac{ikr}{\sqrt{2}} \int_0^{1/kr} \frac{-2i}{\pi} \frac{1}{\sqrt{2}kr(u^2 + 1)^{1/2}} \frac{(kru)^\alpha}{(u^2 + 1)^{1/2}} \, du \\ &= \frac{(kr)^\alpha}{\pi} \int_0^{1/kr} \frac{u^\alpha}{u^2 + 1} \, du \\ &= K_\alpha (kr)^\alpha (1 + o(1)), \end{aligned} \quad (4.46)$$

as $kr \rightarrow 0$. Evaluating the second contribution,

$$\begin{aligned} & \left| \frac{ikr}{\sqrt{2}} \int_{1/kr}^\infty \frac{H_1^{(1)}(\sqrt{2}kr(u^2 + 1)^{1/2})}{(u^2 + 1)^{1/2}} \varphi_0(ru) \, du \right| \\ & \leq \frac{kr}{\sqrt{2}} \int_{1/kr}^\infty \frac{|H_1^{(1)}(\sqrt{2}kr(u^2 + 1)^{1/2})|}{|(u^2 + 1)^{1/2}|} |\varphi_0(ru)| \, du, \end{aligned} \quad (4.47)$$

and using the large argument approximation for $H_1^{(1)}$ [120],

$$\begin{aligned}
& \sim \frac{kr}{\sqrt{2}} \int_{1/kr}^{\infty} \sqrt{\frac{2}{\pi}} \frac{1}{\sqrt{\sqrt{2}kr(u^2+1)^{1/2}}} \frac{|\varphi_0(ru)|}{(u^2+1)^{1/2}} du \\
& \leq \sqrt{\frac{kr}{\pi\sqrt{2}}} \int_{1/kr}^{\infty} \frac{1}{(u^2+1)^{3/4}} du \|\varphi_0\|_{\infty} \\
& \leq \sqrt{kr} \|\varphi_0\|_{\infty} \int_{1/kr}^{\infty} \frac{1}{(u^2+1)^{3/4}} du,
\end{aligned} \tag{4.48}$$

since $\varphi_0(u)$ is bounded by $\|\varphi_0\|_{\infty}$ [1]. Thus the integral is bounded by

$$\sqrt{kr} \|\varphi_0\|_{\infty} \int_{1/kr}^{\infty} \frac{1}{u^{3/2}} du = 2kr \|\varphi_0\|_{\infty}, \tag{4.49}$$

which is $O(kr)$ as $kr \rightarrow 0$. Combining these two results, as $kr \rightarrow 0$, the integral takes the values $K_{\alpha}(kr)^{\alpha} + O(kr)$. For the lemniscate, $\alpha = 1/\nu = 2/3$. In other words, we may take the surface distribution to be

$$\varphi_0(r) = A + B(kr)^{2/3} + O(kr), \tag{4.50}$$

where A and B are suitable constants, as $kr \rightarrow 0$. ■

We are now in a position to evaluate the function $h(t)$ in equation (4.18) by inserting (4.50) in the first term on the right of (4.16) and approximating the other two.

Let $h_1(t)$, $h_2(t)$ denote the first and second terms on the right hand side of (4.16).

Thus

$$h_1(t) = \int_I (H_{\varepsilon}(t, \tau) - H_0(t, \tau)) \varphi_0(\tau) d\tau, \tag{4.51}$$

and

$$h_2(t) = \int_J (H_{\varepsilon}(t, \tau) - H_0(t, \tau)) \varphi_0(\tau) d\tau. \tag{4.52}$$

The following lemmas establish that both $h_1(t)$ and $h_2(t)$ are $O((k\varepsilon)^{2/3})$ as $k\varepsilon \rightarrow 0$, for $t \in I$.

The first three lemmas ((4.3.3), (4.3.5), (4.3.6)) establish the result for $h_1(t)$ by inserting (4.50) into (4.51). Lemma (4.3.7) establishes the result for $h_2(t)$.

Lemma 4.3.3 *Suppose $t \in I$ and $\tau \in J$. Then*

$$H_\varepsilon(t, \tau) - H_0(t, \tau) = O\left(\varepsilon^{2/3}\right), \quad \text{as } \varepsilon \rightarrow 0.$$

Proof. Without loss of generality we assume $t > 0$.

$$\begin{aligned} H_\varepsilon(t, \tau) &= \frac{ik}{2} \frac{H_1^{(1)}(k|\mathbf{x}_\varepsilon(t) - \mathbf{x}_\varepsilon(\tau)|)}{|\mathbf{x}_\varepsilon(t) - \mathbf{x}_\varepsilon(\tau)|} (x'_{\varepsilon,2}(\tau), -x'_{\varepsilon,1}(\tau)) \cdot (\mathbf{x}_\varepsilon(t) - \mathbf{x}_\varepsilon(\tau)) \\ &= \frac{ik}{2} H_1^{(1)}(k|\mathbf{x}_\varepsilon(t) - \mathbf{x}_\varepsilon(\tau)|) |\mathbf{x}_\varepsilon(t) - \mathbf{x}_\varepsilon(\tau)| \frac{(x'_{\varepsilon,2}(\tau), -x'_{\varepsilon,1}(\tau)) \cdot (\mathbf{x}_\varepsilon(t) - \mathbf{x}_\varepsilon(\tau))}{|\mathbf{x}_\varepsilon(t) - \mathbf{x}_\varepsilon(\tau)|^2}. \end{aligned} \quad (4.53)$$

The function $kz H_1^{(1)}(kz)$ is analytic and is bounded on the sets of points

$$\{|\mathbf{x}_\varepsilon(t) - \mathbf{x}_\varepsilon(\tau)| : t, \tau \in [-\pi, \pi]\}, \quad (4.54)$$

and

$$\{|\mathbf{x}_0(t) - \mathbf{x}_0(\tau)| : t, \tau \in [-\pi, \pi]\}; \quad (4.55)$$

also as $\varepsilon \rightarrow 0$,

$$\begin{aligned} &kH_1^{(1)}(k|\mathbf{x}_\varepsilon(t) - \mathbf{x}_\varepsilon(\tau)|) |\mathbf{x}_\varepsilon(t) - \mathbf{x}_\varepsilon(\tau)| \\ &\rightarrow kH_1^{(1)}(k|\mathbf{x}_0(t) - \mathbf{x}_0(\tau)|) |\mathbf{x}_0(t) - \mathbf{x}_0(\tau)|. \end{aligned} \quad (4.56)$$

If $\tau \in J$ and $\varepsilon^{2/3} < \tau < 2\varepsilon^{2/3}$, we use the Taylor series approximation

$$\frac{1}{2} (x'_{\varepsilon,2}(\tau), -x'_{\varepsilon,1}(\tau)) \cdot \frac{\mathbf{x}_\varepsilon''\left(\frac{t+\tau}{2}\right)}{|\mathbf{x}_\varepsilon'\left(\frac{t+\tau}{2}\right)|^2}, \quad (4.57)$$

together with the estimates

$$\begin{aligned} \mathbf{x}'_\varepsilon(\tau) &\sim \left(\frac{\tau}{\sqrt{4\varepsilon^2 + \tau^2}}, -1 \right) \\ &\sim \mathbf{x}'_0(\tau) + O\left(\frac{\varepsilon^2}{\tau^2}\right) \\ &\sim \mathbf{x}'_0(\tau) + O\left(\varepsilon^{2/3}\right) \end{aligned}$$

$$\begin{aligned}\mathbf{x}_\varepsilon''(\tau) &\sim \left(\frac{4\varepsilon^2}{(4\varepsilon^2 + \tau^2)^{3/2}}, 0 \right) \\ &\sim \mathbf{x}_0''(\tau) + O(\varepsilon^{2/3}).\end{aligned}\tag{4.58}$$

Noting that $|\mathbf{x}'_\varepsilon(\tau)|$ is bounded below by a constant independent of ε and τ , we deduce that the quantity (4.57) differs from

$$\frac{1}{2} (x'_{0,2}(\tau), -x'_{0,1}(\tau)) \cdot \frac{\mathbf{x}_0''\left(\frac{t+\tau}{2}\right)}{|\mathbf{x}'_0\left(\frac{t+\tau}{2}\right)|^2},\tag{4.59}$$

by an amount of $O(\varepsilon^{2/3})$, as $\varepsilon \rightarrow 0$.

On the other hand, if $\tau \in J$ and $\tau > 2\varepsilon^{2/3}$, the quantity $\mathbf{x}_\varepsilon(\tau)$ is much bigger than $\mathbf{x}_\varepsilon(t)$ when $t \in I$. It follows that by expanding each of the terms involving $\mathbf{x}_\varepsilon(t)$ or $\mathbf{x}'_\varepsilon(t)$ in

$$\frac{(x'_{\varepsilon,2}(\tau), -x'_{\varepsilon,1}(\tau)) \cdot (\mathbf{x}_\varepsilon(t) - \mathbf{x}_\varepsilon(\tau))}{|\mathbf{x}_\varepsilon(t) - \mathbf{x}_\varepsilon(\tau)|^2},\tag{4.60}$$

that this quantity differs from

$$\frac{(x'_{0,2}(\tau), -x'_{0,1}(\tau)) \cdot (\mathbf{x}_0(t) - \mathbf{x}_0(\tau))}{|\mathbf{x}_0(t) - \mathbf{x}_0(\tau)|^2},\tag{4.61}$$

by an amount of $O(\varepsilon^{2/3})$ as $\varepsilon \rightarrow 0$.

Turning to the case where $\tau \in J$ and $\tau < 0$, a similar argument again shows this difference is $O(\varepsilon^{2/3})$ as $\varepsilon \rightarrow 0$. The result of the lemma now follows.

Corollary 4.3.4 *The result of the previous lemma holds when the relevant Green's function is replaced by the static Green's function, that is, if*

$$H_\varepsilon^0(t, \tau) = \frac{(x'_{\varepsilon,2}(\tau), -x'_{\varepsilon,1}(\tau)) \cdot (\mathbf{x}_\varepsilon(t) - \mathbf{x}_\varepsilon(\tau))}{|\mathbf{x}_\varepsilon(t) - \mathbf{x}_\varepsilon(\tau)|^2},$$

and $H_0^0(t, \tau)$ is similarly defined, then

$$H_\varepsilon^0(t, \tau) - H_0^0(t, \tau) = O(\varepsilon^{2/3}),$$

as $\varepsilon \rightarrow 0$ for $t \in I$, $\tau \in J$.

■

Lemma 4.3.5 *Let A be a constant, Then for $t \in I$,*

$$\int_I (H_\varepsilon(t, \tau) - H_0(t, \tau)) A \, d\tau = O\left(\varepsilon^{2/3}\right), \quad \text{as } \varepsilon \rightarrow 0.$$

Proof. The integral may be approximated by

$$\begin{aligned} & \int_I (H_\varepsilon^0(t, \tau) - H_0^0(t, \tau)) A \, d\tau \\ &= \int_{-\pi}^{\pi} (H_\varepsilon^0(t, \tau) - H_0^0(t, \tau)) A \, d\tau - \int_J (H_\varepsilon^0(t, \tau) - H_0^0(t, \tau)) A \, d\tau. \end{aligned} \quad (4.62)$$

The result of the previous lemma and corollary show that the contribution of the integral over J is $O\left(\varepsilon^{2/3}\right)$ as $\varepsilon \rightarrow 0$.

On the other hand, a fundamental property of the static Green's function is [109],

$$2 \int_{\partial D} \frac{\partial G_0(\mathbf{x}, \mathbf{y})}{\partial \mathbf{n}(\mathbf{y})} \, ds(\mathbf{y}) = -1, \quad \mathbf{x} \in \partial D, \quad (4.63)$$

where D is any domain. Thus

$$\int_{-\pi}^{\pi} H_\varepsilon^0(t, \tau) \, d\tau = -\frac{1}{2}, \quad (4.64)$$

and

$$\int_{-\pi}^{\pi} H_0^0(t, \tau) \, d\tau = -\frac{1}{2}, \quad (4.65)$$

so that

$$\int_{-\pi}^{\pi} (H_\varepsilon^0(t, \tau) - H_0^0(t, \tau)) A \, d\tau = 0. \quad (4.66)$$

The result is now proven. ■

Lemma 4.3.6 *Let $t \in I$. Then*

$$\int_I (H_\varepsilon(t, \tau) - H_0(t, \tau))(k\tau)^{2/3} \, d\tau = O\left((k\varepsilon)^{2/3}\right), \quad \text{as } k\varepsilon \rightarrow 0.$$

We may suppose $t > 0$.

Proof. We consider the contribution to the integral when $\tau \in I$ and $\tau > 0$. First, the

contribution from $H_0(t, \tau)$ may be neglected because using the Taylor approximation,

$$\begin{aligned} H_0(t, \tau) &= \frac{\frac{1}{2} (x'_{0,2}(\tau), -x'_{0,1}(\tau)) \cdot \mathbf{x}_0''(\frac{t+\tau}{2})}{|\mathbf{x}'_0(\frac{t+\tau}{2})|^2} \\ &= O\left((k\varepsilon)^{2/3}\right), \quad \text{as } k\varepsilon \rightarrow 0. \end{aligned} \quad (4.67)$$

The contribution from $H_\varepsilon(t, \tau)$ may be evaluated as follows.

$$\begin{aligned} \int_{I, \tau > 0} H_\varepsilon(t, \tau) (k\tau)^{2/3} d\tau &= \int_0^{\varepsilon^{2/3}} \frac{ik H_1^{(1)}(k|\mathbf{x}_\varepsilon(t) - \mathbf{x}_\varepsilon(\tau)|)}{2 \frac{|\mathbf{x}_\varepsilon(t) - \mathbf{x}_\varepsilon(\tau)|}{|\mathbf{x}'_\varepsilon(\tau)|}} \mathbf{n}(\mathbf{x}_\varepsilon(\tau)) \cdot (\mathbf{x}_\varepsilon(t) - \mathbf{x}_\varepsilon(\tau)) \\ &\quad |\mathbf{x}'_\varepsilon(\tau)| (k\tau)^{2/3} d\tau. \end{aligned} \quad (4.68)$$

Using the small argument approximation for $H_1^{(1)}$ [120], and following the steps (4.20) - (4.24) from Lemma 4.3.1, the integral (4.68) is less than

$$\frac{1}{\sqrt{2\pi}} \int_0^{\varepsilon^{2/3}} \frac{x''_{\varepsilon,1}(\frac{t+\tau}{2})}{1 + \left(x'_{\varepsilon,1}(\frac{t+\tau}{2})\right)^2} (k\tau)^{2/3} d\tau. \quad (4.69)$$

We note that for small t ,

$$\begin{aligned} \mathbf{x}_\varepsilon(t) &\sim \left(\sqrt{4\varepsilon^2 + t^2}, -t\right), \\ \mathbf{x}'_\varepsilon(t) &\sim \left(\frac{t}{\sqrt{4\varepsilon^2 + t^2}}, -1\right), \\ \mathbf{x}''_\varepsilon(t) &\sim \left(\frac{4\varepsilon^2}{(4\varepsilon^2 + t^2)^{3/2}}, 0\right). \end{aligned} \quad (4.70)$$

Inserting these into (4.69):

$$\frac{1}{\sqrt{2\pi}} \int_0^{\varepsilon^{2/3}} \frac{4\varepsilon^2 (k\tau)^{2/3}}{\sqrt{4\varepsilon^2 + (\frac{t+\tau}{2})^2} (4\varepsilon^2 + 2(\frac{t+\tau}{2})^2)} d\tau. \quad (4.71)$$

Applying the substitutions $t = t_1\varepsilon$ and $\tau = \tau_1\varepsilon$, (4.71) is equal to

$$\frac{(k\varepsilon)^{2/3}}{\sqrt{2\pi}} \int_0^{\varepsilon^{-1/3}} \frac{\tau_1^{2/3}}{\sqrt{4 + (\frac{t_1+\tau_1}{2})^2} (4 + 2(\frac{t_1+\tau_1}{2})^2)} d\tau_1$$

$$\begin{aligned}
 &\leq \frac{(k\varepsilon)^{2/3}}{\sqrt{2}\pi} \int_0^{\varepsilon^{-1/3}} \frac{4\tau_1^{2/3}}{\sqrt{16 + \tau_1^2} (16 + 2\tau_1^2)} d\tau_1, \quad \text{since } t > 0, \\
 &\leq \frac{\sqrt{2}(k\varepsilon)^{2/3}}{\pi} \int_0^{\varepsilon^{-1/3}} \frac{\tau_1^{2/3}}{(16 + \tau_1^2)^{3/2}} d\tau_1 \\
 &\leq \frac{\sqrt{2}(k\varepsilon)^{2/3}}{\pi} \int_0^\infty \frac{\tau_1^{2/3}}{(16 + \tau_1^2)^{3/2}} d\tau_1 \\
 &= C(k\varepsilon)^{2/3},
 \end{aligned} \tag{4.72}$$

for some constant C .

We turn to the contribution when $\tau < 0$.

Since $t > 0$ and $\tau < 0$, $|\mathbf{x}_\varepsilon(t) - \mathbf{x}_\varepsilon(\tau)|$ and $|\mathbf{x}_0(t) - \mathbf{x}_0(\tau)|$ never vanish, and for τ large enough we may approximate $H_\varepsilon(t, \tau)$ by $H_0(t, \tau)$; equivalently the dominant contribution to the integral comes from an interval of τ -values near the origin. We split the interval of integration $[-\varepsilon^{2/3}, 0] = [-\varepsilon^{2/3}, -10\varepsilon] \cup [-10\varepsilon, 0]$ and neglect the contribution from the first interval and evaluate

$$\begin{aligned}
 &\int_{-10\varepsilon}^0 (H_\varepsilon(t, \tau) - H_0(t, \tau)) (k\tau)^{2/3} d\tau \\
 &= \int_{-10\varepsilon}^0 H_\varepsilon(t, \tau) (k\tau)^{2/3} d\tau - \int_{-10\varepsilon}^0 H_0(t, \tau) (k\tau)^{2/3} d\tau.
 \end{aligned} \tag{4.73}$$

The first term is approximated by its Taylor expansion

$$\frac{1}{\pi} \int_{-10\varepsilon}^0 \frac{x''_{\varepsilon,1} \left(\frac{t+\tau}{2} \right)}{1 + x'_{\varepsilon,1} \left(\frac{t+\tau}{2} \right)^2} (k\tau)^{2/3} d\tau. \tag{4.74}$$

Now

$$\left| x''_{\varepsilon,1} \left(\frac{t+\tau}{2} \right) \right| \leq \frac{1}{\varepsilon}, \tag{4.75}$$

so the absolute value of the integral is bounded by

$$\frac{10\varepsilon}{\pi} \frac{1}{\varepsilon} (10k\varepsilon)^{2/3} = O\left((k\varepsilon)^{2/3}\right), \quad \text{as } k\varepsilon \rightarrow 0. \tag{4.76}$$

The second term is approximated by

$$\frac{1}{\pi} \int_{-10\varepsilon}^0 \frac{t}{t^2 + \tau^2} (k\tau)^{2/3} d\tau \leq \frac{(k\varepsilon)^{2/3}}{\pi} \left[\arctan \left(\frac{\tau}{t} \right) \right]_{-10\varepsilon}^0 \leq \frac{1}{2} (k\varepsilon)^{2/3}. \tag{4.77}$$

This concludes the proof of the lemma. ■

The previous lemmas ((4.3.3), (4.3.5), (4.3.6)) establish that

$$h_1(t) = O\left((k\varepsilon)^{2/3}\right), \quad \text{as } k\varepsilon \rightarrow 0. \quad (4.78)$$

Turning to $h_2(t)$, we have

Lemma 4.3.7

$$h_2(t) = O\left((k\varepsilon)^{2/3}\right), \quad \text{as } k\varepsilon \rightarrow 0, \text{ for } t \in I.$$

Proof.

$$|h_2(t)| \leq \|\varphi_0\|_\infty \int_I |H_\varepsilon(t, \tau) - H_0(t, \tau)| d\tau, \quad (4.79)$$

where we recall that $\varphi_0(t)$ is the surface distribution on the sharp-cornered lemniscate.

Also we have established

$$H_\varepsilon(t, \tau) - H_0(t, \tau) = O\left((k\varepsilon)^{2/3}\right), \quad \text{as } k\varepsilon \rightarrow 0. \quad (4.80)$$

The result immediately follows. ■

Finally, noting that

$$g_\varepsilon(t) - g_0(t) = O(k\varepsilon), \quad \text{as } k\varepsilon \rightarrow 0, \text{ (Lemma C.1.6),} \quad (4.81)$$

and that

$$h(t) = h_1(t) + h_2(t) + g_\varepsilon(t) - g_0(t), \quad (4.82)$$

we conclude:

Lemma 4.3.8

$$h(t) = O\left((k\varepsilon)^{2/3}\right), \quad \text{as } k\varepsilon \rightarrow 0, \text{ for } t \in I.$$

We can now summarize the main result of this section which directly follows from the insertion of Lemma 4.3.8 into (4.33).

Theorem 4.3.9 *The difference $\Delta(t) = \varphi_0(t) - \varphi_\varepsilon(t)$ between the surface distribution on the lemniscate (4.5) and its rounded counterpart (4.6) satisfies*

$$\Delta(t) = O\left((k\varepsilon)^{2/3}\right), \quad \text{for } t \in I, \text{ as } k\varepsilon \rightarrow 0.$$

4.4 The Far-field Difference

The far-field patterns u_0^∞ and u_ε^∞ of the lemniscate and its rounded version, respectively, may be expressed in terms of the corresponding surface quantities φ_0 and φ_ε induced by the illuminating field [7].

Recall that $\hat{\mathbf{x}} = \hat{\mathbf{x}}(\hat{\theta}) = (\cos \hat{\theta}, \sin \hat{\theta})$, is the unit vector with $\hat{\theta}$ being the angle of observation of the far-field,

$$\begin{aligned} u_0^\infty(\hat{\mathbf{x}}) &= \frac{e^{-i\pi/4}}{\sqrt{8\pi k}} \int_{-\pi}^{\pi} k \boldsymbol{\nu}(\mathbf{x}_0(t)) \cdot \hat{\mathbf{x}} e^{-ik\hat{\mathbf{x}} \cdot \mathbf{x}_0(t)} \varphi_0(t) |\mathbf{x}'_0(t)| dt \\ &= \frac{\sqrt{k} e^{-i\pi/4}}{\sqrt{8\pi}} \int_{-\pi}^{\pi} m(\hat{\mathbf{x}}; \mathbf{x}_0) \varphi_0(t) dt \end{aligned} \quad (4.83)$$

where $m(\hat{\mathbf{x}}; \mathbf{x}) = \boldsymbol{\nu}(\mathbf{x}(t)) \cdot \hat{\mathbf{x}} e^{-ik\hat{\mathbf{x}} \cdot \mathbf{x}(t)} |\mathbf{x}'(t)|$. The far-field for the rounded object $u_\varepsilon^\infty(\hat{\mathbf{x}})$ is similarly defined. Thus

$$\begin{aligned} \sqrt{k} |u_\varepsilon^\infty(\hat{\mathbf{x}}) - u_0^\infty(\hat{\mathbf{x}})| &\leq \frac{k}{\sqrt{8\pi}} \int_{-\pi}^{\pi} \left| \{m(\hat{\mathbf{x}}; \mathbf{x}_\varepsilon(t)) \varphi_\varepsilon(t) - m(\hat{\mathbf{x}}; \mathbf{x}_0(t)) \varphi_0(t)\} \right| dt \\ &= \frac{k}{\sqrt{8\pi}} \int_{-\pi}^{\pi} \left| \{m(\hat{\mathbf{x}}; \mathbf{x}_\varepsilon) \varphi_\varepsilon(t) - m(\hat{\mathbf{x}}; \mathbf{x}_\varepsilon) \varphi_0(t) \right. \\ &\quad \left. + m(\hat{\mathbf{x}}; \mathbf{x}_\varepsilon) \varphi_0(t) - m(\hat{\mathbf{x}}; \mathbf{x}_0) \varphi_0(t)\} \right| dt \\ &= \frac{k}{\sqrt{8\pi}} \int_{-\pi}^{\pi} \left| \{m(\hat{\mathbf{x}}; \mathbf{x}_\varepsilon) (\varphi_\varepsilon(t) - \varphi_0(t)) \right. \\ &\quad \left. + (m(\hat{\mathbf{x}}; \mathbf{x}_\varepsilon) - m(\hat{\mathbf{x}}; \mathbf{x}_0)) \varphi_0(t)\} \right| dt \\ &\leq \frac{k}{\sqrt{8\pi}} \int_{-\pi}^{\pi} |m(\hat{\mathbf{x}}; \mathbf{x}_\varepsilon) (\varphi_\varepsilon(t) - \varphi_0(t))| dt \\ &\quad + \frac{k}{\sqrt{8\pi}} \int_{-\pi}^{\pi} |(m(\hat{\mathbf{x}}; \mathbf{x}_\varepsilon) - m(\hat{\mathbf{x}}; \mathbf{x}_0)) \varphi_0(t)| dt \end{aligned} \quad (4.84)$$

Using the Hölder inequality,

$$\sqrt{k} \|u_\varepsilon^\infty(\hat{\mathbf{x}}) - u_0^\infty(\hat{\mathbf{x}})\|_\infty \leq \frac{k}{\sqrt{8\pi}} \|m(\hat{\mathbf{x}}; \mathbf{x}_\varepsilon)\|_\infty \|\varphi_\varepsilon - \varphi_0\|_1$$

$$\begin{aligned}
& + \frac{k}{\sqrt{8\pi}} \|m(\hat{\mathbf{x}}; \mathbf{x}_\varepsilon) - m(\hat{\mathbf{x}}; \mathbf{x}_0)\|_1 \|\varphi_0\|_\infty \\
& = \frac{k}{\sqrt{8\pi}} \|m(\hat{\mathbf{x}}; \mathbf{x}_\varepsilon)\|_\infty \int_{-\pi}^{\pi} |\varphi_\varepsilon - \varphi_0| dt \\
& \quad + \frac{k}{\sqrt{8\pi}} \|m(\hat{\mathbf{x}}; \mathbf{x}_\varepsilon) - m(\hat{\mathbf{x}}; \mathbf{x}_0)\|_1 \|\varphi_0\|_\infty \\
& \leq \frac{k}{2\sqrt{\pi}} \int_{-\pi}^{\pi} |\Delta(t)| dt + O(k\varepsilon), \tag{4.85}
\end{aligned}$$

since $\|m(\hat{\mathbf{x}}; \mathbf{x}_\varepsilon)\|_\infty \leq \sqrt{2}$ (Lemma C.1.7) and $\frac{k}{\sqrt{8\pi}} \|m(\hat{\mathbf{x}}; \mathbf{x}_\varepsilon) - m(\hat{\mathbf{x}}; \mathbf{x}_0)\|_1$ is $O(k\varepsilon)$ (Lemma C.1.8). We note that φ_0 is the actual solution to the cornered lemniscate problem (4.2), thus $\|\varphi_0\|_\infty$ is a fixed bounded quantity associated with this particular scatterer.

An improved estimate for the second term in (4.84) is obtained by estimating

$$\begin{aligned}
& \frac{k}{2\sqrt{\pi}} \int_{-\pi}^{\pi} (m(\hat{\mathbf{x}}; \mathbf{x}_\varepsilon) - m(\hat{\mathbf{x}}; \mathbf{x}_0)) \varphi_0(t) dt \\
& = \frac{k}{2\sqrt{\pi}} \int_{-\pi}^{\pi} \left(\mathbf{v}(\mathbf{x}_\varepsilon(t)) \cdot \hat{\mathbf{x}} e^{-ik\hat{\mathbf{x}} \cdot \mathbf{x}_\varepsilon(t)} - \mathbf{v}(\mathbf{x}_0(t)) \cdot \hat{\mathbf{x}} e^{-ik\hat{\mathbf{x}} \cdot \mathbf{x}_0(t)} \right) \varphi_0(t) dt \\
& = \frac{k}{2\sqrt{\pi}} \int_{-\pi}^{\pi} (\mathbf{v}(\mathbf{x}_\varepsilon(t)) - \mathbf{v}(\mathbf{x}_0(t))) \cdot \hat{\mathbf{x}} e^{-ik\hat{\mathbf{x}} \cdot \mathbf{x}_0(t)} \varphi_0(t) dt \\
& \quad + \frac{k}{2\sqrt{\pi}} \int_{-\pi}^{\pi} \mathbf{v}(\mathbf{x}_0(t)) \cdot \hat{\mathbf{x}} \left(e^{-ik\hat{\mathbf{x}} \cdot \mathbf{x}_\varepsilon(t)} - e^{-ik\hat{\mathbf{x}} \cdot \mathbf{x}_0(t)} \right) \varphi_0(t) dt, \tag{4.86}
\end{aligned}$$

where $\mathbf{v}(\mathbf{x}(t)) = (x'_2(t), -x'_1(t))$. For convenience let $\tilde{\mathbf{v}}(\mathbf{x}(t))$ denote $(x_2(t), -x_1(t))$.

The second term in this equation is $O((k\varepsilon)^{2-\delta})$ for any $\delta > 0$, using Lemma C.1.10.

The first term on the right of (4.86) is, after an integration by parts,

$$\begin{aligned}
& \frac{k}{2\sqrt{\pi}} \left[(\tilde{\mathbf{v}}(\mathbf{x}_\varepsilon(t)) - \tilde{\mathbf{v}}(\mathbf{x}_0(t))) \cdot \hat{\mathbf{x}} \left(e^{-ik\hat{\mathbf{x}} \cdot \mathbf{x}_\varepsilon(t)} - e^{-ik\hat{\mathbf{x}} \cdot \mathbf{x}_0(t)} \right) \varphi_0(t) \right]_{-\pi}^{\pi} \\
& - \frac{k}{2\sqrt{\pi}} \int_{-\pi}^{\pi} \tilde{\mathbf{v}}(\mathbf{x}_0(t)) \cdot \hat{\mathbf{x}} \frac{d}{dt} \left(\left(e^{-ik\hat{\mathbf{x}} \cdot \mathbf{x}_\varepsilon(t)} - e^{-ik\hat{\mathbf{x}} \cdot \mathbf{x}_0(t)} \right) \varphi_0(t) \right) dt. \tag{4.87}
\end{aligned}$$

The first term is zero, and we estimate the second term by splitting it as a sum over three subintervals $[-\pi, -\varepsilon] \cup [-\varepsilon, \varepsilon] \cup [\varepsilon, \pi]$. On the first and third subintervals the derivative term is bounded by the maximum value M of $2|\varphi'_0(t)| + 2k|\varphi_0(t)|$; this is $O(\varepsilon^{-\frac{1}{3}})$ as $\varepsilon \rightarrow 0$. Thus using (C.7), the contribution to the integral over the first and

third intervals is bounded by (see (C.44))

$$2M \int_{\varepsilon}^{\pi} \frac{\varepsilon^2}{\sin(t/2)} dt; \quad (4.88)$$

this quantity is $O\left(\varepsilon^{\frac{5}{3}} \log \varepsilon\right)$ as $\varepsilon \rightarrow 0$.

On the other hand, regarding that $\tilde{\mathbf{v}}(\mathbf{x}_0(t)) \cdot \hat{\mathbf{x}} = 1 + O(t^2)$, as $t \rightarrow 0$, the contribution over the first interval is bounded by

$$K \left[\left(e^{-ik\hat{\mathbf{x}} \cdot \mathbf{x}_{\varepsilon}(t)} - e^{-ik\hat{\mathbf{x}} \cdot \mathbf{x}_0(t)} \right) \varphi_0(t) \right]_0^{\varepsilon}, \quad (4.89)$$

for some constant K ; this is $O\left(\varepsilon^{\frac{5}{3}}\right)$ as $\varepsilon \rightarrow 0$, since

$$\varphi(t) = \varphi(0) + O\left((kt)^{2/3}\right), \quad \text{as } t \rightarrow 0. \quad (4.90)$$

We now deduce that an improved estimate for the second term in (4.84) is $O\left(\varepsilon^{\frac{4}{3}}\right)$ as $\varepsilon \rightarrow 0$.

Recalling that $I = [-\varepsilon^{2/3}, \varepsilon^{2/3}]$, and that $\Delta(t)$ is assumed to vanish for t outside I , we deduce that

$$\sqrt{k} \|u_{\varepsilon}^{\infty} - u_0^{\infty}\|_{\infty} = \sqrt{k} \max_{\hat{\mathbf{x}} \in [-\pi, \pi]} |u_{\varepsilon}^{\infty}(\hat{\mathbf{x}}) - u_0^{\infty}(\hat{\mathbf{x}})| = O\left((k\varepsilon)^{4/3}\right). \quad (4.91)$$

With the stated choice of I , it should be noted that the requirements (a) and (c) listed in Section 4.3, on geometry and size relative to wavelength, are fulfilled, as $\varepsilon \rightarrow 0$.

4.5 Conclusion

Our numerical studies in Chapter 3 have demonstrated that the maximum difference in the non-dimensionalised far-field patterns of a lemniscate with Dirichlet boundary condition and its rounded counterpart is, to a good approximation, equal to $C(\theta_0)(k\rho)^{4/3}$, for some constant $C(\theta_0)$ dependent on the direction of the incident plane wave θ_0 ; here ρ denotes the radius of curvature in the vicinity of the rounded corner point. An example of the far-field data differences computed for the lemniscate studied in this work, illuminated in the direction $\theta_0 = \pi/4$, is shown in Fig. 4.2; for direction $\varphi_0 = 0$ see

Figure 3.10(a). In each example, the data was collated over a range of wave numbers k and radii of curvature ρ . These results were determined by using a least squares fit to logarithms of the data for $k\rho \leq 0.25$.

In this chapter, a theoretical basis for these numerical results was derived. An approximate integral equation for the difference in the surface quantities on the lemniscate and its rounded counterpart was obtained, and it was shown that the difference is $O((k\varepsilon)^{2/3})$ as $k\varepsilon \rightarrow 0$. As a consequence, the maximum in the non-dimensionalised far-field patterns is $O((k\varepsilon)^{4/3})$ as $k\varepsilon \rightarrow 0$, in accord with the computed results in Chapter 3, since $\rho \sim 2\varepsilon$ (Lemma C.1.1).

These results are readily capable of extension to structures with sharp corners of interior angles other than 90° . A similar approach to the Neumann case will be discussed in future publications.

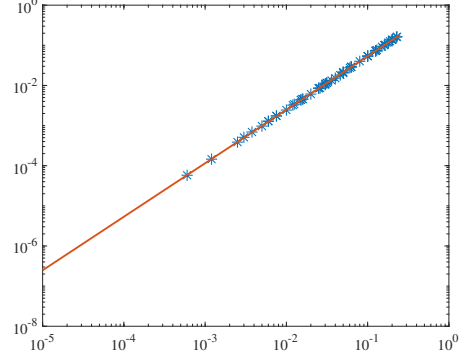


Figure 4.2: Logarithmic plot: $x = k\rho$, $y = \sqrt{k} \|u_0^\infty - u_\rho^\infty\|_\infty$. The data points used are represented by the blue asterisks, the least squares line of fit is shown in red.

Chapter 5

The Total Field, the Normal Derivative and Surface Quantities Near the Vicinity of the Corner

In this chapter the behaviour of three quantities at close proximity to the corner of a scatterer are examined: the total field u^{tot} external to the scatterer, the derivative with respect to the normal $\frac{\partial u^{\text{tot}}}{\partial n}$ measured on the surface of the scatterer and the surface quantity φ that is the solution of the integral equation for determining these quantities.

In the experiments described in Chapter 3 the near-field was measured on a circle of radius equal to a number larger than the width of the scatterer, typically on a circle of radius ten for a scatterer of radius one (Figure 5.1a). Of interest is the behaviour of the total field $u^{\text{tot}}(\mathbf{x})$ at points \mathbf{x} at close proximity to the corner. The interest in this quantity is to verify that the numerical schemes described in Chapter 2 produce a valid solution at points very near the scatterer surface, especially in the vicinity of a corner. This quantity is examined for scatterers with a Dirichlet boundary condition.

Next, the work of Bowman et al. [1] on the wedge of arbitrary angle is used to verify the behaviour of the derivative with respect to the normal $\frac{\partial u^{\text{tot}}}{\partial n}$ measured on the surface near the corner of a scatterer with Dirichlet boundary condition.

We conclude this chapter with a numerical examination of the behaviour of the surface quantity φ near the vicinity of the corner for scatterers with Dirichlet and Neumann boundary condition and establish numerically that it can be approximated based on

the wave number k and the distance along the surface from the corner, $d(\tau)$. We then examine the Neumann result analytically.

The work in this chapter is restricted to scatterers with a single interior acute-angled corner, that is, $0 < \beta \leq \pi/2$ (see equation (2.9)).

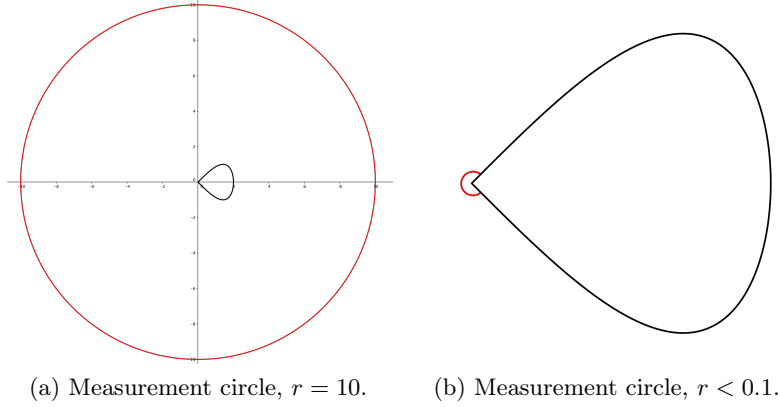


Figure 5.1: Lemniscate: showing near-field measurement.

5.1 The Total Field

In this section we examine the behaviour of the total, $u^{\text{tot}}(\mathbf{x})$, and scattered, $u^{\text{sc}}(\mathbf{x})$, fields in the vicinity of the corner for a scatterer with a Dirichlet boundary condition, where $\mathbf{x} = r(\cos \phi, \sin \phi)$. Measurements are taken on a small circle of radius r , centred at the corner of the lemniscate, for different angles ϕ measured anticlockwise from the surface of the scatterer where $\phi = 0$ (Figure 5.1b). We choose $r = 0.002$. The numerical solution should rapidly converge as the number of mesh points increases if the results are valid. Convergence is measured using the significant measurement technique described in Section 3.1, so that as the number of quadrature points on the surface of the scatterer is increased, the number of significant digits in agreement should also increase. This is indeed the case as Tables 5.1 and 5.2 illustrate. Both tables show the value of the scattered and total fields measured at a distance $r = 0.002$ from the corner of a lemniscate (2.2): Table 5.1 examines $\phi = 3\pi/4$ whilst Table 5.2 examines $\phi = \pi$; rapid convergence to a solution at two different points near the surface in the vicinity of the corner is demonstrated.

For a scatterer with Dirichlet boundary condition it is also expected that $u^{\text{tot}}(\mathbf{x}) \rightarrow 0$

as the distance between an off-body point \mathbf{x} and the scatterer surface approaches zero. Figure 5.2 graphs the behaviour of the total field as $\phi \rightarrow 0$, and demonstrates as the point of measurement approaches the surface that u^{tot} indeed approaches zero.

These results demonstrate that the implemented numerical schemes produce highly accurate solutions for the total and scattered fields measured near the surface of the scatterer, even in the vicinity of the corner.

N	$\text{Re } u^{\text{sc}}(\mathbf{x})$	$\text{Im } u^{\text{sc}}(\mathbf{x})$	$\text{Re } u^{\text{tot}}(\mathbf{x})$	$\text{Im } u^{\text{tot}}(\mathbf{x})$
32	-0.9496904128312	-0.0745301609887	0.0502306554212	-0.0870942871040
64	-0.9496935088382	-0.0745239028649	0.0502275594142	-0.0870880289802
128	-0.9496935134535	-0.0745238951523	0.0502275547989	-0.0870880212676
256	-0.9496935134558	-0.0745238951484	0.0502275547966	-0.0870880212637
512	-0.9496935134558	-0.0745238951484	0.0502275547966	-0.0870880212637

Table 5.1: Scattered and total fields of a lemniscate with Dirichlet boundary condition measured at $\mathbf{x} = r(\cos \phi, \sin \phi)$, where $r = 0.002$ and $\phi = 3\pi/4$. Direction of incident plane wave $\theta_0 = 0$, wave number $ka = 2\pi$.

N	$\text{Re } u^{\text{sc}}(\mathbf{x})$	$\text{Im } u^{\text{sc}}(\mathbf{x})$	$\text{Re } u^{\text{tot}}(\mathbf{x})$	$\text{Im } u^{\text{tot}}(\mathbf{x})$
32	-0.9566778069883	-0.0661858214013	0.0432840926129	-0.0749150450708
64	-0.9567086124778	-0.0661845517917	0.0432532871235	-0.0749137754612
128	-0.9567086187215	-0.0661845450585	0.0432532808798	-0.0749137687280
256	-0.9567086187235	-0.0661845450551	0.0432532808778	-0.0749137687247
512	-0.9567086187235	-0.0661845450551	0.0432532808778	-0.0749137687247

Table 5.2: Scattered and total fields of a lemniscate with Dirichlet boundary condition measured at $\mathbf{x} = r(\cos \phi, \sin \phi)$, where $r = 0.002$ and $\phi = \pi$. Direction of incident plane wave $\theta_0 = 0$, wave number $ka = 2\pi$.

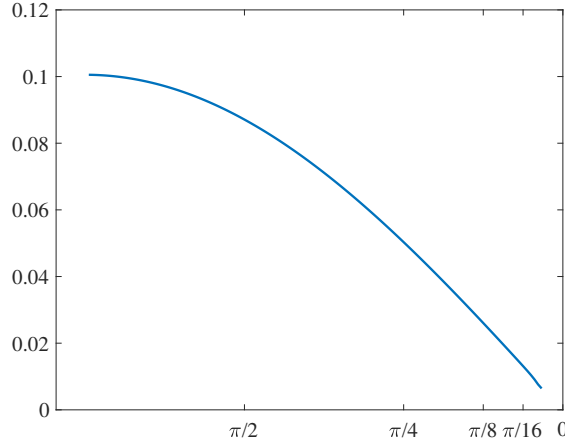


Figure 5.2: Illustrating the behaviour of the total field at points approaching the scatterer surface. $x = \phi$, $y = |u^{\text{tot}}(r, \phi)|$, where $r = 0.002$ and ϕ is measured (in radians) anti-clockwise from the surface of the scatterer.

5.2 The Derivative with Respect to the Normal on the Surface

In this section we examine the behaviour of the derivative with respect to the normal $\frac{\partial u^{\text{tot}}}{\partial n}$ near the corner on the surface of a scatterer, the lemniscate (2.2), with a Dirichlet boundary condition. If \mathbf{u}_ϕ and \mathbf{u}_r denote the standard unit tangent vectors in polar coordinates at (r, ϕ) , then

$$\nabla u^{\text{tot}} = \frac{1}{r} \frac{\partial u^{\text{tot}}}{\partial \phi} \mathbf{u}_\phi + \frac{\partial u^{\text{tot}}}{\partial r} \mathbf{u}_r, \quad (5.1)$$

so the derivative with respect to the (outward) normal to the upper surface ($\phi = \Omega$) is

$$\frac{\partial u^{\text{tot}}}{\partial n} = \mathbf{u}_\phi \cdot \nabla u^{\text{tot}} = \frac{1}{r} \frac{\partial u^{\text{tot}}}{\partial \phi}. \quad (5.2)$$

This is illustrated in Figure 5.3a. On the lower surface the sign is reversed.

We make use of the analysis of the infinite wedge by Bowman et al. [1, p.259] to verify the behaviour of $\frac{\partial u^{\text{tot}}}{\partial n}$ at the corner. In this work, the symbol ρ is used to represent the radius of curvature, and so we rename the radial distance from the vertex represented in [1] by ρ as r . Figure 5.3b describes the geometry of the problem.

Without loss of generality, the corner is oriented so that the x -axis bisects the corner. The interior angle of the wedge is 2Ω . The angle of the incident field ϕ_0 is measured

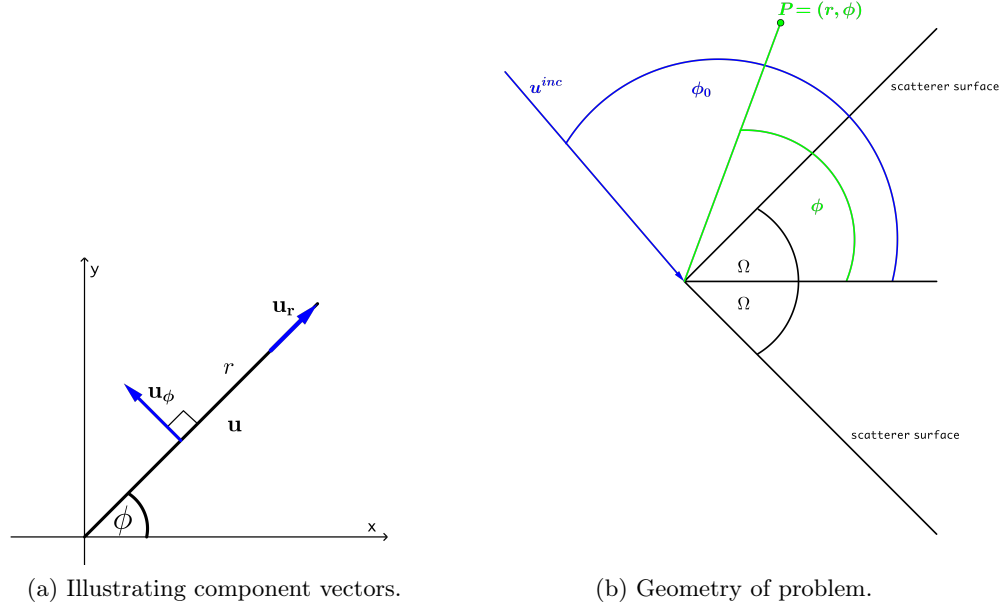


Figure 5.3: Measuring $\frac{\partial u^{\text{tot}}}{\partial n}$ near the corner.

anticlockwise from the positive x -axis, thus for direction of travel θ_0 used in other parts of this work, $\phi_0 = \pi + \theta_0$, making an angle $\phi_0 - \Omega$ with the upper surface of the scatterer. We choose a point $P = (r, \phi)$ where we wish to measure $\frac{\partial u^{\text{tot}}}{\partial n}$. For P on the upper surface, $\phi = \pi/4$. Near the vicinity of the corner, as $r \rightarrow 0$ and when $kr \ll 1$, the Bessel function expansion of the total field u^{tot} has asymptotic behaviour

$$u^{\text{tot}}(r, \phi) = \frac{4}{\Gamma(1/\nu)} \left(\frac{1}{2}kr\right)^{\frac{1}{\nu}} e^{-\frac{i\pi}{2\nu}} \sin\left(\frac{\phi - \Omega}{\nu}\right) \sin\left(\frac{\phi_0 - \Omega}{\nu}\right) + O\left[(kr)^{\min(2/\nu, 2+1/\nu)}\right], \quad (5.3)$$

where $\nu = \frac{2\pi - 2\Omega}{\pi}$ [1]. For a right-angled wedge, $\nu = \frac{3}{2}$, and

$$u^{\text{tot}}(r, \phi) = \frac{4}{\Gamma(\frac{2}{3})} \left(\frac{1}{2}kr\right)^{\frac{2}{3}} e^{-i\frac{\pi}{3}} \sin\left(\frac{2(\phi - \Omega)}{3}\right) \sin\left(\frac{2(\phi_0 - \Omega)}{3}\right), \quad (5.4)$$

ignoring the higher order terms, and thus on the surface of the scatterer ($\phi = \Omega = \pi/4$),

$$\begin{aligned} \frac{\partial u^{\text{tot}}}{\partial n}(r, \phi) &= \frac{1}{r} \frac{\partial u^{\text{tot}}}{\partial \phi} \\ &= r^{-\frac{1}{3}} \frac{2}{3} \frac{4}{\Gamma(\frac{2}{3})} \left(\frac{1}{2}k\right)^{\frac{2}{3}} e^{-i\frac{\pi}{3}} \sin\left|\frac{2}{3}\left(\phi_0 - \frac{\pi}{4}\right)\right|. \end{aligned} \quad (5.5)$$

If we set the direction of the incident field u^{inc} to 0, thus $\phi_0 = \pi$, and

$$\begin{aligned} \frac{\partial u^{\text{tot}}}{\partial n} \left(r, \frac{\pi}{4} \right) &= r^{-\frac{1}{3}} \frac{2}{3} \frac{4}{\Gamma(\frac{2}{3})} \left(\frac{1}{2} k \right)^{\frac{2}{3}} e^{-i\frac{\pi}{3}} \\ &= C(k) r^{-\frac{1}{3}}, \end{aligned} \quad (5.6)$$

where

$$\begin{aligned} C(k) &= \frac{2}{3} \frac{4}{\Gamma(\frac{2}{3})} \left(\frac{1}{2} k \right)^{\frac{2}{3}} e^{-i\frac{\pi}{3}} \\ &\approx 1.2406 e^{-i\frac{\pi}{3}} k^{\frac{2}{3}}. \end{aligned} \quad (5.7)$$

Thus as $r \rightarrow 0$ (that is, at the corner), we expect that on the surface of the scatterer

$$\left| \frac{\partial u^{\text{tot}}}{\partial n} \left(r, \frac{\pi}{4} \right) \right| = \frac{1}{r} \left| \frac{\partial u^{\text{tot}}}{\partial \phi} \right| = |C(k)| r^{-\frac{1}{3}} \sim 1.2406 |k|^{\frac{2}{3}} r^{-\frac{1}{3}}. \quad (5.8)$$

A finite difference method is used to calculate $\frac{\partial u^{\text{tot}}}{\partial \phi}$. We are able to calculate the total field u^{tot} at any point outside the scatterer, and since we are examining a scatterer with the Dirichlet boundary condition we know that $u^{\text{tot}} = 0$ on the surface of the scatterer. The details follow.

The total field u^{tot} is measured at a point P_1 on a circle, of radius r centred at the corner of the scatterer and at the point P_0 on the surface of the scatterer which intersects with the circle. Figure 5.4b illustrates this.

The derivative is approximated as follows

$$\begin{aligned} \frac{\partial u^{\text{tot}}}{\partial \phi} \left(r, \frac{\pi}{4} \right) &= u^{\text{tot}'} \left(r, \frac{\pi}{4} \right) \doteq \frac{u^{\text{tot}} \left(r, \frac{\pi}{4} + h_1 \right) - u^{\text{tot}} \left(r, \frac{\pi}{4} \right)}{h_1} \\ &= \frac{u^{\text{tot}} \left(r, \frac{\pi}{4} + h_1 \right)}{h_1}, \end{aligned} \quad (5.9)$$

since $u^{\text{tot}} \left(r, \frac{\pi}{4} \right) = 0$.

An improved estimate for this quantity may be obtained by recognising that the numerator has second order Taylor series expansion

$$u^{\text{tot}} \left(r, \frac{\pi}{4} + h_1 \right) = u^{\text{tot}} \left(r, \frac{\pi}{4} \right) + h_1 u^{\text{tot}'} \left(r, \frac{\pi}{4} \right) + \frac{h_1^2}{2} u^{\text{tot}''} \left(r, \frac{\pi}{4} \right), \quad (5.10)$$

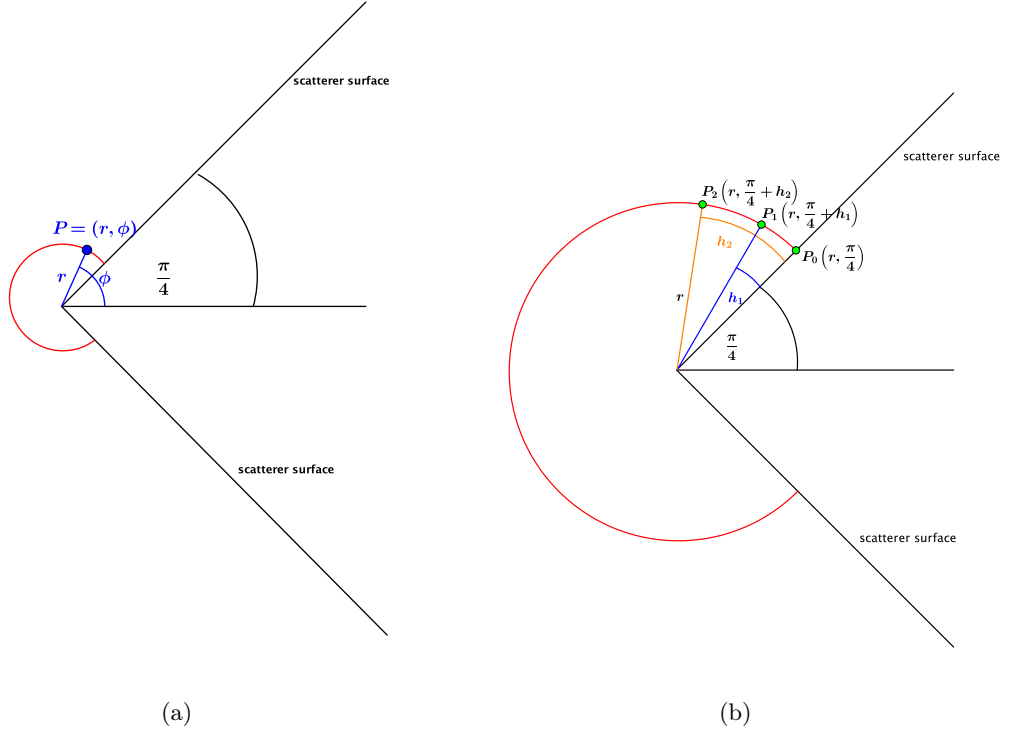


Figure 5.4: Measuring $\frac{\partial u^{\text{tot}}}{\partial \phi}$ near the corner.

so that (5.9) can be represented as

$$\begin{aligned}
 \frac{\partial u^{\text{tot}}}{\partial \phi} \left(r, \frac{\pi}{4} \right) &\doteq \frac{u^{\text{tot}} \left(r, \frac{\pi}{4} \right) + h_1 u^{\text{tot}'} \left(r, \frac{\pi}{4} \right) + \frac{h_1^2}{2} u^{\text{tot}''} \left(r, \frac{\pi}{4} \right) - u^{\text{tot}} \left(r, \frac{\pi}{4} \right)}{h_1} \\
 &= u^{\text{tot}'} \left(r, \frac{\pi}{4} \right) + \frac{h_1}{2} u^{\text{tot}''} \left(r, \frac{\pi}{4} \right) \\
 &= D(h_1).
 \end{aligned} \tag{5.11}$$

We choose another point on the circle, P_2 (refer to Figure 5.4b), such that

$$\begin{aligned}
 \frac{\partial u^{\text{tot}}}{\partial \phi} \left(r, \frac{\pi}{4} \right) &\doteq \frac{u^{\text{tot}} \left(r, \frac{\pi}{4} + h_2 \right)}{h_2} \\
 &= u^{\text{tot}'} \left(r, \frac{\pi}{4} \right) + \frac{h_2}{2} u^{\text{tot}''} \left(r, \frac{\pi}{4} \right) \\
 &= D(h_2).
 \end{aligned} \tag{5.12}$$

The following linear combination of (5.11) and (5.12),

$$h_2 D(h_1) - h_1 D(h_2) = (h_2 - h_1) u^{\text{tot}'} \left(r, \frac{\pi}{4} \right) + \text{h.o.t.}, \tag{5.13}$$

gives an improved estimate for $\frac{\partial u^{\text{tot}}}{\partial \phi} \left(r, \frac{\pi}{4} \right)$ on the surface of the scatterer:

$$\frac{\partial u^{\text{tot}}}{\partial \phi} \left(r, \frac{\pi}{4} \right) = u^{\text{tot}'} \left(r, \frac{\pi}{4} \right) \doteq \frac{h_2 D(h_1) - h_1 D(h_2)}{(h_2 - h_1)}. \quad (5.14)$$

Equation (5.8) shows that, as $r \rightarrow 0$, the quantity

$$\left| \frac{\partial u^{\text{tot}}}{\partial n} (r, \phi) \right| r^{\frac{1}{3}} \rightarrow C(k) = 1.2406 |k|^{\frac{2}{3}}. \quad (5.15)$$

Table 5.3 shows that we do indeed achieve this result numerically for a variety of values of k as $r \rightarrow 0$. Figure 5.5 illustrates the typical behaviour of the derivative of the total field $\left| \frac{\partial u^{\text{tot}}}{\partial n} \right|$ along the surface of the scatterer nearing the corner.

	$ C(1) $	$ C(\pi) $	$ C(2\pi) $	$ C(4\pi) $	$ C(8\pi) $	$ C(16\pi) $
Actual	1.2406	2.6611	4.2242	6.7055	10.6443	16.8968
r						
0.10000	1.2580	2.8116	4.7013	7.9630	13.3433	25.7867
0.05000	1.2474	2.7329	4.4412	7.2928	12.2505	22.8817
0.02500	1.2432	2.6995	4.3249	6.9506	11.3929	20.0536
0.01250	1.2416	2.6855	4.2746	6.7898	10.9175	18.3734
0.00625	1.2409	2.6798	4.2521	6.7185	10.6867	17.5138
0.00500	1.2408	2.6787	4.2456	6.7057	10.6436	17.3477
0.00200	1.2406	2.6765	4.2262	6.6786	10.5497	16.9775

Table 5.3: Demonstrating as $r \rightarrow 0$, $\left| \frac{\partial u^{\text{tot}}}{\partial n} (r, \phi) \right| r^{\frac{1}{3}} \rightarrow |C(k)|$ on the surface of the lemniscate scatterer at the corner.

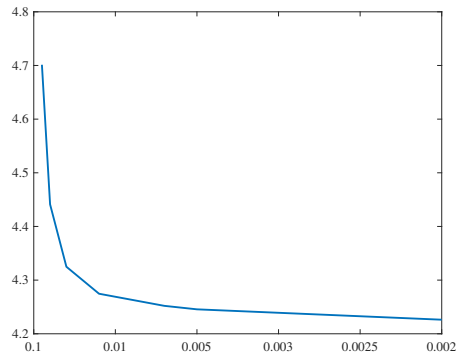


Figure 5.5: $x = r$, distance from the corner of the scatterer; $y = \left| \frac{\partial u^{\text{tot}}}{\partial n} (r, \phi) \right| r^{\frac{1}{3}}$. Scatterer is the lemniscate. Direction of incident plane wave $\theta_0 = 0$ for wave number $k = 2\pi$.

5.3 Behaviour of the Surface Quantity, φ , in the Vicinity of the Corner

In this section, we examine the behaviour of the unknown surface quantity ϕ , found as the solution of the appropriate integral equation, near the corner of the scatterer for both the Dirichlet and the Neumann boundary conditions. Recall that,

$$\nu = \frac{2\pi - \beta}{\pi}, \quad (5.16)$$

where β is the interior angle of the corner. Table 5.4 lists a number of quantities relating to ν for different interior angles β which will be used in this section.

β	ν	$1/\nu$	$(2 - \nu)/\nu$	$(1 - \nu)/\nu$
$\pi/2$	1.500	0.667	0.333	-0.333
$\pi/3$	1.667	0.600	0.200	-0.400
$\pi/4$	1.750	0.571	0.143	-0.429
$\pi/6$	1.833	0.545	0.091	-0.455
$\pi/12$	1.923	0.520	0.043	-0.478
$\pi/18$	1.972	0.507	0.029	-0.486

Table 5.4: Illustrating the relationship between interior angle β and various quantities related to ν .

5.3.1 Dirichlet Boundary Condition

We consider lemniscates with different interior angles, β , and Dirichlet boundary condition (2.19) and examine the quantity

$$|\varphi(\tau) - \varphi(0)|, \quad (5.17)$$

in the vicinity of the corner, where $\varphi(0)$ is the surface density at the corner, and $\varphi(\tau) = \varphi(\mathbf{y}(\tau))$ is a solution to the boundary value problem (2.39) using the boundary parameterisation (2.1),

$$u^{\text{sc}}(\mathbf{x}(t)) = \int_0^{2\pi} \left\{ \frac{\partial G(\mathbf{x}(t), \mathbf{y}(\tau))}{\partial \mathbf{n}(\mathbf{y}(\tau))} - i\eta G(\mathbf{x}(t), \mathbf{y}(\tau)) \right\} \varphi(\mathbf{y}(\tau)) |\mathbf{y}'(\tau)| d\tau, \quad 0 \leq t, \tau \leq 2\pi. \quad (5.18)$$

For this examination, the coupling parameter η is set to 0, thus using only the double-layer potential to solve the scattering problem. We note that this boundary value problem has a unique solution as long as the wave number, k , of the incident field u^{inc} (2.14) is not an eigenvalue of the interior Dirichlet problem [7, p.51]. Applying the boundary condition (2.19) and the jump relation for the double-layer potential (2.29) we obtain the integral equation

$$\frac{\varphi(\mathbf{x}(t))}{2} - \int_0^{2\pi} \frac{\partial G(\mathbf{x}(t), \mathbf{y}(\tau))}{\partial \mathbf{n}(\mathbf{y}(\tau))} \varphi(\mathbf{y}(\tau)) |\mathbf{y}'(\tau)| d\tau = -u^{\text{inc}}(\mathbf{x}(t)), \quad \mathbf{x}(t) \in \partial D, \quad (5.19)$$

for which the unknown continuous density φ is a solution.

We seek an approximation of the quantity of interest (5.17) as $\tau \rightarrow 0$, of the form

$$|\varphi(\tau) - \varphi(0)| \approx C(k\tau)^m. \quad (5.20)$$

Data was collected from acute and right-angled lemniscates (2.9) with $\pi/18 \leq \beta \leq \pi/2$ for various wave numbers ka and different incident angles, θ_0 . A least squares fit to the logarithms of the data for small τ was used. The results for a variety of interior angles β with plane wave incidence $\theta_0 = 0$ are presented in Table 5.5. To illustrate the effect of varying the incident field angle θ_0 , Table 5.6 presents some results for a lemniscate with interior angle $\beta = \pi/4$ and incident field angles $\theta_0 = \pi/32, \pi/16, \pi/8$ and $\pi/4$. Varying the incident field angle for the other lemniscates has a similar effect. Full results are available in Appendix D.2, Table D.1.

Comparing the power m to values in Table 5.4, the numerical results demonstrate that for scatterers with Dirichlet boundary and interior angle β ,

$$|\varphi(\tau) - \varphi(0)| \approx C(\theta_0, \beta)(k\tau)^{1/\nu}, \quad (5.21)$$

and that the constant C is dependent on the angle θ_0 of incidence and on the interior angle β ; it can be readily approximated, where

$$C(\theta_0, \beta) \leq 2\pi/\beta \quad (5.22)$$

with $C(\theta_0, \beta) \approx 2\pi/\beta$ when the incident wave direction $\theta_0 = 0$. The results also show

that the power m is independent of the incident field angle θ_0 , but that the constant C is at a maximum when $\theta_0 = 0$ and diminishes as the incident field angle increases.

k	C	m	C	m	C	m
	Lemniscate, $\beta = \pi/2$		Lemniscate, $\beta = \pi/4$		Lemniscate, $\beta = \pi/12$	
1	4.0	0.67	7.9	0.57	23.4	0.52
$\pi/2$	4.0	0.67	7.9	0.57	23.3	0.52
π	4.0	0.67	7.9	0.57	23.4	0.52
2π	4.0	0.67	7.9	0.57	23.5	0.52
4π	4.0	0.67	7.9	0.57	23.5	0.52
8π	4.0	0.67	8.0	0.57	23.6	0.52
16π	4.0	0.67	7.9	0.57	23.7	0.52
	Lemniscate, $\beta = \pi/3$		Lemniscate, $\beta = \pi/6$		Lemniscate, $\beta = \pi/18$	
1	5.9	0.60	11.9	0.55	35.4	0.51
$\pi/2$	5.9	0.60	11.9	0.55	35.2	0.51
π	5.9	0.60	11.9	0.55	35.4	0.51
2π	5.9	0.60	11.9	0.55	35.6	0.51
4π	5.9	0.60	11.9	0.55	35.8	0.51
8π	6.0	0.60	11.8	0.54	36.4	0.51
16π	6.0	0.60	12.0	0.55	37.9	0.52

Table 5.5: $|\varphi(\tau) - \varphi(0)| \approx C(k\tau)^m$ as $\tau \rightarrow 0$.

Single-cornered scatterers with interior angle, β and Dirichlet boundary condition. Angle of incidence, $\theta_0 = 0$.

k	$\theta_0 = 0$		$\theta_0 = \pi/32$		$\theta_0 = \pi/16$		$\theta_0 = \pi/8$		$\theta_0 = \pi/4$	
	C	m	C	m	C	m	C	m	C	m
1	7.9	0.57	7.9	0.57	7.8	0.57	7.7	0.57	7.1	0.57
$\pi/2$	7.9	0.57	7.9	0.57	7.9	0.57	7.7	0.57	7.1	0.57
π	7.9	0.57	7.9	0.57	7.9	0.57	7.7	0.57	7.1	0.57
2π	7.9	0.57	7.9	0.57	7.9	0.57	7.7	0.57	7.1	0.57
4π	7.9	0.57	7.9	0.57	7.9	0.57	7.7	0.57	7.1	0.57
8π	8.0	0.57	7.9	0.57	7.9	0.57	7.7	0.57	7.1	0.57
16π	7.9	0.57	7.9	0.57	7.9	0.57	7.7	0.57	7.1	0.57

Table 5.6: $|\varphi(\tau) - \varphi(0)| \approx C(k\tau)^m$ as $\tau \rightarrow 0$.

Scatterer with interior angle, $\beta = \pi/4$ and Dirichlet boundary condition. Different angles of incidence, θ_0 .

5.3.2 Neumann Boundary Condition

We consider lemniscates with different interior angles, β , and Neumann boundary condition (2.20) and examine the quantity

$$|\varphi(\tau)|, \tag{5.23}$$

in the vicinity of the corner, that is as $\tau \rightarrow 0$, where $\varphi(\tau) = \varphi(\mathbf{y}(\tau))$ is a solution to the boundary value problem (2.42) using the boundary parameterisation (2.1),

$$u^{\text{sc}}(\mathbf{x}(t)) = \int_0^{2\pi} G(\mathbf{x}(t), \mathbf{y}(\tau)) \varphi(\mathbf{y}(\tau)) |\mathbf{y}'(\tau)| ds(\mathbf{y}(\tau)), \quad 0 \leq t, \tau \leq 2\pi. \quad (5.24)$$

This boundary value problem has a unique solution as long as the wave number, k , of the incident field u^{inc} (2.14) is not an eigenvalue of the interior Neumann problem [7, p.51]. Applying the boundary condition (2.20) and the jump relation for the single-layer potential (2.27) we obtain the integral equation

$$-\frac{\varphi(\mathbf{x}(t))}{2} + \int_0^{2\pi} \frac{\partial G(\mathbf{x}(t), \mathbf{y}(\tau))}{\partial \mathbf{n}(\mathbf{x}(t))} \varphi(\mathbf{y}(\tau)) |\mathbf{y}'(\tau)| ds(\mathbf{y}(\tau)) = -\frac{\partial u^{\text{inc}}(\mathbf{x}(t))}{\partial n(\mathbf{x}(t))}, \quad 0 \leq t, \tau \leq 2\pi, \quad (5.25)$$

for which the unknown continuous density φ is a solution.

We seek an approximation of the quantity of interest (5.17) as $\tau \rightarrow 0$, of the form

$$|\varphi(\tau)| \approx C(k\tau)^m. \quad (5.26)$$

As per the Dirichlet case, data was collected from acute and right-angled lemniscates (2.9) with $\pi/18 \leq \beta \leq \pi/2$ for various wave numbers ka and different incident angles, θ_0 . A least squares fit to the logarithms of the data for small τ was used. The results for a variety of interior angles β with plane wave incidence $\theta_0 = 0$ are presented in Table 5.7. Full results for different incident wave angles are available in Appendix D.2, Table D.2.

The numerical results demonstrate that for scatterers with Neumann boundary and interior angle β ,

$$|\varphi(\tau)| \approx C(\beta, \theta_0)(k\tau)^{\frac{2-\nu}{\nu}} = C(\beta)(k\tau)^{\frac{2}{\nu}-1}, \quad (5.27)$$

when $\theta_0 = 0$ for some constant C dependent on the interior angle β .

This result differs when the incident field angle θ_0 is not equal to 0, or nearly so. To illustrate, Table 5.8, presents some results for a lemniscate with interior angle $\beta = \pi/4$ and incident field angles $\theta_0 = 0, \pi/32, \pi/16, \pi/8$ and $\pi/4$. This demonstrates the effect

of varying the incidence angle. For $\theta_0 \neq 0$,

$$|\varphi(\tau)| \approx C(\beta, \theta_0)(k\tau)^{\frac{1-\nu}{\nu}} = C(\beta, \theta_0)(k\tau)^{\frac{1}{\nu}-1}, \quad (5.28)$$

for some constant C dependent on the interior angle β and incidence angle θ_0 . Varying the incident field angle for the other lemniscates demonstrates the same phenomena. Full results illustrating this are available in Appendix D.2, Table D.2.

The results show that the power m is dependent of the incident field angle θ_0 , that is $m = (2 - \nu)/\nu$ when $\theta_0 = 0$ and $m = (\nu - 1)/\nu$, when $\theta_0 \neq 0$. The constant C is at a maximum when $\theta_0 = 0$ and in the majority of cases, the constant also increases as the wave number k increases. The one exception is for interior angles $\beta = \pi/12$ and $\pi/18$ when the wave number $ka = \pi/2$. In these two instances, the constant C is smaller than when $ka = 1$, then increases as the wave number increases in a similar fashion to all the other cases.

k	C	m	C	m	C	m
Lemniscate, $\beta = \pi/2$			Lemniscate, $\beta = \pi/4$		Lemniscate, $\beta = \pi/12$	
1	1.9	0.33	0.5	0.143	0.1	0.043
$\pi/2$	3.7	0.33	0.9	0.143	0.2	0.043
π	7.1	0.33	1.8	0.143	0.5	0.043
2π	14.1	0.33	3.4	0.143	0.9	0.043
4π	27.0	0.33	6.8	0.143	1.8	0.044
8π	58.9	0.33	13.6	0.143	3.6	0.044
16π	103.8	0.32	27.2	0.143	7.2	0.044
Lemniscate, $\beta = \pi/3$			Lemniscate, $\beta = \pi/6$		Lemniscate, $\beta = \pi/18$	
1	0.7	0.20	0.3	0.091	0.1	0.029
$\pi/2$	1.4	0.20	0.5	0.091	0.1	0.029
π	2.7	0.20	1.0	0.091	0.3	0.029
2π	5.3	0.20	2.0	0.091	0.6	0.029
4π	10.7	0.20	3.9	0.091	1.2	0.029
8π	21.4	0.20	8.0	0.091	2.3	0.029
16π	42.8	0.20	15.9	0.091	4.6	0.029

Table 5.7: $|\varphi(\tau)| \approx C(k\tau)^m$ as $\tau \rightarrow 0$.
Lemniscates with interior angle, β and Neumann boundary condition. Angle of incidence, $\theta_0 = 0$.

k	$\theta_0 = 0$		$\theta_0 = \pi/32$		$\theta_0 = \pi/16$		$\theta_0 = \pi/8$		$\theta_0 = \pi/4$	
	C	m	C	m	C	m	C	m	C	m
1	0.5	0.143	0.3	-0.428	0.5	-0.428	1.1	-0.428	2.2	-0.428
$\pi/2$	0.9	0.143	0.4	-0.426	0.7	-0.427	1.3	-0.428	2.5	-0.428
π	1.8	0.143	0.9	-0.425	1.6	-0.427	3.1	-0.428	5.3	-0.428
2π	3.4	0.143	1.7	-0.425	3.3	-0.427	6.4	-0.428	11.0	-0.428
4π	6.8	0.143	3.2	-0.421	6.0	-0.425	11.7	-0.427	22.8	-0.428
8π	13.6	0.143	6.8	-0.418	12.4	-0.423	24.3	-0.426	46.3	-0.428
16π	27.2	0.143	14.2	-0.413	25.7	-0.421	48.9	-0.425	92.7	-0.427

Table 5.8: $|\varphi(\tau)| \approx C(k\tau)^m$ as $\tau \rightarrow 0$.

Lemniscate with interior angle, $\beta = \pi/4$ and Neumann boundary condition. Different angles of incidence, θ_0 .

5.4 Analysis of the Neumann Result

In this section we derive an asymptotic expression for the surface quantity φ near the corner for the Neumann boundary condition and examine the validity of the numerical results presented in Section 5.3.2, by comparison with an infinite wedge. This analysis is for a scatterer with an interior right-angled-corner, $\beta = \pi/2$.

We again make use of the analysis by Bowman et al. [1, p.261] to estimate the surface quantity φ . When $kr \ll 1$, the Bessel function expansion of the total field u^{tot} for a scatterer with a Neumann boundary condition is

$$\begin{aligned}
u^{\text{tot}}(r, \phi) &= H_z \\
&\sim \frac{2}{\nu} + \frac{4}{\Gamma(1/\nu)} \left(\frac{1}{2}kr\right)^{\frac{1}{\nu}} e^{-\frac{i\pi}{2\nu}} \cos\left(\frac{\phi - \Omega}{\nu}\right) \cos\left(\frac{\phi_0 - \Omega}{\nu}\right) \\
&\quad + O\left[(kr)^{\min(2/\nu, 2)}\right], \tag{5.29}
\end{aligned}$$

where $\nu = \frac{2\pi - 2\Omega}{\pi}$ [1]. Thus

$$u^{\text{sc}}(r, \phi) = H_z - u^{\text{inc}}(r, \phi). \tag{5.30}$$

Figure 5.3b describes the geometry of the problem. We will be measuring the total field on the scatterer surface, hence on the upper ($\phi = \Omega$) and lower ($\phi = 2\pi - \Omega$) surfaces, $\cos \frac{\phi - \Omega}{\nu}$ takes the value 1 and -1 , respectively. We seek the surface density on the wedge

of the form

$$u^{\text{sc}}(\mathbf{x}(t)) = \int_{-\pi}^{\pi} G(\mathbf{x}(t), \mathbf{x}(\tau)) \varphi(\mathbf{x}(\tau)) |\mathbf{x}'(\tau)| d\tau, \quad (5.31)$$

where, using the small argument approximation of $H_0^{(1)}$ [120],

$$\begin{aligned} G(\mathbf{x}(t), \mathbf{x}(\tau)) &= \frac{i}{4} H_0^{(1)}(k|\mathbf{x}(t) - \mathbf{x}(\tau)|) \\ &\sim \frac{1}{2\pi} \log(k|\mathbf{x}(t) - \mathbf{x}(\tau)|), \quad \text{as } |\mathbf{x}(t) - \mathbf{x}(\tau)| \rightarrow 0, \end{aligned} \quad (5.32)$$

and

$$\mathbf{x}(t) = (|t|, t), \quad t \in [-\pi, \pi]. \quad (5.33)$$

If t and τ parameterise points on the same edge of the wedge,

$$|\mathbf{x}(t) - \mathbf{x}(\tau)| = \sqrt{2}|t - \tau|, \quad (5.34)$$

whereas if they are on different edges,

$$|\mathbf{x}(t) - \mathbf{x}(\tau)| = \sqrt{2}\sqrt{t^2 + \tau^2}. \quad (5.35)$$

Consider the infinite wedge as illustrated in Figure 5.6. For

$t > 0$, that is, t is on the upper edge,

$$\begin{aligned} u^{\text{sc}}(\mathbf{x}(t)) &= \frac{i}{4} \int_0^\infty H_0^{(1)}(k\sqrt{2}|t - \tau|) \varphi(\tau) \sqrt{2} d\tau \\ &\quad + \frac{i}{4} \int_{-\infty}^0 H_0^{(1)}(k\sqrt{2}\sqrt{t^2 + \tau^2}) \varphi(\tau) \sqrt{2} d\tau. \end{aligned} \quad (5.36)$$

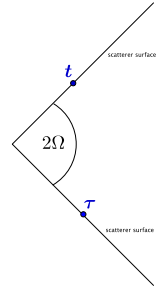


Figure 5.6: Infinite wedge.

For $t < 0$, that is, t is on the lower edge,

$$u^{\text{sc}}(\mathbf{x}(t)) = \frac{\sqrt{2}i}{4} \int_0^\infty H_0^{(1)}(k\sqrt{2}\sqrt{t^2 + \tau^2}) \varphi(\tau) d\tau + \frac{\sqrt{2}i}{4} \int_{-\infty}^0 H_0^{(1)}(k\sqrt{2}|t - \tau|) \varphi(\tau) d\tau. \quad (5.37)$$

Subtracting (5.37) from (5.36),

$$\begin{aligned}
 u^{\text{sc}}(\mathbf{x}(t)) - u^{\text{sc}}(\mathbf{x}(-t)) = & \\
 & \frac{\sqrt{2}i}{4} \int_0^\infty \left(H_0^{(1)}(k\sqrt{2}|t-\tau|) - H_0^{(1)}(k\sqrt{2}\sqrt{t^2+\tau^2}) \right) \varphi(\tau) d\tau \\
 & + \frac{\sqrt{2}i}{4} \int_{-\infty}^0 \left(H_0^{(1)}(k\sqrt{2}\sqrt{t^2+\tau^2}) - H_0^{(1)}(k\sqrt{2}|-t-\tau|) \right) \varphi(\tau) d\tau.
 \end{aligned} \tag{5.38}$$

We examine (5.38) in the vicinity of the tip where $t \rightarrow 0$. Using first order Taylor expansions, the integrand in the first term on the right is, when $\tau > t$,

$$\begin{aligned}
 & \left(H_0^{(1)}(k\sqrt{2}\tau) - H_0^{(1)'}(k\sqrt{2}\tau)(k\sqrt{2}\tau) \right) \\
 & \quad - \left(H_0^{(1)}(k\sqrt{2}\tau) + H_0^{(1)'}(k\sqrt{2}\tau)(k\sqrt{2}(\sqrt{t^2+\tau^2}-\tau)) \right) \\
 & \simeq -H_0^{(1)'}(k\sqrt{2}\tau)t + O\left(\frac{1}{\tau}\right), \quad \text{as } \tau \rightarrow \infty,
 \end{aligned} \tag{5.39}$$

so the error committed by neglecting the contribution on the interval (T, ∞) , where $T \gg t$, is about

$$-k\sqrt{2}t \int_T^\infty H_0^{(1)'}(k\sqrt{2}\tau) \varphi(\tau) d\tau, \tag{5.40}$$

that is $O(kt)$ as $kt \rightarrow 0$.

Thus we use (5.32) to approximate the terms containing $H_0^{(1)}$ in (5.38). This gives

$$u^{\text{sc}}(\mathbf{x}(t)) - u^{\text{sc}}(\mathbf{x}(-t)) = \frac{1}{2\pi} \int_0^\infty \log \frac{|t-\tau|}{\sqrt{t^2+\tau^2}} \varphi(\tau) d\tau + \frac{1}{2\pi} \int_{-\infty}^0 \log \frac{\sqrt{t^2+\tau^2}}{|t-\tau|} \varphi(\tau) d\tau. \tag{5.41}$$

Note that the error committed by the contribution on the interval (T, ∞) is about

$$-t \int_T^\infty \frac{\varphi(\tau)}{\tau} d\tau, \tag{5.42}$$

where $T \gg t$. Thus we are justified in replacing the terms containing $H_0^{(1)}$ in (5.38) by its small argument approximation.

Consider the operator I defined by

$$I(\phi)(t) = \frac{1}{2\pi} \int_0^\infty \log \frac{|t-\tau|}{\sqrt{t^2+\tau^2}} \phi(\tau) d\tau, \tag{5.43}$$

then the operator has the property that the function $\varphi(\tau) = \tau^\alpha$ satisfies

$$I(\varphi)(t) = \hat{C}t\varphi(t) = \hat{C}t^{\alpha+1}, \quad (5.44)$$

for some constant \hat{C} dependent upon α ; in fact

$$\hat{C} = \frac{1}{2\pi} \int_0^\infty \log \frac{|1-u|}{\sqrt{u^2+1}} u^\alpha du. \quad (5.45)$$

The integral is convergent when $-1 < \alpha < 0$. Note: for the Dirichlet case the corresponding result is $I(\varphi)(t) = \hat{C}\varphi(t) = \hat{C}t^\alpha$.

Substituting $\tau = tu$ for $t > 0$ in (5.41),

$$u^{\text{sc}}(\mathbf{x}(t)) - u^{\text{sc}}(\mathbf{x}(-t)) = \frac{1}{2\pi} t \int_0^\infty \log \frac{|1-u|}{\sqrt{1+u^2}} \varphi(tu) du + \frac{1}{2\pi} t \int_{-\infty}^0 \log \frac{\sqrt{1+u^2}}{|1-u|} \varphi(tu) du. \quad (5.46)$$

From (5.17)

$$\begin{aligned} u^{\text{sc}}(\mathbf{x}(t)) - u^{\text{sc}}(\mathbf{x}(-t)) &= H_z(t) - H_z(-t) - u^{\text{inc}}(\mathbf{x}(t)) + u^{\text{inc}}(\mathbf{x}(-t)) \\ &\sim \frac{8}{\Gamma(1/\nu)} \left(\frac{1}{2}kt\right)^{\frac{1}{\nu}} e^{-\frac{i\pi}{2\nu}} + O(kt)^{2/\nu} - u^{\text{inc}}(\mathbf{x}(t)) + u^{\text{inc}}(\mathbf{x}(-t)) \\ &= C(\nu, \phi_0)(kt)^{1/\nu} + O(kt)^{2/\nu} - u^{\text{inc}}(\mathbf{x}(t)) + u^{\text{inc}}(\mathbf{x}(-t)), \end{aligned} \quad (5.47)$$

where

$$C(\nu, \phi_0) = \frac{8}{2^\nu \Gamma(1/\nu)} e^{-\frac{i\pi}{2\nu}}. \quad (5.48)$$

We note that when the direction of the incident field is symmetric to the scatterer, that is $\theta_0 = 0$, then $u^{\text{inc}}(\mathbf{x}(-t)) - u^{\text{inc}}(\mathbf{x}(t)) = 0$, otherwise $u^{\text{inc}}(\mathbf{x}(-t)) - u^{\text{inc}}(\mathbf{x}(t)) \sim O(kt)$ since $u^{\text{inc}}(\mathbf{x}) = 1 + O(kt)$. Also, $C(\nu, \phi_0) = 0$ when $\theta_0 = 0$, since $\phi_0 = \pi$.

Equating (5.46) and (5.47):

$$\begin{aligned} &\frac{1}{2\pi} t \int_0^\infty \log \frac{|1-u|}{\sqrt{1+u^2}} \varphi(tu) du + \frac{1}{2\pi} t \int_{-\infty}^0 \log \frac{\sqrt{1+u^2}}{|1-u|} \varphi(tu) du \\ &\sim C(\nu, \phi_0)(kt)^{1/\nu} + O(kt)^{2/\nu} + O(kt). \end{aligned} \quad (5.49)$$

Thus,

$$\begin{aligned} & \frac{1}{2\pi} \int_0^\infty \log \frac{|1-u|}{\sqrt{1+u^2}} \varphi(tu) du + \frac{1}{2\pi} \int_{-\infty}^0 \log \frac{\sqrt{1+u^2}}{|1-u|} \varphi(tu) du \\ & \sim C(\nu, \phi_0) (kt)^{1/\nu-1} + O(kt)^{2/\nu-1} + O(kt)^0, \end{aligned} \quad (5.50)$$

as $kt \rightarrow 0$, when the direction of the incident field is not 0; otherwise

$$\frac{1}{2\pi} \int_0^\infty \log \frac{|1-u|}{\sqrt{1+u^2}} \varphi(tu) du + \frac{1}{2\pi} \int_{-\infty}^0 \log \frac{\sqrt{1+u^2}}{|1-u|} \varphi(tu) du \sim O(kt)^{2/\nu-1}. \quad (5.51)$$

This is satisfied by

$$\phi(\tau) = \begin{cases} D(k\tau)^{1/\nu-1} + O\left((k\tau)^{\frac{2}{\nu}-1}\right), & \text{when } \tau > 0, \\ D|k\tau|^{1/\nu-1} + O\left(|k\tau|^{\frac{2}{\nu}-1}\right), & \text{when } \tau < 0, \end{cases} \quad (5.52)$$

for some constant D with $D = 0$ when the direction of the incident field θ_0 is 0. Substituting (5.52) into (5.51) yields

$$\frac{1}{2\pi} D(kt)^{1/\nu-1} \int_0^\infty \log \frac{|1-u|}{\sqrt{1+u^2}} u^{1/\nu-1} du + \frac{1}{2\pi} D(kt)^{1/\nu-1} \int_{-\infty}^0 \log \frac{\sqrt{1+u^2}}{|1-u|} u^{1/\nu-1} du, \quad (5.53)$$

and by substituting $u = -v$, followed by $v = u$ in the second integral, this equals

$$\begin{aligned} & \frac{1}{2\pi} D(kt)^{1/\nu-1} \int_0^\infty \left(\log \frac{|1-u|}{\sqrt{1+u^2}} - \log \frac{\sqrt{1+u^2}}{|1-u|} \right) u^{1/\nu-1} du \\ & = \frac{1}{2\pi} D(kt)^{1/\nu-1} \int_0^\infty \log \frac{|1-u|^2}{1+u^2} u^{1/\nu-1} du \\ & = \frac{1}{2\pi} D(kt)^{1/\nu-1} K_\nu, \end{aligned} \quad (5.54)$$

where

$$K_\nu = \int_0^\infty \log \frac{|1-u|^2}{1+u^2} u^{1/\nu-1} du. \quad (5.55)$$

Thus ignoring the higher order terms, we may choose $D = 2\pi C(\nu, \phi_0)/K_\nu$. We note that K_ν is a convergent integral with an integrable singularity. The proof is in Appendix D, Lemma D.1.1.

In conclusion we have established (5.52), showing that $\phi(\tau) = O\left(|k\tau|^{\frac{1}{\nu}-1}\right)$ as $k\tau \rightarrow 0$.

This is in accord with equation (5.28) summarising the numerical results. When the angle of incidence θ_0 equals 0, $\phi(\tau) = O\left(|k\tau|^{\frac{2}{\nu}-1}\right)$ which again is in accord with the numerical results of Section 5.3.2 (equation (5.27)).

5.5 Conclusions

In this chapter we examined the behaviour of three quantities at close proximity to the corner: the total field u^{tot} external to the scatterer, the derivative with respect to the normal $\frac{\partial u^{\text{tot}}}{\partial n}$ measured on the surface of the scatterer and the surface quantity φ .

Firstly, we verified that the numerical schemes described in Section 2 for the solution of the scattering of a plane wave by structures possessing corners, are suitable for measuring the scattered field in close proximity to the scatterer surface at the corner. This was done by examining the total field $u^{\text{tot}}(\mathbf{x})$ at points \mathbf{x} external to the scatterer for a lemniscate (2.2) with Dirichlet boundary condition. The boundary condition imposes a zero total field on the surface, and one expects that the total field approaches zero as the point of measurement nears the surface. Our numerical experiments demonstrate that the implemented schemes produce a rapidly converging solution at points \mathbf{x} very near the corner of the scatterer and that the solution is accurate, since the total field does indeed approach zero as \mathbf{x} approaches the surface (Figure 5.2).

Secondly, we verified that the employed schemes enable the accurate measurement of the derivative with respect to the normal $\frac{\partial u^{\text{tot}}}{\partial n}$ on the surface of the scatterer in the vicinity of the corner. Again, we used a lemniscate (2.2) with Dirichlet boundary condition for our test case and the work of Bowman et al. [1] on the wedge of arbitrary angle. We expect that on points on the surface, as the distance to corner r approaches zero, that

$$\left| \frac{\partial u^{\text{tot}}}{\partial n}(r, \phi) \right| r^{\frac{1}{3}} \rightarrow 1.2406 |k|^{\frac{2}{3}}, \quad (5.56)$$

when the incident wave direction is zero. We demonstrated that this is indeed the case for a variety of k in Table 5.3.

Thus the numerical schemes employed provide accurate measurement of the near-field u^{tot} at very close proximity to the scatterer corner, and also allow for the accurate measurement of the derivative with respect to the normal $\frac{\partial u^{\text{tot}}}{\partial n}$ on the surface of the

scatterer in the vicinity of the corner.

Thirdly, the behaviour of the surface quantity $\varphi(\tau)$ near the vicinity of the corner ($\tau = 0$) for scatterers with a Dirichlet and Neumann boundary condition was examined and it was shown that it can be approximated based on the wave number k and the distance along the surface from the corner, $d(\tau)$. For scatterers with the Dirichlet boundary condition we numerically established as $\tau \rightarrow 0$, the following result

$$|\varphi(\tau) - \varphi(0)| \approx C(k\tau)^{1/\nu}, \quad (5.57)$$

where $\nu = (2\pi - \beta)/\pi$, and

$$C \leq \frac{2\pi}{\beta}, \quad (5.58)$$

with $C \approx 2\pi/\beta$ when the incident wave direction $\theta_0 = 0$. In the Neumann case, we established the following result,

$$|\varphi(\tau)| \approx C(\beta, \theta_0)(k\tau)^{\frac{2}{\nu}-1}, \quad (5.59)$$

when the incident wave direction $\theta_0 = 0$, and

$$|\phi(\tau)| \approx C(\beta, \theta_0)(k\tau)^{\frac{1-\nu}{\nu}} = C(\beta, \theta_0)(k\tau)^{\frac{1}{\nu}-1}, \quad (5.60)$$

when $\theta_0 \neq 0$, for constants C dependent on the incident wave direction θ_0 and the interior angle of the corner β .

We concluded this chapter by establishing the analytical basis for the Neumann results (5.59) and (5.60). The analytical proof of the corresponding Dirichlet result is planned for future work.

Chapter 6

The Nature of the Differences in the Far-field Measured in the Time Domain

In this chapter we continue the analysis of the effect on the scattered field of rounding the corners of structures which possess sharp corners. Previous chapters measured the impact on near- and far-field scattering, as a function of the radius of curvature, in the frequency domain. For completeness an examination of the effect of corner rounding on the far-field in the time domain is included.

6.1 Problem Formulation

In earlier chapters we obtained considerable data measuring the effect of corner rounding in the frequency domain. We make use of discrete Fourier transforms to shift the frequency domain data to the time domain.

For the Dirichlet boundary condition, the far field pattern is calculated as

$$u^\infty(\hat{\mathbf{x}}, \omega) = \frac{e^{-i\frac{\pi}{4}}}{\sqrt{8\pi k}} \int_{\partial D} \{k\mathbf{n}(y) \cdot \hat{\mathbf{x}} + \eta\} e^{-ik\hat{\mathbf{x}} \cdot \mathbf{y}} \varphi(\mathbf{y}, \omega) \, ds(\mathbf{y}), \quad |\hat{\mathbf{x}}| = 1, \quad \mathbf{y} \in \partial D, \quad (6.1)$$

which captures the frequency domain response in the unit direction $\hat{\mathbf{x}}$ to a harmonic

incident plane wave for a given frequency ω . The harmonic incident plane wave is

$$u^{\text{inc}}(\mathbf{x}) = Ae^{ik\mathbf{d}\cdot\mathbf{x}}, \quad (6.2)$$

where $k = \omega/c$ is the wave number and \mathbf{d} is the direction of travel. In this case $\mathbf{d} = (1, 0)$ meaning travel along the x -axis in the positive direction. Following Colton and Kress [7], the time convention $e^{-i\omega t}$ (and henceforth the Green's function $\frac{i}{4}H_0^{(1)}(k|\mathbf{x} - \mathbf{y}|)$) is used which means that

$$\varphi(\mathbf{y}, \omega) e^{-i\omega t} \quad \text{and} \quad u^\infty(\hat{\mathbf{x}}, \omega) e^{-i\omega t}, \quad (6.3)$$

are the responses to the incident field

$$u^{\text{inc}}(\mathbf{x}) e^{-i\omega t} = Ae^{ik(\mathbf{d}\cdot\mathbf{x} - ct)}. \quad (6.4)$$

Without loss of generality we may take $A = 1$. Thus the responses to a harmonic incident wave of form

$$F(-\omega)u^{\text{inc}}e^{-i\omega t} = F(-\omega)e^{ik(\mathbf{d}\cdot\mathbf{x} - ct)}, \quad (6.5)$$

are

$$F(-\omega)\varphi(\mathbf{y}, \omega) e^{-i\omega t} \quad \text{and} \quad F(-\omega)u^\infty(\hat{\mathbf{x}}, \omega) e^{-i\omega t}. \quad (6.6)$$

Here $F(-\omega)$ is a function specifying the relative weighting of each frequency component in the incident field, where $F(\omega)$ is the Fourier transform of the waveform $f(t)$ specifying the temporal shape of the incident field. The time domain response is obtained by adding over all the frequencies

$$\tilde{u}_\infty(\hat{\mathbf{x}}, t) = \int_{-\infty}^{\infty} F(-\omega) u^\infty(\hat{\mathbf{x}}, \omega) e^{-i\omega t} d\omega. \quad (6.7)$$

Normally, to shift from the time domain to the frequency domain, we use a Fourier transform, calculated as follows

$$F(\omega) = \int_{-\infty}^{\infty} f(t)e^{-i\omega t} dt, \quad (6.8)$$

and to shift from the frequency domain to the time domain we use an inverse Fourier

transform

$$f(t) = \frac{1}{2\pi} \int_{-\infty}^{\infty} F(\omega) e^{i\omega t} d\omega. \quad (6.9)$$

However, it is clear that to obtain (6.7), we compute the Fourier transform of $F(-\omega) u^\infty(\hat{\mathbf{x}}, \omega)$, that is

$$\tilde{u}_\infty(\hat{\mathbf{x}}, t) = \int_{-\infty}^{\infty} \tilde{F}(\omega) e^{-i\omega t} d\omega, \quad (6.10)$$

where $\tilde{F}(\omega) = F(-\omega) u^\infty(\hat{\mathbf{x}}, \omega)$.

6.2 The Discrete Fourier Transform

The method for shifting the far-field data from the frequency domain into the time domain using a discrete inverse Fourier transform, requires a set of uniformly sampled frequency values. In effect we are calculating

$$\frac{1}{2\pi} \int_{-\omega_{\max}}^{\omega_{\max}} F(\omega) e^{i\omega t} d\omega \sim \frac{1}{2\pi} \sum_{n=-N}^N F(n\Delta\omega) e^{in\Delta\omega t} \Delta\omega, \quad (6.11)$$

where $\Delta\omega = 2\omega_{\max}/2N$. Thus a set of uniformly sampled frequency values in the range $-\omega_{\max}$ to ω_{\max} including a value for $\omega = 0$ is needed. The frequency domain response work from earlier chapters, produces values for positive frequencies. The values for the negative frequencies are derived by taking the complex conjugate of the positive frequency response, that is, $F(-\omega) = \overline{F(\omega)}$. Determination of an appropriate zero frequency value, $F(0)$, remains. However, we will be using the discrete Fourier transform

$$\tilde{u}_\infty(\hat{\mathbf{x}}, \omega) = \int_{-\infty}^{\infty} F(\hat{\mathbf{x}}, t) e^{-i\omega t} dt \sim \int_{-t_{\max}}^{t_{\max}} F(\hat{\mathbf{x}}, t) e^{-i\omega t} dt \sim \sum_{n=-N}^N F(n\Delta t) e^{-in\omega\Delta t} \Delta t, \quad (6.12)$$

thus to evaluate (E.11) we perform a change of variable, interchanging t and ω , thus $\Delta t = \Delta\omega = 2\omega_{\max}/2N$, hence we are evaluating

$$\tilde{u}_\infty(\hat{\mathbf{x}}, t) = \int_{-\infty}^{\infty} F(\hat{\mathbf{x}}, \omega) e^{-i\omega t} d\omega \sim \int_{-\omega_{\max}}^{\omega_{\max}} F(\hat{\mathbf{x}}, \omega) e^{-i\omega t} d\omega \sim \sum_{n=-N}^N F(n\Delta\omega) e^{-in\Delta\omega t} \Delta\omega. \quad (6.13)$$

6.3 The Incident Pulses

A classical choice of incident pulse is the Gaussian with time displacement t_0

$$f(x, t) = e^{-(x-c(t-t_0))^2/a_0^2}, \quad (6.14)$$

where a_0 is a quarter of the pulse width and c is the speed of waves in the medium ($a_0, c > 0$) and $k = \omega/c$ is the wave number. Thus to calculate the far-field (6.10), we perform a Fourier transform

$$\tilde{u}_\infty(\hat{\mathbf{x}}, t) = \int_{-\infty}^{\infty} F(\hat{\mathbf{x}}, \omega) e^{-i\omega t} d\omega, \quad (6.15)$$

where

$$F(\hat{\mathbf{x}}, \omega) = \sqrt{\pi} \frac{a_0}{c} e^{-a^2 k^2/4} e^{ikct_0} u^\infty(\hat{\mathbf{x}}, \omega). \quad (6.16)$$

Full details of the calculation of this transform are shown in Appendix E.1.1.

Consider the error in the calculation of the finite sum versus the exact integral (assuming that $F(\omega) = 0$ for $|\omega| > \omega_{\max}$):

$$\max_{|\omega| < \omega_{\max}} |F''(\omega)| \frac{2\omega_{\max}}{m(2N)^2}, \quad (6.17)$$

where $m = 6$ or 24 , for the trapezoidal or midpoint rule, respectively. This assumes that the second derivative F'' exists. If the second derivative fails to exist, the rate of convergence is not guaranteed to be $O(\frac{1}{N^2})$, and is generally much worse. Since

$$F(\omega) = u^\infty(\hat{\mathbf{x}}, \omega) \sim \frac{C}{\sqrt{\frac{\omega}{c}} \log(\omega \frac{a_0}{c})}, \quad (6.18)$$

for some constant C when $0 < \omega a_0/c \ll 1$, a careful choice must be made for the time dependent incident pulse, otherwise the singularity that occurs in (6.18) when $\omega = 0$, means that the quadrature rule used in the discrete fast Fourier transform will not converge easily.

The Gaussian pulse (6.14) for which the Fourier transform $F(\omega)$ has non-zero content

when $\omega = 0$. However, we have no experimental results for $\omega = 0$, that is, $k = 0$. To compensate, the zero frequency value is approximated as two times the smallest positive frequency value. The justification is as follows. From (6.18)

$$F(k) = \frac{C}{\sqrt{k} \log(ka_0)}, \quad (6.19)$$

thus we consider the integral

$$\int_0^k \frac{C}{\sqrt{x} \log(xa_0)} dx, \quad (6.20)$$

and using the substitution $u = \sqrt{xa_0}$, we write

$$\frac{2C}{\sqrt{a_0}} \int_0^{\sqrt{ka_0}} \frac{1}{\log u} du, \quad (6.21)$$

and further substituting $t = \log u$

$$\frac{2C}{\sqrt{a_0}} \int_{-\infty}^{\frac{1}{2} \log ka_0} \frac{e^t}{t} dt = \frac{-2C}{\sqrt{a_0}} \int_{\frac{1}{2} \log ka_0}^{-\infty} \frac{e^t}{t} dt. \quad (6.22)$$

Using the substitution $t = -t'$ transforms the integral into the exponential integral

$$\frac{-2C}{\sqrt{a_0}} \int_{-\frac{1}{2} \log ka_0}^{\infty} \frac{e^{-t'}}{t'} dt'. \quad (6.23)$$

We note that $-\frac{1}{2} \log ka_0 > 0$ since $0 < ka_0 < 1$. Using the asymptotic expansion of the exponential integral [121], where

$$E_1(z) \sim e^{-z} \left(\frac{1}{z} + \text{h.o.t.} \right), \quad (6.24)$$

thus

$$\frac{-2C}{\sqrt{a_0}} E_1 \left(-\frac{1}{2} \log ka_0 \right) = \frac{-2C}{\sqrt{a_0}} \frac{e^{\frac{1}{2} \log ka_0}}{-\frac{1}{2} \log ka_0} = \frac{2C\sqrt{k}}{\log \sqrt{ka_0}}. \quad (6.25)$$

Thus the average value over the interval $[0, k]$ is

$$\frac{2\hat{C}}{\sqrt{k} \log \sqrt{ka_0}} = 2F(k). \quad (6.26)$$

An alternative is to use a pulse that has zero content at $\omega = 0$. A number of choices could be used. We chose the derivative of the Gaussian (6.14),

$$f_t(t) = \frac{-2c(c(t-t_0))}{a_0^2} e^{-(c(t-t_0))^2/a_0^2}, \quad (6.27)$$

which is zero when $\omega = 0$, with Fourier transform

$$F(\omega) = \sqrt{\pi} i k a_0 e^{-ikct_0 - a_0^2 k^2/4}. \quad (6.28)$$

and the Gaussian sine packet with time displacement t_0 and dilation ω_0 ,

$$f(t) = e^{-(c(t-t_0))^2/a_0^2} \sin(\omega_0 t), \quad (6.29)$$

with Fourier transform

$$F(\omega) = \frac{\sqrt{\pi}}{2i} \frac{a_0}{c} e^{-it_0\omega} e^{-(\omega_0^2 - \omega^2)a_0^2/4c^2} \left(e^{\omega_0 \left(it_0 + \frac{a_0^2 \omega}{2c^2} \right)} - e^{-\omega_0 \left(it_0 + \frac{a_0^2 \omega}{2c^2} \right)} \right). \quad (6.30)$$

Full details of the calculation of these transforms are shown in Appendices E.1.1, E.1.2 and E.1.3.

The difficulty encountered with the $\omega = 0$ component in 2D scattering is not encountered in scattering problems with 3D objects of *finite extent*: for such objects, the $\omega = 0$ scattered component vanishes. The 2D problem concerns scattering from objects that are of infinite extent in one direction and of finite extent in their cross-section. The non-zero value of the $\omega = 0$ frequency component manifests itself in the 'wake' observed in the time-domain scattered field response of the infinite structure with the finite 2D cross-section.

6.4 Verification that Implementation is Correct

Roy, Sarkar et al. [122], published a set of time-domain results for TM-scattering from a circular scatterer. The paper presents results for the total field E_z on a terminating node measured at a point off the surface [122, Figure 6] and results for the induced current,

H_ϕ , on the surface of the scatterer [122, Figure 5] where

$$H_\phi = \frac{-1}{ik} \frac{\partial E_z}{\partial \rho}. \quad (6.31)$$

The circular scatterer is of radius $r = 0.5$, and the point used to measure the total field is 0.2 m from the surface. We can use these results to verify that our approach to obtaining the time-domain data from the frequency domain is producing correct results by using the following identities

$$E_z(\mathbf{x}) = u^{\text{tot}}(\mathbf{x}), \quad \text{and} \quad \frac{\partial E_z(\mathbf{x})}{\partial \rho} = \frac{\partial u^{\text{tot}}}{\partial r} \Big|_{r=a}, \quad x \in \mathbb{R}^2 \setminus \bar{D}. \quad (6.32)$$

To enable this comparison we calculate the total field outside the scatterer and the derivative of the total field on the surface of the scatterer. Since a circular scatterer is being used for this comparison we will employ the Mie-type series calculations for both required fields.

If the plane wave is travelling in the direction of the unit vector \mathbf{d} , then

$$u^{\text{inc}}(x, y) e^{-i\omega t} = A e^{ik(\mathbf{d} \cdot \mathbf{x} - ct)}, \quad (6.33)$$

where $k = \omega/c$. Without loss of generality we may take $A = 1$. Thus

$$u^{\text{inc}}(x, y) = e^{ik\mathbf{x} \cdot \mathbf{d}}, \quad \mathbf{x} = (x, y) \in \mathbb{R}^2. \quad (6.34)$$

The incident wave has the following well known wave function expansion [7, p.75]:

$$\begin{aligned} u^{\text{inc}}(\mathbf{x}) &= e^{ik\mathbf{x} \cdot \mathbf{d}} \\ &= J_0(kr) + \sum_{n=1}^{\infty} i^n J_n(kr) \cos n(\theta - \alpha) \\ &= \sum_{n=-\infty}^{\infty} i^{|n|} J_{|n|}(kr) e^{in(\theta - \alpha)}, \end{aligned} \quad (6.35)$$

for fixed $\mathbf{d} = (\cos \alpha, \sin \alpha)$, $\mathbf{x} = (r \cos \theta, r \sin \theta) \in \mathbb{R}^2$ and J_n is the Bessel function of the first kind.

Let D be a circle of radius a centred at the origin, and consider the incident field

(6.34) with wave number k . The solution of the exterior Dirichlet problem is

$$u^{\text{sc}}(r, \theta) = - \sum_{n=-\infty}^{\infty} \frac{i^{|n|} J_{|n|}(ka)}{H_{|n|}^{(1)}(ka)} H_{|n|}^{(1)}(kr) e^{in(\theta-\alpha)}, \quad (6.36)$$

where J_n is the Bessel function of the first kind and $H_n^{(1)}$ is the Hankel function of the first kind, both of order n ($n \in \mathbb{Z}$). Thus the total field can be determined by

$$\begin{aligned} u^{\text{tot}}(r, \theta) &= u^{\text{sc}}(r, \theta) + u^{\text{inc}}(r, \theta) \\ &= - \sum_{n=-\infty}^{\infty} \frac{i^{|n|} J_{|n|}(ka)}{H_{|n|}^{(1)}(ka)} H_{|n|}^{(1)}(kr) e^{in(\theta-\alpha)} + \sum_{n=-\infty}^{\infty} i^{|n|} J_{|n|}(kr) e^{in(\theta-\alpha)} \\ &= \sum_{n=-\infty}^{\infty} - \frac{i^{|n|} e^{in(\theta-\alpha)} \left(J_{|n|}(ka) H_{|n|}^{(1)}(kr) - J_{|n|}(kr) H_{|n|}^{(1)}(ka) \right)}{H_{|n|}^{(1)}(ka)}; \end{aligned} \quad (6.37)$$

the radial derivative is

$$\frac{\partial u^{\text{tot}}(r, \theta)}{\partial r} = \sum_{n=-\infty}^{\infty} - \frac{i^{|n|} e^{in(\theta-\alpha)} k \left(J_{|n|}(ka) H_{|n|}^{(1)'}(kr) - J_{|n|}'(kr) H_{|n|}^{(1)}(ka) \right)}{H_{|n|}^{(1)}(ka)}, \quad (6.38)$$

which evaluated at the surface $r = a$ is

$$\left. \frac{\partial u^{\text{tot}}(r, \theta)}{\partial r} \right|_{r=a} = \sum_{n=-\infty}^{\infty} - \frac{i^{|n|} e^{in(\theta-\alpha)} k \left(J_{|n|}(ka) H_{|n|}^{(1)'}(ka) - J_{|n|}'(ka) H_{|n|}^{(1)}(ka) \right)}{H_{|n|}^{(1)}(ka)}. \quad (6.39)$$

The Wronskian $\mathcal{W}(J_\nu(z), H_\nu^{(1)}(z))$ is

$$\begin{aligned} \mathcal{W}(J_\nu(z), H_\nu^{(1)}(z)) &= J_\nu(z) H_\nu^{(1)'}(z) - J_\nu'(z) H_\nu^{(1)}(z) \\ &= \frac{2i}{\pi z}. \end{aligned} \quad (6.40)$$

Substituting into (6.39)

$$\begin{aligned} \left. \frac{\partial u^{\text{tot}}(r, \theta)}{\partial r} \right|_{r=a} &= \sum_{n=-\infty}^{\infty} - \frac{2i}{\pi ka} \frac{i^{|n|} e^{in(\theta-\alpha)} k}{H_{|n|}^{(1)}(ka)} \\ &= \sum_{n=-\infty}^{\infty} - \frac{2}{\pi a} \frac{i^{|n|+1} e^{in\theta} e^{-in\alpha}}{H_{|n|}^{(1)}(ka)}. \end{aligned} \quad (6.41)$$

The technique outlined in Section 6.1 is then applied: multiplying $u^{\text{tot}}(\mathbf{x})$ and $\frac{-1}{ik} \frac{\partial u^{\text{tot}}(r, \theta)}{\partial r} \Big|_{r=a}$ by (E.9) and performing the Fourier transform, allowing us to produce a set of results to be compared to those published by Roy, Sarkar et al. [122]. Figure 6.1 shows the results obtained. These results matched those of [122]. Note that the incident pulse used in [122] is travelling in the opposite direction. This has been accounted for by appropriately changing the points of measurement used.

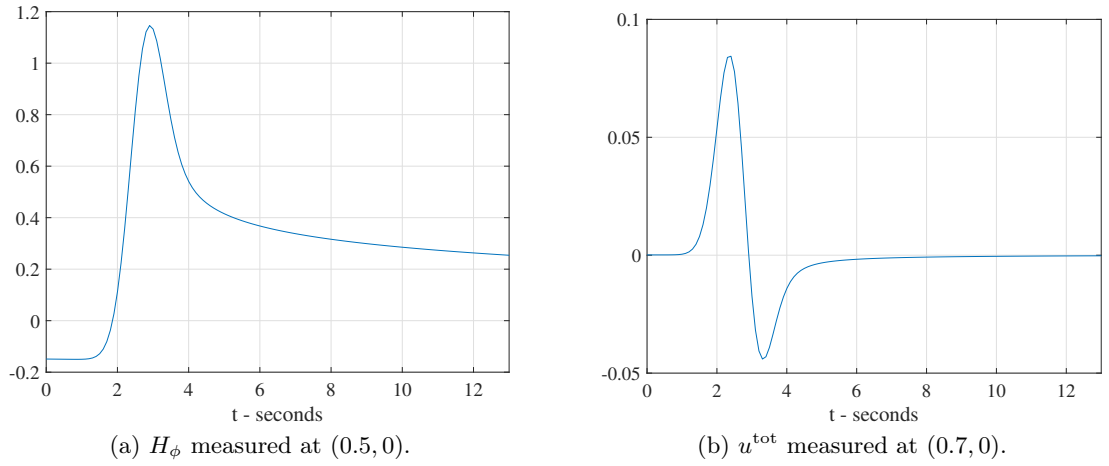


Figure 6.1: Reproducing the results of Roy, Sarkar et al. [122].

6.5 Results

To determine the effect of rounding corners in the time domain we tested the far-field response of a lemniscate (2.2) with Dirichlet boundary condition to the three pulses described in Section 6.3 for wave numbers $0 < k \leq 40$, using differing pulse widths a_0 and time displacements t_0 . A representative sample of the results is presented in Figures 6.2, 6.3 and 6.4. The responses to the different pulses all exhibit the same behaviour: as the radius of curvature of the rounded corner ρ increases, there is a slight phase shift in the time response and an increase in the amplitude. The phase shift is accounted for by recognising that the pulse strikes first at the corner point or the corresponding rounded corner point; this point is displaced by an amount 2ε approximately. One can observe that the maxima of the time domain response are delayed by an amount $2\varepsilon/c$ time units.

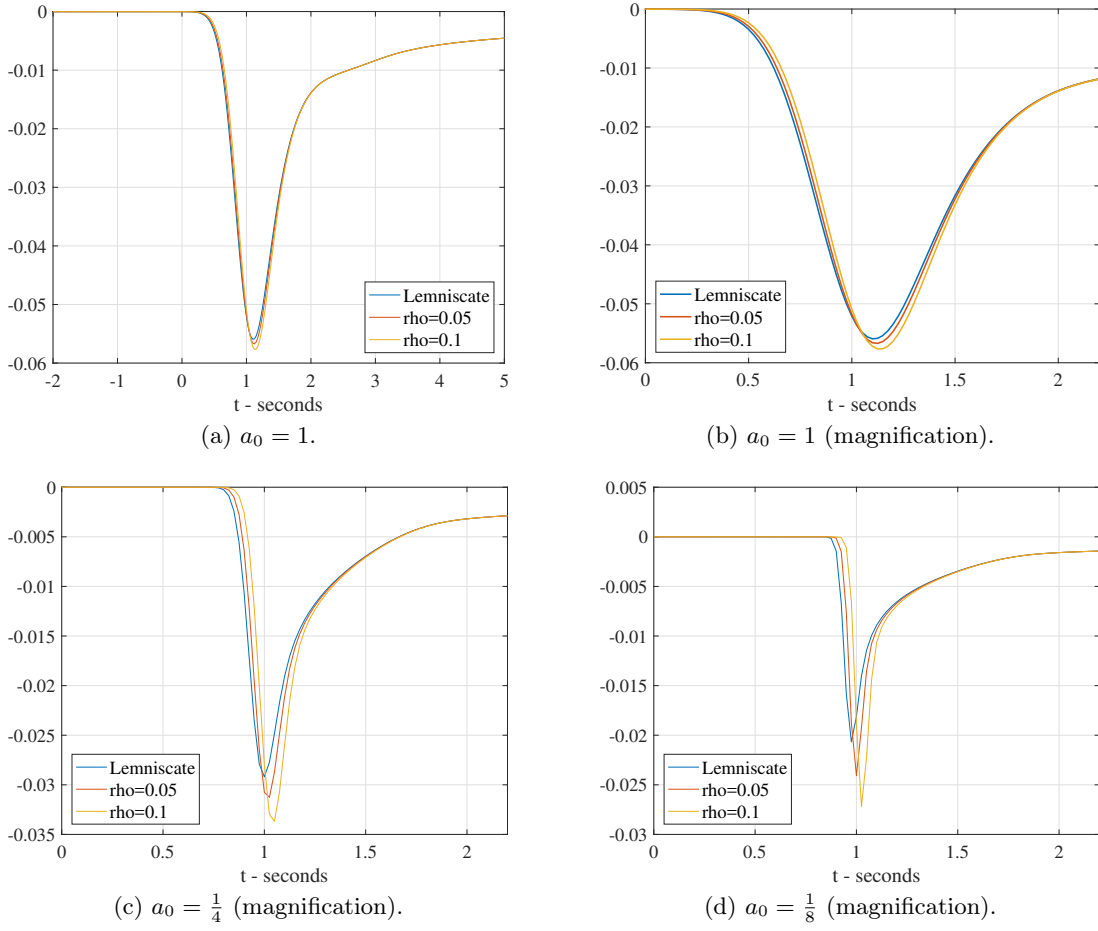


Figure 6.2: Time domain response $\tilde{u}_\infty(\hat{x}, t)$ to Gaussian incident wave
 $f(t) = e^{-(c(t-t_0))^2/a_0^2}$, $c = 1$, $t_0 = 3$, $0 < k \leq 40$, $\Delta\omega = k/c = 0.01$.

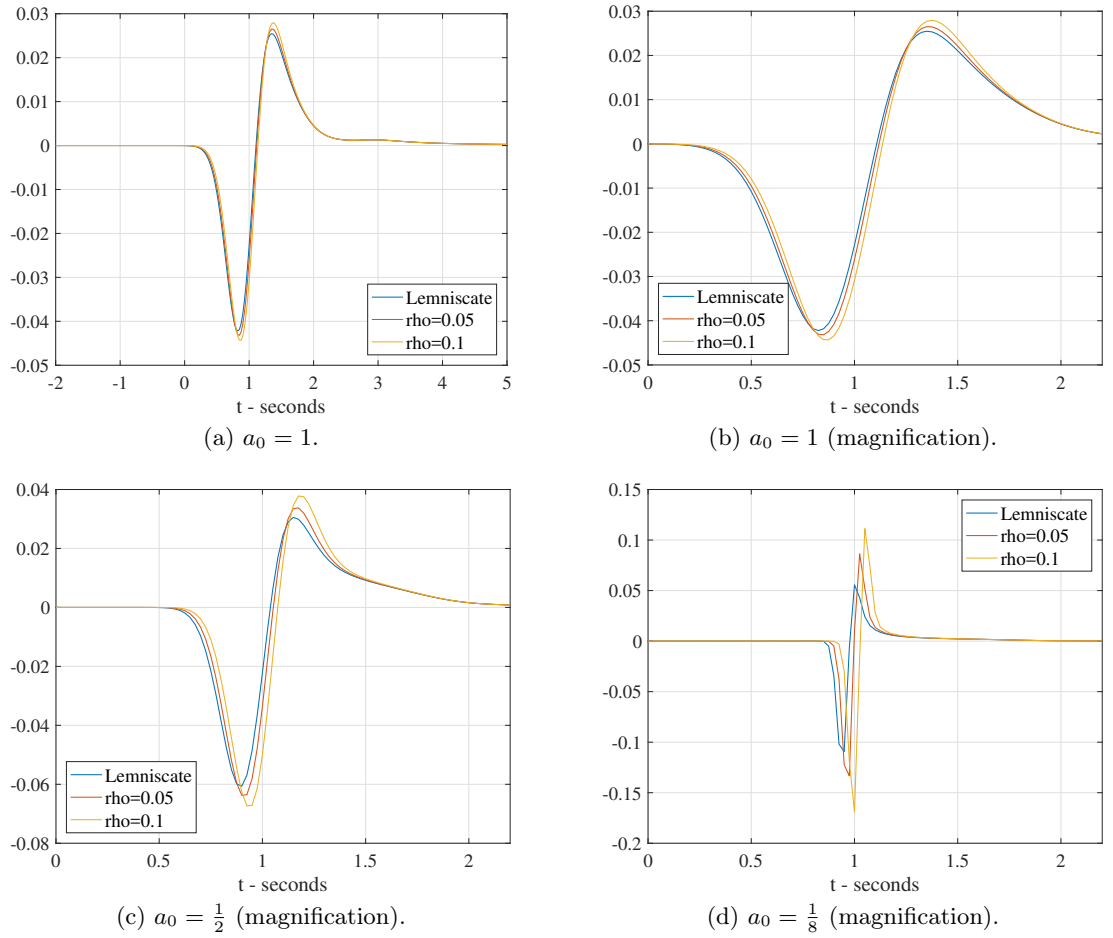


Figure 6.3: Time domain response $\tilde{u}_\infty(\hat{\mathbf{x}}, t)$ to the derivative of the Gaussian incident wave $f(t) = \frac{-2c(c(t-t_0))}{a_0^2} e^{-(c(t-t_0))^2/a_0^2}$, $c = 1$, $t_0 = 3$, $0 < k \leq 40$, $\Delta\omega = k/c = 0.01$.

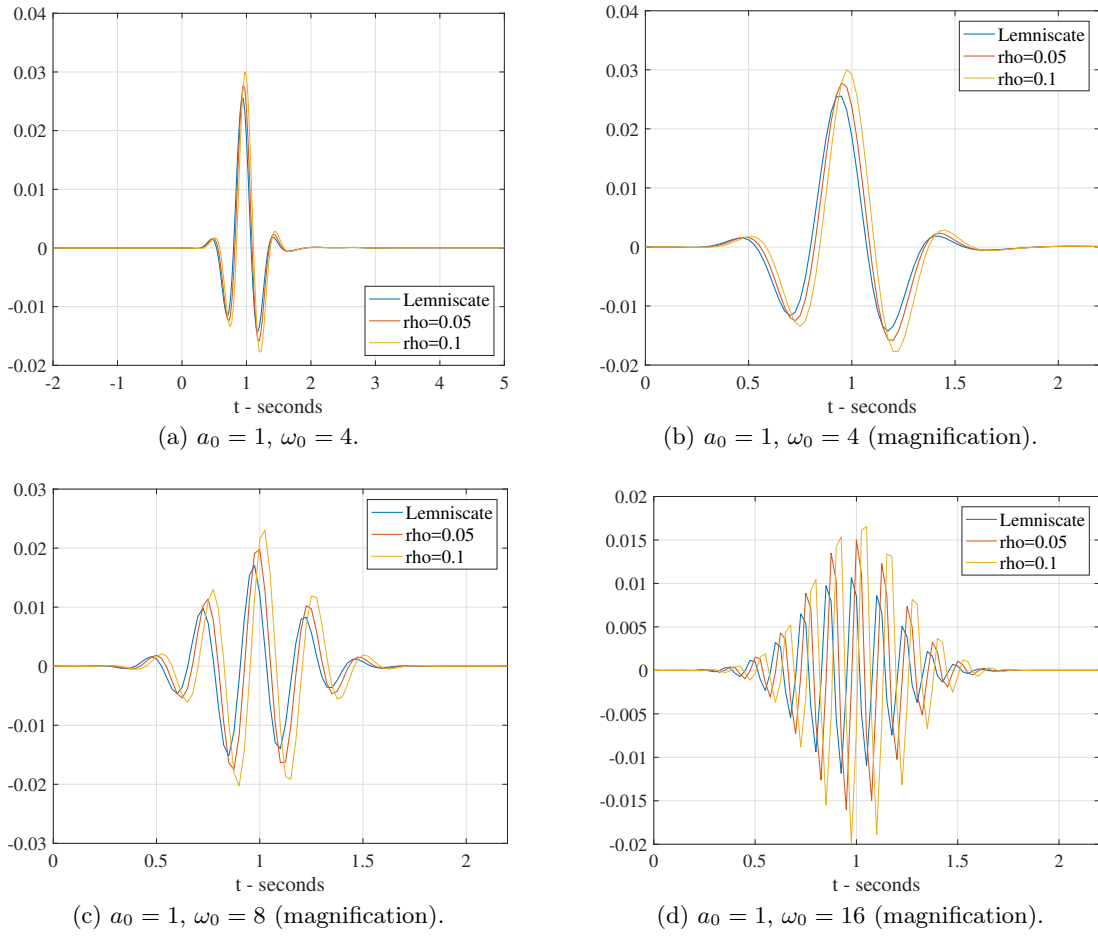


Figure 6.4: Time domain response $\tilde{u}_\infty(\hat{x}, t)$ to Gaussian sine packet incident wave $f(t) = e^{-(c(t-t_0))^2/a_0^2} \sin \omega_0 t$, $c = 1$, $t_0 = 3$, $0 < k \leq 40$, $\triangle\omega = k/c = 0.01$.

Chapter 7

Scatterer Arrays

We have undertaken an in depth analysis of the effect of rounding the corners of scatterers on the near- and far-fields for a variety of scatterers with Dirichlet, Neumann and impedance loaded boundary conditions. In this section, we extend this work to arrays of cornered scatterers.

The multiple scatterer problem is an extension of the single scatterer problem. Part of the interest lies in the strength of the coupling between the scatterers, that is, the degree to which scattering from a single scatterer is changed by the presence of other scatterers. The questions which, in particular, we wish to address are:

- Does increasing the number of scatterers increase the number of quadrature points required to achieve a desired level of accuracy?
- Is the relative difference between the far-fields of the cornered and rounded scatterers amplified when the number of scatterers is increased?
- Are the bounds on the far-field differences applicable to the multiple scatterer problem?

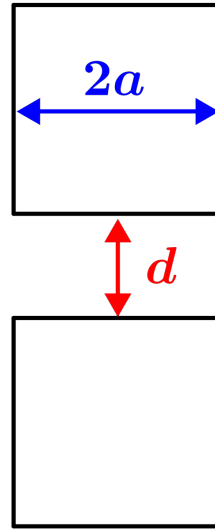
7.1 The Geometries

We began by considering arrays of two and then four scatterers, all the same shape, arranged parallel to the y -axis. Each array contains a single scatterer type: the lemniscate with right or acute interior angles (Figures 7.1a, 7.1b), the square (Figures 7.1c, 7.1d)

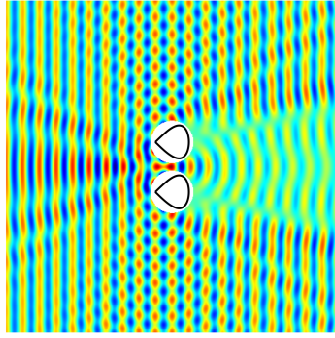
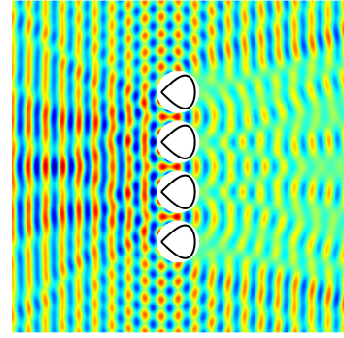
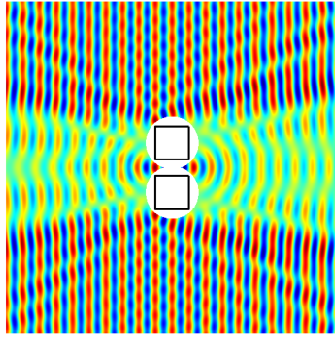
or the diamond (Figures 7.1e, 7.1f). The scatterer size was varied, ranging from a characteristic dimension of half a wavelength up to sixteen wavelengths, spaced uniformly at distances of either 0.1, 0.25, 0.5 or 1 wavelength. The studied arrays can be used to model various applications. The arrays of scatterers with characteristic dimension of half, one or two wavelengths, are representative of sensor arrays used in small antenna applications. Those with larger characteristic dimensions of four, eight and sixteen wavelengths are representative of meta-materials and band-gap materials.

7.1.1 Notation

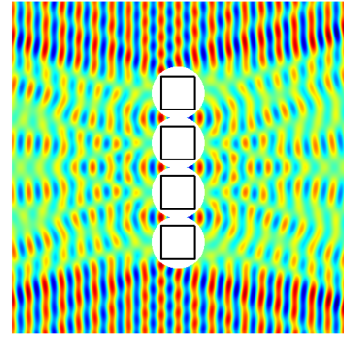
In this chapter we consider the scatterer's characteristic dimension in terms of wavelength. The characteristic dimension of the scatterer is represented as $2a$ and is calculated as follows. For the lemniscate with right or acute interior angles, it is the horizontal length, that is from the corner to the mid-point of the blunt end, which in all cases is equal to 2. For the square, it is the horizontal width, that is, the length of the side of the square. The diamond, is the square rotated by $\pi/4$, so the characteristic dimension in this case is reported as the length of the side of the scatterer. We will refer to the characteristic dimension as the “diameter” of the scatterer for the remainder of this thesis.



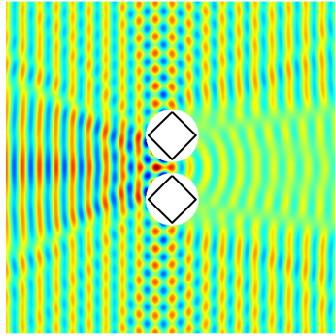
Also considered is the distance between scatterers, measured in wavelengths, denoted as d . This represents the separation distance, and is measured as the distance between the two nearest points on the scatterers.

(a) Lemniscates, $\beta = \pi/2$ (b) Lemniscates, $\beta = \pi/2$ 

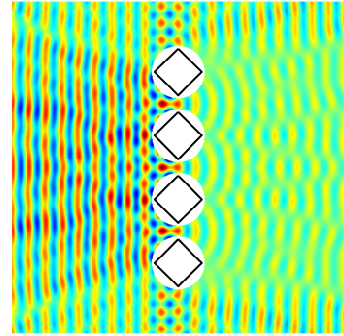
(c) Squares



(d) Squares



(e) Diamonds



(f) Diamonds

Figure 7.1: Sample of arrays of two and four scatterers of diameter two wavelengths, showing $Re(u^{\text{tot}})$. Scatterers are two wavelengths in diameter, distance between the scatterers is one wavelength.

7.2 Approach

To represent the change to our boundary value problems introduced by a multiple scatterer geometry, we re-formulate the problem as a coupled set of integral equations. In this section we describe in detail the method used for arrays of scatterers with the Dirichlet

boundary condition (2.19) and outline the changes required for arrays of scatterers with the Neumann (2.20) or impedance loaded (2.21) boundary conditions.

7.2.1 The Dirichlet Case

The solution to the exterior Dirichlet problem for multiple scatterers is

$$u^{\text{sc}}(\mathbf{x}) = \sum_{\alpha=1}^n \int_{\partial D_{\alpha}} \left\{ \frac{\partial G(\mathbf{x}, \mathbf{y}_{\alpha})}{\partial \mathbf{n}(\mathbf{y}_{\alpha})} - i\eta G(\mathbf{x}, \mathbf{y}_{\alpha}) \right\} \varphi_{\alpha}(\mathbf{y}_{\alpha}) \, ds(\mathbf{y}_{\alpha}), \quad (7.1)$$

for $\mathbf{x} \in \mathbb{R}^2 \setminus (\overline{D}_1 \cup \overline{D}_2 \cup \dots \cup \overline{D}_n)$, $\mathbf{y}_{\alpha} \in \partial D_{\alpha}$, where φ_{α} represents the surface potential on a scatterer ∂D_{α} .

The solution must satisfy the Dirichlet boundary condition for each scatterer, so we use the boundary conditions

$$\begin{aligned} u^{\text{sc}}(\mathbf{x}) &= -u^{\text{inc}}(\mathbf{x}), & \text{for } \mathbf{x} \in D_1, \\ u^{\text{sc}}(\mathbf{x}) &= -u^{\text{inc}}(\mathbf{x}), & \text{for } \mathbf{x} \in D_2, \\ &\vdots \\ u^{\text{sc}}(\mathbf{x}) &= -u^{\text{inc}}(\mathbf{x}), & \text{for } \mathbf{x} \in D_n, \end{aligned} \quad (7.2)$$

and the jump relations for the single- and double-layer potentials, (2.26) and (2.29), to obtain the following set of n integral equations

$$\begin{aligned} \varphi_1(\mathbf{x}) - 2 \sum_{\alpha=1}^n \int_{\partial D_{\alpha}} \left\{ \frac{\partial G(\mathbf{x}, \mathbf{y}_{\alpha})}{\partial \mathbf{n}(\mathbf{y}_{\alpha})} - i\eta G(\mathbf{x}, \mathbf{y}_{\alpha}) \right\} \varphi_{\alpha}(\mathbf{y}_{\alpha}) \, ds(\mathbf{y}_{\alpha}) &= -2u^{\text{inc}}(\mathbf{x}), \quad \mathbf{x} \in \partial D_1, \\ \varphi_2(\mathbf{x}) - 2 \sum_{\alpha=1}^n \int_{\partial D_{\alpha}} \left\{ \frac{\partial G(\mathbf{x}, \mathbf{y}_{\alpha})}{\partial \mathbf{n}(\mathbf{y}_{\alpha})} - i\eta G(\mathbf{x}, \mathbf{y}_{\alpha}) \right\} \varphi_{\alpha}(\mathbf{y}_{\alpha}) \, ds(\mathbf{y}_{\alpha}) &= -2u^{\text{inc}}(\mathbf{x}), \quad \mathbf{x} \in \partial D_2, \\ &\vdots \\ \varphi_n(\mathbf{x}) - 2 \sum_{\alpha=1}^n \int_{\partial D_{\alpha}} \left\{ \frac{\partial G(\mathbf{x}, \mathbf{y}_{\alpha})}{\partial \mathbf{n}(\mathbf{y}_{\alpha})} - i\eta G(\mathbf{x}, \mathbf{y}_{\alpha}) \right\} \varphi_{\alpha}(\mathbf{y}_{\alpha}) \, ds(\mathbf{y}_{\alpha}) &= -2u^{\text{inc}}(\mathbf{x}), \quad \mathbf{x} \in \partial D_n, \end{aligned} \quad (7.3)$$

which are used to solve for the unknown surface densities $\varphi_1, \varphi_2, \dots, \varphi_n$ on the scatterers $\partial D_1, \partial D_2, \dots, \partial D_n$, respectively.

In each equation, the kernel of

$$\int_{\partial D_\alpha} \left(\frac{\partial G(\mathbf{x}, \mathbf{y}_\alpha)}{\partial \mathbf{n}(\mathbf{y}_\alpha)} - i\eta G(\mathbf{x}, \mathbf{y}_\alpha) \right) \varphi_\alpha(\mathbf{y}_\alpha) \, ds(\mathbf{y}_\alpha), \quad (7.4)$$

is not weakly singular at the corners of the scatterer when $\mathbf{x} \in \partial D_\alpha$. The technique described in Section 2.5.4 is utilised and a vanishing term is subtracted. When $\mathbf{x} \notin \partial D_\alpha$, the kernels are not singular and require no special treatment.

Using the case of an array of single-cornered scatterers each with a corner at \mathbf{x}_0^α as an example, (7.3) is transformed into

$$\begin{aligned} \varphi_1(\mathbf{x}) - 2 \sum_{\alpha=1}^n \left(\int_{\partial D_\alpha} \left\{ \frac{\partial G(\mathbf{x}, \mathbf{y}_\alpha)}{\partial \mathbf{n}(\mathbf{y}_\alpha)} - i\eta G(\mathbf{x}, \mathbf{y}_\alpha) \right\} \varphi_\alpha(\mathbf{y}_\alpha) \, ds(\mathbf{y}_\alpha) \right) \\ - 2 \int_{\partial D_1} \frac{\partial G_0(\mathbf{x}, \mathbf{y}_1)}{\partial \mathbf{n}(\mathbf{y}_1)} \varphi_1(\mathbf{x}_0^1) \, ds(\mathbf{y}) = -2u^{\text{inc}}(\mathbf{x}), \quad \mathbf{x} \in \partial D_1, \\ \varphi_2(\mathbf{x}) - 2 \sum_{\alpha=1}^n \left(\int_{\partial D_\alpha} \left\{ \frac{\partial G(\mathbf{x}, \mathbf{y}_\alpha)}{\partial \mathbf{n}(\mathbf{y}_\alpha)} - i\eta G(\mathbf{x}, \mathbf{y}_\alpha) \right\} \varphi_\alpha(\mathbf{y}_\alpha) \, ds(\mathbf{y}_\alpha) \right) \\ - 2 \int_{\partial D_2} \frac{\partial G_0(\mathbf{x}, \mathbf{y}_2)}{\partial \mathbf{n}(\mathbf{y}_2)} \varphi_2(\mathbf{x}_0^2) \, ds(\mathbf{y}) = -2u^{\text{inc}}(\mathbf{x}), \quad \mathbf{x} \in \partial D_2, \\ \vdots \\ \varphi_n(\mathbf{x}) - 2 \sum_{\alpha=1}^n \left(\int_{\partial D_\alpha} \left\{ \frac{\partial G(\mathbf{x}, \mathbf{y}_\alpha)}{\partial \mathbf{n}(\mathbf{y}_\alpha)} - i\eta G(\mathbf{x}, \mathbf{y}_\alpha) \right\} \varphi_\alpha(\mathbf{y}_\alpha) \, ds(\mathbf{y}_\alpha) \right) \\ - 2 \int_{\partial D_n} \frac{\partial G_0(\mathbf{x}, \mathbf{y}_n)}{\partial \mathbf{n}(\mathbf{y}_n)} \varphi_n(\mathbf{x}_0^n) \, ds(\mathbf{y}) = -2u^{\text{inc}}(\mathbf{x}), \quad \mathbf{x} \in \partial D_n. \end{aligned} \quad (7.5)$$

Letting the operators $A_{\alpha\beta}$ being defined by

$$\begin{aligned} A_{\alpha\alpha} \varphi(\mathbf{x}) = 2 \int_{\partial D_\alpha} \left(\frac{\partial G(\mathbf{x}, \mathbf{y}_\alpha)}{\partial \mathbf{n}(\mathbf{y}_\alpha)} - i\eta G(\mathbf{x}, \mathbf{y}_\alpha) \right) \varphi(\mathbf{y}_\alpha) \, ds(\mathbf{y}_\alpha) \\ + 2 \int_{\partial D_\alpha} \frac{\partial G_0(\mathbf{x}, \mathbf{y}_\alpha)}{\partial \mathbf{n}(\mathbf{y}_\alpha)} \varphi(\mathbf{x}_0^\alpha) \, ds(\mathbf{y}_\alpha), \quad \mathbf{x} \in \partial D_\alpha, \end{aligned} \quad (7.6)$$

and

$$A_{\alpha\beta} \varphi(\mathbf{x}) = 2 \int_{\partial D_\beta} \left(\frac{\partial G(\mathbf{x}, \mathbf{y}_\beta)}{\partial \mathbf{n}(\mathbf{y}_\beta)} - i\eta G(\mathbf{x}, \mathbf{y}_\beta) \right) \varphi(\mathbf{y}_\beta) \, ds(\mathbf{y}_\beta), \quad \mathbf{x} \in \partial D_\alpha, \quad \mathbf{x} \notin \partial D_\beta, \quad (7.7)$$

the set of equations (7.5) can be expressed as

$$\begin{aligned} \varphi_1 - A_{11}\varphi_1 - A_{12}\varphi_2 - \cdots - A_{1n}\varphi_n &= f_1 \\ \varphi_2 - A_{21}\varphi_1 - A_{22}\varphi_2 - \cdots - A_{2n}\varphi_n &= f_2 \\ &\vdots \\ \varphi_n - A_{n1}\varphi_1 - A_{n2}\varphi_2 - \cdots - A_{nn}\varphi_n &= f_n, \end{aligned} \quad (7.8)$$

where $f_\alpha = -2u^{\text{inc}}(\mathbf{x})$ for $\mathbf{x} \in \partial D_\alpha$. We then transform this set of integral equations into line integrals as described in Sections 2.5 and A.3.1, and discretise using the appropriate graded mesh ((2.61), (2.65), (2.66)) depending on the geometry of the scatterer. For the singular kernels (7.4), we follow the Martensen-Kussmaul method as described in Section 2.5.2 and A.2. For the non-singular kernels (7.7) we use a trapezoidal rule to evaluate the integral.

We can now express the system of discretised equations that need to be solved in block matrix form as

$$\begin{bmatrix} \mathbf{I} - \mathbf{A}_{11} & -\mathbf{A}_{12} & \cdots & -\mathbf{A}_{1n} \\ -\mathbf{A}_{21} & \mathbf{I} - \mathbf{A}_{22} & \cdots & -\mathbf{A}_{2n} \\ & \vdots & \ddots & \\ -\mathbf{A}_{n1} & -\mathbf{A}_{n2} & \cdots & \mathbf{I} - \mathbf{A}_{nn} \end{bmatrix} \begin{bmatrix} \varphi_1 \\ \varphi_2 \\ \vdots \\ \varphi_n \end{bmatrix} = \begin{bmatrix} f_1 \\ f_2 \\ \vdots \\ f_n \end{bmatrix}. \quad (7.9)$$

The block $\mathbf{A}_{\alpha\beta}$ corresponds to the operator $A_{\alpha\beta}$ in equations (7.6) and (7.7). The components $\mathbf{I} - \mathbf{A}_{\alpha\alpha}$ are identical to the discretised integral equations (A.54) required to be solved for a single cornered scatterer. For scatterers with more than one corner, the set of integral equations (7.5), need to be modified to account for the contribution of each corner as detailed in Section 2.5.4.

7.2.2 The Neumann and Impedance Loaded Cases

For scatterers with Neumann or impedance loaded boundary condition the method is the same as that for the Dirichlet boundary condition. The differences occur in the kernels of the integral equations evaluated. The solution to the exterior Neumann and impedance loaded problems for multiple scatterers is

$$u^{\text{sc}}(\mathbf{x}) = \sum_{\alpha=1}^n \int_{\partial D_{\alpha}} G(\mathbf{x}, \mathbf{y}_{\alpha}) \varphi(\mathbf{y}_{\alpha}) \, ds(\mathbf{y}_{\alpha}), \quad (7.10)$$

for $\mathbf{x} \in \mathbb{R}^2 \setminus (\overline{D}_1 \cup \overline{D}_2 \cup \dots \cup \overline{D}_n)$, $\mathbf{y}_{\alpha} \in \partial D_{\alpha}$, where φ_{α} represents the surface potential on a scatterer ∂D_{α} .

The solution must satisfy the boundary condition for each scatterer, so for the impedance case we use the boundary conditions

$$\begin{aligned} u^{\text{sc}}(\mathbf{x}) &= -\frac{\partial u^{\text{inc}}}{\partial \mathbf{n}}(\mathbf{x}) - ikZu^{\text{inc}}(\mathbf{x}), & \text{for } \mathbf{x} \in D_1, \\ u^{\text{sc}}(\mathbf{x}) &= -\frac{\partial u^{\text{inc}}}{\partial \mathbf{n}}(\mathbf{x}) - ikZu^{\text{inc}}(\mathbf{x}), & \text{for } \mathbf{x} \in D_1, \\ &\vdots \\ u^{\text{sc}}(\mathbf{x}) &= -\frac{\partial u^{\text{inc}}}{\partial \mathbf{n}}(\mathbf{x}) - ikZu^{\text{inc}}(\mathbf{x}), & \text{for } \mathbf{x} \in D_n, \end{aligned} \quad (7.11)$$

and the jump relation for the single-layer potential (2.26), to obtain the following set of n integral equations

$$\begin{aligned} -\varphi_1(\mathbf{x}) + 2 \sum_{\alpha=1}^n \int_{\partial D_{\alpha}} \left\{ \frac{\partial G(\mathbf{x}, \mathbf{y}_{\alpha})}{\partial \mathbf{n}(\mathbf{x})} + ikZG(\mathbf{x}, \mathbf{y}_{\alpha}) \right\} \varphi(\mathbf{y}_{\alpha}) \, ds(\mathbf{y}_{\alpha}) \\ &= -2 \left(\frac{\partial u^{\text{inc}}}{\partial \mathbf{n}}(\mathbf{x}) + ikZu^{\text{inc}}(\mathbf{x}) \right), & \mathbf{x} \in \partial D_1, \\ -\varphi_2(\mathbf{x}) + 2 \sum_{\alpha=1}^n \int_{\partial D_{\alpha}} \left\{ \frac{\partial G(\mathbf{x}, \mathbf{y}_{\alpha})}{\partial \mathbf{n}(\mathbf{x})} + ikZG(\mathbf{x}, \mathbf{y}_{\alpha}) \right\} \varphi(\mathbf{y}_{\alpha}) \, ds(\mathbf{y}_{\alpha}) \\ &= -2 \left(\frac{\partial u^{\text{inc}}}{\partial \mathbf{n}}(\mathbf{x}) + ikZu^{\text{inc}}(\mathbf{x}) \right), & \mathbf{x} \in \partial D_2, \\ &\vdots \\ -\varphi_n(\mathbf{x}) + 2 \sum_{\alpha=1}^n \int_{\partial D_{\alpha}} \left\{ \frac{\partial G(\mathbf{x}, \mathbf{y}_{\alpha})}{\partial \mathbf{n}(\mathbf{x})} + ikZG(\mathbf{x}, \mathbf{y}_{\alpha}) \right\} \varphi(\mathbf{y}_{\alpha}) \, ds(\mathbf{y}_{\alpha}) \end{aligned}$$

$$= -2 \left(\frac{\partial u^{\text{inc}}}{\partial \mathbf{n}}(\mathbf{x}) + ikZu^{\text{inc}}(\mathbf{x}) \right), \quad \mathbf{x} \in \partial D_n. \quad (7.12)$$

In each equation, the kernel of

$$\int_{\partial D_\alpha} \left(\frac{\partial G(\mathbf{x}, \mathbf{y}_\alpha)}{\partial \mathbf{n}(\mathbf{x})} - ikZG(\mathbf{x}, \mathbf{y}_\alpha) \right) \varphi_\alpha(\mathbf{y}_\alpha) \, ds(\mathbf{y}_\alpha), \quad (7.13)$$

is weakly singular when $\mathbf{x} \in \partial D_\alpha$. The technique described in Section 2.5.2 is utilised to isolate and integrate the singular part of the kernel. When $\mathbf{x} \notin \partial D_\alpha$, the kernels are not singular and require no special treatment.

Setting the operator $A_{\alpha\beta}$ to be defined by

$$A_{\alpha\beta} \varphi(\mathbf{x}) = 2 \int_{\partial D_\beta} \left(\frac{\partial G(\mathbf{x}, \mathbf{y}_\beta)}{\partial \mathbf{n}(\mathbf{x})} - ikZG(\mathbf{x}, \mathbf{y}_\beta) \right) \varphi(\mathbf{y}_\beta) \, ds(\mathbf{y}_\beta), \quad \mathbf{x} \in \partial D_\alpha, \quad (7.14)$$

the set of equations (7.12) can be expressed as

$$\begin{aligned} -\varphi_1 + A_{11}\varphi_1 + A_{12}\varphi_2 + \cdots + A_{1n}\varphi_n &= f_1 \\ -\varphi_2 + A_{21}\varphi_1 + A_{22}\varphi_2 + \cdots + A_{2n}\varphi_n &= f_2 \\ &\vdots \\ -\varphi_n + A_{n1}\varphi_1 + A_{n2}\varphi_2 + \cdots + A_{nn}\varphi_n &= f_n, \end{aligned} \quad (7.15)$$

where $f_\alpha = -2 \left(\frac{\partial u^{\text{inc}}}{\partial \mathbf{n}}(\mathbf{x}) + ikZu^{\text{inc}}(\mathbf{x}) \right)$ for $\mathbf{x} \in \partial D_\alpha$. In the same manner as the Dirichlet case, we transform this set of integral equations into line integrals, discretise using the appropriate graded mesh and use the described numerical techniques to evaluate the integrals.

We express the system of discretised equations that need to be solved in block matrix form as

$$\begin{bmatrix} -\mathbf{I} + \mathbf{A}_{11} & \mathbf{A}_{12} & \cdots & \mathbf{A}_{1n} \\ \mathbf{A}_{21} & -\mathbf{I} + \mathbf{A}_{22} & \cdots & \mathbf{A}_{2n} \\ & \vdots & \ddots & \vdots \\ \mathbf{A}_{n1} & \mathbf{A}_{n2} & \cdots & -\mathbf{I} + \mathbf{A}_{nn} \end{bmatrix} \begin{bmatrix} \varphi_1 \\ \varphi_2 \\ \vdots \\ \varphi_n \end{bmatrix} = \begin{bmatrix} f_1 \\ f_2 \\ \vdots \\ f_n \end{bmatrix}. \quad (7.16)$$

The components $-I + \mathbf{A}_{\alpha\alpha}$ are identical to the discretised integral equations (A.54) required to be solved for a single scatterer. For scatterers with the Neumann boundary condition we set $Z = 0$.

7.3 Numerical Results

7.3.1 Test Parameters

For all scenarios presented in this section a variety of angles of incidence, θ_0 , were tested. Also, a number of impedance parameters were tried all producing similar results. In this work we report on the results for impedance parameter $Z = 1+i$. All tests were performed for a variety of scatterer sizes, ranging from a diameter of half a wavelength up to sixteen wavelengths, spaced uniformly at distances of either 0.1, 0.25, 0.5 or 1 wavelength. The results reported in this section are for the far-field. All rates of convergence and significant digits in agreement for the far-field reported in this chapter are measured in the back-scatter region, unless stated otherwise.

7.3.2 Verification of Numerical Results

There are no analytical expressions, nor readily published results with which to compare our results. To validate the results from this section of work, we used the significant digit measurement technique described in Section 3.1 to measure convergence. We also used (3.7) to approximate the far-field from the near-field to verify the far-field solutions.

Once the TMATROM package [27, 100] was released, and appropriate modifications were made, we were able to further verify the numerical results from this section. Full details are presented in Section 8.3.

7.4 Convergence and Quadrature

The rate of convergence and number of quadrature points required for accuracy were evaluated using the significant measurement technique described in Section 3.1. The scenarios tested were for two and four scatterers consisting of either lemniscates of varying acute interior angles ($0 < \beta \leq \pi/2$), squares or diamonds, with diameters, $2a$, ranging from half a wavelength to sixteen wavelengths for all three boundary conditions. All

rates of convergence and significant digits in agreement for the far-field reported in this chapter are measured in the back-scatter region, unless stated otherwise.

Figure 7.2 illustrates the convergence rates for lemniscates with interior angle $\beta = \pi/2$. Shown are the convergence rates for a single lemniscate and arrangements of two and four lemniscates spaced by 0.1, 0.25, 0.5 and 1 wavelengths, using an incident wave direction $\theta_0 = 0$. The results are demonstrative of those with different incident field directions and lemniscates with different interior angles, β . Similarly, Figures 7.3 and 7.4 illustrate the convergence rates for similar arrangements of squares and diamonds, respectively. These, also, are representative of the results when the incident angle, θ_0 varies. These figures clearly demonstrate that the number of quadrature points required on each scatterer for a desired degree of accuracy is the nearly same, whether we are solving a single or multiple scatterer problem (see Figure 3.4 for single scatterer results). The dependency of the required number of quadrature points is on the scatterer shape, not the geometry of the scatterer array. The accuracy of the solution for a given number of quadrature points varies by at most, one and occasionally two significant digits.

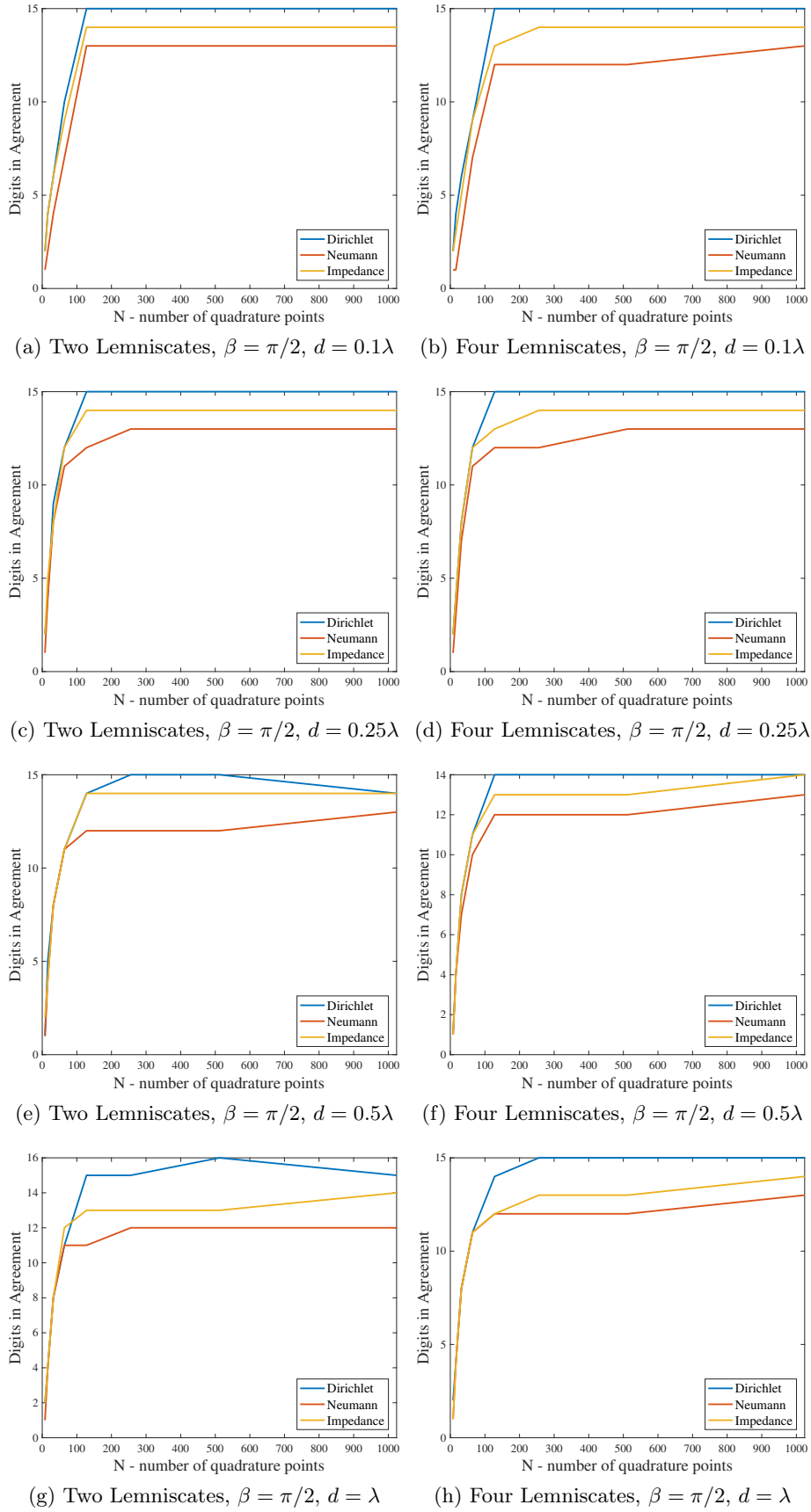


Figure 7.2: Illustrating the convergence rates for the far-field $|u^\infty(\hat{\mathbf{x}})|$ using significant digits in agreement, for arrays of two or four lemniscates, one wavelength in diameter, using different separations d , for the three boundary conditions. Direction of plane wave $\theta_0 = 0$.

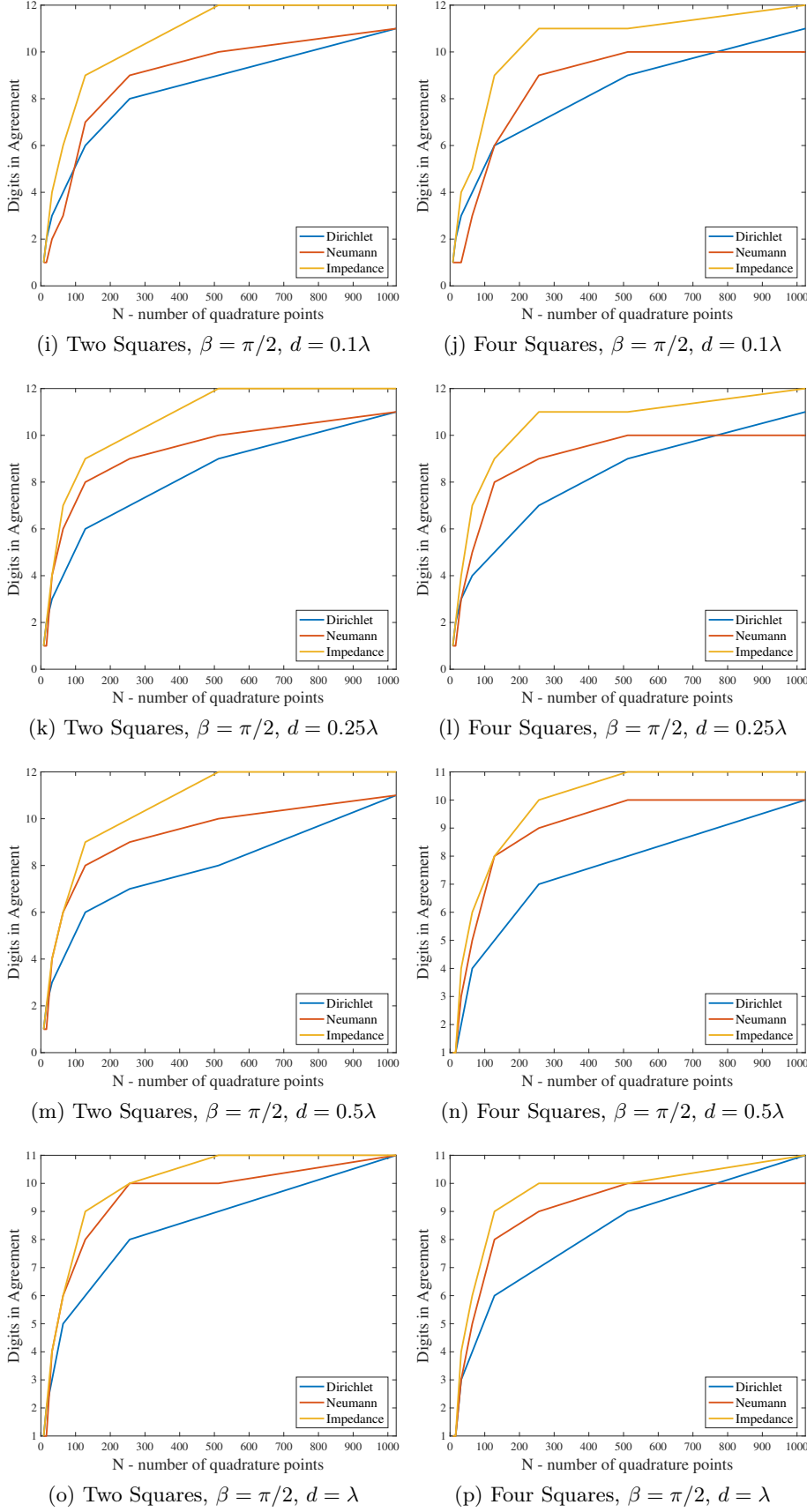


Figure 7.3: Illustrating the convergence rates for the far-field $|u^\infty(\hat{\mathbf{x}})|$ using significant digits in agreement, for arrays of two or four Squares, one wavelength in diameter, using different separations d , for the three boundary conditions. Direction of plane wave $\theta_0 = 0$.

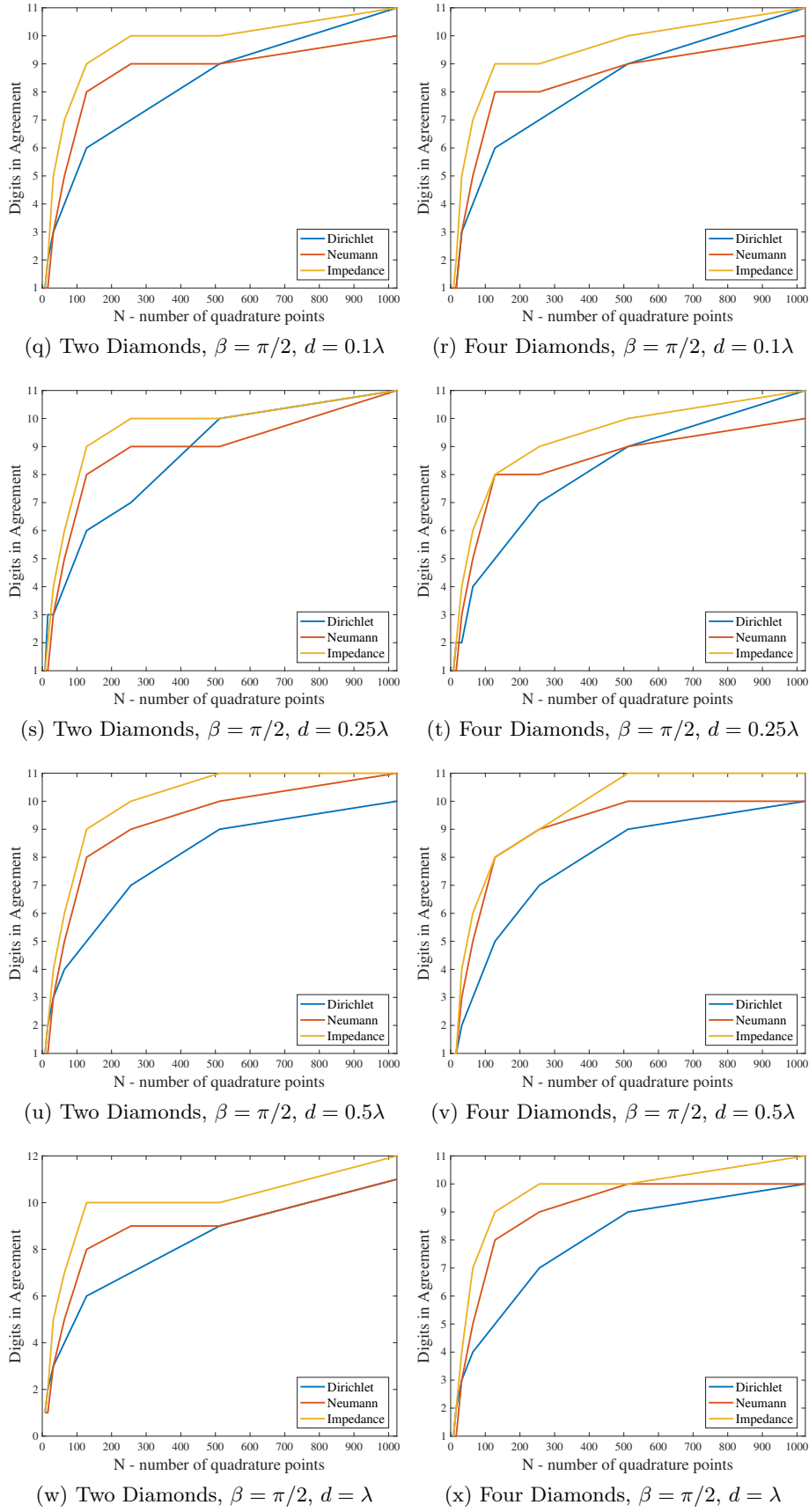


Figure 7.4: Illustrating the convergence rates for the far-field $|u^\infty(\hat{\mathbf{x}})|$ using significant digits in agreement, for arrays of two or four Diamonds, one wavelength in diameter, using different separations d , for the three boundary conditions. Direction of plane wave $\theta_0 = 0$.

7.5 Relative Differences

In this section we address the question: is the relative difference between the far-fields of the cornered scatterers and their rounded counterparts amplified when the number of scatterers is increased? We use a similar method for measuring the effect on the far-field of rounding corners to that used for single scatterers (Section 3.4). The deviation from the far-field solution produced by an array of cornered scatterers, $u_0^\infty(\hat{\mathbf{x}})$, where $\hat{\mathbf{x}} = \hat{\mathbf{x}}(\hat{\theta}) = (\cos \hat{\theta}, \sin \hat{\theta})$, with $\hat{\theta} \in [0, 2\pi]$ being the angle of observation of the far-field, and that produced by rounding $u_\rho^\infty(\hat{\mathbf{x}})$, with associated radius of curvature ρ , is measured using the L^1 norm

$$\|u_0^\infty - u_\rho^\infty\|_1 = \int_0^{2\pi} |u_0^\infty(\hat{\mathbf{x}}) - u_\rho^\infty(\hat{\mathbf{x}})| d\hat{\mathbf{x}}, \quad (7.17)$$

and L^∞ norm

$$\|u_0^\infty - u_\rho^\infty\|_\infty = \max_{\hat{\mathbf{x}} \in [0, 2\pi]} |u_0^\infty(\hat{\mathbf{x}}) - u_\rho^\infty(\hat{\mathbf{x}})|. \quad (7.18)$$

We examine arrays of two and four scatterers of a particular shape and boundary condition arranged in a line parallel to the y-axis (Figure 7.1). Three shapes are examined: the lemniscate (2.2), square (2.6) and diamond (a square rotated by $\pi/4$) and their rounded counterparts (2.3), (2.7), for the three boundary conditions: Dirichlet (2.19), Neumann (2.20) and impedance loaded (2.21). Both the absolute and relative difference were measured and the relative difference is reported. The relative difference is expressed as a percentage of the same norm of the scatterer's far-field. The L^1 relative difference is

$$\frac{\|u_0^\infty - u_\rho^\infty\|_1}{\|u_0^\infty\|_1}, \quad (7.19)$$

and the L^∞ relative difference is

$$\frac{\|u_0^\infty - u_\rho^\infty\|_\infty}{\|u_0^\infty\|_\infty}. \quad (7.20)$$

Full results for scatterers of diameter $2a = 0.5, 1$ and 2 wavelengths, separated by distances $d = 0.1, 0.25, 0.5$ and 1 wavelengths are available in Appendix F.1. Tables F.1 and F.2 are for the lemniscate, Tables F.3 and F.4 for the square and Tables F.5 and F.6

for diamonds.

Table 7.1 presents a sample of the results collected. It shows data for a single lemniscate, an array of two lemniscates and an array of four lemniscates for all three boundary conditions. The lemniscates are 1 wavelength in diameter and separated by distances of $d = 0.1, 0.25, 0.5$ and 1 wavelength. The results are for incident wave angle $\theta_0 = 0$.

An analysis of the results reveals the following. Firstly, as in the case of single scatterers, the smaller the radius of curvature used for the rounding, the smaller the measured relative difference. Secondly, increasing the number of scatterers from one to two or even four, does not increase the relative norm differences by an equivalent ratio. The effect of rounding on arrays of scatterers is of a similar order as that of a single scatterer, and sometimes the effect of rounding is even less. Specific changes to the relative differences are dependent on the scatterer shape and the boundary condition, as the following sections explain.

7.5.1 Dirichlet Boundary Condition

In the case of the Dirichlet boundary condition, the scatterer shape and, to a smaller extent the scatterer size, determines the change in the L^1 relative differences as the number of scatterers increases. In the case of the lemniscate, increasing the number of scatterers makes little difference in the L^1 norm and in the majority of cases it is less than that of a single lemniscate. In all cases where there is an increase to the relative difference, the increase is less than 10%. The L^∞ norm relative differences, not unexpectedly, exhibit similar behaviour.

As an example, a single lemniscate with radius of curvature $\rho = 0.02$ has an L^1 and L^∞ relative difference of 1.2% and 1.07%, respectively. For an array of two lemniscates the same relative differences range from 0.9% to 1.28% and 0.73% to 1.13%, respectively. In the case of a four lemniscate array, the respective differences range from 0.86% to 1.32% and 0.61% to 1.3%.

For squares and diamonds the distance between the scatterers has more impact on the differences. When the scatterers are spaced at a distance of 0.1 wavelength the relative differences are similar to that of a single scatterer and are reduced when the spacing is increased to one wavelength. The largest difference occurs when the scatterers are

separated by half a wavelength. These results are independent of the scatterer diameter.

A single square, one wavelength in diameter, has relative L^1 and L^∞ norm differences of 0.76% and 0.63%, respectively. For an array of two squares these differences range from 0.75% to 0.99% and 0.53% to 0.76%, respectively when the scatterers are separated by 0.1, 0.25, and 1 wavelengths. For an array of four squares the relative norm differences range from 0.77% to 1.12% and 0.44% to 0.9%, respectively for the same separations. When the scatterer separation is 0.5λ there is a jump in the relative differences to 1.82% and 1.48% for the two scatterer case, and 2.06% and 1.94% for the four scatterer case.

A single diamond, one wavelength in diameter, has L^1 and L^∞ relative differences of 0.71% and 0.56%, respectively. For an array of two diamonds, these differences range from 0.76% to 0.87% and 0.6% to 0.75%, respectively. In the case of a four diamond array, the respective differences range from 0.77% to 0.98% and 0.72% to 0.94%. There is a bigger jump in the L^1 relative norm difference only, when the scatterers are separated by half a wavelength. In the case of a two scatterer array it is 1.23% and in the case of four, 1.35%. This jump does not occur in the L^∞ norm.

In summary, for the Dirichlet case, even though there is some variation, both the relative norm differences are of the same order as that of the single scatterer with equivalent rounding, regardless of the distance between the scatterers or the scatterer size.

7.5.2 Neumann Boundary Condition

For lemniscates with the Neumann boundary condition, increasing the number of scatterers increases the L^1 norm differences by a factor of two or less and the L^∞ norm differences up to a factor of three. A single lemniscate with radius of curvature $\rho = 0.02$, one wavelength in diameter has L^1 and L^∞ relative differences of 0.4% and 0.31%, respectively. For an array of two lemniscates these differences range from 0.56% to 0.8% and 0.41% to 0.74%, respectively. In the case of a four lemniscate array, the respective differences range from 0.55% to 0.9% and 0.37% to 1%. Even though there are increases to the relative differences as the number of scatterers increase they are still small.

In the case of squares with Neumann boundary condition the separation distance is slightly more significant. The closer the scatterers, the larger the relative differences. Increasing the distance between the scatterers reduces the difference. Once the scatterers

are separated by one wavelength, the relative difference is the same as that of the single scatterer. This is most notable in the L^1 norm. To illustrate: a single square, one wavelength in diameter with radius of curvature $\rho = 0.02$, has an L^1 norm difference of 0.67%. Increasing the number of scatterers to two produces differences of 1.54%, 1.04%, 0.77% and 0.66% for separation distances of 0.1, 0.25, 0.5, and 1 wavelengths, respectively. For four scatterers the respective differences are 1.9%, 1.24%, 0.77% and 0.67%. The L^∞ relative difference changes with separation distance are less marked. A separation distance of half or one wavelength actually results in a smaller difference than that of a single scatterer. There is a slight increase when the scatterers are separated by 0.1 wavelength. To illustrate: the same single rounded square has an L^∞ norm difference of 0.67%. Increasing the number of scatterers to two produces differences of 0.71%, 0.65%, 0.63% and 0.58% for separation distances of 0.1, 0.25, 0.5, and 1 wavelengths, respectively. For four scatterers the respective differences are 0.76%, 0.72%, 0.63% and 0.56%.

The effect of rounding diamonds with Neumann boundary condition is a little different than for squares. Similarly, the L^1 relative difference is greatest when the scatterers are close (0.1 λ separation) and reduces as the separation distance increases, however, unlike the square where the difference is negligible, once the separation is one wavelength, the relative difference increases in the case of diamonds. As an illustration: a single diamond, one wavelength in diameter, with radius of curvature $\rho = 0.02$ has L^1 relative difference of 0.76%. Increasing the number of scatterers to two produces differences of 1.54%, 1.02%, 0.75% and 1.04% for separation distances 0.1, 0.25, 0.5, and 1 wavelengths, respectively. For four scatterers the respective differences are 1.65%, 1.08%, 0.84% and 0.94%. The L^∞ relative difference exhibits the same behaviour. Using the same example, a single scatterer has L^∞ relative difference of 0.97%. Increasing the number of scatterers to two produces differences of 1.13%, 1.06%, 0.81% and 1.38% for separation distances 0.1, 0.25, 0.5, and 1 wavelengths, respectively. For four scatterers the respective differences are 1.53%, 1.03%, 0.73% and 1.39%. We also note that for two and four scatterer arrays the smallest relative differences in both norms occur at separation distance of half a wavelength regardless of scatterer diameter. In the case of the L^∞ norm, the relative difference is less than that of a single scatterer for two and four scatterer arrays separated

by a half wavelength - again, regardless of scatterer diameter.

Thus in the Neumann case, while there is some variation depending on the scatterer type, size and separation, the relative norm differences are of similar order. The largest differences were observed for squares separated by 0.1λ where the L^1 difference is two to three times that of a single rounded square with the same radius of curvature.

7.5.3 Impedance Loaded Boundary Condition

There is little variation in the L^1 relative difference for lemniscates with an impedance boundary condition. As in the Dirichlet case, for arrays of lemniscates of diameter one or two wavelengths, once separated by a single wavelength, the L^1 relative difference is less than that of a single scatterer. When the diameter is half a wavelength the difference is slightly larger. In all other cases the increase to the norm difference is approximately 10% or less. The L^1 relative difference for a single lemniscate, diameter one wavelength, with radius of curvature $\rho = 0.02$ is 1.23%. Increasing the number of scatterers to two produces differences of 1.24%, 1.43%, 1.34% and 1.09% for separation distances 0.1, 0.25, 0.5, and 1 wavelengths, respectively. For four scatterers the respective differences are 1.39%, 1.56%, 1.39% and 0.99%. Examining the L^∞ relative difference shows that for arrays smaller diameter lemniscates (diameter 0.25λ) there is a small increase when the scatterers are separated by a distance of 0.1 or 1 wavelengths but is less than that for a single lemniscate when the separation distance is 0.25 or 0.5 wavelengths. It is the reverse for arrays of lemniscates of one or two wavelengths diameter. In these cases, the relative L^∞ difference is higher than for a single lemniscate at separation distances 0.25 for 0.5 wavelengths and smaller for separation distances of 0.1 or 1 wavelengths. The L^∞ relative difference for the same lemniscate is 0.71%. Increasing the number of scatterers to two produces differences of 0.63%, 0.79%, 0.83% and 0.56% for separation distances 0.1, 0.25, 0.5, and 1 wavelengths, respectively. For four scatterers the respective differences are 0.65%, 0.86%, 0.85% and 0.43%. In summary, even though there is some variation to the relative norm differences when the number of scatterers increases, they are of the same order as that of a single lemniscate.

All impedance loaded squares and diamonds, exhibit the same behaviour in the L^∞ relative difference: it is higher than that of a single scatterer at separation distances 0.25

and 0.5 wavelengths and smaller for distances of 0.1 or 1 wavelength. The L^1 relative difference for smaller scatterers (diameter 0.25λ) behaves in the same fashion. For the larger diameter scatterers the L^1 relative difference for arrays is always higher than that of a single scatterer except when the separation distance is one wavelength where it is the same. It should be noted that these differences are small. Using a square of diameter one wavelength with radius of curvature $\rho = 0.02$ to illustrate, a single square has a relative L^1 difference of 1.08%. Increasing the number of scatterers to two produces differences of 1.15%, 1.41%, 1.18% and 1.06% for separation distances 0.1, 0.25, 0.5, and 1 wavelengths, respectively. For four scatterers the respective differences are 1.23%, 1.54%, 1.21% and 1.05%. The same scatterer has L^∞ difference of 0.56%. Increasing the number of scatterers to two produces differences of 0.53%, 0.72%, 0.56% and 0.51% for separation distances 0.1, 0.25, 0.5, and 1 wavelengths, respectively. For four scatterers the respective differences are 0.54%, 0.81%, 0.56% and 0.48%.

In general, for the impedance loaded case, the changes to the relative L^1 and L^∞ norm differences are small and remain of the same order as that for a single scatterer.

L^1	ρ	Single	2 Lemniscates				4 Lemniscates			
		Lemniscate	$d=0.1\lambda$	$d=0.25\lambda$	$d=0.5\lambda$	$d=\lambda$	$d=0.1\lambda$	$d=0.25\lambda$	$d=0.5\lambda$	$d=\lambda$
Dirichlet										
	0.05	4.00	3.00	3.91	4.27	3.44	2.94	4.29	4.40	3.04
	0.04	2.98	2.24	2.93	3.19	2.54	2.21	3.23	3.28	2.23
	0.03	2.04	1.54	2.02	2.18	1.73	1.52	2.23	2.25	1.50
	0.02	1.20	0.90	1.19	1.28	1.00	0.90	1.32	1.32	0.86
	0.01	0.48	0.36	0.48	0.51	0.40	0.37	0.54	0.53	0.34
Neumann										
	0.05	1.94	2.58	2.56	2.68	2.59	3.21	2.58	3.00	3.39
	0.04	1.33	1.78	1.77	1.99	1.86	2.24	1.78	2.20	2.45
	0.03	0.81	1.11	1.10	1.36	1.22	1.41	1.09	1.49	1.61
	0.02	0.40	0.56	0.56	0.80	0.67	0.73	0.55	0.86	0.90
	0.01	0.12	0.18	0.18	0.33	0.24	0.25	0.17	0.34	0.33
Impedance, $Z = 1 + i$										
	0.05	3.51	3.44	4.01	3.87	3.11	3.82	4.39	3.99	2.80
	0.04	2.71	2.67	3.11	2.97	2.39	2.98	3.40	3.07	2.16
	0.03	1.94	1.93	2.24	2.13	1.72	2.17	2.45	2.20	1.55
	0.02	1.23	1.24	1.43	1.34	1.09	1.39	1.56	1.39	0.99
	0.01	0.58	0.59	0.67	0.62	0.51	0.66	0.73	0.65	0.46
<hr/>										
L^∞										
Dirichlet										
	0.05	3.53	2.50	3.49	3.63	2.98	2.09	4.02	3.58	2.60
	0.04	2.64	1.85	2.66	2.69	2.20	1.55	3.07	2.65	1.89
	0.03	1.81	1.25	1.87	1.84	1.49	1.05	2.16	1.80	1.26
	0.02	1.07	0.73	1.13	1.07	0.87	0.61	1.30	1.05	0.71
	0.01	0.43	0.29	0.46	0.42	0.34	0.24	0.54	0.41	0.28
Neumann										
	0.05	1.55	2.15	2.17	1.49	2.99	2.68	2.38	1.72	4.24
	0.04	1.05	1.44	1.51	1.15	2.14	1.79	1.59	1.12	3.00
	0.03	0.64	0.86	0.94	0.81	1.38	1.06	0.96	0.65	1.91
	0.02	0.31	0.41	0.48	0.49	0.74	0.50	0.47	0.37	1.00
	0.01	0.09	0.13	0.16	0.20	0.26	0.14	0.14	0.16	0.33
Impedance, $Z = 1 + i$										
	0.05	2.04	1.68	2.21	2.40	1.58	1.68	2.40	2.48	1.22
	0.04	1.57	1.32	1.71	1.84	1.22	1.34	1.86	1.90	0.94
	0.03	1.13	0.97	1.24	1.31	0.87	1.00	1.35	1.36	0.68
	0.02	0.71	0.63	0.79	0.83	0.56	0.65	0.86	0.85	0.43
	0.01	0.33	0.30	0.37	0.38	0.26	0.32	0.41	0.39	0.21

Table 7.1: Relative L^1 (7.19) and L^∞ (7.20) norm differences (%), for lemniscates with interior angle $\beta = \pi/2$, diameter, $2a = \lambda$. Incidence angle $\theta_0 = 0$.

7.6 Far-field Differences

In this section we examine the quantity

$$\sqrt{k} \|u_0^\infty - u_\rho^\infty\|_\infty, \quad (7.21)$$

for the scatterer arrays described in Section 7.1, where u_0^∞ is the far-field of the cornered scatterers and u_ρ^∞ is the far-field of the rounded scatterers with radius of curvature ρ , as ρ approaches 0. As previously noted, the \sqrt{k} factor correctly non-dimensionalises the far-field quantities.

We particularly want to establish whether the following bounds established in Section 3.7 hold when the number of scatterers is increased. For scatterers with a Dirichlet boundary condition:

$$\sqrt{k} \|u_0^\infty - u_\rho^\infty\|_\infty \approx C(\theta_0)(k\rho)^m, \quad (7.22)$$

for some constant C dependent on the incident field angle θ_0 , where $m = 2/\nu$, $\nu = (2\pi - \beta)/\pi$ and β is the interior angle of the scatterer corners; for scatterer arrays with an impedance loaded boundary condition:

$$\sqrt{k} \|u_0^\infty - u_\rho^\infty\|_\infty \approx C(\theta_0)(k\rho)^m, \quad (7.23)$$

where $m = 1$, and for scatterer arrays with Neumann boundary condition:

$$\sqrt{k} \|u_0^\infty - u_\rho^\infty\|_\infty \leq C(\theta_0)(k\rho)^m, \quad (7.24)$$

where $m = 2/\nu$.

The same methodology described in Section 3.7 was followed. Data was collected for all the described cornered scatterer arrays (Section 7.1), for all three boundary conditions for various wave numbers ka using different incident angles, θ_0 . The same data was collected for their rounded counterparts, using many different radii of curvature. A least squares fit to the logarithms of the data was used for $k\rho \leq 0.25$ to determine the constants C and m . Complete results for all three boundary conditions and different incident angles θ_0 are available in Appendix F.2. Tables F.7 and F.8 contain the results for arrays of

two and four scatterers, respectively, with Dirichlet boundary condition; Tables F.9 and F.10 for the Neumann boundary condition; and Tables F.11 and F.12 for the impedance loaded cases.

An analysis of the results yields the following. For arrays of two and four scatterers with Dirichlet boundary condition,

$$\sqrt{k}\|u_0^\infty - u_\rho^\infty\|_\infty \approx C(\theta_0, d)(k\rho)^{2/\nu}, \quad (7.25)$$

for some constant C dependent on the incident field angle θ_0 and the separation distance d . We note that for very small interior corner angles ($\beta < \pi/18$) that the far-field difference tends to zero faster than $(k\rho)^{2/\nu}$, that is

$$\sqrt{k}\|u_0^\infty - u_\rho^\infty\|_\infty \leq C(\theta_0)(k\rho)^{2/\nu}. \quad (7.26)$$

For the same arrays but with Neumann boundary condition, we also have the same approximation

$$\sqrt{k}\|u_0^\infty - u_\rho^\infty\|_\infty \approx C(\theta_0, d)(k\rho)^{2/\nu}, \quad (7.27)$$

for some constant C dependent on the incident field angle θ_0 and the separation distance d , even for very small interior corner angles. This differs from the single scatterer results where the angle of the incident field, θ_0 , affected the rate that the far-field difference tended towards zero for the curvilinear scatterers. When the incident angle was incident to the corner, that is $\theta_0 = 0$, for single scatterers the far-field difference tended to zero much faster than $(k\rho)^{2/\nu}$: to the powers 1.7 to 1.9. This effect disappears when the number of scatterers is increased from one. We also note a slight slowing of the rate of convergence, from 1.33 to 1.28-1.30 for scatterer arrays of diamonds when the angle of incidence is $\pi/4$ and the separation distance is a half or one wavelength. This slowing is also apparent when the angle of incidence is $3\pi/8$ and in this case it is regardless of separation distance. This effect is more noticeable when the number of scatterers in the array is increased from two to four. Thus for scatterer arrays of diamonds when the angle of incidence increases, the rate that the far-field difference approaches zero as the radius of curvature approaches zero slows a little.

For the scatterer arrays with impedance loaded boundary condition,

$$\sqrt{k}\|u_0^\infty - u_\rho^\infty\|_\infty \approx C(\theta_0, d)(k\rho)^1, \quad (7.28)$$

for some constant C dependent on the incident field angle θ_0 and the separation distance d . We note that for arrays of squares the rate of convergence is slightly faster (up to 1.06) for $\pi/4 \leq \theta_0 \leq 3\pi/8$, and similarly for arrays of diamonds (up to 1.08) when $0 \leq \theta_0 \leq \pi/8$. The effect is more pronounced when the number of scatterers increases from two to four.

7.7 Conclusion

In this chapter we have explored the effect of rounding the corners of scatterers arranged in single arrays of two and four scatterers. The changes to the numerical methods described in Chapter 2 required to accommodate the effect of multiple scatterers were outlined. The results were validated using a variety of methods.

The main area of interest of this chapter lies in the strength of the coupling between the scatterers, that is, the degree to which scattering from a single scatterer is changed by the presence of other scatterers.

Firstly, we have demonstrated that the number of quadrature points required on each scatterer for a desired degree of accuracy is nearly the same, whether we are solving a single or multiple scatterer problem. The dependency is on the scatterer shape, not the geometry of the scatterer array. The accuracy of the solution for a given number of quadrature points varies by at most, one and occasionally two significant digits.

Secondly, we examined the relative differences of the far-field solutions produced by arrays of two and four scatterers using the L^1 and L^∞ norms. As in the case of single scatterers, the smaller the radius of curvature used for the rounding, the smaller the measured relative difference. Increasing the number of scatterers from one to two and then four, does not increase the relative norm differences by an equivalent ratio. The effect of rounding on arrays of scatterers is of a similar order as that of a single scatterer, and sometimes even less.

Thirdly, we showed that the bounds on the far-field differences $\sqrt{k}\|u_0^\infty - u_\rho^\infty\|_\infty$ es-

established in Section 3.7 for single scatterers can be applied to scatterer arrays. For arrays of scatterers with Dirichlet boundary condition, the approximation for single scatterers

$$\sqrt{k}\|u_0^\infty - u_\rho^\infty\|_\infty \approx C(\theta_0, d)(k\rho)^{2/\nu}, \quad (7.29)$$

holds, with the constant C now being dependent on the separation distance between the scatterers d as well as the incident field direction θ_0 , for all scatterers studied with the exception of those with very small interior angles ($\beta < \pi/18$), where the far-field difference tends to zero faster than $(k\rho)^{2/\nu}$. For arrays of scatterers with a Neumann boundary condition, the bound established for single scatterers now becomes an approximation,

$$\sqrt{k}\|u_0^\infty - u_\rho^\infty\|_\infty \approx C(\theta_0, d)(k\rho)^{2/\nu}, \quad (7.30)$$

where the constant is also dependent on the separation distance of the scatterers. In the single scatterer case, the angle of the incident field affected the rate of convergence for curvilinear scatterers. This phenomena disappears when working with scatterer arrays. It is noted that there is a slight slowing of the rate of convergence from 1.33 to 1.28-1.3, for arrays of diamonds as the incident field angle increases from $\pi/4$ onwards. For arrays of scatterers with the impedance loaded boundary condition the approximation for single scatterers

$$\sqrt{k}\|u_0^\infty - u_\rho^\infty\|_\infty \approx C(\theta_0, d)(k\rho)^1, \quad (7.31)$$

holds, again with the constant C now being dependent on the separation distance between the scatterers. There is a slight increase in the rate of convergence for arrays of squares and diamonds (up to 1.08) which is dependent on the angle of the incident field.

The classical coupling method combined with the Nyström scheme using graded mesh produces highly accurate solutions but is computationally demanding as the number of scatterers increases. For investigations into larger scatterer arrays, alternative methods for efficient solutions should be considered. In the following chapters we do so.

Chapter 8

TMATROM

In October 2017, Ganesh and Hawkins [27] released TMATROM - a Matlab object-oriented T-matrix software package. The package implements a numerically stable algorithm developed by Ganesh and Hawkins [103, 104, 118], to compute the T-matrix of a two-dimensional scatterer. The package is available for download [100] with full instructions for installation and use [102].

The T-matrix method for solving scattering problems was originally developed by Waterman for electromagnetic scattering by three dimensional scatterers [123] and then for acoustic scattering from two and three dimensional scatterers [124]. Waterman uses the Extended Boundary Condition Method (EBCM, or Near Field Method (NFM)) to compute the T-matrix

$$T = -(Rg)QQ^{-1}, \quad (8.1)$$

where the matrix Q expresses the null-field condition relating the incident and internal fields, whilst $(Rg)Q$ describes the formation of the scattered field from the internal field. The matrix elements of $(Rg)Q$ are calculated by surface integrals involving regular wave functions and Q using Hankel functions of the first kind integrated over the surface. Peterson and Ström [125] extended Waterman's method to the case of an arbitrary number of scatterers. The T-matrix method is used in various applications, such as electromagnetic and acoustic scattering. Waterman's approach, though widely used to calculate the T-matrix entries, is numerically unstable under certain conditions: for scatterers that are large compared with wavelength, or have extreme geometries with large aspect ratios [126–128]. The instabilities arise from the methods used to compute the T-matrix

entries using surface integrals. Strategies have been developed to mitigate this instability, such as the use of extended precision arithmetic [129, 130], and using the symmetries of the scatterer [131]. Petrov et al. [132] split the Q matrix into two halves to reduce computational time and improve accuracy. Other methods have been used to calculate the T-matrix: the Invariant Imbedding Method [133] and Point Matching Method [47, 134] are such examples. However, common to all these methods and variations, the T-matrix entries are computed using surface integrals and thus the resulting numerical instability.

Ganesh and Hawkins have developed a numerically stable algorithm [103, 104] for the calculation of the T-matrix entries which is based on a boundary integral method. Numerical stability has been achieved by using the far-field to compute the T-matrix entries rather than the near-field on the scatterer surface (the cause of the numerical instabilities). Initially this new method was used for three-dimensional electromagnetic scattering [135], then acoustic three-dimensional scattering [103] and two-dimensional acoustic scattering [136].

The reasons for using the TMATROM package are two-fold: to independently verify work done to date, but more importantly, to make use of computational efficiencies provided by the toolbox for larger multiple scattering problems.

In this chapter, we examine the TMATROM package, the advantages that its use provides as well as some constraints. We outline our implementation and conclude with a detailed verification of the results of earlier work. TMATROM was released publicly late 2017 and to the best of our knowledge we are the first adopter as is [137]. In the next chapter we employ TMATROM to solve larger array scattering problems.

8.1 The TMATROM Package

The TMATROM package uses a reduced order model (ROM) for modelling two-dimensional wave propagation of acoustic and electromagnetic waves based on the T-matrix. It provides off-line tools for computing the T-matrix of any two dimensional obstacle using any forward wave propagation solver [102]. The T-matrix is independent of incident and receiver directions.

TMATROM provides an efficient framework to use the resultant T-matrix to change the position and orientation of the scatterer as well as to assemble various types of

multi-scatterer architectures. Changes to the position or orientation of a scatterer use techniques based on the translation-addition theorem for Hankel functions [104, 138] to quickly calculate a new T-matrix from the original. The toolbox also allows for the incorporation of a user's own forward single-scatterer solver. All that is required is that the solver can compute the far-fields associated with incident circular waves [118]. Details required for coding user defined solvers are fully described in [102].

A Nyström solver for smooth scatterers with sound-soft, sound-hard or impedance loaded boundary conditions developed by Ganesh and Hawkins is included in the toolbox as well as an example showing the use of Barnett and Betcke's MPSPack [99] as the forward solver for polygonal shapes. MPSPack uses non-polynomial finite elements and the method of fundamental solutions. Also included in the package are the routines required to evaluate regular and radiating wave functions and routines implementing the translation-addition theorem which is required for multiple scatterer problems. A number of programmed examples are included: single, multiple, rotated and translated scattering problems using the Nyström solver for sound-soft, sound-hard and impedance loaded scatterers, and some scattering problems solved using MPSPack. Scatterer geometry examples include a circle, ellipse, pinched ball, trefoil, hexagon and sample code to enable implementation of any two-dimensional scatterer parameterised using polar coordinates.

8.2 Implementation of Single Scatterer Problems

TMATROM requires that the user have some proficiency in object-oriented programming - more so if the user is intending to incorporate other solvers and scatterers than those provided. The use of MPSPack also requires knowledge of object-oriented programming.

The first step is to download and test the software using the included examples. If the included MPSPack example is to be used, then the MPSPack software [98] will also need to be downloaded and tested. The user should be familiar with MPSPack and the details provided in the user guide [99].

The next step is to set up any scatterer geometries of interest that are not included in the TMATROM package. In our case, programming was required for the geometries for all of the scatterers considered in this chapter: lemniscates (2.2), rounded lemniscates (2.10) with interior angles $0 < \beta \leq \pi/2$, squares (2.6) and rounded squares (2.7), all with

both uniform and graded mesh.

The final step is to choose or implement the solver. The forward Nyström solver included with TMATROM is suitable for smooth-surfaced scatterers and uses a uniform mesh to discretise the surface. The included MPSPack interface (with some customisation) used in conjunction with MPSPack is suitable for piecewise-homogeneous scatterers, including polygons. We also implemented our own Nyström solver for scatterers with corners which treats the hypersingularity in the kernel of the Dirichlet problem using the methods described in Section 2.5.4 and allows for discretisation using a graded mesh.

8.2.1 Parameter Selection

In this section we discuss the process and decisions required to enable implementation of our scattering problems using TMATROM. For full details of the Ganesh-Hawkins algorithm for two-dimensional scatterers we refer the reader to [136] and implementation of the TMATROM package to [27]. Convergence results of the T-matrix are reported in [118].

The T-matrix is calculated for each scatterer geometry for a given wave number. It is independent of scatterer orientation or position. The dimension of the T-matrix is set by a parameter n which is the same parameter used for the truncation of the series expansion of the incident field in regular wave functions [27],

$$u^{\text{inc}}(r, \theta) = \sum_n f_n J_{|n|}(kr) e^{in\theta}, \quad (8.2)$$

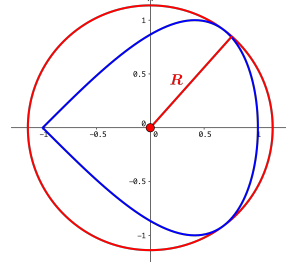


Figure 8.1

for expansion coefficients f_n . Ganesh and Hawkins equip the TMATROM package with an object which suggests an order, n . This calculation uses the Wiscombe formula [139] for Mie-type series truncation to determine the order. The result is determined by the wave number ka and the radius R of a circle centred at the centre of the scatterer. This radius is set such that the circle circumscribes the scatterer (Figure 8.1).

An infinite T-matrix satisfies the following symmetry relation:

$$T + T^* + 2TT^* = 0, \quad (8.3)$$

for scatterers with Dirichlet, Neumann, impedance (restricted to cases with a real impedance load factor Z) and transmission boundary conditions. This symmetry relationship also holds when the wave function series expansions are truncated to a finite order n , with a corresponding $(2n+1) \times (2n+1)$ T-matrix T_n . The TMATROM package reports the following quantity

$$\max_{l,m=-n,\dots,n} |(T_n + T_n^* + 2T_n T_n^*)_{l,m}|, \quad (8.4)$$

as a measure of the truncation error. This error is dependent on the solver used and the order n chosen for the series truncation. The smaller the truncation error, the more accurate the scattering solution. Note, a complex - not real - impedance load parameter Z has been used for all impedance experiments in this work. As such, a relatively large symmetry error is reported (order 10^{-2}) for those experiments. This is not a reflection of the accuracy of the solution produced by TMATROM, but rather the T-matrix truncation error reporting being not helpful in this instance and other measures of accuracy should be employed. For scatterers with a Dirichlet or Neumann boundary condition the truncation error (8.4) holds.

We have found that changes to the suggested order of the series truncation are required to reduce the size of the T-matrix error for the geometries of the scatterers in our project and to improve the accuracy of the results. The trade-off is of course computational efficiency as a larger order n generates a larger T-matrix. Figure 8.2 illustrates the effect on the T-matrix error that changes to the order of the series truncation elicit. The figures on the left show the effect of increasing the order of truncation has on the T-matrix error and the figures on the right show the resulting maximum far-field differences

$$\|u_0^\infty - u_{TM}^\infty\|_\infty = \max_{\hat{\mathbf{x}} \in [0, 2\pi]} |u_0^\infty(\hat{\mathbf{x}}) - u_{TM}^\infty(\hat{\mathbf{x}})| \quad (8.5)$$

where u_0^∞ is the far-field generated by our original code (Chapter 3) and u_{TM}^∞ that generated by TMATROM equipped with our cornered solver. The x -axis indicates the number added to the suggested order given by TMATROM. Thus $n^+ = 0$ indicates the suggested order, $n^+ = 5$ shows the result from adding 5 to the suggested order and so on. Figures 8.2a and 8.2b illustrate the effect of increasing the truncation order for a

lemniscate (2.2) for various wave numbers ka and figures 8.2c and 8.2d for a square (2.6), sides of length 2. For the lemniscate the TMATROM suggested orders ($n^+ = 0$) are 11, 16, 43, 75 for wave numbers $ka = \pi, 2\pi, 8\pi$ and 16π respectively. For the square they are 12, 32, 51 and 90 for the same wave numbers.

An analysis of our results shows that if the T-matrix error is $10^{-\bar{N}}$, for some \bar{N} , then the maximum error between the two far-fields, is $\sim 10^{-\bar{N}+1}$. We also measured the far-field differences using the L^2 norm $\|u_0^\infty - u_{TM}^\infty\|_2$. The differences between the two far-fields using this measure is $\sim 10^{-\bar{N}+2}$. The results show that for lower and mid-wave numbers, increasing the order by 10 more than suggested produces highly accurate results. For wave numbers greater than $ka = 8\pi$, increasing the suggested truncation order by 15 yields a further improvement in the accuracy of the results for those wave numbers. Based on our results, it was decided to run all further experiments in TMATROM for the geometries of interest with truncation order $n = (\text{suggested } n) + 10$, unless otherwise stated.

The Nyström solvers included with TMATROM discretise the surface of the scatterer to solve the integral equations associated with the scattering problem. If employed, consideration must also be given to the number of surface quadrature points required.

8.2.2 MPSPack

During the course of our experiments, we employed Barnett and Betcke's MPSPack as the forward solver for squares with Dirichlet and Neumann boundary conditions. MPSPack uses the method of fundamental solutions (a non-polynomial finite element method) to solve the scattering problem. The scatterer is enclosed by an artificial circular boundary, radius r . This circular domain is subdivided such that each corner of the polygon resides in a different sub-domain, though this is not strictly necessary (Figure 8.3). In each sub-domain the total field is approximated by a linear combination of Fourier-Bessel functions

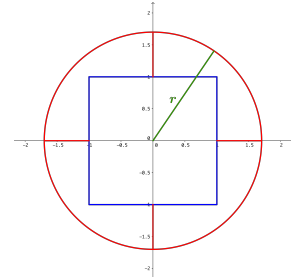


Figure 8.3

$$u^{\text{tot}}(r, \theta) = \sum_{j=1}^{N_i} c_j^{(i)} J_{ja_i}(kr) \sin ja_i \theta. \quad (8.6)$$

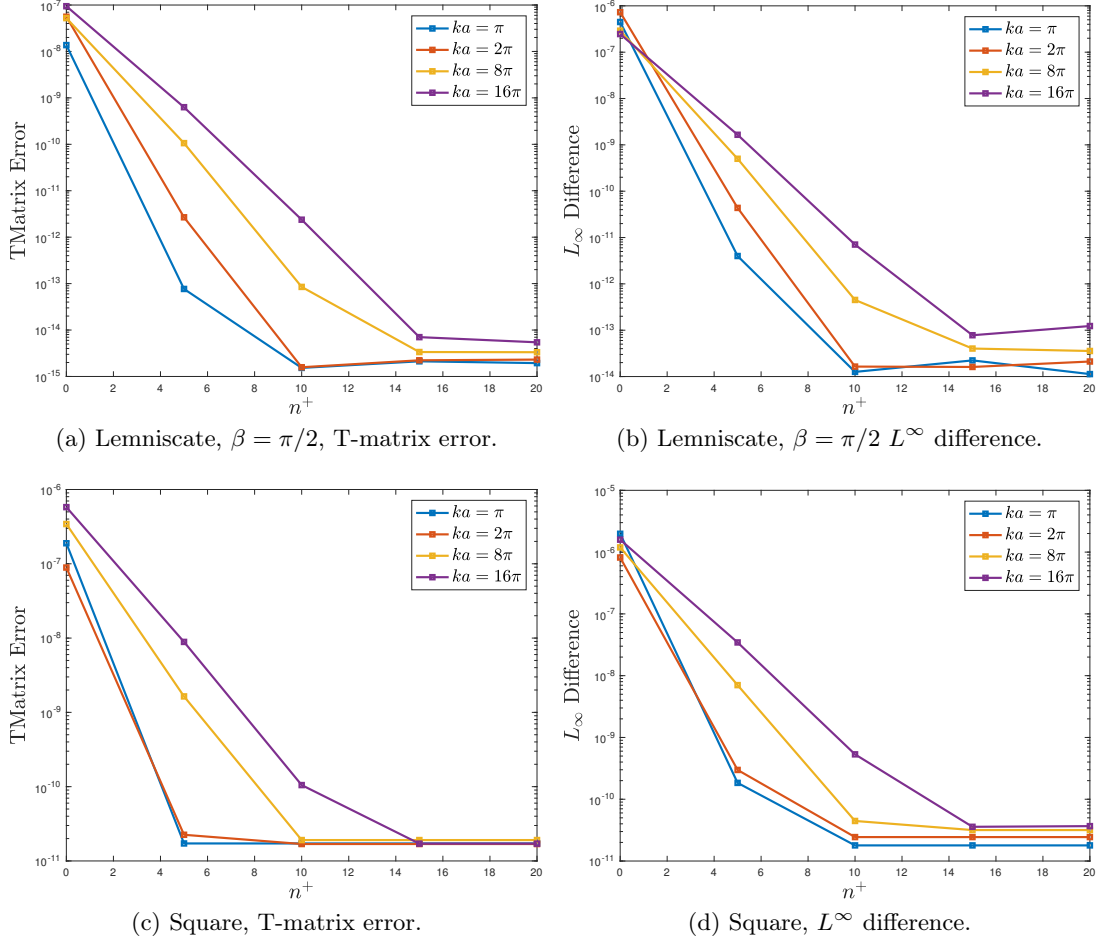


Figure 8.2: Illustrating the effect of increasing the order of series truncation in TMA-TROM equipped with our forward solver for cornered scatterers. The suggested order by TMA-TROM is shown at $n^+ = 0$, increasing by 5 is $n^+ = 5$ and so on. Figures on the left show effect on T-matrix error (8.4), and on the right the maximum difference between the far-field produced by TMA-TROM u_{TM}^∞ and that using our original code u_0^∞ (Chapter 3): $\|u_0^\infty - u_{TM}^\infty\|_\infty = \max_{\hat{\mathbf{x}} \in [0, 2\pi]} |u_0^\infty(\hat{\mathbf{x}}) - u_{TM}^\infty(\hat{\mathbf{x}})|$. Incident wave angle is $\theta_0 = 0$ for the lemniscate, $\theta_0 = \pi/4$ for the square. Both scatterers have a Dirichlet BC.

The choice of N determines the number of basis functions used for a desired solution accuracy. When employing MPSpack using TMA-TROM, two different circles are required. The first is the circle radius R described in the previous section used to calculate the T-matrix (Figure 8.1). The second is the circle radius r , for the circular domain required by MPSpack (Figure 8.3). The choice of radius R for the T-matrix circle is determined by the scatterer geometry and does not require any end-user decision - it just must encircle the scatterer exactly (Figure 8.1). However, the choice of radius r for the MPSpack domain has a significant effect on the convergence and accuracy of the solution.

As Barnett and Betcke discuss in [20]: “What is the optimal value of r ? If r is small,

then the singular corners of the square have a large relative distance to the neighbouring elements, suggesting a fast convergence on these elements. However, the rate of convergence for the Method of Fundamental Solutions (MFS) approximations will be slow since the radius r is close to the radius of the corners of the polygon. If r is large, then the MFS approximations converge fast but the relative distance of a singular corner to a neighbouring element is very small, leading to slow convergence on the finite elements.” They suggest that the optimal radius reached “when the asymptotic rate of convergence of the MFS is identical to the asymptotic rate of convergence on the finite elements.” In their paper, they present a theorem which estimates the rate of convergence. They include numerical results for a unit square ($2a = 1$) showing actual convergence compared to the estimated rate of convergence for different choices of radius r , and plot the asymptotic convergence factors from their theorem for different r . The optimal asymptotic rate is achieved when $r = 1.036$. Subsequently Barnett and Betcke use the optimal radius $r = 1$ for their experiments.

An optimal choice of r is required for each scatterer for which MPSPack is used as the forward solver. The square studied in this work has sides of length 2 ($2a = 2$). The L^2 boundary error (BE) norm is used as a measure of accuracy within MPSPack. The smaller the norm the more accurate the final scattering solution. Our results show that simply doubling the radius r when doubling the length of the side of the square does not provide an optimal radius. A number of values of r were tested ranging from 1.45 to 2 for varying wave numbers ka . Figure 8.4 illustrates the effect on the L^2 BE norm calculated by MPSPack as r varies from 1.45 to 2 for a square with sides length 2 with the Dirichlet or Neumann boundary conditions. The optimal r lies between 1.6 and 1.72. Table 8.1 shows the optimal radius for the various wave numbers ka for each boundary condition: $1.65 \leq r \leq 1.71$. Based on these results a value of $r = 1.68$ was chosen for all future experiments when using this geometry and MPSPack as the forward solver in TMAPROM.

In addition to choosing an optimum radius r for the domain external to the scatterer, the user must also choose the correct number of corner basis functions N (8.6) in each sub-domain. In their paper [20], for a square with sides of 1 unit length, Barnett and Betcke choose $N = 100$ and optimal radius $r = 1$ for their reporting. We tested $N = 80$,

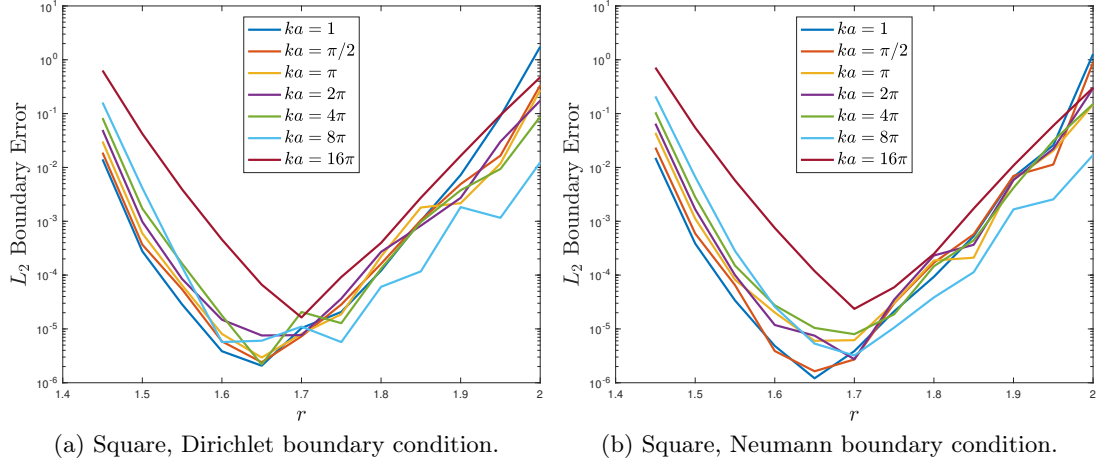


Figure 8.4: Showing the L^2 boundary error (BE) norm from MPSPack for different radii r and different wave numbers ka , for a square of side length 2 ($2a = 2$), for Dirichlet and Neumann boundary conditions with incident wave direction $\theta_0 = \pi/4$.

ka	Dirichlet		Neumann	
	r	L^2 BE norm	r	L^2 BE norm
1	1.66	1.90e-06	1.66	1.27e-06
$\pi/2$	1.65	2.40e-06	1.65	1.63e-06
π	1.66	1.92e-06	1.66	2.36e-06
2π	1.67	3.14e-06	1.7	2.74e-06
4π	1.67	2.10e-06	1.66	4.35e-06
8π	1.67	1.97e-06	1.7	3.21e-06
16π	1.7	1.63e-05	1.71	1.98e-05

Table 8.1: Showing the smallest L^2 boundary error (BE) norm from MPSPack and the corresponding radius r , for a square of side length 2 ($2a = 2$), for Dirichlet and Neumann boundary conditions with incident wave direction $\theta_0 = \pi/4$.

100, 120 and $N = 150$ for the unit square using the same optimal radius for both Dirichlet and Neumann boundary conditions with wave number $ka = 2\pi$. The L^2 BE norms were $3\text{e-}12$, $2\text{e-}12$, $3\text{e-}12$ and $2\text{e-}11$ respectively in the Dirichlet case, and $5\text{e-}12$, $2\text{e-}12$, $2\text{e-}12$ and $2\text{e-}11$ in the Neumann case, for an incident field angle $\theta_0 = \pi/4$, demonstrating that, in this case, an increase to the number of corner basis functions does not correlate to an increase in accuracy and may even result in a decrease. However, increasing the number of basis functions does increase the processing time. As an example, for the Neumann case the respective processing times are 0.87, 0.99, 1.11 and 1.32 seconds.

We next tested the square of side length 2 ($2a = 2$) as this is the scatterer of interest. The domain radius was set to $r = 1.68$ for all wave numbers ka except for $ka = 16\pi$ where a domain radius of $r = 1.71$ was used. Figure 8.5 illustrates the effect of changing the

basis functions. In the Dirichlet case, $N = 80$ gives the best results: $10\text{e-}06$ - $10\text{e-}07$ for wave numbers other than 16π where $N = 110$ yields an optimal result. In the Neumann case, $N = 70$ or 80 yields similar results for wave numbers less than 8π , $N = 90$ is best for $ka = 8\pi$ and $N = 110$ for $ka = 16\pi$.

For quadrature Barnett and Betcke use the Clenshaw-Curtis rule [140], and have chosen the number of points M to be high enough that further increases have a negligible effect on the accuracy of the solution. This number is usually a small multiple of the number of basis functions, N . In their published results they used $M = 200$. Testing a Dirichlet square with sides length 2, using a domain radius $r = 1.71$ and number of basis functions $N = 110$ for wave number $ka = 16\pi$, yielded an L^2 BE norms of $9.6\text{e-}07, 9.6\text{e-}07$ and $1.2\text{e-}06$ for quadrature points $M = 100, 200$ and 400 , respectively with corresponding processing times for calculating the coefficients of 0.97, 2.1 and 4.4 seconds. Again, demonstrating that increasing the number of quadrature points does not necessarily produce an increase in the solution accuracy.

All the above experiments were run using MPSPack independent of TMAPROM to determine the best parameters to use when using MPSPack as the forward solver in TMAPROM.

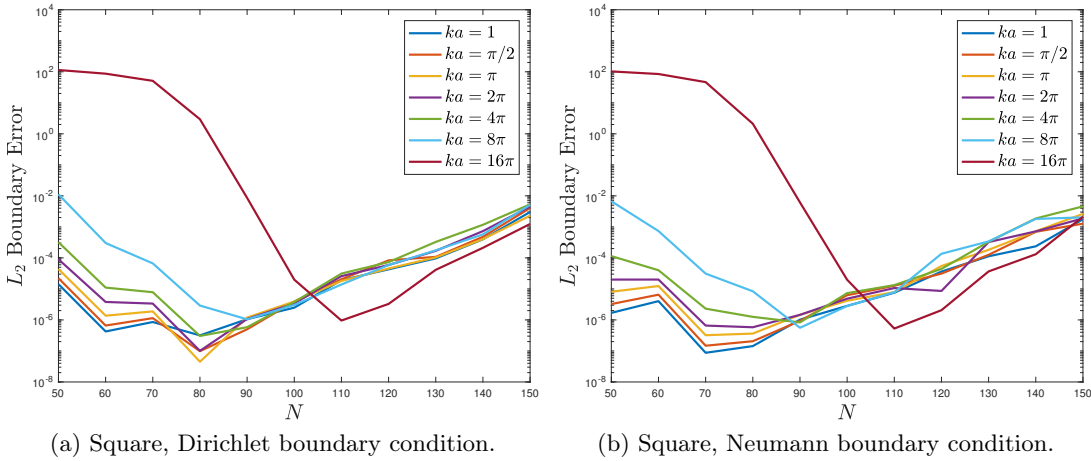


Figure 8.5: Showing the L^2 boundary error (BE) norm from MPSPack for different numbers of corner basis functions, N , and different wave numbers ka , for a square of side length 2 ($2a = 2$), for Dirichlet and Neumann boundary conditions with incident wave direction $\theta_0 = \pi/4$.

8.3 Verification of Our Single Scatterer Results

As discussed in Section 3.1, there is no analytical expression for the scattered field from a non-circular scatterer and as such, there is no true solution to which we can compare results. We reported on the methods used to verify our results: significant digit measurement, comparison to published data and approximating the far-field from the near scattered field. Another avenue for verification is to set up our scatterer problems in available packages, such as MPSPack [99]. This requires a not always insubstantial investment of time to learn the package and understand any limitations and induced numerical errors. However, with the release of TMatrom and the possible computational gains to be made by using TMatrom for larger scatterer array problems, it was decided to implement TMatrom for our scatterers and incorporate our cornered forward solver into the package. An added benefit is the ability to verify our results independently. In this section we present our verification results. All results presented are for the far-field. Similar results were obtained for the near-field.

Unless stated otherwise, all experiments in this section were run using the recommended parameters from the preceding sections. Thus the series truncation order in TMatrom, n , was increased by 10. When using MPSPack as the forward solver for squares, the artificial domain boundary radius was set to $r = 1.68$, the number of corner basis functions was set to $N = 80$ and the number of quadrature points $M = 160$, that is $2N$. All rates of convergence and significant digits in agreement for the far-field reported in this chapter are measured in the back-scatter region, unless stated otherwise.

We began by testing rounded lemniscates (2.10) for various interior angles, $0 < \beta \leq \pi/2$, and rounded squares (2.7) with different radii of curvature, ρ , as well as cornered lemniscates (2.2) and squares (2.6) in TMatrom using the included Nyström solver. The included solver is for smooth scatterers and employs a uniform mesh $t_j = \pi j/n$, for $j = 0, 1, \dots, 2n - 1$, in the parameterisation (2.1) of the scatterer. As such, the results should be the same as our earlier results (Section 3.3) when using a uniform mesh. All three boundary conditions were tested for a variety of wave numbers, ka and incident field directions θ_0 . For the rounded scatterers we tested radii of curvature $\rho = 0.1, 0.09, \dots, 0.01, 0.005, 0.0025, 0.00125$ in the corners. The results for the scatterers with corners, as expected, exhibit non-convergence when using a uniform mesh. Figures 8.6a, 8.6d and

8.6g illustrate some typical results and Figures 8.6b, 8.6e and 8.6h illustrate the results of the same experiments using our original code (Chapter 3). It is clear that the same results are achieved, thus verifying our earlier results and code for smooth scatterers with uniform mesh. We then re-ran the same experiments in TMATROM, this time using our cornered solver and a graded mesh. The results are presented in Figures 8.6c, 8.6f and 8.6i and exhibit the same dramatic improvement in the rate of convergence for the rounded scatterers and, of course, for the cornered ones as our original code when employing a graded mesh (Figures 3.4 and 3.5).

We next compared the far-field produced using TMATROM equipped with our cornered solver and the far-field generated by our original code for cornered structures using graded mesh. All three boundary conditions were tested for different incident fields, θ_0 . For the single scatterer problem, we tested wave numbers $ka = \pi/2, \pi, 2\pi, 4\pi, 8\pi$ and 16π . The difference between the solution produced by our original code, $u_0^\infty(\hat{\mathbf{x}})$ for $\hat{\mathbf{x}} \in [0, 2\pi]$, and that produced by TMATROM equipped with our cornered solver $u_{TM}^\infty(\hat{\mathbf{x}})$, is measured using the L^2 norm

$$\|u_0^\infty - u_{TM}^\infty\|_2 = \left(\int_0^{2\pi} |u_0^\infty(\hat{\mathbf{x}}) - u_{TM}^\infty(\hat{\mathbf{x}})|^2 d\hat{\mathbf{x}} \right)^{\frac{1}{2}}, \quad (8.7)$$

and L^∞ norm

$$\|u_0^\infty - u_{TM}^\infty\|_\infty = \max_{\hat{\mathbf{x}} \in [0, 2\pi]} |u_0^\infty(\hat{\mathbf{x}}) - u_{TM}^\infty(\hat{\mathbf{x}})|. \quad (8.8)$$

Detailed results are provided in Appendix G. Tables G.1, G.2 and G.3 show the results for the Dirichlet, Neumann and impedance loaded boundary conditions, respectively, for the different single scatterers studied in Chapter 3, for different wave numbers ka and some incidence field angles, θ_0 . The results are similar for other incident field angles. Shown are the T-matrix errors and the far-field differences measured using the L^2 and L^∞ norms. In all cases the order of the far-field differences is of the same order or better than the T-matrix error. For example, a lemniscate with interior angle $\beta = \pi/2$ and Neumann boundary condition illuminated by an incident wave with wave number π has a T-matrix error of 7.98e-10 and the differences in the far-fields is 7.31e-15 using the L^2 norm and 1.01e-14 using the L^∞ norm. Increasing the wave number to 16π gives T-matrix error 7.98e-09 and far-field differences of 1.33e-10 and 9.55e-11, respectively. As discussed

in Section 8.2.1, the T-matrix error cannot be used as a predictor of accuracy for the impedance loaded cases as we are using an imaginary impedance loading Z . However, the measured differences in the far-fields show a high degree of agreement to our original code. For all boundary conditions and all scenarios tested the results show agreement to our original work of order 10^{-10} to 10^{-15} , which validates our results.

These results show that the implementation of our cornered forward solver in TMA-TROM produces the same results as when using our original code. To further verify our work, we proceeded to use MPSPack as the solver in TMA-TROM. This independently verifies our results for the square, and since our code for the square scattering problem is the same as that for our other scatterers, we are in effect verifying our cornered solver. Tables G.1 and G.2 show these results for square with a Dirichlet or Neumann boundary condition, respectively, for incident field angles $\theta_0 = 0$ and $\theta_0 = \pi/4$. We show the results for the number of corner basis functions $N = 80$ and $N = 100$ in MPSPack as $N = 80$ produces better results for the lower frequencies (scatterer less than 8λ in diameter) and $N = 100$ for the higher frequencies (scatterers 8λ in diameter or larger). The MPSPack results show agreement to our original work of order 10^{-9} to 10^{-12} , which again validates our results. We note that the T-matrix error when using our cornered forward solver is of similar order or better than when using MPSPack. Because of this and the need to use different parameters in MPSPack for different test conditions, we used our own cornered solver in TMA-TROM for all future work.

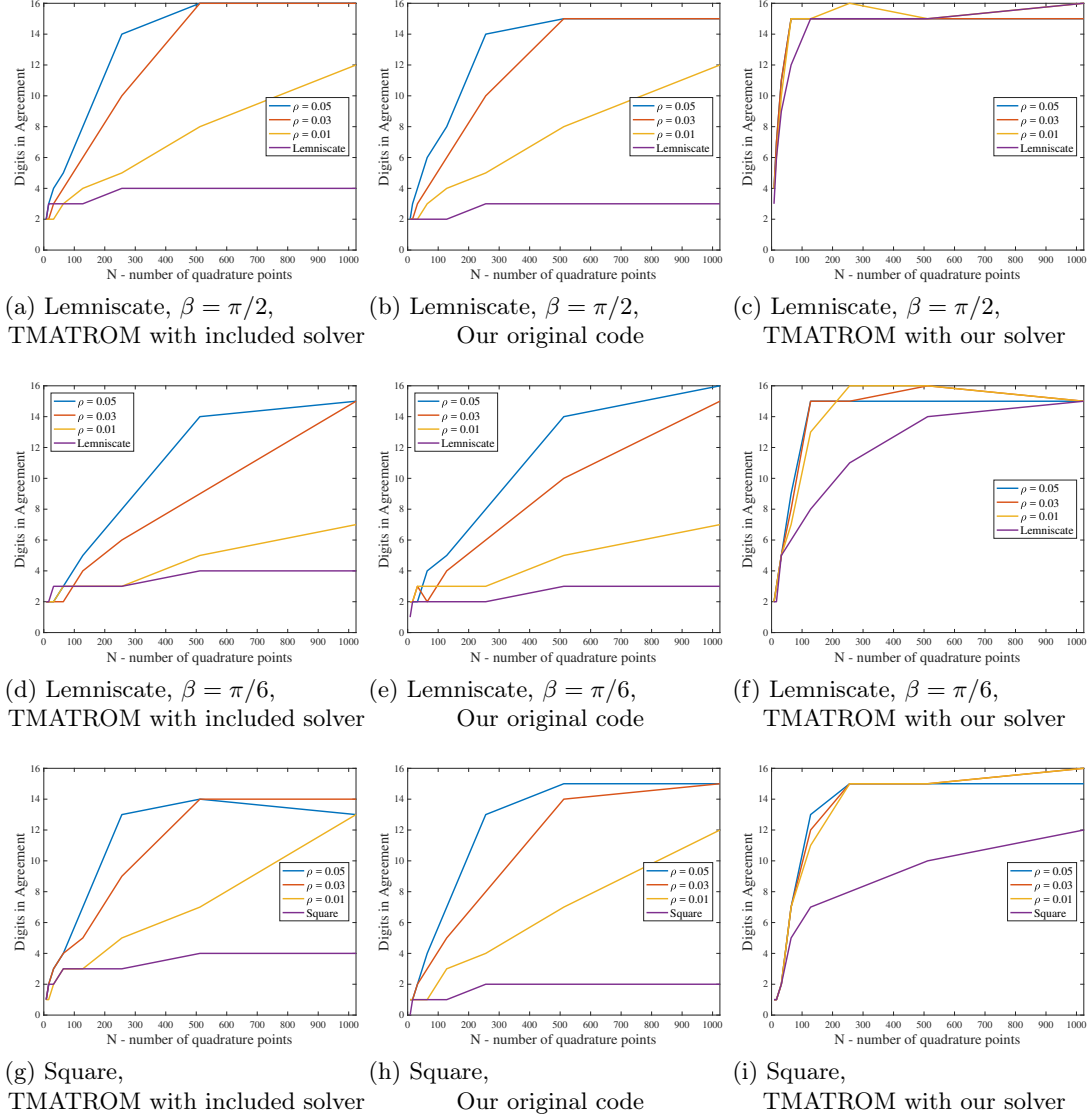


Figure 8.6: Significant digits in agreement of the far-field. The leftmost column shows the rate of convergence (3.8) using the TMATROM provided Nyström solver which employs an equispaced mesh. The centre column shows the rate of convergence using our original code with the same equispaced mesh. The rightmost column shows the rate of convergence using TMATROM equipped with our cornered solver which employs a graded mesh. All scatterers have a Dirichlet boundary condition. Incidence angle is $\theta_0 = 0$ for the lemniscates, $\theta_0 = \pi/4$ for the square. Wave numbers $ka = \pi/2$ for the lemniscate with interior angle $\beta = \pi/2$, $ka = \pi$ for the lemniscate with interior angle $\beta = \pi/6$ and $ka = \pi/2$ for the square.

8.4 Multiple Scatterer Configurations

As described in Section 7.2, the scattered field for a multiple scatterer problem is calculated by summing the scattered field from each of the scatterers:

$$u^{\text{sc}}(\mathbf{x}) = \sum_{i=1}^n u_i^{\text{sc}}(\mathbf{x}), \quad (8.9)$$

where u_i^{sc} is the scattered field from scatterer i and \mathbf{x} is a point exterior to any of the scatterers. The scattered field for each scatterer is calculated from the T-matrix for that scatterer multiplied by the incident field, represented as radiating wave function expansions, on the scatterer. The incident field on each scatterer consists of the sum of the incident wave and the scattered field generated by the other scatterers in the arrangement:

$$u^{\text{inc}}(\mathbf{x}) + \sum_{\substack{j=1 \\ j \neq i}}^n u_j^{\text{sc}}(\mathbf{x}). \quad (8.10)$$

This creates a linear system of scattered fields for each scatterer which require to be solved. TMATROM employs Matlab's Generalised Minimum Residual Method (GMRES) to solve this problem iteratively. There are two variables used by GMRES that are set by TMATROM: the tolerance of the method, set at 1e-08, and the number of iterations that re-starts the method. This calculation is determined by the number of scatterers and the series truncation parameter, n . In the majority of multiple scatterer configurations the parameters determined by TMATROM provide very accurate solutions and require no adjustment by the end user.

The multiple scatterer problem takes advantage of the T-matrix approach and its implementation in TMATROM. The T-matrix for each different scatterer used in a configuration is only required to be calculated and stored once. Changes to the scatterer position and orientation use techniques based on the translation-addition theorem [138] to quickly re-calculate a new T-matrix based on the original [104]. The implementation of the translation-addition theorem introduces an error in the far-field at least of the order 10^{-8} [104].

In addition to computational time savings, there are significant memory savings when using the T-matrix method for a multiple scatterer problem versus the traditional ap-

proach used in Chapter 7. The T-matrix is constructed using the far-field calculated by either an included forward solver or that of the end-user. If the forward solver uses a Nyström method the size of the system to be solved to enable calculation of the far-field is determined by the number of quadrature points used to discretise the surface of the scatterer. The T-matrix calculated from this far-field is significantly smaller. To illustrate: using 512 quadrature points to discretise the surface of a lemniscate with Dirichlet boundary condition and incident wave number $ka = 2\pi$ requires a 512x512 system to be solved by the forward solver. The T-matrix is then calculated and is only size 63x63. Increasing the number of scatterers to 2 requires a 1024x1024 system to be solved using the traditional approach. However, when employing TROM for the same problem, the original 512x512 problem is used in the forward solver resulting in a T-matrix of order 63. The T-matrix for the additional scatterer is calculated from this one and the size of the linear system to be solved by TROM (8.10) is only 126x126. Increasing the number of scatterers to 4, requires solving a 2048x2048 system when using the traditional method. By contrast, TROM required the original 512x512 problem to be solved and then the linear system to be solved by TROM increases to 252x252. This efficiency allows for much larger array problems to be solved than when using the classical method employed in Chapter 7.

However, TROM is not suitable for all scatterer array configurations. Comparison of the far-field results from TROM to those produced using the traditional approach used in Chapter 7 showed larger differences than expected when the scatterers are separated by small distances. Some difference was expected attributable to the use of the translation-addition theorem for multiple scatterer problems by TROM but the differences were significantly larger.

We found the impact of the separation distance on the accuracy of the far-field results produced using the TROM package is similar regardless of boundary condition or the number of scatterers in the array. To illustrate, we will use a two-diamond array with Dirichlet boundary condition and incident wave angle, $\theta_0 = 0$. We note the far-field differences are of approximately the same order, whether measured using the L^2 or L^∞ norms and use the L^2 norm in the examples listed in Table 8.2. As can be seen, these early experiments achieved low orders of agreement: varying from 10^{-3} up to 10^{-5} .

Advice was sought from the package authors, and a number of suggestions were made. Firstly, to verify the T-matrix quality using the T-matrix error. Secondly, to consider increasing the truncation order from that suggested. And, finally, to consider increasing the number of GMRES iterations. These suggestions were applied and we now illustrate the effect on the differences between the far-fields implementing these suggestions made. We continue to use the array of two diamonds with Dirichlet boundary condition for this example, but the effect on the results of implementing these strategies was the same for all the scatterer configurations considered.

	N=100					N=500				
	T-mat Err	d 0.1 λ	0.25 λ	0.5 λ	λ	T-mat Err	d 0.1 λ	0.25 λ	0.5 λ	λ
$2a$										
0.5 λ	1.7e-05	2e-04	2e-04	1e-04	5e-05	1.6e-08	2e-04	1e-04	3e-05	1e-06
λ	1.4e-05	1e-03	1e-03	2e-04	6e-05	1.9e-07	1e-03	1e-03	2e-04	4e-06
2 λ	1.3e-05	2e-03	2e-03	4e-04	6e-05	8.9e-08	2e-03	2e-03	4e-04	2e-06

Table 8.2: Showing the effect of increasing the number of quadrature points N on the surface of the scatterer on the T-matrix error (8.4), and the difference in the far-fields produced using TMATROM equipped with our Nyström corner solver and that produced by our original MATLAB programs for an array of two diamonds of diameter $2a$ with different separation distances d . The difference in the far-fields is measured using the L^2 norm (8.7). The scatterers have Dirichlet boundary condition and the incident wave direction is $\theta_0 = 0$.

When using a Nyström scheme, the T-matrix error is affected by the number of quadrature points chosen to discretise the surface of the scatterer, N , and the series truncation order, n . Table 8.2, shows the improvement in the T-matrix error that increasing the number of quadrature points on the scatterer from $N = 100$ to $N = 500$. The T-matrix error improves from order $\sim 10^{-5}$ to $\sim 10^{-8}$, but there is almost no change to the far-field differences measured using the L^2 norm.

Table 8.3 shows the further improvement to the T-matrix error that increasing the series truncation order from that suggested by TMATROM by 5 and 10. Increasing the order by 5 improves both the T-matrix error and the order of the far-field differences. Increasing the order by another 5, that is by 10, produces no change in the T-matrix error but further improves the far-field difference order in most cases. This is because the series truncation order is also used to calculate the suggested number of iterations for the GMRES function. We next increased the number of quadrature points to $N = 1000$

on the surface of the scatterer. Table 8.4 shows the combined results of increasing the quadrature points and the series truncation order. This improves the T-matrix error to $\sim 10^{-11}$ and shows some improvement to the far-field differences for separation distance of $d = \lambda$.

Sug. Order +5, N=500						Sug. Order +10, N=500					
d						d					
T-mat	Err	0.1 λ	0.25 λ	0.5 λ	λ	T-mat	Err	0.1 λ	0.25 λ	0.5 λ	λ
$2a$											
0.5 λ	1.3e-09	3e-05	4e-06	6e-08	5e-09	1.3e-09	3e-04	4e-06	9e-09	5e-09	
λ	1.1e-09	3e-04	1e-04	4e-06	1e-08	1.1e-09	6e-05	1e-05	1e-07	1e-08	
2 λ	9.9e-10	8e-04	5e-04	4e-05	3e-08	9.9e-10	3e-04	1e-04	6e-06	5e-09	

Table 8.3: Showing the effect of increasing the series truncation order n on the T-matrix error (8.4), and the difference in the far-fields produced using TMATROM equipped with our Nyström corner solver and that produced by our original MATLAB programs for an array of two diamonds of diameter $2a$ with different separation distances d . The difference in the far-fields is measured using the L^2 norm (8.7). The scatterers have Dirichlet boundary condition, the number of quadrature points on each scatterer is $N = 500$ and the incident wave direction is $\theta_0 = 0$.

Sug. Order +5, N=1000						Sug. Order +10, N=1000					
d						d					
T-mat	Err	0.1 λ	0.25 λ	0.5 λ	λ	T-mat	Err	0.1 λ	0.25 λ	0.5 λ	λ
$2a$											
0.5 λ	3.1e-11	3e-05	4e-06	6e-08	5e-11	3.1e-11	9e-05	2e-06	9e-09	6e-11	
λ	2.6e-11	3e-04	1e-04	4e-06	1e-08	2.6e-11	6e-05	1e-05	1e-07	1e-08	
2 λ	2.3e-11	8e-04	5e-04	4e-05	3e-08	2.3e-11	3e-04	1e-04	6e-06	8e-10	

Table 8.4: Showing the effect of increasing the series truncation order n when the number of quadrature points is increased to $N = 1000$ on the T-matrix error (8.4), and the difference in the far-fields produced using TMATROM equipped with our Nyström corner solver and that produced by our original MATLAB programs for an array of two diamonds of diameter $2a$ with different separation distances d . The difference in the far-fields is measured using the L^2 norm (8.7). The scatterers have Dirichlet boundary condition and the incident wave direction is $\theta_0 = 0$.

The final suggestion was to increase the number of GMRES iterations. Table 8.5 shows the effect on the different two scatterer arrays when all three suggestions are implemented: increasing the number of GMRES iterations from that suggested by TMA-TROM by 10, using discretisation $N = 1000$ and increasing the order series truncation by 10. The final strategy was to increase the number of GMRES iterations to the maximum. This is pre-determined by GMRES based on the size of the matrices to be solved. There was no change to the far-field differences in the case of lemniscates or diamonds but there was some improvement for the array of squares. Thus increasing the number

quadrature points N and the series truncation order n , produced the best results for arrays of lemniscates and diamonds. For arrays of squares, we also recommend increasing the number of GMRES iteration to the maximum.

	Iter+10				Max iter			
	d				d			
	0.1λ	0.25λ	0.5λ	λ	0.1λ	0.25λ	0.5λ	λ
Diamonds								
$2a$								
0.5λ	9e-05	2e-06	9e-09	6e-11	9e-05	2e-06	9e-09	6e-11
λ	6e-05	1e-05	1e-07	1e-08	6e-05	1e-05	1e-07	1e-08
2λ	3e-04	1e-04	6e-06	8e-10	3e-04	1e-04	6e-06	8e-10
Squares								
$2a$								
0.5λ	4e+00	2e-04	6e-08	2e-10	8e-01	6e-04	5e-08	6e-11
λ	7e-02	3e-02	6e-05	2e-10	7e-02	3e-02	6e-05	1e-10
2λ	2e-01	3e-01	2e-01	6e-06	2e-01	3e-01	2e-01	6e-06
Lemniscates								
$2a$								
0.5λ	3e-05	1e-06	5e-09	1e-08	3e-05	1e-06	5e-09	1e-08
λ	5e-05	1e-06	5e-08	2e-09	5e-05	1e-06	5e-08	2e-09
2λ	2e-05	5e-07	2e-08	2e-09	2e-05	5e-07	2e-08	2e-09

Table 8.5: Showing the effect of increasing the number of GMRES iterations from that suggested by TMatrom on the difference in the far-fields produced using TMatrom equipped with our Nyström corner solver and that produced by our original MATLAB programs for an array of two scatterers of diameter $2a$ with different separation distances d . The difference in the far-fields is measured using the L^2 norm (8.7). The scatterers have Dirichlet boundary condition and the incident wave direction is $\theta_0 = 0$.

Having implemented the above strategies, we compared all the results produced by our original code for scatterer arrays (Chapter 7) to the far-field produced using TMatrom equipped with our cornered solver. Unless stated otherwise, all experiments in this section were run using the recommended parameters from the preceding sections. To summarise: the series truncation order in TMatrom, n , was increased by 10. When using MPSpack as the forward solver for squares and diamonds, the artificial domain boundary radius was set to $r = 1.68$, the number of corner basis functions was set to $N = 80$ and the number of quadrature points $M = 160$, that is $2N$. For arrays of squares we also set the GMRES iterations to the maximum for the size of the system to be solved.

All three boundary conditions were tested for different incident fields, θ_0 . We compared scatterers of diameter $2a = 0.5\lambda$, λ and 2λ separated by distances $d = 0.1\lambda$, 0.25λ , 0.5λ and λ . The far-field difference results for arrays of two and four scatterers are in Tables G.4 to G.9 in Appendix G. The results were consistent for the different boundary

conditions. For the lemniscates, when the separation distance $d = 0.1\lambda$ the differences in the two far-fields is order 10^{-5} . Increasing the distances to $0.25\lambda, 0.5\lambda$ and λ decreases the differences to order $\sim 10^{-6}, 10^{-8}, 10^{-9}$, respectively. The array of diamonds exhibit similar trends albeit with a degree or two less accuracy. The far-field differences of the array of squares also exhibit the same behaviour but with very low order of agreement ($\sim 10^{-1}$) for separation distances less than half the diameter of the scatterer. These results are the best that were able to be achieved.

The differences for small separation distances were larger than anticipated, especially so in the case of the squares. The outstanding question is why? We first checked that in the case of the squares (and diamonds) that these differences are not caused by the implementation of our solver within TMATROM. Thus we re-ran the same experiments using MPSpack as the forward solver. The far-field differences were of the same order as when using our solver. These results are available in Tables G.4 and G.7. We then tested convergence using the significant measurement technique outlined in Section 3.1. Figure 8.7 illustrates the convergence of some of the examples from Table 8.5 using TMATROM equipped with our cornered solver. Figure 8.8 illustrates the convergence of the same examples using our original multi-scatterer code. These two figures clearly demonstrate the effect of scatterer separation distance d on the on the accuracy of the solution when using TMATROM and the independence of the traditional method on separation distance.

We concluded by considering the effect of the encapsulating circle required for the calculation of the T-matrix on the far-field differences for multiple scatterers. If these circles overlap, but do not cross into the space occupied by another scatterer (Figure 8.9) there is no impact on the accuracy of the solution produced by TMATROM. By fixing the scatterer width at $2a = 2$ units, the circumscribing circle has radius ~ 1.373 units for the lemniscate and $\sqrt{2}$ units for the squares and diamonds. If overlapping circles affected the results it would impose a minimum distance between lemniscates of ~ 0.275 units, ~ 0.828 units for the squares and 0 units for diamonds. Table 8.6 shows for

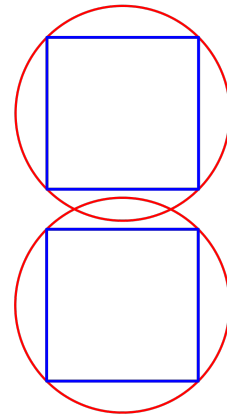


Figure 8.9

each scatterer width, expressed in terms of wavelength, the number of units that the separation distance equals. Highlighted in blue and red are the configurations where the circumscribing circles overlap. If we consider the lemniscate arrays and the diamond arrays, we would expect the diamond arrays to produce highly accurate results regardless of separation distance and the lemniscates results to be affected when the circles overlap. Our results show that this is not the case indicating the overlapping circles are not the cause since both the lemniscate and diamond arrays are affected in the same manner by separation distance. Once the separation distance is less than half the scatterer diameter, the difference in the far-fields is more marked and is below order 10^{-8} attributable to the translation-addition effect.

Lemniscate					Square					Diamond							
$2a$	d	0.1λ	0.25λ	0.5λ	λ	$2a$	d	0.1λ	0.25λ	0.5λ	λ	$2a$	d	0.1λ	0.25λ	0.5λ	λ
0.5λ	0.4	1	2	4	0.5λ	0.4	1	2	4	0.5λ	0.4	1	2	4			
λ	0.2	0.5	1	2	λ	0.2	0.5	1	2	λ	0.2	0.5	1	2			
2λ	0.1	0.25	0.5	1	2λ	0.1	0.25	0.5	1	2λ	0.1	0.25	0.5	1			

Table 8.6: Showing the distance between the scatterers expressed in units if the scatterer width $2a$ is set to 2. Highlighted in blue are the configurations for which the T-matrix encapsulating circles overlap. Highlighted in red are the configurations where the encapsulating circle not only overlaps but crosses into the space occupied by the adjoining scatterer.

We note that the arrays of square scatterers show very low agreement to our original results in some cases. If the distance between the scatterers is less than ~ 0.42 units, then the encapsulating circle crosses into the space occupied by the adjoining square, highlighted in red in Table 8.6. It is in these cases that TMatROM is unable to produce a solution better than order 10^{-1} . This limitation is unavoidable due to the formulation of scattering used by TMatROM.

Subject to these limitations, we have been able to verify our solutions to the multiple scatterer problems studied in Chapter 7, to within the error bound introduced by the use of the translation-addition theorem (10^{-8}).

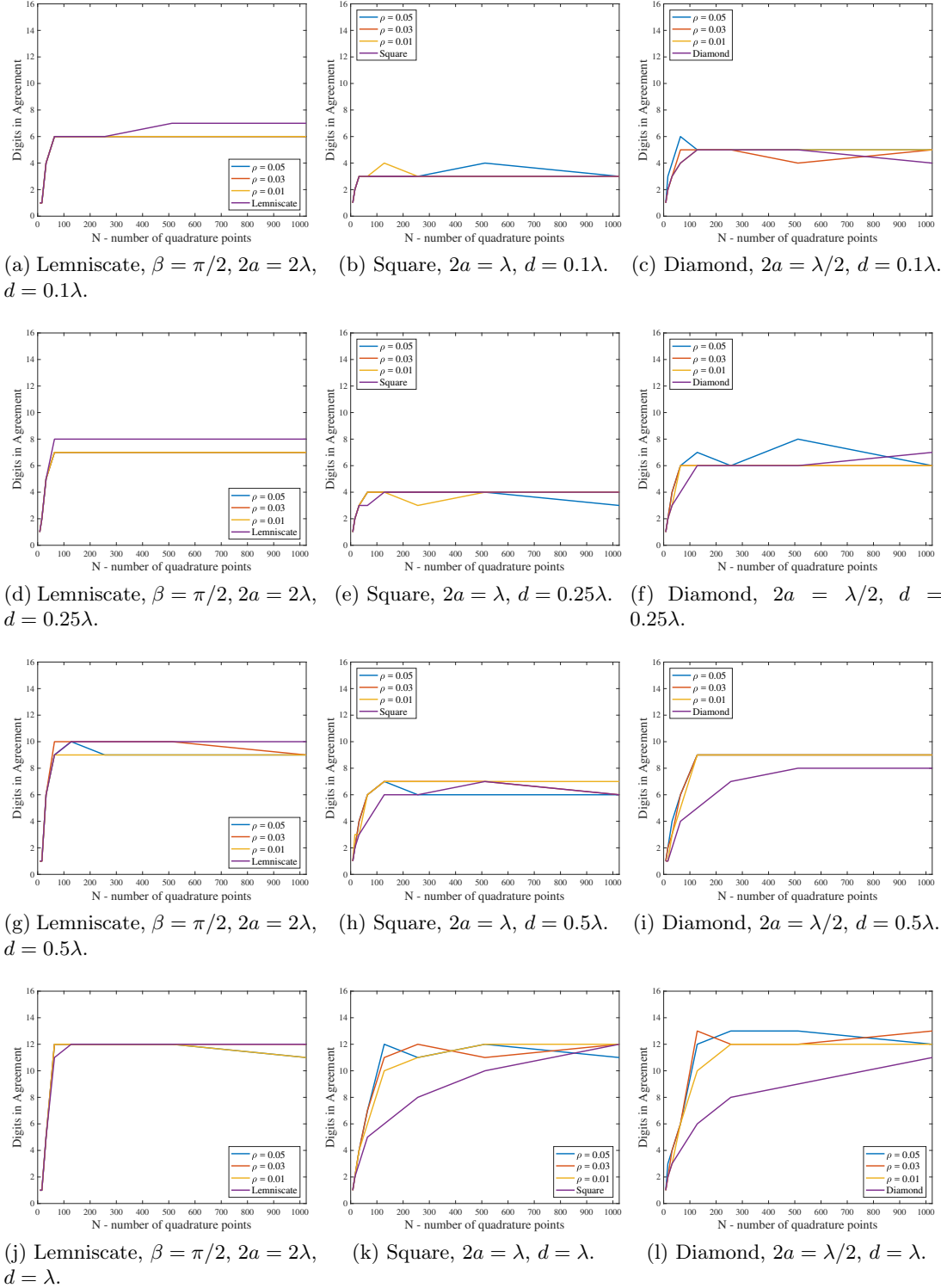


Figure 8.7: Significant digits in agreement of the far-field for two scatterer arrays. All figures produced using TMATROM equipped with our corner forward solver. All scatterers have a Dirichlet boundary condition. Incidence angle is $\theta_0 = 0$.

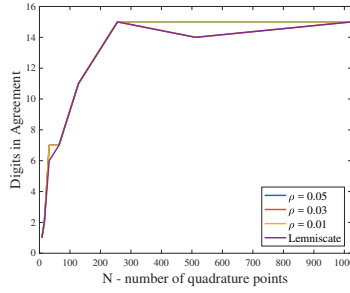
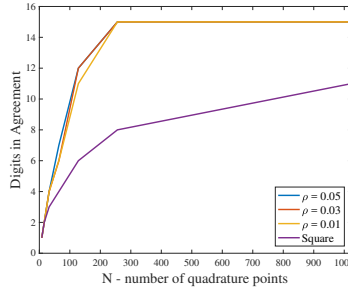
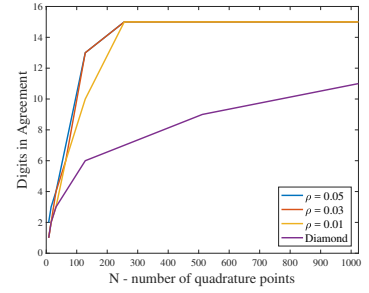
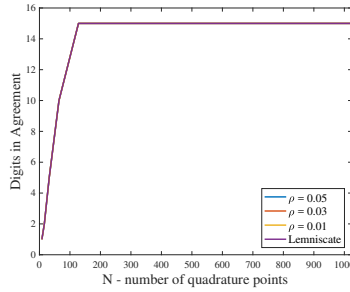
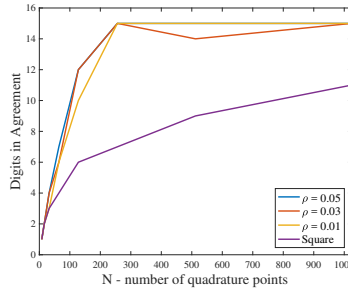
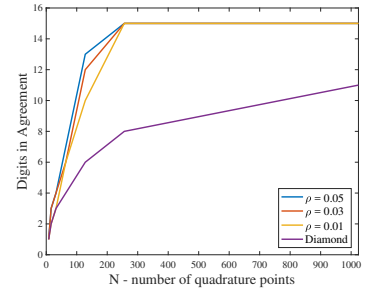
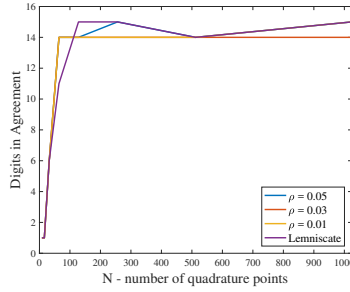
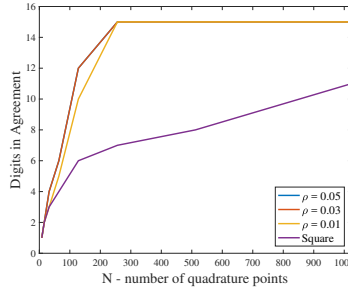
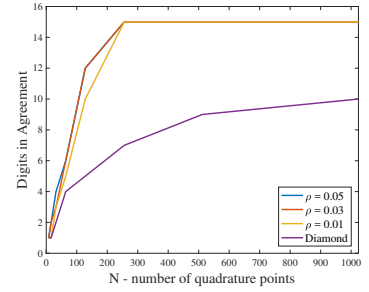
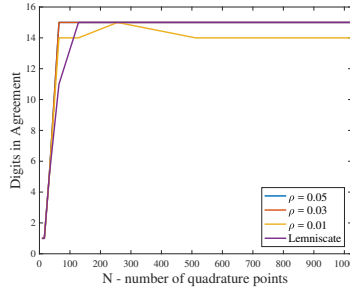
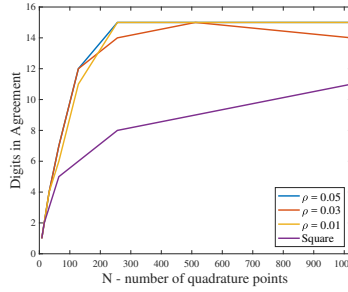
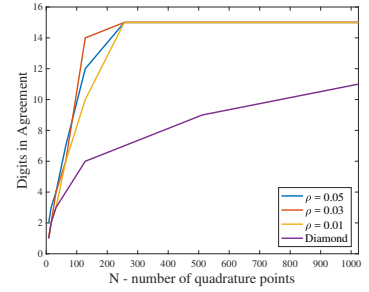
(a) Lemniscate, $\beta = \pi/2$, $2a = 2\lambda$, $d = 0.1\lambda$.(b) Square, $2a = \lambda$, $d = 0.1\lambda$.(c) Diamond, $2a = \lambda/2$, $d = 0.1\lambda$.(d) Lemniscate, $\beta = \pi/2$, $2a = 2\lambda$, $d = 0.25\lambda$.(e) Square, $2a = \lambda$, $d = 0.25\lambda$.(f) Diamond, $2a = \lambda/2$, $d = 0.25\lambda$.(g) Lemniscate, $\beta = \pi/2$, $2a = 2\lambda$, $d = 0.5\lambda$.(h) Square, $2a = \lambda$, $d = 0.5\lambda$.(i) Diamond, $2a = \lambda/2$, $d = 0.5\lambda$.(j) Lemniscate, $\beta = \pi/2$, $2a = 2\lambda$, $d = \lambda$.(k) Square, $2a = \lambda$, $d = \lambda$.(l) Diamond, $2a = \lambda/2$, $d = \lambda$.

Figure 8.8: Significant digits in agreement of the far-field for two scatterer arrays. All figures produced using TMatrom equipped with our corner forward solver. All scatterers have a Dirichlet boundary condition. Incidence angle is $\theta_0 = 0$.

8.5 The Advantages of Using TMATROM

The TMATROM package provides an efficient framework for two dimensional scattering models with multiple sets of parameters, for example, monostatic acoustic cross-section simulations. It enables calculation of the T-matrix for a scatterer which then can be stored off-line for later use, eliminating the need to re-calculate, saving computational time, especially for multiple scattering problems as the T-matrix is independent of incident and receiver directions. Changes to the scatterer position and orientation use techniques based on the translation-addition theorem [138] to quickly recalculate a new T-matrix based on the original [104]. These methods result in significant memory and computational time savings when solving problems with multiple scatterers.

A well written manual is provided which allows the user to quickly use the included working examples. The package components are explained and instructions on how to use the included solvers are provided. Most helpfully, detailed instructions with a working example are provided on how to incorporate a user's own solver. The package is equipped with working examples of some scattering problems: a bistatic (single parameter) scattering simulation and the corresponding monostatic (multi parameter) simulation with 1000 input incident waves. Examples are provided for Dirichlet, Neumann and impedance loaded boundary conditions. Included also is an example of a multi-scatterer problem. It is straightforward for a user to add other geometries to the included examples.

The TMATROM package is independent of any specific numerical method. This allows for the package to be used with any forward wave propagation solver of choice. The only requirement is that the solver can compute the far-fields associated with incident circular wave. The package is equipped with a Nyström solver for smooth surfaced scatterers. It also provides an example of how to include an end-user forward solver by using Barnett and Betcke's MPSPack [99] as an example. Once implemented within TMATROM, a user's own single particle scattering software can be easily extended for multiple scattering simulations. The package also provides a framework for different kinds of solvers to interact, allowing easy simulation of multiple scattering for systems with scatterers of mixed kind.

8.6 Constraints

The use of TMATROM requires a MATLAB software licence, some proficiency in MATLAB and also some knowledge of object-oriented programming. As with any software package, a time investment is required to learn how to use the package. A longer time investment is required if the end-user wishes to include their own solvers. TMATROM is equipped with a well written user manual which minimises this.

The included Nyström solver and examples make implementation of many scattering problems fairly easy. However, in our case, we are studying scatterer geometries and configurations that required the inclusion of our own forward solver. This in itself was quite straightforward and greatly assisted by the examples included with TMATROM and the user manual. Modifications to the TMATROM suggested parameters such as the wave expansion series truncation order or GMRES iterations were needed to achieve a more accurate result. This required some investigation and experimentation to find the most suitable parameters for our specific scattering problems.

The application of the translation-addition theorem within TMATROM greatly simplifies the implementation of multiple scatterer geometries. However, it introduces an error in the far-field at least of the order 10^{-8} [104]. This may be a consideration for modelling applications which require a highly accurate result.

TMATROM is suitable for acoustic scattering simulations exterior to the circle circumscribing and centred inside the scatterer. This circumscription introduces some limitations on the types of problems able to be implemented using TMATROM. Firstly, quantities near or on the scatterer surface may not be able to be examined. As such it is not a suitable tool for the work on the quantities near the vicinity of the corner presented in Chapter 5. Secondly, in a multiple scatterer problem, if the scatterer separation is such that the circumscribing circle encroaches into the space occupied by another scatterer in the arrangement, an accurate result is unable to be achieved and an alternative tool for those scatterer problems should be considered. This in particular limits the separation distance between square scatterers. In our case for squares of side length 2, the separation distance must be greater than $\sqrt{2} - 1$.

We also found that for some of the multiple scatterer geometries studied in Chapter 7 the results produced by TMATROM using the default parameterisation were not as

accurate as those produced using our traditional approach. These differences were larger than could be attributed to the use of the translation-addition theorem. Once parameter changes were implemented to maximise the accuracy of the results, we found that TROMATROM produces accurate solutions when the scatterers are separated by at least half the scatterer width. As the scatterer separation decreases, the accuracy of the solution also decreases.

8.7 Acknowledgement

The author would like to thank Dr Stuart Hawkins, one of the authors of the TROMATROM package for his invaluable instruction and generous advice during the implementation of the package.

8.8 Conclusion

In this chapter we examined the TROMATROM package. The reasons for this are two-fold: to independently verify work done to date, but more importantly, to make use of computational efficiencies provided by the package for larger multiple scattering problems. The TROMATROM package provides an efficient framework for scattering models with multiple sets of parameters, for example, monostatic acoustic cross-section simulations. It enables calculation of the T-matrix for a scatterer which then can be stored off-line for later use, eliminating the need to re-calculate, saving computational time, especially for multiple scattering problems as the T-matrix is independent of incident and receiver directions. Changes to the scatterer position and orientation use techniques based on the translation-addition theorem [138] to quickly recalculate a new T-matrix based on the original [104].

The steps we undertook to implement the package were outlined. This consisted of adding into TROMATROM all the scatterer geometries we are studying and our own forward solver for scatterers with corners. This required some experimentation to determine necessary changes to the standard TROMATROM parameters to maximise the accuracy of our results. For single scatterer problems it required increasing the order of the wave function series truncation suggested by TROMATROM by 10.

We also employed the included interface to Barnett and Betcke's MPSPack [99] for some of our testing. The sample square included in MPSPack has sides of length 1, whereas the square scatterer we have been employing has sides length 2. This required a number of changes to the parameters used by MPSPack and some experimentation to determine these changes. This included determining the ideal radius of artificial circular boundary required by MPSPack: we chose $r = 1.68$. In addition we needed to determine the ideal number of corner basis functions, N , to achieve optimal results. In the Dirichlet case, for wave numbers less than 16π it was determined that $N = 80$ gives the best results and $N = 110$ for the larger wave numbers. In the Neumann case, for wave numbers less than 8π , $N = 70$ or 80 yields optimal results, and $N = 90$ and 110 for wave numbers 8π and 16π , respectively.

The results for the far-field produced by TROM equipped with our corner solver to those produced using our original code (Chapter 3) were compared using the L^2 (8.7) and L^∞ (8.8) norms to measure the differences. A high order of agreement was demonstrated: order 10^{-10} to 10^{-15} , which validates our results. We also compared the results for the far-field produced by TROM equipped with MPSPack as the forward solver to those produced using our original code for squares. The MPSPack results show agreement to our original work of order 10^{-9} to 10^{-12} , which further validates our results. We note that the T-matrix error when using our cornered forward solver is of similar order or better than when using MPSPack. Because of this and the need to use different parameters in MPSPack for different test conditions, we used our own cornered solver in TROM for all future work.

The two and four scatterer array problems studied in Chapter 7 were tested using the TROM features for multiple scatterer problems: generating the T-matrix for a geometry once and employing the translation-addition theorem methods that use the generated T-matrix. We originally found that we had poor agreement to our original results and larger T-matrix errors ($\geq 10^{-5}$). We consulted with the package authors and based on their recommendation found that increasing the quadrature points on the surface of the scatterer, increasing the suggested order of the series truncation and setting the number of Matlab GMRES iterations to the maximum for the system to be solved in the case of squares improved the results.

We found that the TROMATROM package provides an efficient method for solving multiple scatterer problems, producing accurate solutions when the scatterers are separated by at least half the scatterer diameter, $2a$. In these cases, the solutions produced using TROMATROM equipped with our cornered solver are within the error bound introduced by the use of the translation-addition theorem (10^{-8}). As the scatterer separation further decreases the accuracy of the solution also decreases down to order 10^{-3} in some cases.

A limitation identified in the TROMATROM package is the following: if the multiple scatterers are configured so that the circumscribing circle of a scatterer encroaches into the space occupied by another scatterer, an accurate result is impossible to be achieved, and alternative approaches to that scattering problem must be considered. In the case of squares with side length 2, this limits the separation distance to be greater than $\sqrt{2} - 1$.

The computational efficiency of TROMATROM is seen by considering a set of M identical scatterers, each requiring an $N \times N$ system for an accurate solution as an isolated scatterer (i.e. in the absence of the other scatterers). The basic method described in Chapter 7 thus requires the solution of a system of order MN , of computational complexity $O((MN)^3)$ if standard Gaussian elimination is employed. On the other hand, TROMATROM requires the solution of two systems, one of order N (corresponding to a single isolated scatterer) and another of order MP where P is the size of the computed T-matrix and M the number of scatterers. The order of P is a fraction of N , and TROMATROM uses the (iterative) GMRES method to solve the linear system MP . This reduces the overall computational complexity for the example of two and four scatterers studied in this chapter to $O(N^3)$.

In the next chapter we employ TROMATROM equipped with our cornered solver to investigate much larger array scattering problems.

Chapter 9

Large Arrays

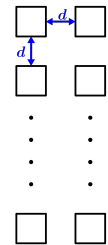
In Chapter 8 we evaluated the TMATROM [27, 102] package and used it to verify some of our earlier numerical work. In this chapter we utilise the most powerful feature of the TMATROM package, that is the ease and computational efficiency of modelling multiple scatterer structures, and demonstrate that the TMATROM package employing our own forward solvers efficiently enables the study of large scatterer arrays of cornered structures. Of particular interest is the simulation of infinite array behaviour including phenomena such as diffraction grating lobes by large but finite arrays. The key question is the minimum number of scatterers required in an array to observe this behaviour.

9.1 The Geometries

We examine two types of array configurations: single and double arrays. A single array consists of a number of scatterers, from 2 up to 256, arranged parallel to the y -axis. A double array consists of two arrays of scatterers each parallel to the y -axis arranged in configurations ranging from 2×2 to 128×2 .

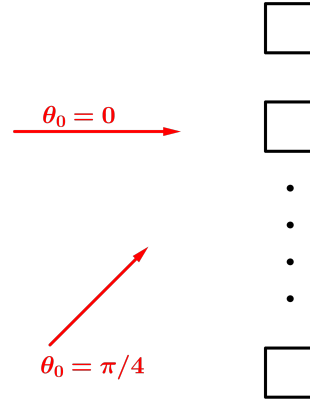


Single array.



Double array.

Both types of arrays consist of scatterers of the same shape and boundary condition. The scatterers are of diameter $2a$ and separated by distance d . For the double array: the second array of scatterers is a distance d from the first. Thus if the scatterers are separated by half a wavelength, the second array of scatterers is separated by half a wavelength from the first. We primarily used two angles of the incident plane wave $\theta_0 = 0$ and $\theta_0 = \pi/4$ for test-



ing. Since we are using the implementation of the TMatROM package as described in Sections 8.2 and 8.4, the restrictions on the scatterer separation (Section 8.6) apply. The scatterer configurations studied in this section are summarised in Table 9.1 and all three boundary conditions: Dirichlet, Neumann and impedance loaded (with $Z = 1 + i$) were tested. Note that the term lemniscate in this section refers to one with an interior right-angle (2.2).

Polar plot diagrams produced by Matlab illustrate the far-field generated by the array structures studied in this chapter. The arrays are aligned along the vertical line from $\hat{\mathbf{x}}(\hat{\theta}) = \pi/2$ to $3\pi/2$.

d	Lemniscate			Square			Diamond		
	$2a$			$2a$			$2a$		
	0.5λ	λ	2λ	0.5λ	λ	2λ	0.7λ	1.4λ	2.8λ
0.25λ	x	x		x			x	x	x
0.5λ	x	x	x	x	x		x	x	x
λ	x	x	x	x	x	x	x	x	x

Table 9.1: Array configurations: 'x' indicates that the configuration was tested for the indicated scatterer of diameter $2a$ with separation distance d .

9.2 Far-field behaviour

In this section we examine the behaviour of the far-field as the number of scatterers, N , in an array gets large. The far-field data $u^\infty(\hat{\mathbf{x}}(\hat{\theta}))$, where $\hat{\theta}$ is the angle of observation, was collected for each of the scatterer configurations in Table 9.1, for incident wave directions $\theta_0 = 0$ and $\pi/4$, and for all three boundary conditions. The far-field was

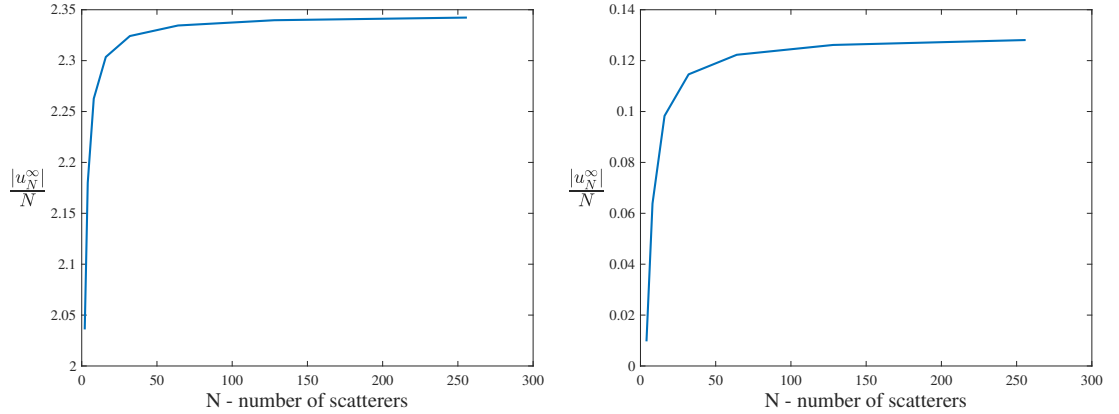
measured for angles of observation $\hat{\theta} \in [0, 2\pi]$. Both the forward- and back-scatter behaviour is of interest. For the incident wave angle $\theta_0 = 0$, the maximum back-scatter is observed at $\hat{\theta} = 0$, and maximum forward-scatter at $\hat{\theta} = \pi$. For incident angle $\theta_0 = \pi/4$, the maximum back-scatter is observed at $\hat{\theta} = \pi/4$, but the maximum forward-scatter direction varies by scatterer configuration.

9.2.1 Limiting Behaviour

We begin by examining the behaviour of the far-field $u_N^\infty(\hat{\mathbf{x}}(\hat{\theta}))$ in the forward and back-scatter directions as N increases. Measuring the maxima in each direction we found that

$$\frac{|u_N^\infty(\hat{\mathbf{x}})|}{N} \longrightarrow C, \quad (9.1)$$

as N becomes large for some constant C dependent on the scatterer configuration, boundary condition, and angle of observation. Figure 9.1 illustrates two typical examples of normalised forward- and back-scatter as a function of N .



(a) Back-scatter for diamonds in single array with Dirichlet BC, $2a = 0.7\lambda$, $d = 0.5\lambda$, $\theta_0 = 0$.

(b) Forward-scatter for diamonds in double array with Neumann BC, $2a = 2.8\lambda$, $d = \lambda$, $\theta_0 = \pi/4$.

Figure 9.1: Demonstrating that $\frac{|u_N^\infty(\hat{\mathbf{x}})|}{N} \longrightarrow C$, for some constant C as N gets large.

We then estimated the rate of convergence as N gets large, by the quantity

$$\left| \frac{|u_N^\infty(\hat{\mathbf{x}})|}{N} - \frac{|u_{N_{\max}}^\infty(\hat{\mathbf{x}})|}{N_{\max}} \right|, \quad (9.2)$$

as a function of N , where, for both the single and double array configurations, $N_{\max} = 256$. This quantity was measured for both the maximum back- and forward-scatter

directions. A least squares fit to the logarithms of the data ($N = 8, 16, 32, 64$ and 128) was used (see Figure 9.2).

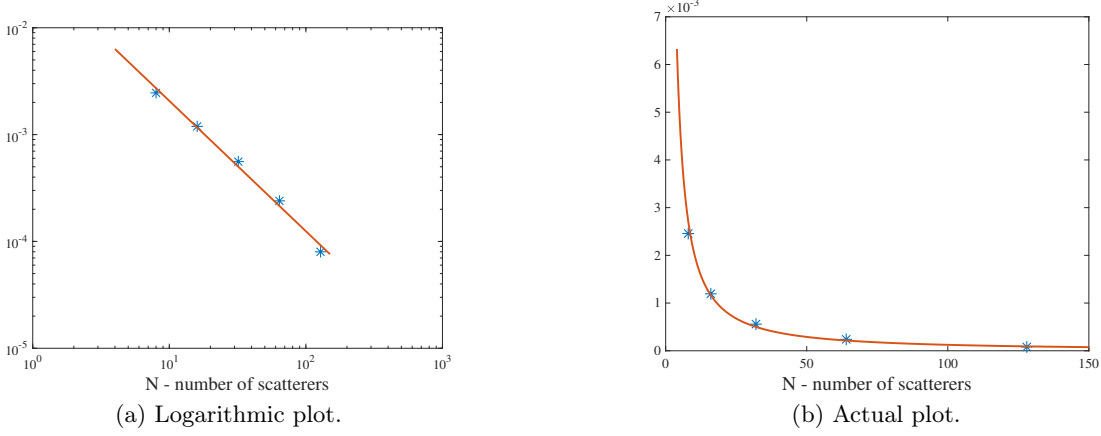


Figure 9.2: Plot of the far-field difference $\left| \frac{|u_N^\infty(\hat{\mathbf{x}})|}{N} - \frac{|u_{256}^\infty(\hat{\mathbf{x}})|}{256} \right|$, measured in the maximum back-scatter direction, for a single array of squares with diameter $2a = \lambda$, and separation $d = 0.5\lambda$, all with an Neumann boundary condition. Incident wave direction $\theta_0 = 0$. The data points used are represented by the blue asterisks, the least squares line of fit is shown in red.

It is found that

$$\left| \frac{|u_N^\infty(\hat{\mathbf{x}})|}{N} - \frac{|u_{256}^\infty(\hat{\mathbf{x}})|}{256} \right| \sim C \frac{1}{N^m}, \quad (9.3)$$

for some constant C dependent on the scatterer shape, configuration, boundary condition and incident field direction. However, the power m is independent of these factors. In the case of single arrays $m \sim 1.2$ and for double arrays $m \sim 1.3$. This applies to the maxima in both the forward- and back-scatter directions.

There were a few exceptions for certain array configurations. After careful study of the far-fields produced by these arrays, it was found that if there is evidence of side-fire, then the rates of convergence (9.3) differ and in fact are slower. For example, in the case of a single array of squares half a wavelength in diameter, $2a = 0.5\lambda$, separated by half a wavelength, $d = 0.5\lambda$, $m \sim 0.9$ instead of 1.2. The term side-fire describes local maxima ('lobes') occurring in the far-field in the direction $\pi/2$ (90°) and $3\pi/2$ (270°). Figure 9.3 shows a logarithmic plot of the far-fields for a single array of squares with Dirichlet boundary condition with different configurations. Figures 9.3b, 9.3e, 9.3f show configurations with side-fire, and when measured, the rate of convergence was slower than $\frac{1}{N^{1.2}}$. Figures 9.3a, 9.3c, 9.3d show no evidence of side-fire and the measured rate

of convergence for these configurations was $\sim \frac{1}{N^{1.2}}$. It is straightforward to determine which configurations will exhibit side-fire phenomena. In Section 9.2.2 we discuss how the direction of the maximum lobes in the backscatter region may be predicted. Scatterer array configurations with side-fire have maximum lobes occurring at $\pi/2$ and $3\pi/2$.

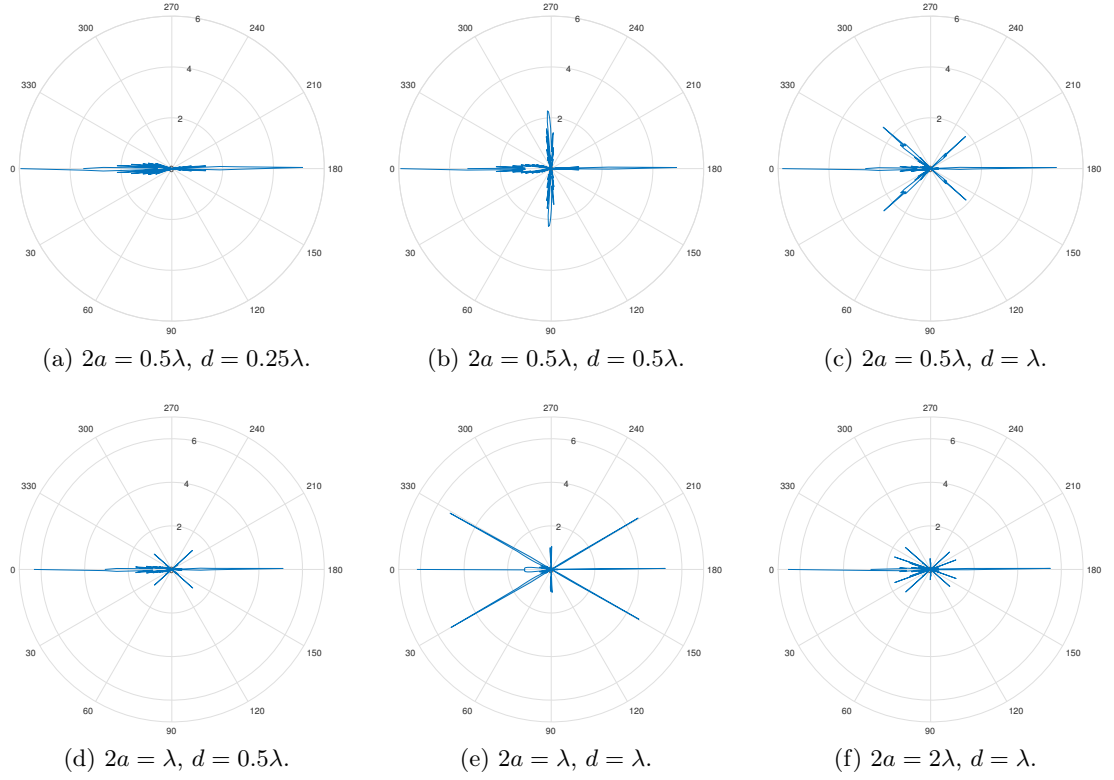


Figure 9.3: Logarithmic plot of the far-field $|u^\infty|$, for a single array of squares with differing diameters $2a$, and separation d , all with an impedance loaded boundary condition. Number of scatterers $N = 256$ in the array; incident wave direction $\theta_0 = 0$.

9.2.2 Diffraction Grating

We next examined the characteristics of the far-field for each of the scenarios earlier described. Figure 9.4 is illustrative of the typical behaviour observed. It shows the most pronounced local maxima (or lobes) are readily observed and become increasingly sharply defined as N increases.

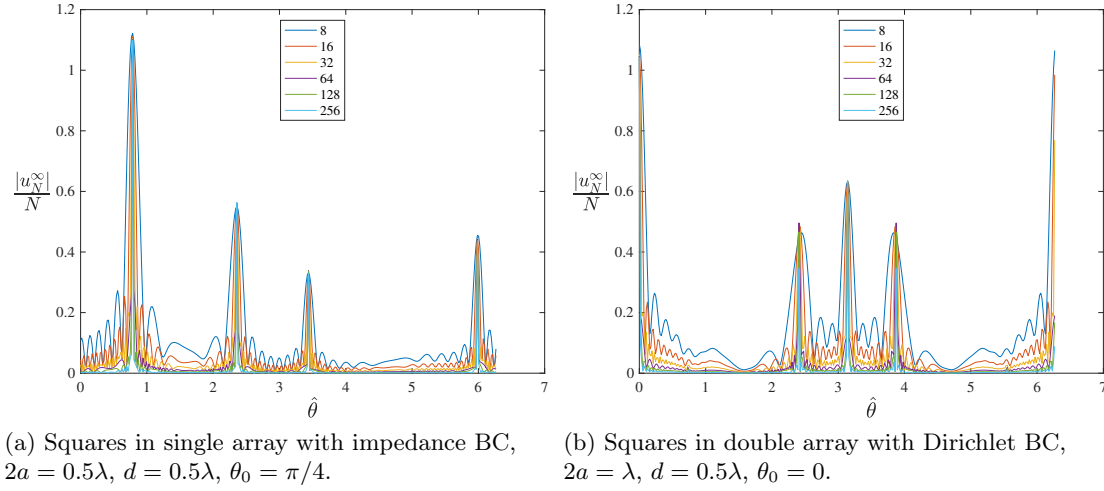


Figure 9.4: Illustrating $\frac{|u_N^\infty(\hat{\mathbf{x}}(\hat{\theta}))|}{N}$, for $\hat{\theta} \in [0, 2\pi]$ for differing N .

The so-called grating equation is characteristic of infinite array structures [141]. The periodicity and structure of the arrays studied are representative of a grating structure and diffraction grating patterns should be evident. Questions of interest are: how large does the finite array need to be to exhibit this behaviour? and, how many grating lobes are excited? A pattern of maxima in the back-scatter region is expected to occur at angles $\hat{\theta}_m$ in response to the incident field direction, θ_0 , which is governed by the diffraction equation [141],

$$\hat{\theta}_m = \arcsin\left(\sin(\theta_0) - \frac{m\lambda}{T}\right), \quad \text{for } m \in \mathbb{Z}, \quad (9.4)$$

where θ_0 is measured from the array's normal vector, and T is the distance from the centre of one scatterer to the next, measured in wavelengths. Table 9.2 shows the angles of expected maxima for the two incident angles $\theta_0 = 0$, and $\pi/4$. The angles have been translated to match the polar plot diagrams used in this chapter.

Figures H.1 to H.4 in Appendix H show the logarithmic far-field plots for $N = 64$ for

a representative sample of array structures: single arrays of squares and of diamonds, with Dirichlet and Neumann boundary conditions, respectively, and double arrays of lemniscates and of squares both with Neumann boundary condition. Grating lobes can be seen and these match the expected angles $\hat{\theta}_m$ listed in Table 9.2. For a more detailed and methodical analysis, we collected data for each array structure studied in this chapter about the back-scatter lobes, and measured the far-field value $|u_N^\infty|$ and the angle $\hat{\theta}$ at which the lobe occurs. This was done for array sizes $N = 8, 16, 32, 64, 128$ and 256 . Table 9.3 shows a sample of the data that was captured and analysed. For each configuration the header row shows the expected diffraction lobe angle $\hat{\theta}$ and for each number of scatterer N the actual measured lobe angle as well as the value of the far-field $|u^\infty(\hat{\mathbf{x}}(\hat{\theta}))|$ measured at that angle. Highlighted in red are the lobes where excitation has not yet occurred. Our data shows that for values $N = 8, 16$ the grating lobes are evident but occur one to two degrees away from the expected value. We also note that at for these smaller values of N the grating lobes, though evident, may not be the dominant lobes, with the exception of the maximum back-scatter value, which occurs at $\hat{\theta} = 0$ or $\pi/4$ for incident wave angles $\theta_0 = 0$ and $\pi/4$ respectively. When $N = 32$ we see the the grating lobes begin to be more dominant, and for $N \geq 64$ the lobes occur at the precisely the expected angles $\hat{\theta}_m$ and are the dominant lobes.

To illustrate the emergence of the grating lobes as N increases and to examine the difference between a single and double array structure view refer to Figures 9.5 and 9.6, where we show the logarithmic polar plots for an array of square scatterers with impedance boundary condition for $N = 8, 16, 32, 64, 128$ and 256 . All the arrays are of squares diameter $2a$ of two wavelengths with separation distance d of one wavelength, illuminated by an incident field with direction $\theta_0 = 0$. The single array plots are shown in Figure 9.5, the double array in Figure 9.6. Both sets of figures demonstrate that the grating lobes are dominant for $N \geq 64$ and that the behaviour is similar for both single and double arrays. The numerical data complementing these two figures is found in the first two entries of Table 9.3.

$\theta_0 = 0$								
$2a$	d	$m = 0$	$m = 1$	$m = -1$	$m = 2$	$m = -2$	$m = 3$	$m = -3$
Lemniscates, Squares								
0.5	0.25	0	-	-	-	-	-	-
0.5	0.5	0	90	270	-	-	-	-
0.5	1	0	42	318	-	-	-	-
1	0.25	0	53	307	-	-	-	-
1	0.5	0	42	318	-	-	-	-
1	1	0	30	330	90	270	-	-
2	0.25	0	26	334	63	297	-	-
2	0.5	0	24	336	53	307	-	-
2	1	0	19	341	42	318	90	270
Diamonds								
0.7	0.25	0						
0.7	0.5	0	56	304				
0.7	1	0	36	324				
1.4	0.25	0	37	323				
1.4	0.5	0	31	329				
1.4	1	0	24	336	56	304		
2.8	0.25	0	19	341	41	319	77	283
2.8	0.5	0	17	343	37	323	64	296
2.8	1	0	15	345	31	329	52	308
$\theta_0 = \pi/4$								
$2a$	d	$m = 0$	$m = 1$	$m = 2$	$m = 3$	$m = 4$	$m = 5$	$m = 6$
Lemniscates, Squares								
0.5	0.25	45	321	-	-	-	-	-
0.5	0.5	45	343	-	-	-	-	-
0.5	1	45	2	321	-	-	-	-
1	0.25	45	355	297	-	-	-	-
1	0.5	45	2	321	-	-	-	-
1	1	45	12	343	308	-	-	-
2	0.25	45	15	350	321	-	-	-
2	0.5	45	18	355	330	297	-	-
2	1	45	22	2	343	321	286	-
Diamonds								
0.7	0.25	45	340	-	-	-	-	-
0.7	0.5	45	353	288	-	-	-	-
0.7	1	45	7	332	-	-	-	-
1.4	0.25	45	6	330	-	-	-	-
1.4	0.5	45	11	340	301	-	-	-
1.4	1	45	17	353	328	288	-	-
2.8	0.25	45	22	3	344	324	293	-
2.8	0.5	45	24	6	349	330	307	-
2.8	1	45	26	11	356	340	323	301

Table 9.2: Listing diffraction grating lobe angles $\hat{\theta}_m$ for different array configurations of scatterers of diameter $2a$ wavelengths separated by distance d wavelengths, for incident wave angles $\theta_0 = 0$ and $\pi/4$.

Single array, square impedance BC, $2a = 2\lambda, d = \lambda, \theta_0 = 0$														
Expected $\hat{\theta}_m$	$\hat{\theta} = 0$	$ u_N^\infty $	$\hat{\theta} = 19$	$ u_N^\infty $	$\hat{\theta} = 341$	$ u_N^\infty $	$\hat{\theta} = 42$	$ u_N^\infty $	$\hat{\theta} = 318$	$ u_N^\infty $	$\hat{\theta} = 90$	$ u_N^\infty $	$\hat{\theta} = 270$	$ u_N^\infty $
N														
8	0	21.61	19	4.79	341	4.79	41	2.61	319	2.61	90	0.12	270	0.12
16	0	43.39	19	7.95	341	7.95	42	4.85	318	4.85	90	0.13	270	0.13
32	0	86.93	19	6.16	341	6.16	42	9.16	318	9.16	90	0.15	270	0.15
64	0	174.00	19	8.62	341	8.62	42	13.61	318	13.61	90	0.19	270	0.19
128	0	348.12	19	5.86	341	5.86	42	2.44	318	2.44	90	0.26	270	0.26
256	0	696.34	19	5.76	341	5.76	42	4.67	318	4.67	90	0.36	270	0.36
Double array, square impedance BC, $2a = 2\lambda, d = \lambda, \theta_0 = 0$														
Expected $\hat{\theta}_m$	$\hat{\theta} = 0$	$ u_N^\infty $	$\hat{\theta} = 19$	$ u_N^\infty $	$\hat{\theta} = 341$	$ u_N^\infty $	$\hat{\theta} = 42$	$ u_N^\infty $	$\hat{\theta} = 318$	$ u_N^\infty $	$\hat{\theta} = 90$	$ u_N^\infty $	$\hat{\theta} = 270$	$ u_N^\infty $
N														
8	0	12.89	20	1.68	340	1.68	44	0.80	316	0.80	90	0.18	270	0.18
16	0	26.20	20	2.91	340	2.91	43	1.38	317	1.38	90	0.20	270	0.20
32	0	52.82	20	4.35	340	4.35	42	2.81	318	2.81	90	0.25	270	0.25
64	0	106.08	19	2.87	341	2.87	42	5.44	318	5.44	90	0.32	270	0.32
128	0	212.60	19	4.35	341	4.35	42	8.26	318	8.26	90	0.42	270	0.42
256	0	425.65	19	3.98	341	3.98	42	1.71	318	1.71	90	0.55	270	0.55
Double array, square Neumann BC, $2a = 2\lambda, d = \lambda, \theta_0 = \pi/4$														
Expected $\hat{\theta}_m$	$\hat{\theta} = 45$	$ u_N^\infty $	$\hat{\theta} = 22$	$ u_N^\infty $	$\hat{\theta} = 2$	$ u_N^\infty $	$\hat{\theta} = 343$	$ u_N^\infty $	$\hat{\theta} = 321$	$ u_N^\infty $	$\hat{\theta} = 286$	$ u_N^\infty $		
N														
8	45	10.77	24	1.25	1	1.57	342	2.38	319	3.44	290	1.57		
16	45	18.55	23	1.48	2	2.57	343	4.23	320	4.17	288	2.84		
32	45	33.54	22	1.27	2	4.56	343	8.60	321	7.30	287	5.45		
64	45	63.76	22	2.46	2	6.00	343	17.35	321	15.44	286	10.80		
128	45	124.16	22	4.94	1	1.94	343	34.48	321	20.91	286	19.38		
256	45	244.97	22	8.93	2	2.48	343	65.79	321	9.67	286	20.69		
Single array, diamond Dirichlet BC, $2a = 2.8\lambda, d = 1.4\lambda, \theta_0 = \pi/4$														
Expected $\hat{\theta}_m$	$\hat{\theta} = 45$	$ u_N^\infty $	$\hat{\theta} = 26$	$ u_N^\infty $	$\hat{\theta} = 11$	$ u_N^\infty $	$\hat{\theta} = 356$	$ u_N^\infty $	$\hat{\theta} = 340$	$ u_N^\infty $	$\hat{\theta} = 323$	$ u_N^\infty $	$\hat{\theta} = 301$	$ u_N^\infty $
N														
8	45	20.71	27	3.52	11	3.54	355	1.87	340	3.03	323	1.97	300	0.75
16	45	41.36	26	4.68	11	5.80	356	2.68	340	5.66	323	3.89	301	1.21
32	45	82.64	26	0.93	11	4.43	355	1.80	340	7.76	323	6.73	301	1.94
64	45	165.22	26	1.98	11	6.26	356	2.34	340	1.26	323	6.03	301	1.54
128	45	330.38	26	3.73	11	3.75	356	2.35	340	2.59	323	7.29	301	2.08
256	45	660.69	26	4.45	11	2.06	356	2.50	340	4.97	323	3.66	301	0.72
Double array, diamond impedance BC, $2a = 2.8\lambda, d = 0.7\lambda, \theta_0 = 0$														
Expected $\hat{\theta}_m$	$\hat{\theta} = 0$	$ u_N^\infty $	$\hat{\theta} = 17$	$ u_N^\infty $	$\hat{\theta} = 343$	$ u_N^\infty $	$\hat{\theta} = 37$	$ u_N^\infty $	$\hat{\theta} = 323$	$ u_N^\infty $	$\hat{\theta} = 64$	$ u_N^\infty $	$\hat{\theta} = 296$	$ u_N^\infty $
N														
8	0	12.68	16	1.84	344	1.84	40	0.58	320	0.58	66	0.72	294	0.72
16	0	25.34	17	2.98	343	2.98	38	0.93	322	0.93	65	0.86	295	0.86
32	0	50.11	17	4.65	343	4.65	37	2.10	323	2.10	65	1.08	296	1.08
64	0	101.31	17	2.05	343	2.21	37	4.57	323	4.57	64	1.37	296	1.37
128	0	202.59	17	3.69	343	3.69	37	9.13	323	9.13	64	1.33	296	1.33
256	0	405.16	17	4.68	343	4.68	37	15.26	323	15.26	65	0.83	296	0.83

Table 9.3: Showing diffraction grating expected versus actual lobe angles $\hat{\theta}_m$ for different array configurations of scatterers of diameter $2a$ wavelengths separated by distance d wavelengths, for incident wave angles θ_0 , and the far-field $|u_N^\infty|$ measured at those lobes.

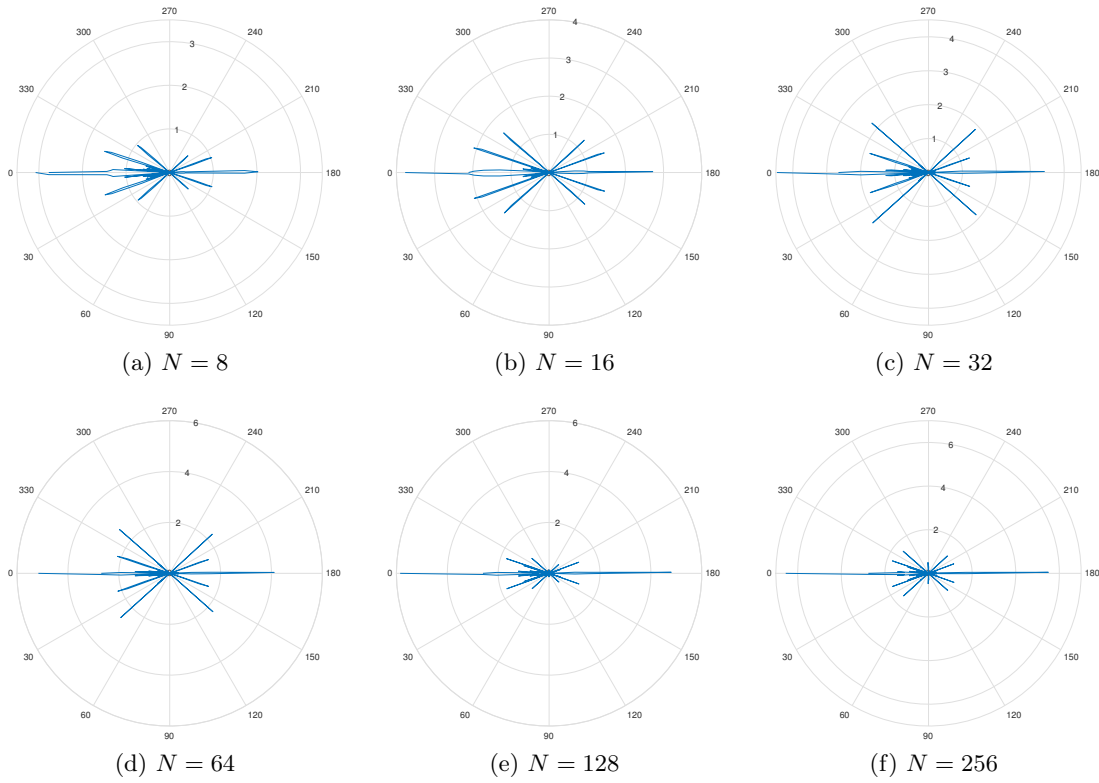


Figure 9.5: Logarithmic plot of the far-field $|u^\infty|$, for a single array of squares of diameter $2a = 2\lambda$ and separation $d = \lambda$ all with impedance loaded boundary condition. Incident wave direction $\theta_0 = 0$.

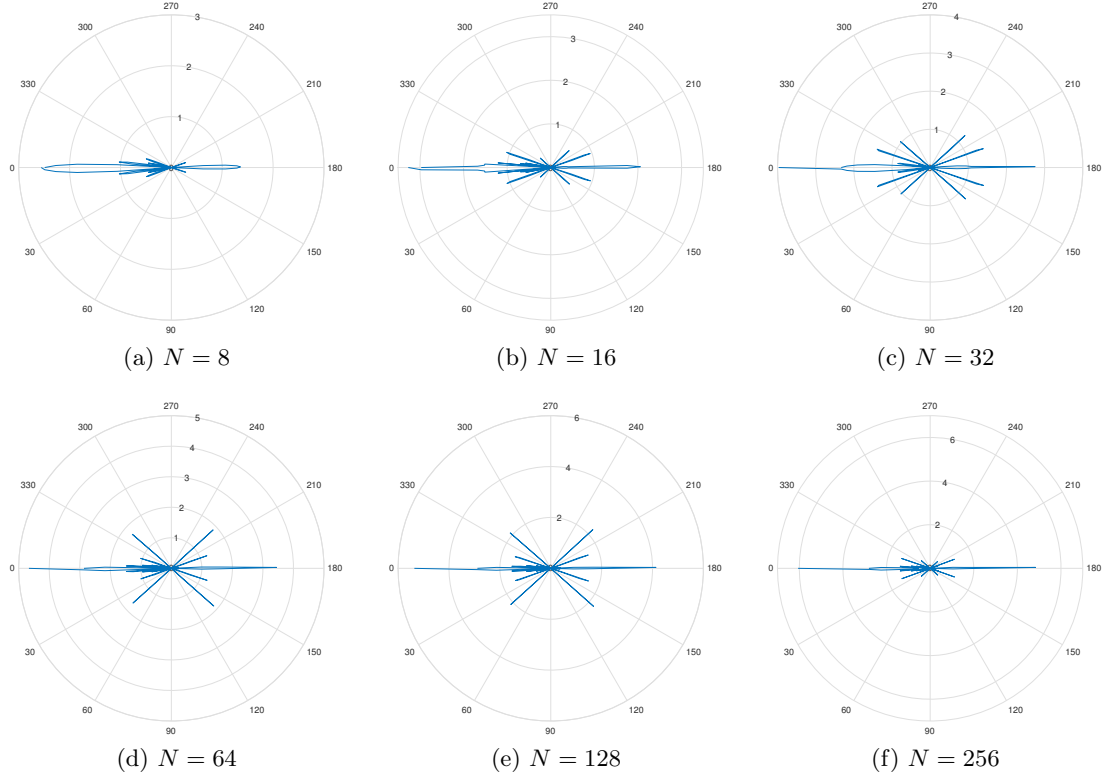


Figure 9.6: Logarithmic plot of the far-field $|u^\infty|$, for a double array of squares of diameter $2a = 2\lambda$ and separation $d = \lambda$ all with impedance loaded boundary condition. Incident wave direction $\theta_0 = 0$.

9.3 Conclusion

In Chapter 8 we demonstrated a capacity for modelling with different basic array elements, both smooth or sharp-cornered using TMATROM with our own forward solvers. In this chapter we have shown that this software is a suitable tool for evaluating large array behaviour. This is relevant to many physical applications such as the modelling of meta-materials, photonic crystal structures and band-gap materials.

We have numerically demonstrated that the far-field patterns of a finite grating converge to infinite grating results with an appropriate scaling. We established a bound on the differences between the far-fields

$$\left| \frac{|u_N^\infty(\hat{\mathbf{x}})|}{N} - \frac{|u_{N_{\max}}^\infty(\hat{\mathbf{x}})|}{N_{\max}} \right| \leq C \frac{1}{N^m}, \quad (9.5)$$

for some constant C dependent on the scatterer shape, configuration, boundary condition and incident field direction. The power m is ~ 1.2 for single arrays and ~ 1.3 for double

arrays, except for configurations with side-fire, that is, with grating lobes occurring at $\hat{x}(\hat{\theta}) = \pi/2$ and $3\pi/2$, where the rate of convergence is slower.

We have also numerically established that the termination effect, that is the difference between finite and infinite array scattering pattern grating lobes, appears when $N \geq 64$ for the structures studied in this chapter. Thus we recommend a minimum array size of $N = 64$ when modelling infinite array behaviour for physical and engineering applications.

The emergence of grating diffraction lobes as the size of each finite array is increased was observed. The angles of the main lobes of the pattern were in excellent agreement with those produced by (9.4). This qualitative feature provides a different sort of test of the ability of our simulation to predict important physical phenomena associated with arrays and gratings.

Chapter 10

Summary and Conclusions

In this thesis we have undertaken a rigorous examination of two-dimensional diffraction from cylindrical scatterers which possess corners, that is, points at which the normal changes discontinuously, and quantified the effect on the resulting scattered field when these corners are rounded. We examined three different boundary conditions: soft, hard and an impedance loaded boundary condition, enforced at all points on the cross-sectional boundary of the cylinder. The problems studied are in the acoustic resonance regime $ka \leq 16\pi$ corresponding to diameters less than 16 wavelengths; a second kind integral equation formulation of the problem is used. Accuracy was of paramount importance in this study in assessing the effects of rounding a corner.

In this work we use a numerical method that is suitable for examining the scattering of acoustic or appropriately polarised electromagnetic plane waves by structures possessing some points of small or zero radius of curvature (that is, having a sharp corner). We implement the Nyström method expounded by [7, 26] for a scatterer with a single corner and soft boundary condition to obtain numerical solutions of this integral equation. We then adapt and extend this technique to scatterers with hard and impedance loaded boundary conditions and scatterers with more than one corner.

We examined single scatterer problems numerically and systematically measured the differences in the near- and far-fields. We demonstrated that the field scattered by the rounded structure converges, in both the L^2 and L^∞ norm, to that scattered by the corresponding sharp cornered object as the radius of curvature in the vicinity of the corner tends to zero. For the soft boundary condition, the L^∞ norm difference between the far-

field of a right-angled cornered scatterer and that of the rounded scatterer is less than 3% when the radius of curvature is restricted so that $k\rho \leq 3\pi/50$. This percentage reduces to 1% or 2% respectively, when the boundary condition is replaced by the hard boundary condition or the impedance boundary condition (with $Z = 1 + i$), respectively. We also demonstrated that the maximum differences between the far-fields of the cornered and rounded scatterers occur in the back-scatter region and the magnitude of these differences is dependent on the radius of curvature, ρ , used for the rounding, the wave number, ka , and the angle of the incident plane wave, θ_0 . We verified that the described quadrature schemes produce accurate and rapidly converging solutions to scattering problems for structures with corners that are not right-angled, that is, for structures with interior angles $\pi/12 \leq \beta \leq 35\pi/36$, where β is the interior angle of the corner.

The most significant findings of these numerical studies were: firstly, when the scatterer possesses sharp corners or rounded corners of small radii of curvature, it is essential to use an appropriate quadrature scheme - a graded mesh - in order to obtain numerical results efficiently. Use of a uniform mesh is, at best, grossly inefficient, and at worst, produces non-convergence of the numerical process. Secondly, we demonstrated the dependence on the maximum differences in the far-field of a cornered scatterer and its rounded counterpart on the radius of curvature in the rounded corner, the wave number and direction of travel of the illuminating incident plane wave. In the Dirichlet case, the non-dimensionalised maximum difference in the far-fields has the form $C(\theta_0)(k\rho)^{2/\nu}$, for some constant $C(\theta_0)$ dependent on the angle of illumination, as $k\rho \rightarrow 0$. The quantity ν is dependent on the interior angle of the scatterer β and is calculated as $\nu = \frac{2\pi-\beta}{\pi}$. For the impedance loaded case with $Z = 1 + i$, the exponent $2/\nu$ is replaced by 1. For the Neumann case, the exponent is dependent on the angle of illumination, but the maximum difference is bounded by $C(\theta_0)(k\rho)^{2/\nu}$.

Having established the power law dependence of the maximum difference in the far-field of a cornered scatterer and its rounded counterpart numerically, a theoretical basis for these numerical results was derived. This was achieved by introducing suitable surface parameterisations for the rounded and unrounded scatterers and then analysing the underlying integral equations. An approximate integral equation for the difference in the surface quantities on the lemniscate and its rounded counterpart was obtained, and it

was shown that the difference is $O((k\varepsilon)^{2/3})$ as $k\varepsilon \rightarrow 0$. As a consequence, the maximum in the non-dimensionalised far-field patterns is $O((k\varepsilon)^{4/3})$ as $k\varepsilon \rightarrow 0$, in accord with the computed results, since $\rho \sim 2\varepsilon$. These results are readily capable of extension to structures with sharp corners of interior angles other than $\pi/2$. A similar approach to the Neumann case is planned for future work; the similarity arises because many of the approximations for the kernel in question are identical, or nearly so, to those employed for the Dirichlet case.

We next examined the behaviour of three quantities at close proximity to the corner of a scatterer: the total field u^{tot} external to the scatterer, the derivative with respect to the normal $\frac{\partial u^{\text{tot}}}{\partial n}$ measured on the surface of the scatterer and the surface quantity φ . Firstly, we verified that the numerical schemes developed for the solution of the scattering of a plane wave by structures possessing corners, are suitable for measuring the scattered field in close proximity to the scatterer surface at the corner. Secondly, we verified that the employed schemes enable the accurate measurement of the derivative with respect to the normal on the surface of the scatterer in the vicinity of the corner. Thirdly, the behaviour of the surface quantity $\varphi(\tau)$ near the vicinity of the corner for scatterers with a Dirichlet and Neumann boundary condition was examined and it was shown that it can be approximated based on the wave number and the distance along the surface from the corner. For scatterers with the Dirichlet boundary condition and interior angle β we numerically established that $|\varphi(\tau) - \varphi(0)| \approx C(k\tau)^{1/\nu}$, as $\tau \rightarrow 0$, and that the constant $C \leq \frac{2\pi}{\beta}$, and if the incident wave direction $\theta_0 = 0$, then $C \approx 2\pi/\beta$. For the Neumann case, we established that, $|\varphi(\tau)| \approx C(\beta, \theta_0)(k\tau)^{\frac{2}{\nu}-1}$, when the incident wave direction $\theta_0 = 0$, and $|\varphi(\tau)| \approx C(\beta, \theta_0)(k\tau)^{\frac{1}{\nu}-1}$, when $\theta_0 \neq 0$, for constants C dependent on the incident wave direction θ_0 and the interior angle of the corner β . We then established the analytical basis for the numerical Neumann results. The analytical proof of the corresponding Dirichlet result follows similar lines, and is planned for future work.

To complete our examination of the effect of corner rounding on single scatterers we extended our analysis to examine the effect of corner rounding on the far-field in the time domain. We used discrete Fourier transforms to shift the previously collected frequency domain data to the time domain and measured the response to three different pulses: the Gaussian, the derivative of the Gaussian and the Gaussian sine packet. The response

in all cases was the same: as the radius of curvature of the rounded corner ρ increases, there is a slight phase shift in the time response and an increase in the amplitude.

We continued our analysis of the effect of rounding the corners of scatterers on the near- and far-fields by extending the scattering problems studied to arrays of two and four scatterers. The main area of interest lies in the strength of the coupling between the scatterers, that is, the degree to which scattering from a single scatterer is changed by the presence of other scatterers. Firstly, we demonstrated that the number of quadrature points required on each scatterer for a desired degree of accuracy is nearly the same whether we are solving a single or multiple scatterer problem. The dependency is on the scatterer shape, not the geometry of the scatterer array. The accuracy of the solution for a given number of quadrature points varies by at most one and occasionally two significant digits. Secondly, we examined the relative differences of the far-field solutions produced by arrays of two and four scatterers using the L^1 and L^∞ norms. As in the case of single scatterers, the smaller the radius of curvature used for the rounding, the smaller the measured relative difference. Increasing the number of scatterers from one to two and then four, does not increase the relative norm differences by an equivalent ratio. The effect of rounding on arrays of scatterers is of a similar order as that of a single scatterer, and sometimes even less. Thirdly, we showed that the bounds on the far-field differences $\sqrt{k}\|u_0^\infty - u_\rho^\infty\|_\infty$ established for single scatterers hold for scatterer arrays.

We used a classical coupling method for the two and four scatterer array problems, combined with the Nyström scheme using graded mesh. This produces highly accurate solutions but is computationally demanding as the number of scatterers increases. For investigations into larger scatterer arrays alternative methods need to be considered, and we used TMATROM [27], a Matlab object-oriented T-matrix software package. We detailed the steps undertaken to implement the package: adding into TMATROM all the scatterer geometries we are studying and more crucially, incorporating our own forward solver for scatterers with corners. We compared the results for single scatterers of the far-field produced by TMATROM equipped with our corner solver to those produced using our original code using the L^2 and L^∞ norms to measure the differences. A high order of agreement was demonstrated: order 10^{-10} to 10^{-15} , which validates our earlier results. We also tested the two and four scatterer array problems studied using the TMATROM

features for multiple scatterer problems: generating the T-matrix for a geometry once and employing the translation-addition theorem methods that use the generated T-matrix. We found that the TROM package provides an efficient method for solving multiple scatterer problems, producing accurate solutions when the scatterers are separated by at least half the scatterer diameter. In these cases, the solutions produced using TROM equipped with our cornered solver are within the error bound introduced by the use of the translation-addition theorem (10^{-8}). As the scatterer separation decreases from less than half the scatterer diameter, the accuracy of the solution also decreases down to order 10^{-3} in some cases. More importantly, if the scatterer separation is such that the encapsulating circle required by TROM encroaches into the space occupied by another scatterer in the arrangement, an accurate result is unable to be achieved and alternative methods for those scatterer problems should be considered.

We concluded this thesis by utilising our implementation of TROM to study some of the properties of large scatterer arrays of cornered structures. We numerically demonstrated that finite grating converges to infinite grating results with an appropriate scaling. We established a bound on the differences between the far-fields $\left| \frac{|u_N^\infty|}{N} - \frac{|u_{N_{\max}}^\infty|}{N_{\max}} \right| \leq \frac{C}{N^m}$, for some constant C dependent on the scatterer shape, configuration, boundary condition and incident field direction. The power m is ~ 1.2 for single arrays and ~ 1.3 for double arrays, except for configurations with side-fire (with grating lobes occurring at far-field observation angle $\hat{\theta} = \pi/2$ and $3\pi/2$), where the rate of convergence is slower. We also demonstrated that we were able to simulate infinite array behaviour such as the appearance of diffraction grating lobes with a finite number of scatterers. This qualitative feature provides a different sort of test of the ability of our simulation to predict important physical phenomena associated with arrays and gratings. We established that TROM provides an effective and efficient tool for studying termination effects, that is the difference between finite and infinite array scattering grating lobes. For the array structures studied, it appears that N must be chosen to be at least 64 for the differences between the finite and infinite structures to be negligible.

This thesis has considered single and multiple closed scatterers with corners. It would be fruitful to study the corresponding scattering problems for open scatterers with corners, or scatterers with slits or cavities.

Appendices

Appendix A

Problem Formulation Details

A.1 Singularity of the Green's Function

The two-dimensional free-space Green's function (2.23) has a singularity when $\mathbf{x} = \mathbf{y}$. In this section we show that this singularity is logarithmic and as such integrable. We can express the Green's function (2.23) in terms of Bessel functions as

$$G(\mathbf{x}, \mathbf{y}) = \frac{i}{4} J_0(k |\mathbf{x} - \mathbf{y}|) - \frac{1}{4} Y_0(k |\mathbf{x} - \mathbf{y}|). \quad (\text{A.1})$$

The Bessel function of the first kind $J_0(x)$ is analytic and bounded, but the Neumann function $Y_0(x)$ is singular at $x = 0$. Since we need to integrate (A.1) with respect to \mathbf{y} on a domain containing \mathbf{x} , we will have an instance of $\mathbf{x} = \mathbf{y}$ when $\mathbf{x} \in \partial D$ and the Green's function will be singular. We will now show that the Neumann function's singularity is of logarithmic magnitude and that

$$\lim_{x \rightarrow 0^+} \left(\frac{i}{4} H_0^{(1)}(x) + \frac{1}{2\pi} \ln \frac{x}{2} \right) = \frac{i}{4} + \frac{\gamma}{2\pi}, \quad (\text{A.2})$$

where γ is Euler's constant. This allows us to then integrate these singular functions since the natural logarithm has an integrable singularity.

The expansion of $Y_0(x)$ is [120] :

$$Y_0(x) = \frac{2}{\pi} \left(J_0(x) \left(\ln \left(\frac{x}{2} \right) + \gamma \right) + \sum_{m=1}^{\infty} \frac{(-1)^{m-1} h_m}{2^{2m} (m!)^2} x^{2m} \right), \quad (\text{A.3})$$

where γ is Euler's constant and $h_m = 1 + \frac{1}{2} + \frac{1}{3} + \dots + \frac{1}{m}$. Now

$$\lim_{x \rightarrow 0^+} J_0(x) = 1, \quad (\text{A.4})$$

and

$$\lim_{x \rightarrow 0^+} \sum_{m=1}^{\infty} \frac{(-1)^{m-1} h_m}{2^{2m} (m!)^2} x^{2m} = 0, \quad (\text{A.5})$$

since the sum is absolutely convergent for all values of x . Thus as $x \rightarrow 0^+$,

$$Y_0(x) \sim \frac{2}{\pi} \ln \left(\frac{x}{2} \right), \quad (\text{A.6})$$

which clearly shows the logarithmic singularity.

We now consider the difference between $Y_0(x)$ and its logarithmic approximation near $x = 0$:

$$\begin{aligned} & \lim_{x \rightarrow 0^+} Y_0(x) - \frac{2}{\pi} \ln \left(\frac{x}{2} \right) \\ &= \lim_{x \rightarrow 0^+} \frac{2}{\pi} \left(J_0(x) \left(\ln \left(\frac{x}{2} \right) - \gamma \right) + \sum_{m=1}^{\infty} \frac{(-1)^{m-1} h_m}{2^{2m} (m!)^2} x^{2m} \right) - \frac{2}{\pi} \ln \left(\frac{x}{2} \right) \\ &= \lim_{x \rightarrow 0^+} \left(\frac{2}{\pi} (J_0(x) - 1) \ln \left(\frac{x}{2} \right) - \frac{2}{\pi} \gamma J_0(x) \right) \\ &= \lim_{x \rightarrow 0^+} \frac{2}{\pi} (J_0(x) - 1) \ln \left(\frac{x}{2} \right) + \frac{2\gamma}{\pi}, \end{aligned} \quad (\text{A.7})$$

using (A.4) and (A.5). The expansion of $J_0(x)$ is [120]:

$$J_0(x) = \sum_{m=0}^{\infty} \frac{(-1)^m x^{2m}}{2^{2m} (m!)^2}, \quad (\text{A.8})$$

so

$$\lim_{x \rightarrow 0^+} \left(\frac{J_0(x) - 1}{x^2} \right) = -\frac{1}{4}. \quad (\text{A.9})$$

Thus

$$\lim_{x \rightarrow 0^+} (J_0(x) - 1) \ln \left(\frac{x}{2} \right) = \lim_{x \rightarrow 0^+} \left(\frac{J_0(x) - 1}{x^2} \right) \lim_{x \rightarrow 0^+} \left(x^2 \ln \left(\frac{x}{2} \right) \right) = 0, \quad (\text{A.10})$$

using $x^2 \ln x \rightarrow 0$ as $x \rightarrow 0$. Thus

$$\lim_{x \rightarrow 0^+} Y_0(x) - \frac{2}{\pi} \ln \left(\frac{x}{2} \right) = \frac{-2\gamma}{\pi}, \quad (\text{A.11})$$

and

$$\begin{aligned} \lim_{x \rightarrow 0^+} \left(\frac{i}{4} H_0^{(1)}(x) + \frac{1}{2\pi} \ln \frac{x}{2} \right) &= \lim_{x \rightarrow 0^+} \left(\frac{i}{4} J_0(x) - \frac{1}{4} \left(Y_0(x) - \frac{2}{\pi} \ln \left(\frac{x}{2} \right) \right) \right) \\ &= \frac{i}{4} + \frac{\gamma}{2\pi}. \end{aligned} \quad (\text{A.12})$$

A.2 The Nyström Method

In Section 2.4.4 we reformulated our scattering problem as integral equations. These integral equations, in general, cannot be solved analytically, and a numerical method is needed to approximate the solutions of these equations.

Consider the general integral equation on $[0, 2\pi]$,

$$\varphi(t) + \int_0^{2\pi} \hat{K}(t, \tau) \varphi(\tau) d\tau = g(t), \quad t \in [0, 2\pi], \quad (\text{A.13})$$

where \hat{K} is the kernel of an integral operator $\hat{\mathcal{K}}$, which we wish to solve for φ , that is, the corresponding operator equation we wish to solve is $(I + \hat{\mathcal{K}}) \varphi = g$ for φ . The Nyström method uses a quadrature rule

$$\int_0^{2\pi} h(t) dx \approx \sum_{k=1}^n w_k h(t_k), \quad (\text{A.14})$$

for a set of quadrature points t_k and weights w_k to discretise an integral equation. For example, using the set of quadrature points

$$t_j = \frac{\pi j}{n}, \quad \text{for } j = 0, \dots, 2n-1, \quad (\text{A.15})$$

the integral equation (A.13) using the Nyström method is approximated by

$$\varphi(t) + \sum_{j=0}^{2n-1} w_j \hat{K}(t, t_j) \varphi(t_j) \approx g(t), \quad (\text{A.16})$$

for all $t \in [0, 2\pi]$. Requiring that equality holds in (A.16) for the quadrature points (A.15) produces an approximation φ_i for $\varphi(t_i)$, given by

$$\varphi_i + \sum_{j=0}^{2n-1} w_j \hat{K}(t_i, t_j) \varphi_j = g(t_i), \quad \text{for } i = 0, \dots, 2n-1. \quad (\text{A.17})$$

This set of $2n$ equations with $2n$ unknowns $\varphi_0, \dots, \varphi_{2n-1}$ has the matrix representation

$$\begin{pmatrix} 1 + \hat{K}_{0,0}w_0 & \hat{K}_{0,1}w_1 & \dots & \hat{K}_{0,2n-1}w_{2n-1} \\ \hat{K}_{1,0}w_0 & 1 + \hat{K}_{1,1}w_1 & \dots & \hat{K}_{1,2n-1}w_{2n-1} \\ \vdots & \vdots & \ddots & \vdots \\ \hat{K}_{2n-1,0}w_0 & \hat{K}_{2n-1,1}w_1 & \dots & 1 + \hat{K}_{2n-1,2n-1}w_{2n-1} \end{pmatrix} \begin{pmatrix} \varphi_0 \\ \varphi_1 \\ \vdots \\ \varphi_{2n-1} \end{pmatrix} = \begin{pmatrix} g_0 \\ g_1 \\ \vdots \\ g_{2n-1} \end{pmatrix} \quad (\text{A.18})$$

where $\hat{K}_{i,j} = \hat{K}(t_i, t_j)$. If the matrix in (A.18) is invertible, we can solve this linear system for $\varphi_0, \dots, \varphi_{2n-1}$.

The method may be straightforwardly applied when the kernel $\hat{K}(t, \tau)$ is continuous. The convergence of the approximate solution to the exact solution as $N \rightarrow \infty$ has been well established in the literature [109, 142]. The method needs adaptation when the kernel has a diagonal singularity. This adaptation is detailed in the following section.

A.2.1 The Nyström Method and the Kernel Singularities

In Section 2.4.4 we formulated the solution of various scattering problems as the solution of appropriate integral equations. In Section 2.5 we transformed these integral equations into line integral form: the exterior Dirichlet problem (2.56) is

$$\varphi(t) + \int_0^{2\pi} \{K_0(t, \tau) - i\eta S_0(t, \tau)\} \varphi(\tau) d\tau = g(t), \quad 0 \leq t \leq 2\pi, \quad (\text{A.19})$$

the exterior Neumann problem (2.57)

$$-\varphi(t) + \int_0^{2\pi} K'_0(t, \tau) \varphi(\tau) d\tau = h(t), \quad 0 \leq t \leq 2\pi, \quad (\text{A.20})$$

and the impedance problem (2.58)

$$-\varphi(t) + \int_0^{2\pi} \{K'_0(t, \tau) + ik\lambda S_0(t, \tau)\} \varphi(\tau) d\tau = m(t), \quad 0 \leq t \leq 2\pi. \quad (\text{A.21})$$

The outward pointing unit normal at $\mathbf{x}(\tau)$ is

$$\mathbf{n}(\mathbf{x}(\tau)) = \frac{(x'_2(\tau), -x'_1(\tau))}{J(\tau)}, \quad (\text{A.22})$$

where $J(\tau)$ is the Jacobian factor

$$J(\tau) = \sqrt{(x'_1(\tau))^2 + (x'_2(\tau))^2} = |\mathbf{x}'(\tau)|. \quad (\text{A.23})$$

Thus for $t \neq \tau$, the kernels are as follows:

$$\begin{aligned} K_0(t, \tau) &= 2 \frac{\partial G(t, \tau)}{\partial \mathbf{n}(\tau)} J(\tau) \\ &= 2 \nabla_{\mathbf{x}(\tau)} G(\mathbf{x}(t), \mathbf{x}(\tau)) \cdot \mathbf{n}(\mathbf{x}(\tau)) J(\mathbf{x}(\tau)) \\ &= \frac{ik}{2} \frac{H_1^{(1)}(k|\mathbf{x}(t) - \mathbf{x}(\tau)|)}{|\mathbf{x}(t) - \mathbf{x}(\tau)|} (\mathbf{x}(t) - \mathbf{x}(\tau)) \cdot (x'_2(\tau), -x'_1(\tau)) \\ &= -\frac{ik}{2} \{x'_2(\tau)[x_1(\tau) - x_1(t)] - x'_1(\tau)[x_2(\tau) - x_2(t)]\} \frac{H_1^{(1)}(k|\mathbf{x}(t) - \mathbf{x}(\tau)|)}{|\mathbf{x}(t) - \mathbf{x}(\tau)|}, \end{aligned} \quad (\text{A.24})$$

$$\begin{aligned} S_0(t, \tau) &= 2G(t, \tau)J(\tau) \\ &= 2G(\mathbf{x}(t), \mathbf{x}(\tau))J(\mathbf{x}(\tau)) \\ &= \frac{i}{2} H_0^{(1)}(k|\mathbf{x}(t) - \mathbf{x}(\tau)|) |\mathbf{x}'(\tau)|, \end{aligned} \quad (\text{A.25})$$

and

$$\begin{aligned} K'_0(t, \tau) &= 2 \frac{\partial G(t, \tau)}{\partial \mathbf{n}(t)} J(\tau) \\ &= 2 \nabla_{\mathbf{x}(t)} G(\mathbf{x}(t), \mathbf{x}(\tau)) \cdot \mathbf{n}(\mathbf{x}(t)) J(\mathbf{x}(\tau)) \\ &= -\frac{ik}{2} \frac{H_1^{(1)}(k|\mathbf{x}(t) - \mathbf{x}(\tau)|)}{|\mathbf{x}(t) - \mathbf{x}(\tau)|} (\mathbf{x}(t) - \mathbf{x}(\tau)) \cdot \frac{(x'_2(t), -x'_1(t))}{J(t)} J(\tau) \\ &= -\frac{ik}{2} \frac{\{x'_2(t)[x_1(t) - x_1(\tau)] - x'_1(t)[x_2(t) - x_2(\tau)]\}}{|\mathbf{x}'(t)|} \frac{H_1^{(1)}(k|\mathbf{x}(t) - \mathbf{x}(\tau)|)}{|\mathbf{x}(t) - \mathbf{x}(\tau)|} |\mathbf{x}'(\tau)|. \end{aligned} \quad (\text{A.26})$$

The kernel S_0 has a logarithmic singularity when $t = \tau$. In Appendix A.1 we showed that this singularity is integrable. Using the Nyström method as described in Section A.2, we observe that the diagonal values of the resultant matrix (A.18), which we use to

solve the integrals, are singular. We must adapt the method to take account of the kernel singularity. Moreover the kernels K_0 and K'_0 , although continuous, have a logarithmic singularity in their derivatives; the use of a simple quadrature rule such as the trapezoidal rule will not provide exponentially fast convergence. The Martensen-Kusmaul method of splitting the singularity [7, p.76-79] provides an effective means of obtaining super-algebraic convergence.

A.2.2 The Martensen-Kusmaul Method

The Martensen-Kusmaul method splits the kernel to isolate the logarithmic singularity. The smooth components of the kernel are evaluated using the Nyström method with a rectangular quadrature rule. A different quadrature rule is used to estimate the singular part of the kernels. The technique was developed by Martensen [58] and Kusmaul [59] and is described in Colton and Kress [7, p.76-79]. The quadrature rule for the singularity replaces the integrand by its trigonometric interpolation polynomial and integrates this interpolant exactly.

We isolate the singular parts of the kernels (A.24), (A.25) and (A.26) in the following manner,

$$K_0(t, \tau) = K_1(t, \tau) \ln \left(4 \sin^2 \frac{t - \tau}{2} \right) + K_2(t, \tau), \quad (\text{A.27})$$

$$S_0(t, \tau) = S_1(t, \tau) \ln \left(4 \sin^2 \frac{t - \tau}{2} \right) + S_2(t, \tau), \quad (\text{A.28})$$

$$K'_0(t, \tau) = K'_1(t, \tau) \ln \left(4 \sin^2 \frac{t - \tau}{2} \right) + K'_2(t, \tau). \quad (\text{A.29})$$

The kernels K_1 , K_2 , S_1 , S_2 , K'_1 and K'_2 are analytic [7, p.77], and are defined as

$$K_1(t, \tau) = \frac{-ik}{2\pi} \{x'_2(\tau)[x_1(\tau) - x_1(t)] - x'_1(\tau)[x_2(\tau) - x_2(t)]\} \frac{J_1(k|\mathbf{x}(t) - \mathbf{x}(\tau)|)}{|\mathbf{x}(t) - \mathbf{x}(\tau)|}, \quad (\text{A.30})$$

$$K_2(t, \tau) = K(t, \tau) - K_1(t, \tau) \ln \left(4 \sin^2 \frac{t - \tau}{2} \right), \quad (\text{A.31})$$

$$S_1(t, \tau) = -\frac{1}{2\pi} J_0(k|\mathbf{x}(t) - \mathbf{x}(\tau)|) |\mathbf{x}'(\tau)|, \quad (\text{A.32})$$

$$S_2(t, \tau) = S(t, \tau) - S_1(t, \tau) \ln \left(4 \sin^2 \frac{t - \tau}{2} \right), \quad (\text{A.33})$$

$$K_1'(t, \tau) = \frac{-ik}{2} \frac{\{x_2'(t)[x_1(t) - x_1(\tau)] - x_1'(t)[x_2(t) - x_2(\tau)]\}}{|\mathbf{x}'(t)|} \frac{J_1^{(1)}(k|\mathbf{x}(t) - \mathbf{x}(\tau)|)}{|\mathbf{x}(t) - \mathbf{x}(\tau)|} |\mathbf{x}'(\tau)|, \quad (\text{A.34})$$

$$K_2'(t, \tau) = K'(t, \tau) - K_1'(t, \tau) \ln \left(4 \sin^2 \frac{t - \tau}{2} \right). \quad (\text{A.35})$$

For the diagonal terms of the K_2 and K_2' we use the limit as $t \rightarrow \tau$ of (A.24) and (A.26) respectively. Thus

$$K_2(t, t) = \frac{-1}{2\pi} \frac{x_1'(t)x_2''(t) - x_2'(t)x_1''(t)}{|\mathbf{x}'(t)|^2}, \quad (\text{A.36})$$

$$K_2'(t, t) = \frac{1}{2\pi} \frac{x_1'(t)x_2''(t) - x_2'(t)x_1''(t)}{|\mathbf{x}'(t)|^2}. \quad (\text{A.37})$$

The limiting value for the S_2 kernel may be calculated to be [7, p.73]

$$S_2(t, t) = \left\{ \frac{i}{2} - \frac{C}{\pi} - \frac{1}{\pi} \ln \left(\frac{k}{2} |\mathbf{x}'(t)| \right) \right\} |\mathbf{x}'(t)|. \quad (\text{A.38})$$

Thus in general terms, we will numerically solve integral equations of the form

$$\varphi(t) + \int_0^{2\pi} \hat{K}_0(t, \tau) \varphi(\tau) d\tau = g(t), \quad (\text{A.39})$$

where the kernel \hat{K} represents any of the kernels (A.27), (A.28) and (A.29), and may be written in the form

$$\hat{K}_0(t, \tau) = \hat{K}_1(t, \tau) \ln \left(4 \sin^2 \frac{t - \tau}{2} \right) + \hat{K}_2(t, \tau), \quad (\text{A.40})$$

where \hat{K}_1 and \hat{K}_2 are analytic. The smooth components of the kernel $\hat{K}_0(t, \tau)$ are evaluated using the trapezoidal rule to approximate

$$\int_0^{2\pi} \hat{K}_2(t, \tau) \varphi(\tau) d\tau \approx \frac{\pi}{n} \sum_{j=0}^{2n-1} \hat{K}_2(t, t_j) \varphi(\tau_j) dt. \quad (\text{A.41})$$

A different quadrature rule is used to estimate the singular part of the kernel $\hat{K}_0(t, \tau)$ which replaces the integrand by its trigonometric interpolation polynomial and integrates

this interpolant exactly. The following quadrature rule

$$\int_0^{2\pi} \ln \left(4 \sin^2 \frac{t-\tau}{2} \right) \hat{K}_1(t, \tau) d\tau \approx \sum_{j=0}^{2n-1} R_j^{(n)}(t) \hat{K}_1(t, t_j), \quad \text{for } 0 \leq t \leq 2\pi, \quad (\text{A.42})$$

is used to approximate the integral of the logarithmic part of the kernel $\hat{K}_0(t, \tau)$. The quadrature weights $R_j^{(n)}$ are given by

$$R_j^{(n)}(t) = -\frac{2\pi}{n} \sum_{m=1}^{n-1} \frac{1}{m} \cos m(t - t_j) - \frac{\pi}{n^2} \cos n(t - t_j), \quad \text{for } j = 0, \dots, 2n-1. \quad (\text{A.43})$$

Discretising in the same manner as (A.17) with $\varphi_i \approx \varphi(t_i)$ produces

$$\varphi_i + \sum_{j=0}^{2n-1} \left[R_{|i-j|}(t) \{K_1(t_i, t_j) - i\eta S_1(t_i, t_j)\} + \frac{\pi}{n} \{K_2(t_i, t_j) - i\eta S_2(t_i, t_j)\} \right] \varphi_j = g(t_i), \quad (\text{A.44})$$

for $i = 0, \dots, 2n-1$, and

$$-\varphi_i + \sum_{j=0}^{2n-1} \left[R_{|i-j|}(t) K_1'(t_i, t_j) + \frac{\pi}{n} K_2'(t_i, t_j) \right] \varphi_j = h(t_i), \quad (\text{A.45})$$

for $i = 0, \dots, 2n-1$, and

$$\begin{aligned} -\varphi_i + \sum_{j=0}^{2n-1} \left[R_{|i-j|}(t) \{K_1'(t_i, t_j) + ik\lambda S_1(t_i, t_j)\} + \frac{\pi}{n} \{K_2'(t_i, t_j) + ik\lambda S_2(t_i, t_j)\} \right] \varphi_j \\ = m(t_i), \end{aligned} \quad (\text{A.46})$$

for $i = 0, \dots, 2n-1$, as the discretised formulations of the integral equations (A.19), (A.20) and (A.21) respectively.

Figures A.1a, A.1b, A.1c, A.1d, A.1e and A.1f plot the kernels K_1 , K_2 , S_1 , S_2 , K_1' , and K_2' respectively, for a fixed value of $t(\frac{\pi}{4})$ and varying τ , on a circular scatterer radius 1, using a wave number $k = \pi$. The figures demonstrate the smoothness of these kernels as a result of the singularity being isolated in (A.27), (A.28) and (A.29).

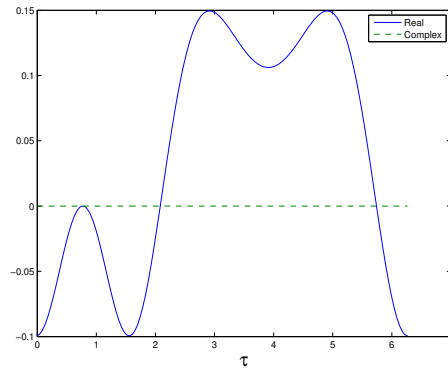
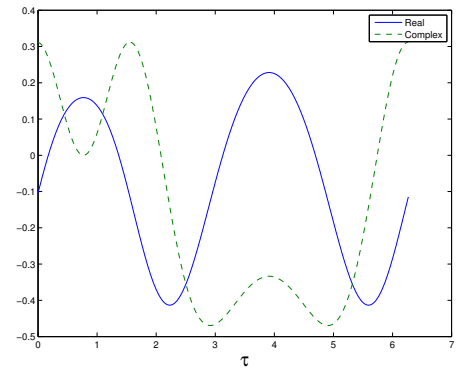
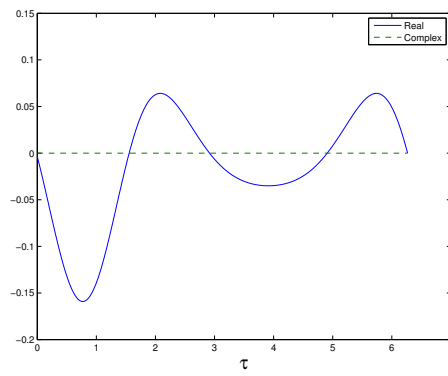
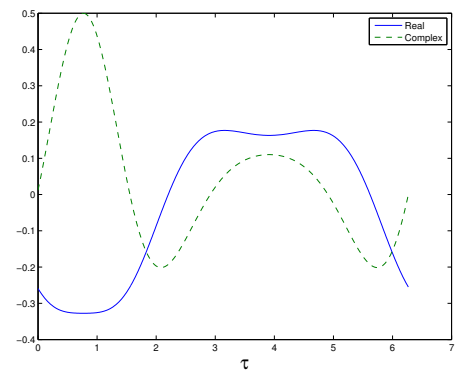
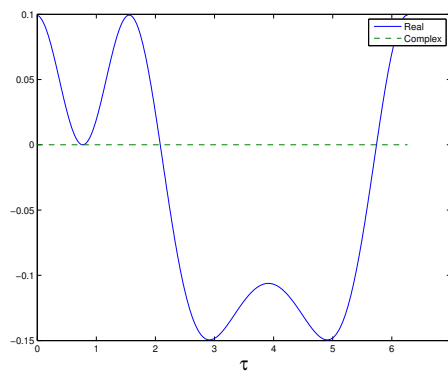
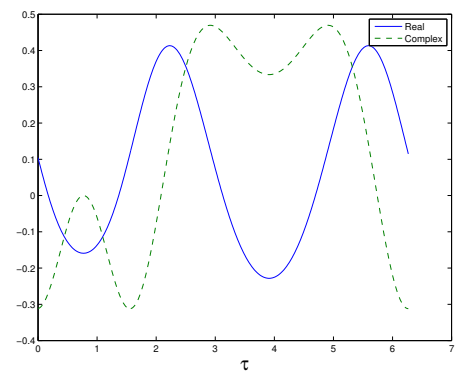
(a) $K_1\left(\frac{\pi}{4}, \tau\right)$ (b) $K_2\left(\frac{\pi}{4}, \tau\right)$ (c) $S_1\left(\frac{\pi}{4}, \tau\right)$ (d) $S_2\left(\frac{\pi}{4}, \tau\right)$ (e) $K'_1\left(\frac{\pi}{4}, \tau\right)$ (f) $K'_2\left(\frac{\pi}{4}, \tau\right)$

Figure A.1

A.3 The Dirichlet Boundary Condition and Structures with Corners

Implementation of the graded mesh ensures an exponentially fast convergence rate (as a function of n) for scatterers with one or two corners with the Neumann and impedance boundary conditions. In the case where these scatterers have a Dirichlet boundary condition further modifications are necessary to achieve comparable convergence rates. For these domains the kernel of (2.39) is no longer weakly singular at the corner. The following section presents in detail the method in [7] to enable integration of this stronger singularity.

A.3.1 Single Cornered Domains

The modification for domains with a single corner at \mathbf{x}_0 and the Dirichlet boundary condition [7], uses the fundamental solution

$$G_0(\mathbf{x}, \mathbf{y}) = \frac{1}{2\pi} \ln \frac{1}{|\mathbf{x} - \mathbf{y}|}, \quad \mathbf{x} \neq \mathbf{y}, \quad (\text{A.47})$$

to the Laplace equation in \mathbb{R}^2 to subtract a vanishing term. This transforms (2.39) into

$$u^{\text{sc}}(\mathbf{x}) = \int_{\partial D} \left\{ \left\{ \frac{\partial G(\mathbf{x}, \mathbf{y})}{\partial \mathbf{n}(\mathbf{y})} - i\eta G(\mathbf{x}, \mathbf{y}) \right\} \varphi(\mathbf{y}) - \frac{\partial G_0(\mathbf{x}, \mathbf{y})}{\partial \mathbf{n}(\mathbf{y})} \varphi(\mathbf{x}_0) \right\} ds(\mathbf{y}), \quad \mathbf{x} \in \mathbb{R}^2 \setminus \bar{D}, \quad (\text{A.48})$$

and the associated boundary equation (2.41) is reformulated as

$$\begin{aligned} \varphi(\mathbf{x}) - \varphi(\mathbf{x}_0) + 2 \int_{\partial D} \left\{ \frac{\partial G(\mathbf{x}, \mathbf{y})}{\partial \mathbf{n}(\mathbf{y})} - i\eta G(\mathbf{x}, \mathbf{y}) \right\} \varphi(\mathbf{y}) ds(\mathbf{y}) \\ - 2 \int_{\partial D} \frac{\partial G_0(\mathbf{x}, \mathbf{y})}{\partial \mathbf{n}(\mathbf{y})} \varphi(\mathbf{x}_0) ds(\mathbf{y}) = -2u^{\text{inc}}(\mathbf{x}), \quad \mathbf{x} \in \partial D. \end{aligned} \quad (\text{A.49})$$

An analysis showing the existence of a solution to (A.49) is provided in [7]. The integral equation (A.49) is rewritten in parameterised form

$$\varphi(t) - \varphi(0) - \int_0^{2\pi} \hat{K}(t, \tau) \varphi(\tau) d\tau - \int_0^{2\pi} H(t, \tau) \varphi(0) d\tau = g(t), \quad 0 \leq t \leq 2\pi, \quad (\text{A.50})$$

where

$$H(t) = \begin{cases} \frac{1}{\pi} \frac{x'_2(\tau)[x_1(t) - x_1(\tau)] - x'_1(\tau)[x_2(t) - x_2(\tau)]}{|\mathbf{x}(t) - \mathbf{x}(\tau)|^2}, & t \neq \tau, \\ \frac{1}{2\pi} \frac{x'_2(t)x''_1(t) - x'_1(t)x''_2(t)}{|\mathbf{x}'(t)|^2}, & t = \tau, t \neq 0, 2\pi, \end{cases} \quad (\text{A.51})$$

and

$$\hat{K}(t, \tau) = K(t, \tau) - i\eta S(t, \tau), \quad 0 \leq t \leq 2\pi. \quad (\text{A.52})$$

We now apply the substitution (2.60) to (A.50) and obtain

$$\begin{aligned} \int_0^{2\pi} \hat{K}(t, \tau) \varphi(\tau) d\tau - \int_0^{2\pi} H(t, \tau) \varphi(0) d\tau &= \int_0^{2\pi} \hat{K}(w(s), w(\sigma)) w'(\sigma) \varphi(w(\sigma)) d\sigma \\ &\quad - \int_0^{2\pi} H(w(s), w(\sigma)) w'(\sigma) \varphi(0) d\sigma. \end{aligned} \quad (\text{A.53})$$

The logarithmic singularity present in the kernel $\hat{K}(t, \tau)$ remains to be accounted for. This is done in the same manner as (2.64). Using the quadrature rules (A.41) and (A.42) to discretise the kernel, and the trapezoidal rule to discretise the kernel $H(t, \tau)$ and $\varphi_0 = \varphi(0)$ at the corner $s_0 = 0$ gives

$$\begin{aligned} \varphi_i - \varphi_0 + \sum_{j=1}^{2n-1} [R_{|i-j|}(t) \{K_1(w(s_i), w(s_j)) - i\eta S_1(w(s_i), w(s_j))\} \\ + \frac{\pi}{n} \{K_2(w(s_i), w(s_j)) - i\eta S_2(w(s_i), w(s_j))\}] a_j \varphi_j \\ - \sum_{j=1}^{2n-1} \frac{\pi}{n} H(w(s_i), w(s_j)) a_j \varphi_0 = g(w(s_i)), \quad \text{for } i = 0, \dots, 2n-1. \end{aligned} \quad (\text{A.54})$$

We have obtained a system of $2n-1$ linear equations for the boundary values $\varphi(t_j)$, for $j = 1, 2, \dots, 2n-1$, that is a discretisation of the integral equation (A.49). The solution is obtained by the usual Gaussian elimination procedure.

The described modification (A.49) applied to (2.41) ensures that exponentially fast convergence is achieved for scatterers with the Dirichlet boundary condition and a single corner on ∂D .

Appendix B

Comparison to Rawlins' Results

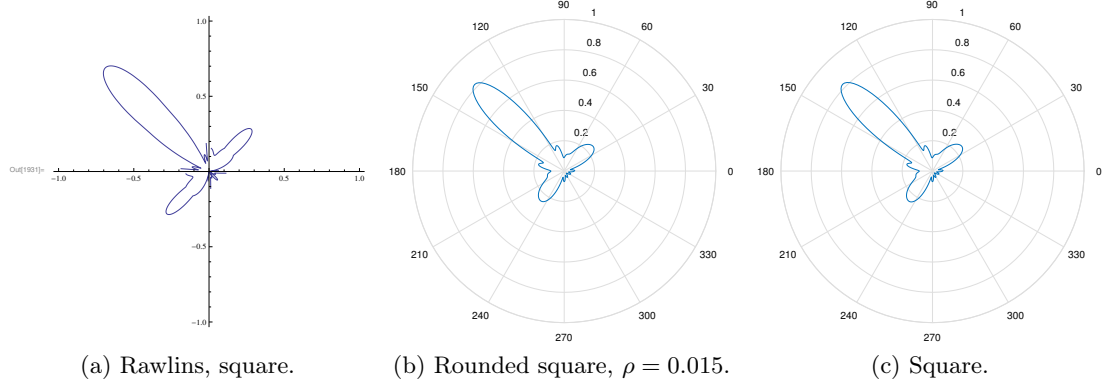


Figure B.1: Plot of $u^{\text{sc}}(\mathbf{x})$, for $\mathbf{x} = 10(\cos t, \sin t)$, $t \in [0, 2\pi]$. Impedance parameter $1+i$. Incident wave direction $\theta_0 = 3\pi/4$, wave number $k = 2\pi$.

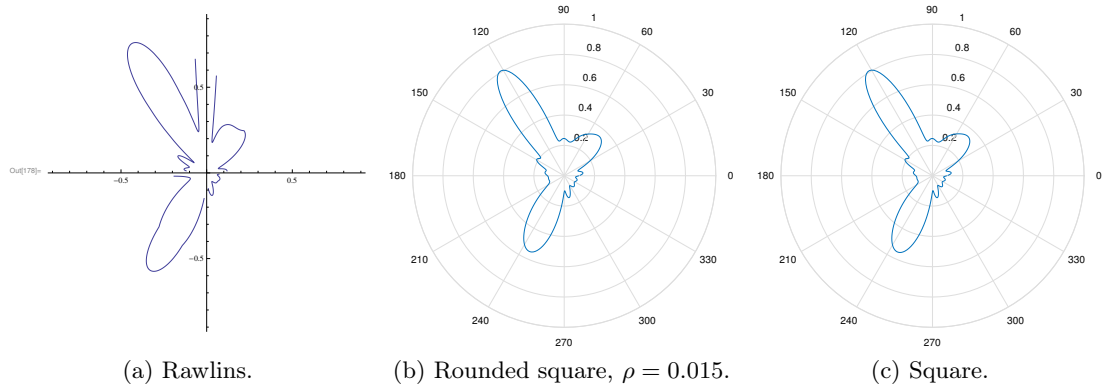


Figure B.2: Plot of $u^{\text{sc}}(\mathbf{x})$, for $\mathbf{x} = 10(\cos t, \sin t)$, $t \in [0, 2\pi]$. Impedance parameter $1+10i$. Incident wave direction $\theta_0 = 2\pi/3$, wave number $k = 2\pi$.

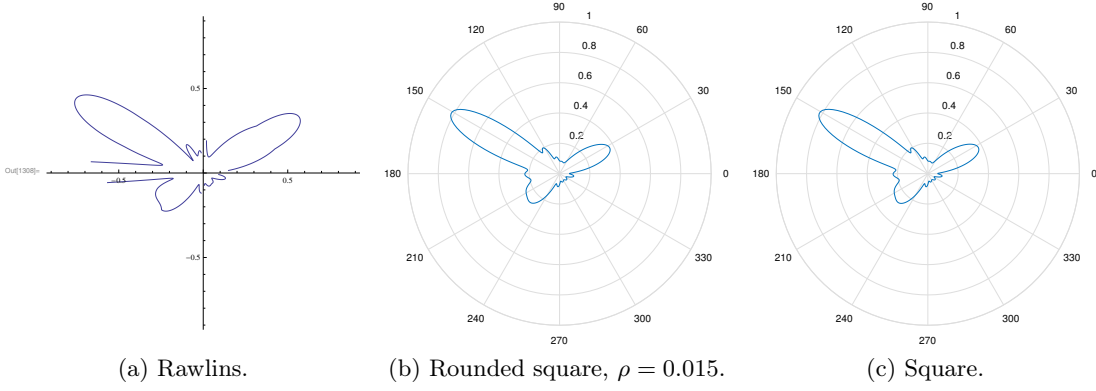


Figure B.3: Plot of $u^{\text{sc}}(\mathbf{x})$, for $\mathbf{x} = 10(\cos t, \sin t)$, $t \in [0, 2\pi]$. Impedance parameter $4 + i$. Incident wave direction $\theta_0 = 5\pi/6$, wave number $k = 2\pi$.

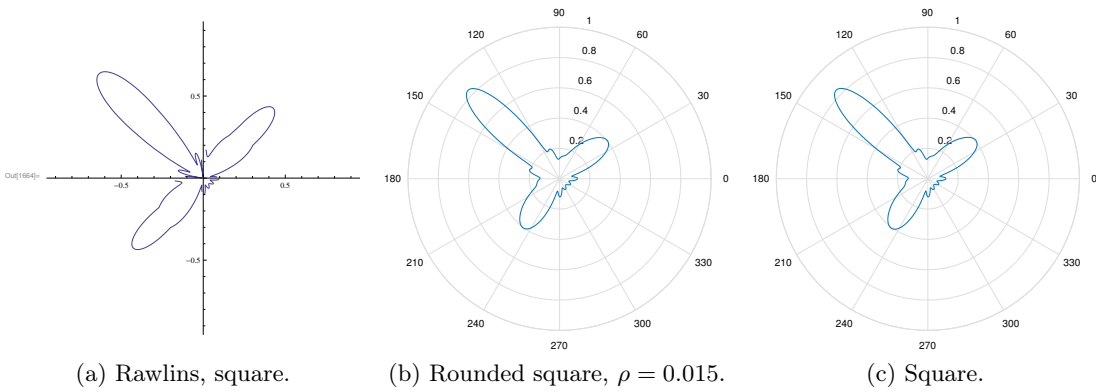


Figure B.4: Plot of $u^{\text{sc}}(\mathbf{x})$, for $\mathbf{x} = 10(\cos t, \sin t)$, $t \in [0, 2\pi]$. Impedance parameter $10 + i$. Incident wave direction $\theta_0 = 3\pi/4$, wave number $k = 2\pi$.

Appendix C

Bounds Analysis Supporting Details

This chapter contains supporting Lemmas and numerical results for Chapter 4.

After introducing suitable surface parameterisations for the rounded and cornered scatterers, we analyse the underlying integral equations for each scatterer, and deduce an approximate integral equation for the difference in the surface density, in terms of the difference in the illuminating incident field at corresponding points on each scatterer and of the surface quantity on the sharp cornered object. We take the lemniscate and its rounded counterpart scatterer studied in Chapter 3 as a test case. The approximate solution of the integral equation is shown to be $O((k\rho)^{2/3})$, from which it is deduced that $\sqrt{k} \|u_0^\infty - u_\rho^\infty\|_\infty = O((k\rho)^{4/3})$, as $k\rho \rightarrow 0$.

C.1 Lemmas used in Chapter 4

Lemma C.1.1 *The rounded lemniscate with the following parameterisation,*

$$\mathbf{x}_\varepsilon(t) = \left(2\sqrt{\varepsilon^2 + (1 - \varepsilon^2) \sin^2(t/2)}, -\sin t \right),$$

for $t \in [-\pi, \pi]$, has radius of curvature $\rho = 2\varepsilon + O(\varepsilon^3)$ as $\varepsilon \rightarrow 0$.

Proof. The radius of curvature ρ at the rounded corner points is calculated from the general formula for the parameterised curve $\mathbf{x}(t) = (x_1(t), x_2(t))$,

$$\rho(t) = \left| \frac{(x_1'(t)^2 + x_2'(t)^2)^{3/2}}{x_1'(t)x_2''(t) - x_2'(t)x_1''(t)} \right|, \quad t \in [-\pi, \pi], \quad (\text{C.1})$$

where, in the case of the rounded lemniscate (C.1.1)

$$\mathbf{x}'(t) = \left(\frac{(1 - \varepsilon^2) \sin t}{2\sqrt{\varepsilon^2 + (1 - \varepsilon^2) \sin^2 \frac{t}{2}}}, -\cos t \right), \quad (\text{C.2})$$

and

$$\mathbf{x}''(t) = \left(\frac{(1 - \varepsilon^2) \cos t}{2(\varepsilon^2 + (1 - \varepsilon^2) \sin^2 \frac{t}{2})^{1/2}} - \frac{(1 - \varepsilon^2)^2 \sin^2 t}{8(\varepsilon^2 + (1 - \varepsilon^2) \sin^2 \frac{t}{2})^{3/2}}, \sin t \right). \quad (\text{C.3})$$

At the rounded corner point $t = 0$,

$$\rho(0) = \left| \frac{2\varepsilon}{1 - \varepsilon^2} \right| = 2\varepsilon + O(\varepsilon^3), \quad \text{as } \varepsilon \rightarrow 0. \quad (\text{C.4})$$

■

Lemma C.1.2 *For the lemniscate with the following parameterisation,*

$$\mathbf{x}_0(t) = (2 \sin(|t|/2), -\sin t), \quad (\text{C.5})$$

and the corresponding rounded object depending upon a (small) positive parameter ε ,

$$\mathbf{x}_\varepsilon(t) = \left(2\sqrt{\varepsilon^2 + (1 - \varepsilon^2) \sin^2(t/2)}, -\sin t \right), \quad (\text{C.6})$$

for $t \in J$, where $J = [-\pi, -\varepsilon^{2/3}] \cup [\varepsilon^{2/3}, \pi]$,

$$\|\mathbf{x}_0 - \mathbf{x}_\varepsilon\|_{\infty, J} = \max_{t \in J} |\mathbf{x}_0(t) - \mathbf{x}_\varepsilon(t)| = 4\varepsilon^{4/3} + O(\varepsilon^2),$$

as $\varepsilon \rightarrow 0$. Also,

$$\|\mathbf{x}_0 - \mathbf{x}_\varepsilon\|_\infty = \max_{t \in [-\pi, \pi]} |\mathbf{x}_0(t) - \mathbf{x}_\varepsilon(t)| = 2\varepsilon.$$

Proof.

$$\begin{aligned} |\mathbf{x}_0(t) - \mathbf{x}_\varepsilon(t)| &= \left| 2 \sin(|t|/2) - 2\sqrt{\varepsilon^2 + (1 - \varepsilon^2) \sin^2(t/2)} \right| \\ &= \frac{2\varepsilon^2 \cos^2(|t|/2)}{\sin(|t|/2) + \sqrt{\varepsilon^2 + (1 - \varepsilon^2) \sin^2(t/2)}} \\ &\leq \frac{2\varepsilon^2}{\sin(|t|/2)} \end{aligned}$$

$$\begin{aligned}
&\leq \frac{2\varepsilon^2}{\sin\left(\frac{1}{2}\varepsilon^{2/3}\right)} \\
&= 4\varepsilon^{4/3} + O(\varepsilon^2), \quad \text{as } \varepsilon \rightarrow 0.
\end{aligned} \tag{C.7}$$

The maximum occurs at the end points where $t = \pm\varepsilon^{2/3}$.

Also, if $t \in [-\pi, \pi]$,

$$|\mathbf{x}_0(t) - \mathbf{x}_\varepsilon(t)| = \frac{2\varepsilon^2 \cos^2(|t|/2)}{\sin(|t|/2) + \sqrt{\varepsilon^2 + (1 - \varepsilon^2) \sin^2(t/2)}} \leq 2\varepsilon, \tag{C.8}$$

the maximum being attained at $t = 0$. ■

Lemma C.1.3 *For the lemniscate with the parameterisation (C.5) and the corresponding rounded lemniscate with parameterisation (C.6) and the interval $J = [-\pi, -\varepsilon^{2/3}] \cup [\varepsilon^{2/3}, \pi]$,*

$$\|\mathbf{x}'_0(t) - \mathbf{x}'_\varepsilon(t)\|_{\infty, J} = \max_{t \in J} |\mathbf{x}'_0(t) - \mathbf{x}'_\varepsilon(t)| = 2\varepsilon^{2/3} + O(\varepsilon^{4/3}),$$

as $\varepsilon \rightarrow 0$.

Proof. First fix $t > 0$.

$$\begin{aligned}
|\mathbf{x}'_0(t) - \mathbf{x}'_\varepsilon(t)| &= \left| \cos \frac{t}{2} - \frac{(1 - \varepsilon^2) \sin \frac{t}{2} \cos \frac{t}{2}}{\sqrt{\varepsilon^2 + (1 - \varepsilon^2) \sin^2 \frac{t}{2}}} \right| \\
&\leq \left(1 - \frac{(1 - \varepsilon^2) \sin \frac{t}{2}}{\sqrt{\varepsilon^2 + (1 - \varepsilon^2) \sin^2 \frac{t}{2}}} \right).
\end{aligned} \tag{C.9}$$

Since $t \in J$, we may use the Taylor series expansions,

$$\begin{aligned}
&1 - \frac{(1 - \varepsilon^2) \sin \frac{t}{2}}{\sqrt{\varepsilon^2 + (1 - \varepsilon^2) \sin^2 \frac{t}{2}}} \\
&= 1 - (1 - \varepsilon^2)^{1/2} \left(1 + \frac{\varepsilon^2}{(1 - \varepsilon^2) \sin^2 \frac{t}{2}} \right)^{1/2} \\
&= 1 - \left(1 - \frac{1}{2}\varepsilon^2 - \frac{1}{8}\varepsilon^4 - \text{h.o.t.} \right) \left(1 - \frac{1}{2} \frac{\varepsilon^2}{(1 - \varepsilon^2) \sin^2 \frac{t}{2}} + \frac{3}{8} \frac{\varepsilon^4}{(1 - \varepsilon^2)^2 \sin^4 \frac{t}{2}} + \text{h.o.t.} \right) \\
&= 1 - \left(1 - \frac{1}{2} \frac{\varepsilon^2}{(1 - \varepsilon^2) \sin^2 \frac{t}{2}} + \frac{3}{8} \frac{\varepsilon^4}{(1 - \varepsilon^2)^2 \sin^4 \frac{t}{2}} - \frac{1}{2}\varepsilon^2 - \frac{1}{8}\varepsilon^4 + \text{h.o.t.} \right) \\
&= \frac{1}{2} \frac{\varepsilon^2}{(1 - \varepsilon^2) \sin^2 \frac{t}{2}} + \text{h.o.t.}
\end{aligned} \tag{C.10}$$

Since $t \in J$, this is bounded by

$$\begin{aligned} & \frac{1}{2} \frac{\varepsilon^2}{(\varepsilon^{2/3}/2)^2} + O\left(\varepsilon^{4/3}\right) \\ &= 2\varepsilon^{2/3} + O\left(\varepsilon^{4/3}\right), \quad \text{as } \varepsilon \rightarrow 0. \end{aligned} \tag{C.11}$$

The proof for $t < 0$ is similar, and the result follows. The maximum occurs at the endpoints when $t = \pm\varepsilon^{2/3}$. ■

Lemma C.1.4 *The parameterisations (C.5) and (C.6) obey $|\mathbf{x}'_0(t)| \leq \sqrt{2}$ and $|\mathbf{x}'_\varepsilon(t)| \leq \sqrt{2}$ for $t \in [-\pi, \pi]$.*

Proof.

$$|\mathbf{x}'_0(t)| = \left(\cos^2 \frac{t}{2} + \cos^2 t \right)^{1/2} \leq \sqrt{2}. \tag{C.12}$$

And,

$$\begin{aligned} |\mathbf{x}'_\varepsilon(t)| &= \left(\frac{(1 - \varepsilon^2)^2 \sin^2 \frac{t}{2} \cos^2 \frac{t}{2}}{\varepsilon^2 + (1 - \varepsilon^2) \sin^2 \frac{t}{2}} + \cos^2 t \right)^{1/2} \\ &\leq \left(\frac{(1 - \varepsilon^2)^2 \sin^2 \frac{t}{2}}{\varepsilon^2 + (1 - \varepsilon^2) \sin^2 \frac{t}{2}} + 1 \right)^{1/2} \\ &\leq \left(\frac{(1 - \varepsilon^2)^2 \sin^2 \frac{t}{2}}{(1 - \varepsilon^2) \sin^2 \frac{t}{2}} + 1 \right)^{1/2} \\ &= ((1 - \varepsilon^2) + 1)^{1/2} \\ &\leq \sqrt{2}. \end{aligned} \tag{C.13}$$

■

Lemma C.1.5 *Let $t \in I$, where $I = [-\pi, \pi]$. The static Green's function difference obeys*

$$\int_J |G_0(\mathbf{x}_\varepsilon(t), \mathbf{x}_\varepsilon(\tau)) - G_0(\mathbf{x}_0(t), \mathbf{x}_0(\tau))| d\tau = O\left(\varepsilon^{2/3}\right), \quad \text{as } \varepsilon \rightarrow 0. \quad (\text{C.14})$$

Proof. Without loss of generality, we may suppose $t > 0$.

$$\begin{aligned} & |G_0(\mathbf{x}_\varepsilon(t), \mathbf{x}_\varepsilon(\tau)) - G_0(\mathbf{x}_0(t), \mathbf{x}_0(\tau))| \\ &= \frac{1}{2\pi} \left| \log \frac{|\mathbf{x}_0(t) - \mathbf{x}_0(\tau)|}{|\mathbf{x}_\varepsilon(t) - \mathbf{x}_\varepsilon(\tau)|} \right| \\ &= \frac{1}{2\pi} \left| \log \left(1 + \left(\frac{|\mathbf{x}_0(t) - \mathbf{x}_0(\tau)|}{|\mathbf{x}_\varepsilon(t) - \mathbf{x}_\varepsilon(\tau)|} - 1 \right) \right) \right| \\ &\leq \frac{1}{2\pi} \left(\frac{|\mathbf{x}_0(t) - \mathbf{x}_0(\tau)|}{|\mathbf{x}_\varepsilon(t) - \mathbf{x}_\varepsilon(\tau)|} - 1 \right), \quad \text{using } \log(1+z) < z, \text{ for } z > 0 \\ &= \frac{1}{2\pi} \frac{|\mathbf{x}_0(t) - \mathbf{x}_0(\tau)| - |\mathbf{x}_\varepsilon(t) - \mathbf{x}_\varepsilon(\tau)|}{|\mathbf{x}_\varepsilon(t) - \mathbf{x}_\varepsilon(\tau)|} \\ &\leq \frac{1}{2\pi} \frac{|(\mathbf{x}_0(t) - \mathbf{x}_0(\tau)) - (\mathbf{x}_\varepsilon(t) - \mathbf{x}_\varepsilon(\tau))|}{|\mathbf{x}_\varepsilon(t) - \mathbf{x}_\varepsilon(\tau)|}. \end{aligned} \quad (\text{C.15})$$

First suppose $t > 4\varepsilon$. Then

$$\begin{aligned} \mathbf{x}_\varepsilon(t) &= \left(2\sqrt{\varepsilon^2 + (1 - \varepsilon^2) \sin^2(t/2)}, -\sin t \right) \\ &= \left(2\sqrt{\varepsilon^2 \cos^2(t/2) + \sin^2(t/2)}, -\sin t \right) \\ &= \left(2\sin(t/2) \left(1 + \frac{1}{2} \varepsilon^2 \frac{\cos^2(t/2)}{\sin^2(t/2)} \right)^{1/2}, -\sin t \right) \\ &= \left(2\sin(t/2) \left(1 + \frac{1}{2} \varepsilon^2 \frac{\cos^2(t/2)}{\sin^2(t/2)} + \text{h.o.t.} \right), -\sin t \right) \\ &= \left(2\sin(t/2) + \varepsilon^2 \frac{\cos^2(t/2)}{\sin(t/2)} + \text{h.o.t.}, -\sin t \right), \end{aligned} \quad (\text{C.16})$$

as $\varepsilon \rightarrow 0$. Likewise if $\tau > \varepsilon^{2/3}$,

$$\mathbf{x}_\varepsilon(\tau) = \left(2\sin(\tau/2) + \varepsilon^2 \frac{\cos^2(\tau/2)}{\sin(\tau/2)} + \text{h.o.t.}, -\sin \tau \right). \quad (\text{C.17})$$

Recalling that $\mathbf{x}_0(t) = (2\sin(t/2), -\sin t)$, the numerator of the quantity (C.15) is bounded by

$$\varepsilon^2 \left(\frac{\cos^2(t/2)}{\sin(t/2)} - \frac{\cos^2(\tau/2)}{\sin(\tau/2)} \right) + \text{h.o.t.}, \quad (\text{C.18})$$

whilst the denominator is bounded below by

$$\begin{aligned} & \sqrt{\varepsilon^2 + (1 - \varepsilon^2) \sin^2(\tau/2)} - \sqrt{\varepsilon^2 + (1 - \varepsilon^2) \sin^2(t/2)} \\ &= \frac{(1 - \varepsilon^2)(\sin^2(\tau/2) - \sin^2(t/2))}{\sqrt{\varepsilon^2 + (1 - \varepsilon^2) \sin^2(\tau/2)} + \sqrt{\varepsilon^2 + (1 - \varepsilon^2) \sin^2(t/2)}}. \end{aligned} \quad (\text{C.19})$$

Now

$$\sqrt{\varepsilon^2 + (1 - \varepsilon^2) \sin^2(t/2)} < \sqrt{(1 - \varepsilon^2) \sin^2(t/2) + (1 - \varepsilon^2) \sin^2(t/2)} < \sqrt{2} \sin(t/2), \quad (\text{C.20})$$

because $t > 4\varepsilon$. Thus the denominator is bounded below by

$$(1 - \varepsilon^2)(\sin(\tau/2) - \sin(t/2))/\sqrt{2}, \quad (\text{C.21})$$

and the quantity (C.15) is bounded by

$$\begin{aligned} & \frac{\sqrt{2}\varepsilon^2 \left(\left(\frac{1}{\sin(t/2)} - \frac{1}{\sin(\tau/2)} \right) - (\sin(t/2) - \sin(\tau/2)) \right)}{(1 - \varepsilon^2)(\sin(\tau/2) - \sin(t/2))} \\ &= \frac{\sqrt{2}\varepsilon^2}{1 - \varepsilon^2} \left(1 + \frac{1}{\sin(t/2) \sin(\tau/2)} \right). \end{aligned} \quad (\text{C.22})$$

Since $t > 4\varepsilon$, this quantity is bounded by

$$\frac{\sqrt{2}\varepsilon}{\sin(\tau/2)} + O(\varepsilon^2), \quad \text{as } \varepsilon \rightarrow 0. \quad (\text{C.23})$$

The same estimate holds when $\tau < 0$, namely

$$\frac{\sqrt{2}\varepsilon}{|\sin(\tau/2)|} + O(\varepsilon^2). \quad (\text{C.24})$$

We now establish the same estimate for $t \in I$, and $0 < t < 4\varepsilon$, whilst $\tau \in J$. In this case $|\mathbf{x}_\varepsilon(\tau)|$ is much greater than $|\mathbf{x}_\varepsilon(t)|$ and

$$\begin{aligned} \frac{|\mathbf{x}_0(\tau) - \mathbf{x}_0(t)|^2}{|\mathbf{x}_\varepsilon(\tau) - \mathbf{x}_\varepsilon(t)|^2} &= \frac{|\mathbf{x}_0(\tau)|^2 - 2\mathbf{x}_0(\tau) \cdot \mathbf{x}_0(t) + |\mathbf{x}_0(t)|^2}{|\mathbf{x}_\varepsilon(\tau)|^2 - 2\mathbf{x}_\varepsilon(\tau) \cdot \mathbf{x}_\varepsilon(t) + |\mathbf{x}_\varepsilon(t)|^2} \\ &= \frac{|\mathbf{x}_0(\tau)|^2}{|\mathbf{x}_\varepsilon(\tau)|^2} \left(\frac{1 - 2 \frac{\mathbf{x}_0(\tau)}{|\mathbf{x}_0(\tau)|} \cdot \frac{\mathbf{x}_0(t)}{|\mathbf{x}_0(\tau)|} + \frac{|\mathbf{x}_0(t)|^2}{|\mathbf{x}_0(\tau)|^2}}{1 - 2 \frac{\mathbf{x}_\varepsilon(\tau)}{|\mathbf{x}_\varepsilon(\tau)|} \cdot \frac{\mathbf{x}_\varepsilon(t)}{|\mathbf{x}_\varepsilon(\tau)|} + \frac{|\mathbf{x}_\varepsilon(t)|^2}{|\mathbf{x}_\varepsilon(\tau)|^2}} \right). \end{aligned} \quad (\text{C.25})$$

Now

$$\begin{aligned} \frac{|\mathbf{x}_0(\tau)|^2}{|\mathbf{x}_\varepsilon(\tau)|^2} &= 1 - \frac{4\varepsilon^2 \cos^2(\tau/2)}{4\varepsilon^2 \cos^2(\tau/2) + 4\sin^2(\tau/2) + \sin^2(\tau)} \\ &= 1 + O\left(\varepsilon^{2/3}\right), \quad \text{since } \tau \in J; \end{aligned} \quad (\text{C.26})$$

and

$$\begin{aligned} \frac{|\mathbf{x}_\varepsilon(t)|^2}{|\mathbf{x}_\varepsilon(\tau)|^2} &= \frac{4\left(\varepsilon^2 \cos^2(t/2) + \sin^2(t/2)\right) + \sin^2(t)}{4\left(\varepsilon^2 \cos^2(\tau/2) + \sin^2(\tau/2)\right) + \sin^2(\tau)} \\ &= O\left(\varepsilon^{2/3}\right), \quad \text{since } t \leq 4\varepsilon \text{ and } \tau \in J; \end{aligned} \quad (\text{C.27})$$

and

$$\begin{aligned} \frac{|\mathbf{x}_0(t)|^2}{|\mathbf{x}_0(\tau)|^2} &= \frac{4\sin^2(t/2) + \sin^2(t)}{4\sin^2(\tau/2) + \sin^2(\tau)} \\ &= O\left(\varepsilon^{2/3}\right). \end{aligned} \quad (\text{C.28})$$

We conclude that the quantity (C.25) is

$$1 + O\left(\varepsilon^{2/3}\right), \quad \text{as } \varepsilon \rightarrow 0, \quad (\text{C.29})$$

and thus its logarithm is $O\left(\varepsilon^{2/3}\right)$ as $\varepsilon \rightarrow 0$.

We may now calculate a bound for the desired integral. If $t > 4\varepsilon$ and $t \in I$,

$$\begin{aligned} &\int_J |G_0(\mathbf{x}_\varepsilon(t), \mathbf{x}_\varepsilon(\tau)) - G_0(\mathbf{x}_0(t), \mathbf{x}_0(\tau))| d\tau \\ &\leq 2 \int_{\varepsilon^{2/3}}^{\pi} \frac{\sqrt{2}\varepsilon}{\sin(\tau/2)} d\tau + O\left(\varepsilon^2\right) \\ &= 2\sqrt{2}\varepsilon \left[-\log \cot \frac{\tau}{4} \right]_{\varepsilon^{2/3}}^{\pi} + O\left(\varepsilon^2\right) \\ &= 2\sqrt{2}\varepsilon \left| \log \tan \left(\frac{1}{4}\varepsilon^{2/3} \right) \right| + O\left(\varepsilon^2\right) \\ &= \frac{4}{3}\sqrt{2}\varepsilon |\log \varepsilon| + O\left(\varepsilon\right), \quad \text{as } \varepsilon \rightarrow 0. \end{aligned} \quad (\text{C.30})$$

If $t < 4\varepsilon$, the desired integral is bounded by $O\left(\varepsilon^{2/3}\right)$ as $\varepsilon \rightarrow 0$. ■

Lemma C.1.6

$$|u_\varepsilon^{\text{inc}}(t) - u_0^{\text{inc}}(t)| = |e^{-ik\hat{\mathbf{x}} \cdot \mathbf{x}_\varepsilon(t)} - e^{-ik\hat{\mathbf{x}} \cdot \mathbf{x}_0(t)}| \leq 2k\varepsilon,$$

for all $t \in [-\pi, \pi]$.

Proof. Let $\Delta \mathbf{x} = \Delta \mathbf{x}(t) = \mathbf{x}_\varepsilon(t) - \mathbf{x}_0(t)$, and note that $\hat{\mathbf{x}} \cdot \Delta \mathbf{x}$ is small. Thus

$$\begin{aligned} |e^{-ik\hat{\mathbf{x}} \cdot \mathbf{x}_\varepsilon(t)} - e^{-ik\hat{\mathbf{x}} \cdot \mathbf{x}_0(t)}| &= |e^{-ik\hat{\mathbf{x}} \cdot \Delta \mathbf{x}} - 1| \\ &= 2 \left| \sin \frac{k\hat{\mathbf{x}} \cdot \Delta \mathbf{x}}{2} \right| \\ &\leq |k| |\hat{\mathbf{x}}| |\Delta \mathbf{x}| \\ &= k |\mathbf{x}_\varepsilon(t) - \mathbf{x}_0(t)| \\ &\leq 2k\varepsilon, \end{aligned} \tag{C.31}$$

applying the result from Lemma C.1.2. ■

Lemma C.1.7

$$\|m(\hat{\mathbf{x}}; \mathbf{x}_\varepsilon)\|_\infty \leq \sqrt{2},$$

for all $t \in [-\pi, \pi]$, where

$$m(\hat{\mathbf{x}}; \mathbf{x}_\varepsilon) = \boldsymbol{\nu}(\mathbf{x}_\varepsilon(t)) \cdot \hat{\mathbf{x}} e^{-ik\hat{\mathbf{x}} \cdot \mathbf{x}_\varepsilon(t)} |\mathbf{x}_\varepsilon'(t)|.$$

Proof.

$$\begin{aligned} |m(\hat{\mathbf{x}}; \mathbf{x}_\varepsilon(t))| &= |\boldsymbol{\nu}(\mathbf{x}_\varepsilon(t)) \cdot \hat{\mathbf{x}} e^{-ik\hat{\mathbf{x}} \cdot \mathbf{x}_\varepsilon(t)} |\mathbf{x}_\varepsilon'(t)|| \\ &\leq \sqrt{2} |\boldsymbol{\nu}(\mathbf{x}_\varepsilon(t))| |\hat{\mathbf{x}}| |e^{-ik\hat{\mathbf{x}} \cdot \mathbf{x}_\varepsilon(t)}| \quad (\text{Lemma C.1.4}) \\ &= \sqrt{2}, \end{aligned} \tag{C.32}$$

since $|\boldsymbol{\nu}(\mathbf{x}_\varepsilon(t))| = 1$ and $|\hat{\mathbf{x}}| = 1$. ■

Lemma C.1.8

$$\frac{k}{\sqrt{8\pi}} \|m(\hat{\mathbf{x}}; \mathbf{x}_\varepsilon) - m(\hat{\mathbf{x}}; \mathbf{x}_0)\|_1 = O(k\varepsilon), \quad \text{as } k\varepsilon \rightarrow 0,$$

where

$$m(\hat{\mathbf{x}}; \mathbf{x}) = \boldsymbol{\nu}(\mathbf{x}(t)) \cdot \hat{\mathbf{x}} e^{-ik\hat{\mathbf{x}} \cdot \mathbf{x}(t)} |\mathbf{x}'(t)|.$$

Proof. Let

$$\mathbf{v}(\mathbf{x}(t)) = \boldsymbol{\nu}(\mathbf{x}(t)) \cdot |\mathbf{x}'(t)| = (x'_2(t), -x'_1(t)). \quad (\text{C.33})$$

Then

$$\begin{aligned} & |m(\hat{\mathbf{x}}; \mathbf{x}_\varepsilon) - m(\hat{\mathbf{x}}; \mathbf{x}_0)| \\ & \leq |\mathbf{v}(\mathbf{x}_\varepsilon(t)) e^{-ik\hat{\mathbf{x}} \cdot \mathbf{x}_\varepsilon(t)} - \mathbf{v}(\mathbf{x}_0(t)) e^{-ik\hat{\mathbf{x}} \cdot \mathbf{x}_0(t)}| \\ & \leq \left| (\mathbf{v}(\mathbf{x}_\varepsilon(t)) - \mathbf{v}(\mathbf{x}_0(t))) e^{-ik\hat{\mathbf{x}} \cdot \mathbf{x}_\varepsilon(t)} + \mathbf{v}(\mathbf{x}_0(t)) (e^{-ik\hat{\mathbf{x}} \cdot \mathbf{x}_\varepsilon(t)} - e^{-ik\hat{\mathbf{x}} \cdot \mathbf{x}_0(t)}) \right| \\ & \leq |\mathbf{v}(\mathbf{x}_\varepsilon(t)) - \mathbf{v}(\mathbf{x}_0(t))| + |\mathbf{v}(\mathbf{x}_0(t))| |e^{-ik\hat{\mathbf{x}} \cdot (\mathbf{x}_\varepsilon(t) - \mathbf{x}_0(t))} - 1| \\ & \leq |\mathbf{x}'_\varepsilon(t) - \mathbf{x}'_0(t)| + |\mathbf{x}'_0(t)| |e^{-ik\hat{\mathbf{x}} \cdot (\mathbf{x}_\varepsilon(t) - \mathbf{x}_0(t))} - 1| \\ & \leq |\mathbf{x}'_\varepsilon(t) - \mathbf{x}'_0(t)| + \sqrt{2} |e^{-ik\hat{\mathbf{x}} \cdot (\mathbf{x}_\varepsilon(t) - \mathbf{x}_0(t))} - 1|. \end{aligned} \quad (\text{C.34})$$

Thus

$$\frac{k}{\sqrt{8\pi}} \|m(\hat{\mathbf{x}}; \mathbf{x}_\varepsilon) - m(\hat{\mathbf{x}}; \mathbf{x}_0)\|_1 \leq \frac{k}{\sqrt{8\pi}} \|\mathbf{x}'_\varepsilon - \mathbf{x}'_0\|_1 + \frac{k}{2\sqrt{\pi}} \int_{-\pi}^{\pi} |e^{-ik\hat{\mathbf{x}} \cdot (\mathbf{x}_\varepsilon(t) - \mathbf{x}_0(t))} - 1| dt. \quad (\text{C.35})$$

Using the results of Lemma C.1.9 and Lemma C.1.10 we obtain

$$\begin{aligned} & \frac{k}{\sqrt{8\pi}} \|m(\hat{\mathbf{x}}; \mathbf{x}_\varepsilon) - m(\hat{\mathbf{x}}; \mathbf{x}_0)\|_1 \\ & \leq \frac{\sqrt{2} k\varepsilon}{\sqrt{\pi}} + O\left((k\varepsilon)^{2-\delta}\right), \quad \text{for any } \delta > 0, \\ & = O(k\varepsilon), \quad \text{as } k\varepsilon \rightarrow 0. \end{aligned} \quad (\text{C.36})$$

■

Lemma C.1.9 *For the lemniscate with the parameterisation (C.5) and the corresponding rounded lemniscate with parameterisation (C.6),*

$$\|\mathbf{x}'_\varepsilon - \mathbf{x}'_0\|_1 = \int_{-\pi}^{\pi} |\mathbf{x}'_\varepsilon(t) - \mathbf{x}'_0(t)| dt = 4\varepsilon.$$

Proof. We begin with the case $t \in [0, \pi]$. Then

$$\begin{aligned} |\mathbf{x}'_\varepsilon(t) - \mathbf{x}'_0(t)| &= \left| \frac{(1 - \varepsilon^2) \sin \frac{t}{2} \cos \frac{t}{2}}{\sqrt{\varepsilon^2 + (1 - \varepsilon^2) \sin^2 \frac{t}{2}}} - \cos \frac{t}{2} \right| \\ &= \cos \frac{t}{2} \left(1 - \frac{(1 - \varepsilon^2) \sin \frac{t}{2}}{\sqrt{\varepsilon^2 + (1 - \varepsilon^2) \sin^2 \frac{t}{2}}} \right), \end{aligned} \quad (\text{C.37})$$

since

$$\frac{(1 - \varepsilon^2) \sin \frac{t}{2}}{\sqrt{\varepsilon^2 + (1 - \varepsilon^2) \sin^2 \frac{t}{2}}} \leq 1, \quad (\text{C.38})$$

for $0 < \varepsilon < 1$ and $\sin \frac{t}{2} > 0$.

For the case $t \in [-\pi, 0]$,

$$|\mathbf{x}'_\varepsilon(t) - \mathbf{x}'_0(t)| = \cos \frac{t}{2} \left(1 + \frac{(1 - \varepsilon^2) \sin \frac{t}{2}}{\sqrt{\varepsilon^2 + (1 - \varepsilon^2) \sin^2 \frac{t}{2}}} \right), \quad (\text{C.39})$$

since $\sin \frac{t}{2} < 0$. Thus

$$\begin{aligned} \int_{-\pi}^{\pi} |\mathbf{x}'_\varepsilon(t) - \mathbf{x}'_0(t)| dt &= \int_0^{\pi} \cos \frac{t}{2} \left(1 - \frac{(1 - \varepsilon^2) \sin \frac{t}{2}}{\sqrt{\varepsilon^2 + (1 - \varepsilon^2) \sin^2 \frac{t}{2}}} \right) dt \\ &\quad + \int_{-\pi}^0 \cos \frac{t}{2} \left(1 + \frac{(1 - \varepsilon^2) \sin \frac{t}{2}}{\sqrt{\varepsilon^2 + (1 - \varepsilon^2) \sin^2 \frac{t}{2}}} \right) dt \\ &= \left[2 \sin \frac{t}{2} - 2 \sqrt{\varepsilon^2 + (1 - \varepsilon^2) \sin^2 \frac{t}{2}} \right]_0^{\pi} \\ &\quad + \left[2 \sin \frac{t}{2} + 2 \sqrt{\varepsilon^2 + (1 - \varepsilon^2) \sin^2 \frac{t}{2}} \right]_{-\pi}^0 \\ &= 4\varepsilon. \end{aligned} \quad (\text{C.40})$$

■

Lemma C.1.10

$$\begin{aligned} \frac{k}{2\sqrt{\pi}} \int_{-\pi}^{\pi} |e^{-ik\hat{\mathbf{x}} \cdot (\mathbf{x}_{\varepsilon}(t) - \mathbf{x}_0(t))} - 1| dt &\leq \frac{2}{\sqrt{\pi}} (k\varepsilon)^2 + \frac{2(k\varepsilon)^2}{\sqrt{\pi}} \log \varepsilon + O((k\varepsilon)^2) \\ &= O((k\varepsilon)^{2-\delta}), \end{aligned}$$

for any $\delta > 0$.

Proof. We have established that $|\mathbf{x}_{\varepsilon}(t) - \mathbf{x}_0(t)| \leq 2\varepsilon$ for $t \in [-\pi, \pi]$ in Lemma C.1.2. Noting that the integrand is $2|\sin\{\frac{k}{2}\hat{\mathbf{x}} \cdot (\mathbf{x}_{\varepsilon}(t) - \mathbf{x}_0(t))\}|$; the integral is bounded by

$$\frac{k^2}{2\sqrt{\pi}} \int_{-\pi}^{\pi} |\mathbf{x}_{\varepsilon}(t) - \mathbf{x}_0(t)| dt. \quad (\text{C.41})$$

We split the integral over the intervals $I_1 = [-\varepsilon, \varepsilon]$ and $I_2 = [-\pi, \pi] \setminus I_1$, thus (C.41) is equal to

$$\frac{k^2}{2\sqrt{\pi}} \int_{I_1} |\mathbf{x}_{\varepsilon}(t) - \mathbf{x}_0(t)| dt + \frac{k^2}{2\sqrt{\pi}} \int_{I_2} |\mathbf{x}_{\varepsilon}(t) - \mathbf{x}_0(t)| dt. \quad (\text{C.42})$$

Evaluating the first integral,

$$\begin{aligned} \frac{k^2}{2\sqrt{\pi}} \int_{I_1} |\mathbf{x}_{\varepsilon}(t) - \mathbf{x}_0(t)| dt &= \frac{k^2}{2\sqrt{\pi}} \int_{-\varepsilon}^{\varepsilon} |\mathbf{x}_{\varepsilon}(t) - \mathbf{x}_0(t)| dt \\ &\leq \frac{k^2}{2\pi} \int_{-\varepsilon}^{\varepsilon} 2\varepsilon dt \\ &= \frac{2}{\sqrt{\pi}} (k\varepsilon)^2. \end{aligned} \quad (\text{C.43})$$

The second integral, is equal to

$$\begin{aligned} &\frac{k^2}{2\sqrt{\pi}} \int_{\varepsilon}^{\pi} |\mathbf{x}_{\varepsilon}(t) - \mathbf{x}_0(t)| dt + \frac{k^2}{2\sqrt{\pi}} \int_{-\pi}^{-\varepsilon} |\mathbf{x}_{\varepsilon}(t) - \mathbf{x}_0(t)| dt \\ &\leq \frac{2k^2}{\sqrt{\pi}} \int_{\varepsilon}^{\pi} \frac{\varepsilon^2}{\sin \frac{|t|}{2}} dt && \text{from (C.7)} \\ &= \frac{2(k\varepsilon)^2}{\sqrt{\pi}} \int_{\varepsilon}^{\pi} \frac{1}{\sin |t|/2} dt \\ &= \frac{2(k\varepsilon)^2}{\sqrt{\pi}} \left[-\log \cot \frac{t}{4} \right]_{\varepsilon}^{\pi} \end{aligned}$$

$$\begin{aligned}
& \sim \frac{2(k\varepsilon)^2}{\sqrt{\pi}} \left(-\log \frac{\varepsilon}{4} \right) \\
& = \frac{2(k\varepsilon)^2}{\sqrt{\pi}} \log \varepsilon + O((k\varepsilon)^2), \quad \text{as } k\varepsilon \rightarrow 0.
\end{aligned} \tag{C.44}$$

The result stated now follows. ■

C.2 $\|\psi_\varepsilon - \psi_0\|_{\infty, J}$ and $\|\psi_\varepsilon - \psi_0\|_{1, J}$ are negligibly small

In this section we demonstrate numerically that for $t \in J$, where $J = [-\pi, -\varepsilon^{2/3}] \cup [\varepsilon^{2/3}, \pi]$,

$$\|\psi_\varepsilon(t) - \psi_0(t)\|_{\infty, J} \sim C(\theta_0) (k\varepsilon)^m \sim C(\theta_0) (k\varepsilon)^{0.75}, \tag{C.45}$$

for some constant C dependent on the direction of the incident wave θ_0 , and that

$$\|\psi_\varepsilon(t) - \psi_0(t)\|_{1, J} \sim C_1(\theta_0) k^n \varepsilon^{m_1} \sim C_1(\theta_0) k^{0.2} \varepsilon^{0.97}, \tag{C.46}$$

for some constant C_1 dependent on the direction of the incident wave θ_0 . As such,

$$\|\psi_\varepsilon(t) - \psi_0(t)\|_{\infty, J} \quad \text{and} \quad \|\psi_\varepsilon(t) - \psi_0(t)\|_{1, J}, \tag{C.47}$$

approach zero as $\varepsilon \rightarrow 0$.

Data was collected for the differences between the surface quantities $|\psi_\varepsilon(t) - \psi_0(t)|$ on the interval J , using the supremum norm

$$\|\psi_\varepsilon(t) - \psi_0(t)\|_{\infty, J} = \max_{t \in J} |\psi_\varepsilon(t) - \psi_0(t)|, \tag{C.48}$$

and the L^1 norm

$$\|\psi_\varepsilon(t) - \psi_0(t)\|_{1, J} = \int_J |\psi_\varepsilon(t) - \psi_0(t)| dt. \tag{C.49}$$

This data was collected for a lemniscate (2.2) and its rounded counterpart (2.3) with Dirichlet boundary condition (2.19) for incident field directions $\theta_0 = 0, \pi/32, \pi/16, \pi/8, \pi/4$; wave numbers $k = 1, 5, 2\pi, 10, 4\pi, 8\pi$ and 16π ; and different radii of curvature ρ ranging from 0.05 to 6e-06, which correspond to values of ε of 0.025 to 3e-06. A least squares fit to the logarithms of the data (see Figures C.1a and C.1b), was used for

θ	C	m
0	0.60	0.74
$\pi/32$	0.61	0.74
$\pi/16$	0.61	0.75
$\pi/8$	0.62	0.75
$\pi/4$	0.63	0.75

Table C.1: Showing the constants C and m derived using least squares fit for $\|\psi_\varepsilon(t) - \psi_0(t)\|_{\infty, J} \sim C(\theta_0) (k\varepsilon)^m$.

θ	C_1	n	m_1
0	4.5	0.21	0.97
$\pi/32$	4.5	0.21	0.97
$\pi/16$	4.5	0.21	0.97
$\pi/8$	4.4	0.22	0.96
$\pi/4$	4.0	0.23	0.96

Table C.2: Showing the constants C_1 , n and m_1 derived using least squares fit for $\|\psi_\varepsilon(t) - \psi_0(t)\|_{1, J} \sim C_1(\theta_0) k^n \varepsilon^{m_1}$.

Tables: For the lemniscate with Dirichlet boundary condition.

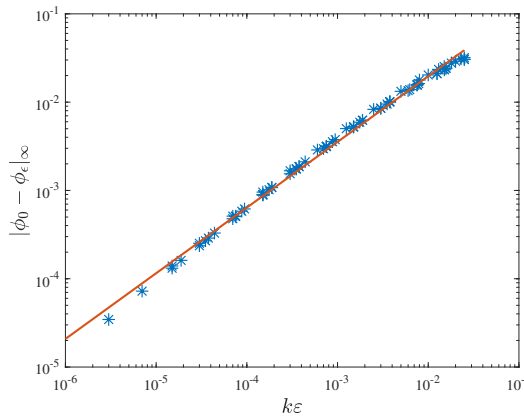
$k\varepsilon \leq 0.025$ to determine the constants C , m , C_1 , m_1 and n . The results presented in Tables C.1, and C.2, respectively, and show that

$$\|\psi_\varepsilon(t) - \psi_0(t)\|_{\infty, J} \sim C(\theta_0) (k\varepsilon)^{0.75}, \quad (\text{C.50})$$

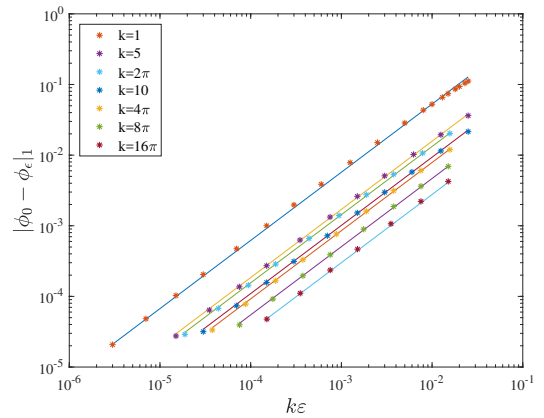
for some constant C dependent on the direction of the incident wave θ_0 , and

$$\|\psi_\varepsilon(t) - \psi_0(t)\|_{\infty, J} \sim C_1(\theta_0) k^{0.2} \varepsilon^{0.97}, \quad (\text{C.51})$$

for some constant C_1 dependent on the direction of the incident wave θ_0 .



(a) $y = \|\psi_\varepsilon(t) - \psi_0(t)\|_{\infty, J}$, for $\theta_0 = 0$.



(b) $y = \|\psi_\varepsilon(t) - \psi_0(t)\|_{1, J}$, for $\theta_0 = 0$.

Figure C.1: Logarithmic plot of the differences in the surface quantity on the lemniscate $\psi_0(t)$ and on its rounded counterpart $\psi_\varepsilon(t)$ for $t \in J$.

The data points used are represented by the asterisks, the lines are the least squares line of fit.

Appendix D

Surface Quantities Supporting Material

D.1 Convergence of Integral K_ν

Lemma D.1.1 *The integral*

$$\int_0^\infty \log \frac{|1-u|^2}{1+u^2} u^{1/\nu-1} du,$$

where $0 < 1/\nu < 1$, is convergent.

Proof. We will split the integral into three parts to consider the singularities at $u = 0$, $u = 1$ and its limiting behaviour:

$$\begin{aligned} \int_0^\infty \log \frac{|1-u|^2}{1+u^2} u^{1/\nu-1} du &= \int_0^{1/2} \log \frac{|1-u|^2}{1+u^2} u^{1/\nu-1} du + \int_{1/2}^2 \log \frac{|1-u|^2}{1+u^2} u^{1/\nu-1} du \\ &\quad + \int_2^\infty \log \frac{|1-u|^2}{1+u^2} u^{1/\nu-1} du. \end{aligned} \tag{D.1}$$

Evaluating the first component,

$$\left| \int_0^{1/2} \log \frac{|1-u|^2}{1+u^2} u^{1/\nu-1} du \right| \leq \log 5 \int_0^{1/2} |u^{1/\nu-1}| du = \frac{2^\nu}{\nu} \log 5 < \infty. \tag{D.2}$$

Evaluating the second component,

$$\begin{aligned} \left| \int_{1/2}^2 \log \frac{|1-u|^2}{1+u^2} u^{1/\nu-1} du \right| &\leq 2^{1-1/\nu} \int_{1/2}^2 |\log |1-u|^2| du \\ &= 2^{2-1/\nu} \int_{-1}^{1/2} |\log |v|| dv < \infty, \end{aligned} \quad (\text{D.3})$$

noting that $\log v$ has an integrable singularity when $v = 0$. To evaluate the third component integral, we will use the Taylor series approximations

$$\log \left| 1 - \frac{1}{u} \right| = \frac{1}{u} + O\left(\frac{1}{u^2}\right), \quad (\text{D.4})$$

and

$$\log \left(1 + \frac{1}{u^2} \right) = \frac{1}{u^2} + O\left(\frac{1}{u^4}\right), \quad (\text{D.5})$$

as $u \rightarrow \infty$. Thus

$$2 \log |1 - u^{-1}| - \log(1 + u^{-2}) = \frac{2}{u} + O\left(\frac{1}{u^2}\right), \quad (\text{D.6})$$

as $u \rightarrow \infty$. Evaluating the third component in (D.1), the integrand

$$\log \frac{|1-u|^2}{1+u^2} u^{1/\nu-1} = \left(\frac{2}{u} + O\left(\frac{1}{u^2}\right) \right) u^{1/\nu-1} = 2u^{1/\nu-2} + O\left(u^{1/\nu-3}\right), \quad (\text{D.7})$$

as $u \rightarrow \infty$, so the integral

$$\int_2^\infty \log \frac{|1-u|^2}{1+u^2} u^{1/\nu-1} du, \quad (\text{D.8})$$

is finite, as $1/\nu < 1$. ■

D.2 Surface Quantity, φ , in the Vicinity of the Corner: Numerical Results

In this section we present the numerical results for the surface quantity, φ , for lemniscates with differing interior angles. These results demonstrate that, for a Dirichlet boundary condition,

$$|\varphi(\tau) - \varphi(0)| \approx C(k\tau)^m, \quad (\text{D.9})$$

as $\tau \rightarrow 0$, for some constant C . The corresponding results for a Neumann boundary condition, show that

$$|\varphi(\tau)| \approx C(k\tau)^m, \quad (\text{D.10})$$

as $\tau \rightarrow 0$, for some other constant C .

The estimates for the constants C and m have been obtained by a least squares linear fit to the logarithm of the quantities $|\varphi(\tau) - \varphi(0)|$ and $|\varphi(\tau)|$ in (D.9) and (D.10), as appropriate.

ka	$\theta_0 = 0$		$\theta_0 = \pi/32$		$\theta_0 = \pi/16$		$\theta_0 = \pi/8$		$\theta_0 = \pi/4$	
	C	m	C	m	C	m	C	m	C	m
Lemniscate, $\beta = \pi/2$										
1	4.0	0.67	4.0	0.67	4.0	0.67	3.9	0.67	3.4	0.67
$\pi/2$	4.0	0.67	4.0	0.67	4.0	0.67	3.9	0.67	3.5	0.67
π	4.0	0.67	4.0	0.67	4.0	0.67	3.9	0.67	3.5	0.67
2π	4.0	0.67	4.0	0.67	4.0	0.67	3.9	0.67	3.5	0.67
4π	4.0	0.67	4.0	0.67	4.0	0.67	3.9	0.67	3.5	0.67
8π	4.0	0.67	4.0	0.66	4.0	0.67	3.9	0.67	3.5	0.67
16π	4.0	0.67	4.0	0.67	4.0	0.67	3.9	0.67	3.5	0.67
Lemniscate, $\beta = \pi/3$										
1	5.9	0.60	5.9	0.60	5.9	0.60	5.7	0.60	5.2	0.60
$\pi/2$	5.9	0.60	5.9	0.60	5.9	0.60	5.8	0.60	5.3	0.60
π	5.9	0.60	5.9	0.60	5.9	0.60	5.8	0.60	5.3	0.60
2π	5.9	0.60	5.9	0.60	5.9	0.60	5.8	0.60	5.3	0.60
4π	5.9	0.60	5.9	0.60	5.9	0.60	5.8	0.60	5.3	0.60
8π	6.0	0.60	5.9	0.60	5.9	0.60	5.8	0.60	5.3	0.60
16π	6.0	0.60	5.9	0.60	5.9	0.60	5.8	0.60	5.3	0.60
Lemniscate, $\beta = \pi/4$										
1	7.9	0.571	7.9	0.571	7.8	0.571	7.7	0.571	7.1	0.571
$\pi/2$	7.9	0.571	7.9	0.571	7.9	0.571	7.7	0.571	7.1	0.571
π	7.9	0.571	7.9	0.571	7.9	0.571	7.7	0.571	7.1	0.571
2π	7.9	0.571	7.9	0.571	7.9	0.571	7.7	0.571	7.1	0.571
4π	7.9	0.571	7.9	0.571	7.9	0.571	7.7	0.571	7.1	0.571
8π	8.0	0.572	7.9	0.572	7.9	0.572	7.7	0.572	7.1	0.571
16π	7.9	0.571	7.9	0.572	7.9	0.572	7.7	0.571	7.1	0.571
Lemniscate, $\beta = \pi/6$										
1	11.9	0.545	11.9	0.545	11.9	0.545	11.7	0.545	10.8	0.545
$\pi/2$	11.9	0.545	11.9	0.545	11.8	0.545	11.6	0.545	10.8	0.545
π	11.9	0.545	11.9	0.545	11.9	0.545	11.6	0.545	10.8	0.545
2π	11.9	0.545	11.9	0.545	11.9	0.545	11.6	0.545	10.8	0.545
4π	11.9	0.545	11.9	0.545	11.9	0.545	11.6	0.545	10.8	0.545
8π	11.8	0.544	11.8	0.545	11.8	0.545	11.6	0.545	10.8	0.545
16π	12.0	0.546	11.9	0.546	11.9	0.546	11.7	0.546	10.9	0.546
Lemniscate, $\beta = \pi/12$										
1	23.4	0.519	23.4	0.519	23.3	0.519	22.9	0.519	21.5	0.519
$\pi/2$	23.3	0.519	23.3	0.519	23.2	0.519	22.8	0.519	21.4	0.519
π	23.4	0.519	23.4	0.519	23.3	0.519	22.9	0.519	21.5	0.519
2π	23.5	0.519	23.4	0.519	23.3	0.519	23.0	0.519	21.5	0.519
4π	23.5	0.519	23.5	0.519	23.4	0.519	23.0	0.519	21.6	0.519
8π	23.6	0.519	23.5	0.519	23.4	0.519	23.1	0.519	21.6	0.519
16π	23.7	0.519	23.7	0.519	23.5	0.519	23.2	0.519	21.7	0.519
Lemniscate, $\beta = \pi/18$										
1	35.4	0.510	35.3	0.510	35.2	0.510	34.7	0.510	32.6	0.510
$\pi/2$	35.2	0.510	35.2	0.510	35.0	0.510	34.5	0.510	32.5	0.510
π	35.4	0.510	35.3	0.510	35.2	0.510	34.7	0.510	32.6	0.510
2π	35.6	0.511	35.5	0.511	35.4	0.511	34.8	0.511	32.7	0.510
4π	35.8	0.511	35.8	0.511	35.6	0.511	35.0	0.511	32.8	0.511
8π	36.4	0.513	36.3	0.513	36.1	0.512	35.3	0.512	33.1	0.511
16π	37.9	0.518	37.6	0.517	36.7	0.514	36.1	0.514	33.8	0.514

Table D.1: Numerical results $|\varphi(\tau) - \varphi(0)| \approx C(k\tau)^m$ as $\tau \rightarrow 0$, for lemniscates with differing interior angles, β and Dirichlet boundary condition. Different angles of incidence, θ_0 , and different wave numbers ka .

ka	$\theta_0 = 0$		$\theta_0 = \pi/32$		$\theta_0 = \pi/16$		$\theta_0 = \pi/8$		$\theta_0 = \pi/4$	
	C	m	C	m	C	m	C	m	C	m
Lemniscate, $\beta = \pi/2$										
1	1.9	0.33	0.1	-0.33	0.3	-0.33	0.5	-0.33	1.0	-0.33
$\pi/2$	3.7	0.33	0.3	-0.33	0.5	-0.33	1.0	-0.33	1.9	-0.33
π	7.1	0.33	0.4	-0.32	0.8	-0.33	1.6	-0.33	3.1	-0.33
2π	14	0.33	0.9	-0.31	1.7	-0.32	3.3	-0.33	6.0	-0.33
4π	27	0.33	2.2	-0.31	3.7	-0.32	6.6	-0.33	12	-0.33
8π	59	0.33	5.0	-0.30	8.2	-0.31	14	-0.32	25	-0.33
16π	104	0.32	10	-0.29	17	-0.31	29	-0.32	51	-0.33
Lemniscate, $\beta = \pi/3$										
1	0.7	0.20	0.2	-0.40	0.4	-0.40	0.8	-0.40	1.6	-0.40
$\pi/2$	1.4	0.20	0.3	-0.40	0.6	-0.40	1.2	-0.40	2.2	-0.40
π	2.7	0.20	0.7	-0.40	1.3	-0.40	2.6	-0.40	4.5	-0.40
2π	5.3	0.20	1.2	-0.39	2.2	-0.40	4.5	-0.40	8.9	-0.40
4π	11	0.20	2.6	-0.39	4.8	-0.39	9.5	-0.40	18	-0.40
8π	21	0.20	5.8	-0.38	10	-0.39	19	-0.40	36	-0.40
16π	43	0.20	13	-0.37	21	-0.39	39	-0.39	72	-0.40
Lemniscate, $\beta = \pi/4$										
1	0.5	0.143	0.3	-0.428	0.5	-0.428	1.1	-0.428	2.2	-0.428
$\pi/2$	0.9	0.143	0.4	-0.426	0.7	-0.427	1.3	-0.428	2.5	-0.428
π	1.8	0.143	0.9	-0.425	1.6	-0.427	3.1	-0.428	5.3	-0.428
2π	3.4	0.143	1.7	-0.425	3.3	-0.427	6.4	-0.428	11	-0.428
4π	6.8	0.143	3.2	-0.421	6.0	-0.425	12	-0.427	23	-0.428
8π	14	0.143	6.8	-0.418	12	-0.423	24	-0.426	46	-0.428
16π	27	0.143	14	-0.413	26	-0.421	49	-0.425	93	-0.427
Lemniscate, $\beta = \pi/6$										
1	0.3	0.091	0.4	-0.454	0.8	-0.454	1.7	-0.454	3.5	-0.454
$\pi/2$	0.5	0.091	0.4	-0.453	0.8	-0.454	1.6	-0.454	3.1	-0.454
π	1.0	0.091	1.0	-0.453	2.0	-0.454	3.7	-0.454	7.0	-0.454
2π	2.0	0.091	2.4	-0.452	4.7	-0.453	8.6	-0.454	16	-0.454
4π	3.9	0.091	4.6	-0.452	9.1	-0.453	18	-0.454	34	-0.454
8π	8.0	0.091	9.1	-0.449	17	-0.452	35	-0.453	67	-0.454
16π	15.9	0.091	19	-0.447	35	-0.451	68	-0.453	132	-0.454
Lemniscate, $\beta = \pi/12$										
1	0.1	0.043	0.9	-0.478	1.8	-0.478	3.6	-0.478	7.4	-0.478
$\pi/2$	0.2	0.043	0.6	-0.478	1.1	-0.478	2.2	-0.478	4.9	-0.478
π	0.5	0.043	1.4	-0.478	2.7	-0.478	5.1	-0.478	13	-0.478
2π	0.9	0.043	3.4	-0.477	6.6	-0.478	12	-0.478	34	-0.478
4π	1.8	0.044	8.4	-0.477	16	-0.478	28	-0.478	59	-0.478
8π	3.6	0.044	18	-0.477	35	-0.478	62	-0.478	122	-0.478
16π	7.2	0.044	31	-0.476	66	-0.477	130	-0.478	246	-0.478
Lemniscate, $\beta = \pi/18$										
1	0.1	0.029	1.3	-0.487	2.7	-0.487	5.4	-0.487	11	-0.487
$\pi/2$	0.1	0.029	0.7	-0.486	1.5	-0.486	2.8	-0.487	6.9	-0.487
π	0.3	0.029	1.7	-0.486	3.4	-0.486	6.5	-0.486	20	-0.487
2π	0.6	0.029	4.1	-0.486	7.9	-0.486	15	-0.486	52	-0.487
4π	1.2	0.029	10	-0.486	19	-0.486	38	-0.486	81	-0.487
8π	2.3	0.029	24	-0.486	45	-0.486	93	-0.486	173	-0.486
16π	4.6	0.029	52	-0.486	96	-0.486	190	-0.486	364	-0.486

Table D.2: Numerical results $|\varphi(\tau)| \approx C(k\tau)^m$ as $\tau \rightarrow 0$, for lemniscates with differing interior angles, β and Neumann boundary condition. Different angles of incidence, θ_0 , and different wave numbers ka .

Appendix E

Time Domain Supporting Material

This chapter contains the supporting analysis and calculations required for measuring the effect of corner rounding in the time domain (Chapter 6).

E.1 Time Domain Incident Pulses

E.1.1 The Gaussian

The function

$$f(x, t) = e^{-(x-ct)^2/a_0^2} = e^{-(ct-x)^2/a_0^2}, \quad (\text{E.1})$$

which represents the Gaussian pulse where a_0 is a quarter of the pulse width and c is the speed of waves in the medium or light in free space ($a_0, c > 0$), has Fourier transform

$$\begin{aligned} F(x, \omega) &= \sqrt{\pi} \frac{a_0}{c} e^{-(ix\omega/c + a_0^2(\omega/c)^2/4)} \\ &= \sqrt{\pi} \frac{a_0}{c} e^{-(ikx + a_0^2k^2/4)}, \end{aligned} \quad (\text{E.2})$$

where $k = \omega/c$ is the wave number. The Gaussian pulse with time displacement t_0

$$f(x, t) = e^{-(x-c(t-t_0))^2/a_0^2}, \quad (\text{E.3})$$

has Fourier transform

$$F(x, \omega) = \sqrt{\pi} \frac{a_0}{c} e^{-ikct_0 - a_0^2k^2/4} e^{-ikx}. \quad (\text{E.4})$$

The factor e^{ikx} is already included in (6.1) because

$$\phi(\mathbf{y}, \omega) e^{-i\omega t} \quad \text{and} \quad u^\infty(\hat{\mathbf{x}}, \omega) e^{-i\omega t}, \quad (\text{E.5})$$

are the responses to

$$u^{\text{inc}} e^{-i\omega t} = e^{ik(\mathbf{d} \cdot \mathbf{x} - ct)} = e^{ik\mathbf{d} \cdot \mathbf{x} - i\omega t}, \quad (\text{E.6})$$

(see (6.5) and (6.6) with $\mathbf{d} = (1, 0)$). In other words the spatial variation of the incident field has been already automatically included in the calculation of $u^\infty(\hat{\mathbf{x}}, \omega)$ and $\phi(\mathbf{y}, \omega)$.

We note that

$$F(-\omega) = \int_{-\infty}^{\infty} f(t) e^{-i(-\omega)t} dt = \int_{-\infty}^{\infty} f(t) e^{i\omega t} dt, \quad (\text{E.7})$$

and

$$\overline{F(\omega)} = \int_{-\infty}^{\infty} \overline{f(t) e^{-i\omega t}} dt = \int_{-\infty}^{\infty} f(t) e^{i\omega t} dt, \quad (\text{E.8})$$

when $f(t)$ is real (true for the Gaussian (E.1)), that is $F(-\omega) = \overline{F(\omega)}$. Thus multiplying the frequency domain response (6.1) by

$$\begin{aligned} F(-\omega) &= \overline{F(\omega)} \\ &= \overline{\sqrt{\pi} \frac{a_0}{c} e^{-ikct_0 - a_0^2 k^2 / 4}} \\ &= \sqrt{\pi} \frac{a_0}{c} e^{ikct_0 - a_0^2 k^2 / 4}, \end{aligned} \quad (\text{E.9})$$

enables application of the Fourier transform to obtain the time domain response of the scatterer to the time dependent incident pulse

$$\tilde{u}_\infty(\hat{\mathbf{x}}, t) = \int_{-\infty}^{\infty} \sqrt{\pi} \frac{a_0}{c} e^{-a_0^2 k^2 / 4} e^{ikct_0} u^\infty(\hat{\mathbf{x}}, \omega) e^{-i\omega t} d\omega. \quad (\text{E.10})$$

Thus to calculate (E.10), we perform a Fourier transform

$$\tilde{u}_\infty(\hat{\mathbf{x}}, t) = \int_{-\infty}^{\infty} F(\hat{\mathbf{x}}, \omega) e^{-i\omega t} d\omega, \quad (\text{E.11})$$

where

$$F(\hat{\mathbf{x}}, \omega) = \hat{F}(-\omega) u^\infty(\hat{\mathbf{x}}, \omega)$$

$$= \sqrt{\pi} \frac{a_0}{c} e^{-a^2 k^2 / 4} e^{i k c t_0} u^\infty(\hat{\mathbf{x}}, \omega).$$

E.1.2 The Derivative of the Gaussian

The Gaussian pulse (E.3) with the spatial component removed since the spatial variation of the incident field $e^{i k x}$ has already been automatically included in the calculation of $u^\infty(\hat{\mathbf{x}}, \omega)$ and $\phi(\mathbf{y}, \omega)$ is

$$f(t) = e^{-(c(t-t_0))^2/a_o^2}, \quad (\text{E.12})$$

with derivative

$$f_t(t) = \frac{-2c(c(t-t_0))}{a_0^2} e^{-(c(t-t_0))^2/a_0^2}, \quad (\text{E.13})$$

which is zero when $\omega = 0$ ($c = \omega/k$). Using the property of the derivative of Fourier transforms

$$\text{if } f(t) \Longleftrightarrow F(\omega), \text{ then } f_t(t) \Longleftrightarrow i\omega F(\omega), \quad (\text{E.14})$$

then (E.13) has Fourier transform

$$F(\omega) = i\omega \sqrt{\pi} \frac{a_0}{c} e^{-i k c t_0 - a_0^2 k^2 / 4} = \sqrt{\pi} i k a_0 e^{-i k c t_0 - a_0^2 k^2 / 4}. \quad (\text{E.15})$$

E.1.3 The Sine Packet

Another alternative is to use the sine packet

$$f(t) = e^{-t^2} \sin(\omega_0 t), \quad (\text{E.16})$$

which has Fourier transform

$$F(\omega) = \frac{\sqrt{\pi}}{2i} \left(e^{-(\omega_0 - \omega)^2 / 4} - e^{-(\omega_0 + \omega)^2 / 4} \right); \quad (\text{E.17})$$

this is zero when $\omega = 0$.

The Gaussian sine packet with displacement and dilation is

$$f(t) = e^{-(c(t-t_0))^2/a_o^2} \sin(\omega_0 t), \quad (\text{E.18})$$

with Fourier transform

$$F(\omega) = \frac{\sqrt{\pi}}{2i} \frac{a_0}{c} e^{-it_0\omega} e^{-(\omega_0^2 - \omega^2)a_0^2/4c^2} \left(e^{\omega_0\left(it_0 + \frac{a_0^2\omega}{2c^2}\right)} - e^{-\omega_0\left(it_0 + \frac{a_0^2\omega}{2c^2}\right)} \right). \quad (\text{E.19})$$

Appendix F

Scatterer Arrays Numerical results

F.1 Relative Differences

This section contains the results of measuring the deviation from the solution produced by an array of cornered scatterers to that produced when the corners are rounded. The difference between the solution produced by a cornered scatterer, $u_0^\infty(\hat{\mathbf{x}})$, where $\hat{\mathbf{x}} = \hat{\mathbf{x}}(\hat{\theta})$ for $\hat{\theta} \in [0, 2\pi]$, and that produced by rounding $u_\rho^\infty(\hat{\mathbf{x}})$, with associated radius of curvature ρ , is measured using the L^1 norm

$$\|u_0^\infty - u_\rho^\infty\|_1 = \int_0^{2\pi} |u_0^\infty(\hat{\mathbf{x}}) - u_\rho^\infty(\hat{\mathbf{x}})| d\hat{\mathbf{x}}, \quad (\text{F.1})$$

and L^∞ norm

$$\|u_0^\infty - u_\rho^\infty\|_\infty = \max_{\hat{\mathbf{x}} \in [0, 2\pi]} |u_0^\infty(\hat{\mathbf{x}}) - u_\rho^\infty(\hat{\mathbf{x}})|. \quad (\text{F.2})$$

The results in this section are for arrays of two and four scatterers of a single shape and boundary condition arranged in a line parallel to the y-axis (Figure 7.1). Three shapes are examined: the lemniscate (2.2), square (2.6) and diamond (square rotated by $\pi/4$) and their rounded counterparts (2.3), (2.7), for the three boundary conditions (2.19), (2.20) and (2.21). Data is also provided for a single scatterer with the same conditions to enable understanding of the effect of rounding as the number of scatterers increases.

Results are presented for scatterers of diameter $2a = 0.5, 1$ and 2 wavelengths, separated by distances $d = 0.1, 0.25, 0.5$ and 1 wavelengths. Both the absolute and relative

difference were measured and the relative difference is reported. The relative difference is expressed as a percentage of the same norm of the scatterer's far-field. The L^1 relative difference (%) is

$$\frac{\|u_0^\infty - u_\rho^\infty\|_1}{\|u_0^\infty\|_1}, \quad (\text{F.3})$$

and the L^∞ difference (%) is

$$\frac{\|u_0^\infty - u_\rho^\infty\|_\infty}{\|u_0^\infty\|_\infty}. \quad (\text{F.4})$$

All results are for incident wave angle $\theta_0 = 0$. Tables F.1 and F.2 are for the lemniscate, Tables F.3 and F.4 for the square and Tables F.5 and F.6 for diamonds.

Discussion and analysis of the results are in Section 7.5.

2a	ρ	Single	2 Lemniscates		4 Lemniscates					
		Lemniscate	$d=0.1\lambda$	$d=0.25\lambda$	$d=0.5\lambda$	$d=\lambda$	$d=0.1\lambda$	$d=0.25\lambda$	$d=0.5\lambda$	$d=\lambda$
Dirichlet										
0.5 λ	0.05	2.10	2.26	1.95	1.62	2.45	2.36	2.05	1.42	2.52
	0.04	1.57	1.68	1.44	1.21	1.83	1.75	1.52	1.06	1.88
	0.03	1.07	1.14	0.98	0.83	1.26	1.20	1.04	0.73	1.29
	0.02	0.63	0.67	0.57	0.48	0.74	0.70	0.60	0.43	0.76
	0.01	0.25	0.27	0.23	0.19	0.29	0.28	0.24	0.17	0.30
λ	0.05	4.00	3.00	3.91	4.27	3.44	2.94	4.29	4.40	3.04
	0.04	2.98	2.24	2.93	3.19	2.54	2.21	3.23	3.28	2.23
	0.03	2.04	1.54	2.02	2.18	1.73	1.52	2.23	2.25	1.50
	0.02	1.20	0.90	1.19	1.28	1.00	0.90	1.32	1.32	0.86
	0.01	0.48	0.36	0.48	0.51	0.40	0.37	0.54	0.53	0.34
2 λ	0.05	7.67	6.26	6.96	7.91	6.14	6.22	7.47	7.87	5.44
	0.04	5.73	4.67	5.22	5.94	4.50	4.65	5.62	5.92	3.92
	0.03	3.93	3.20	3.60	4.10	3.02	3.20	3.89	4.08	2.58
	0.02	2.31	1.88	2.13	2.42	1.73	1.89	2.31	2.41	1.45
	0.01	0.93	0.75	0.86	0.98	0.68	0.77	0.94	0.98	0.55
Neumann										
0.5 λ	0.05	0.81	1.50	0.81	1.03	1.46	0.77	1.07	1.50	1.72
	0.04	0.55	1.14	0.61	0.73	1.08	0.56	0.79	1.09	1.27
	0.03	0.33	0.80	0.42	0.46	0.74	0.38	0.54	0.72	0.85
	0.02	0.16	0.48	0.25	0.25	0.43	0.22	0.31	0.41	0.49
	0.01	0.05	0.20	0.11	0.08	0.17	0.09	0.13	0.15	0.19
λ	0.05	1.94	2.58	2.56	2.68	2.59	3.21	2.58	3.00	3.39
	0.04	1.33	1.78	1.77	1.99	1.86	2.24	1.78	2.20	2.45
	0.03	0.81	1.11	1.10	1.36	1.22	1.41	1.09	1.49	1.61
	0.02	0.40	0.56	0.56	0.80	0.67	0.73	0.55	0.86	0.90
	0.01	0.12	0.18	0.18	0.33	0.24	0.25	0.17	0.34	0.33
2 λ	0.05	4.55	6.40	6.87	5.78	4.41	7.91	6.86	5.21	4.61
	0.04	3.14	4.64	4.99	4.35	3.04	5.70	4.92	3.76	3.18
	0.03	1.93	3.06	3.33	3.04	1.88	3.73	3.20	2.49	1.96
	0.02	0.97	1.70	1.90	1.85	0.95	2.04	1.75	1.41	0.99
	0.01	0.29	0.63	0.76	0.79	0.29	0.75	0.64	0.56	0.30
Impedance, $Z = 1 + i$										
0.5 λ	0.05	2.17	1.93	1.68	2.17	2.26	1.97	1.71	2.27	2.28
	0.04	1.69	1.49	1.30	1.70	1.76	1.53	1.32	1.78	1.77
	0.03	1.23	1.08	0.94	1.24	1.28	1.10	0.95	1.30	1.29
	0.02	0.79	0.69	0.60	0.80	0.82	0.70	0.61	0.84	0.83
	0.01	0.38	0.32	0.29	0.38	0.39	0.33	0.29	0.41	0.40
λ	0.05	3.51	3.44	4.01	3.87	3.11	3.82	4.39	3.99	2.80
	0.04	2.71	2.67	3.11	2.97	2.39	2.98	3.40	3.07	2.16
	0.03	1.94	1.93	2.24	2.13	1.72	2.17	2.45	2.20	1.55
	0.02	1.23	1.24	1.43	1.34	1.09	1.39	1.56	1.39	0.99
	0.01	0.58	0.59	0.67	0.62	0.51	0.66	0.73	0.65	0.46
2 λ	0.05	6.09	5.97	6.63	6.90	5.36	6.43	7.36	7.26	4.94
	0.04	4.65	4.58	5.10	5.26	4.09	4.96	5.67	5.54	3.77
	0.03	3.30	3.26	3.64	3.72	2.90	3.56	4.06	3.92	2.68
	0.02	2.05	2.04	2.28	2.30	1.80	2.25	2.55	2.42	1.68
	0.01	0.93	0.93	1.05	1.04	0.82	1.04	1.17	1.09	0.77

Table F.1: Relative L^1 norm differences (%) (F.1), for lemniscates with interior angle $\beta = \pi/2$, with different radii of curvature, ρ . Scatterer diameter is $2a$ and separation distance, d , for incidence angle $\theta_0 = 0$.

2a	ρ	Single	2 Lemniscates		4 Lemniscates					
		Lemniscate	d=0.1 λ	d=0.25 λ	d=0.5 λ	d= λ	d=0.1 λ	d=0.25 λ	d=0.5 λ	d= λ
Dirichlet										
0.5 λ	0.05	2.44	3.95	2.92	1.13	3.50	4.63	3.45	0.66	3.96
	0.04	1.82	2.94	2.15	0.85	2.61	3.45	2.55	0.50	2.96
	0.03	1.25	2.01	1.46	0.59	1.79	2.36	1.72	0.36	2.03
	0.02	0.73	1.18	0.84	0.35	1.05	1.38	0.99	0.22	1.19
	0.01	0.29	0.47	0.33	0.14	0.42	0.55	0.39	0.09	0.48
λ	0.05	3.53	2.50	3.49	3.63	2.98	2.09	4.02	3.58	2.60
	0.04	2.64	1.85	2.66	2.69	2.20	1.55	3.07	2.65	1.89
	0.03	1.81	1.25	1.87	1.84	1.49	1.05	2.16	1.80	1.26
	0.02	1.07	0.73	1.13	1.07	0.87	0.61	1.30	1.05	0.71
	0.01	0.43	0.29	0.46	0.42	0.34	0.24	0.54	0.41	0.28
2 λ	0.05	4.73	3.92	4.31	4.95	3.86	3.32	4.77	4.86	3.35
	0.04	3.55	2.89	3.32	3.77	2.88	2.44	3.68	3.71	2.39
	0.03	2.45	1.96	2.34	2.64	1.97	1.65	2.60	2.61	1.62
	0.02	1.44	1.14	1.42	1.58	1.15	0.96	1.58	1.57	0.93
	0.01	0.58	0.45	0.59	0.65	0.46	0.38	0.65	0.65	0.37
Neumann										
0.5 λ	0.05	0.91	1.39	0.67	1.17	1.11	0.43	0.68	1.35	1.05
	0.04	0.61	1.06	0.51	0.80	0.85	0.29	0.49	0.94	0.70
	0.03	0.37	0.75	0.36	0.49	0.59	0.18	0.34	0.59	0.47
	0.02	0.18	0.46	0.22	0.25	0.36	0.11	0.20	0.31	0.29
	0.01	0.05	0.19	0.10	0.08	0.15	0.04	0.08	0.11	0.12
λ	0.05	1.55	2.15	2.17	1.49	2.99	2.68	2.38	1.72	4.24
	0.04	1.05	1.44	1.51	1.15	2.14	1.79	1.59	1.12	3.00
	0.03	0.64	0.86	0.94	0.81	1.38	1.06	0.96	0.65	1.91
	0.02	0.31	0.41	0.48	0.49	0.74	0.50	0.47	0.37	1.00
	0.01	0.09	0.13	0.16	0.20	0.26	0.14	0.14	0.16	0.33
2 λ	0.05	2.18	5.67	4.48	2.12	2.49	7.88	5.55	2.22	2.95
	0.04	1.49	4.08	2.98	1.54	1.68	5.58	3.73	1.40	2.00
	0.03	0.91	2.66	1.86	1.08	1.01	3.53	2.22	0.78	1.21
	0.02	0.45	1.43	0.97	0.67	0.49	1.83	1.05	0.48	0.61
	0.01	0.13	0.50	0.32	0.29	0.14	0.58	0.28	0.22	0.19
Impedance, $Z = 1 + i$										
0.5 λ	0.05	1.79	2.06	1.37	1.49	2.17	2.24	1.32	1.37	2.29
	0.04	1.39	1.59	1.06	1.16	1.68	1.73	1.01	1.07	1.78
	0.03	1.01	1.15	0.76	0.85	1.22	1.24	0.72	0.79	1.29
	0.02	0.65	0.73	0.48	0.55	0.78	0.79	0.45	0.51	0.83
	0.01	0.31	0.35	0.23	0.26	0.37	0.37	0.21	0.25	0.39
λ	0.05	2.04	1.68	2.21	2.40	1.58	1.68	2.40	2.48	1.22
	0.04	1.57	1.32	1.71	1.84	1.22	1.34	1.86	1.90	0.94
	0.03	1.13	0.97	1.24	1.31	0.87	1.00	1.35	1.36	0.68
	0.02	0.71	0.63	0.79	0.83	0.56	0.65	0.86	0.85	0.43
	0.01	0.33	0.30	0.37	0.38	0.26	0.32	0.41	0.39	0.21
2 λ	0.05	2.36	1.93	2.28	3.04	2.11	1.82	2.44	3.23	1.88
	0.04	1.80	1.47	1.78	2.32	1.61	1.39	1.91	2.47	1.44
	0.03	1.28	1.06	1.28	1.65	1.14	1.01	1.38	1.75	1.02
	0.02	0.80	0.68	0.81	1.02	0.71	0.66	0.88	1.08	0.63
	0.01	0.36	0.32	0.38	0.46	0.32	0.32	0.41	0.49	0.29

Table F.2: Relative L^∞ norm differences (%) (F.2), for lemniscates with interior angle $\beta = \pi/2$, with different radii of curvature, ρ . Scatterer diameter is $2a$ and separation distance, d , for incidence angle $\theta_0 = 0$.

$2a$	ρ	Single Square	2 Squares				4 Squares			
			$d=0.1\lambda$	$d=0.25\lambda$	$d=0.5\lambda$	$d=\lambda$	$d=0.1\lambda$	$d=0.25\lambda$	$d=0.5\lambda$	$d=\lambda$
Dirichlet										
0.5λ	0.05	1.21	1.13	1.29	2.58	1.15	1.08	1.29	3.13	1.11
	0.04	0.87	0.81	0.93	1.86	0.83	0.78	0.93	2.25	0.79
	0.03	0.60	0.55	0.63	1.27	0.57	0.53	0.63	1.54	0.54
	0.02	0.36	0.34	0.38	0.77	0.34	0.32	0.38	0.93	0.33
	0.01	0.14	0.13	0.15	0.31	0.14	0.13	0.15	0.37	0.13
λ	0.05	2.54	2.55	3.35	6.12	2.47	2.66	3.79	6.94	2.39
	0.04	1.82	1.82	2.40	4.39	1.77	1.89	2.71	4.98	1.71
	0.03	1.25	1.24	1.63	3.00	1.21	1.28	1.84	3.40	1.17
	0.02	0.76	0.75	0.99	1.82	0.73	0.77	1.12	2.06	0.71
	0.01	0.30	0.30	0.39	0.72	0.29	0.31	0.44	0.82	0.28
2λ	0.05	5.46	5.74	7.38	12.91	5.29	6.11	8.53	15.02	5.10
	0.04	3.90	4.07	5.25	9.25	3.78	4.30	6.05	10.74	3.64
	0.03	2.66	2.75	3.56	6.31	2.57	2.88	4.10	7.32	2.47
	0.02	1.61	1.65	2.14	3.81	1.55	1.72	2.46	4.42	1.49
	0.01	0.64	0.65	0.85	1.51	0.62	0.67	0.97	1.75	0.59
Neumann										
0.5λ	0.05	2.26	4.88	3.23	2.12	1.38	5.18	3.35	2.00	1.35
	0.04	1.62	3.46	2.31	1.52	0.99	3.65	2.39	1.44	0.97
	0.03	1.11	2.34	1.57	1.04	0.68	2.46	1.63	0.98	0.66
	0.02	0.67	1.40	0.95	0.63	0.41	1.47	0.98	0.60	0.40
	0.01	0.27	0.55	0.38	0.25	0.16	0.58	0.39	0.24	0.16
λ	0.05	2.32	5.69	3.57	2.60	2.34	6.76	4.20	2.62	2.60
	0.04	1.64	3.94	2.54	1.86	1.64	4.75	3.01	1.87	1.77
	0.03	1.11	2.61	1.72	1.27	1.10	3.19	2.05	1.27	1.15
	0.02	0.67	1.54	1.04	0.77	0.66	1.90	1.24	0.77	0.67
	0.01	0.26	0.60	0.41	0.30	0.26	0.74	0.49	0.30	0.26
2λ	0.05	5.21	15.18	8.22	6.01	5.27	17.22	9.79	6.24	6.16
	0.04	3.72	10.46	5.87	4.35	3.67	12.22	7.08	4.51	4.13
	0.03	2.53	6.77	3.96	2.98	2.44	8.11	4.84	3.08	2.64
	0.02	1.52	3.87	2.37	1.81	1.44	4.73	2.91	1.87	1.49
	0.01	0.59	1.44	0.92	0.72	0.55	1.79	1.15	0.74	0.55
Impedance, $Z = 1 + i$										
0.5λ	0.05	1.62	1.47	1.79	1.86	1.45	1.42	1.70	1.99	1.39
	0.04	1.24	1.12	1.37	1.42	1.11	1.09	1.30	1.52	1.06
	0.03	0.91	0.83	1.01	1.04	0.82	0.80	0.96	1.12	0.79
	0.02	0.61	0.56	0.68	0.70	0.55	0.54	0.64	0.75	0.53
	0.01	0.30	0.27	0.33	0.34	0.27	0.27	0.31	0.37	0.26
λ	0.05	2.93	3.14	3.83	3.21	2.90	3.33	4.17	3.31	2.86
	0.04	2.21	2.37	2.90	2.43	2.19	2.51	3.15	2.50	2.16
	0.03	1.61	1.73	2.12	1.77	1.60	1.83	2.30	1.82	1.57
	0.02	1.08	1.15	1.41	1.18	1.06	1.23	1.54	1.21	1.05
	0.01	0.52	0.56	0.68	0.57	0.51	0.60	0.74	0.58	0.51
2λ	0.05	5.36	5.93	7.24	5.69	5.39	6.40	8.08	6.07	5.32
	0.04	3.98	4.38	5.38	4.24	3.99	4.70	6.00	4.53	3.94
	0.03	2.85	3.12	3.85	3.05	2.86	3.34	4.30	3.26	2.81
	0.02	1.86	2.03	2.51	1.99	1.86	2.17	2.80	2.13	1.83
	0.01	0.87	0.95	1.18	0.93	0.87	1.02	1.32	1.00	0.86

Table F.3: Relative L^1 norm differences (%) (F.1), for squares with different radii of curvature, ρ . Scatterer diameter is $2a$ and separation distance, d , for incidence angle $\theta_0 = 0$.

		Single	2 Squares				4 Squares			
$2a$	ρ	Square	$d=0.1\lambda$	$d=0.25\lambda$	$d=0.5\lambda$	$d=\lambda$	$d=0.1\lambda$	$d=0.25\lambda$	$d=0.5\lambda$	$d=\lambda$
Dirichlet										
0.5λ	0.05	1.48	1.24	1.76	2.14	1.32	1.22	1.95	2.52	1.25
	0.04	1.07	0.89	1.26	1.54	0.95	0.87	1.40	1.81	0.90
	0.03	0.73	0.61	0.86	1.05	0.65	0.59	0.96	1.24	0.61
	0.02	0.44	0.37	0.52	0.64	0.39	0.36	0.58	0.76	0.37
	0.01	0.18	0.15	0.21	0.26	0.16	0.14	0.23	0.30	0.15
λ	0.05	2.10	1.81	2.60	4.94	1.78	1.79	3.10	6.47	1.59
	0.04	1.51	1.29	1.86	3.56	1.28	1.26	2.20	4.65	1.14
	0.03	1.03	0.87	1.26	2.44	0.87	0.85	1.49	3.19	0.78
	0.02	0.63	0.53	0.76	1.48	0.53	0.51	0.90	1.94	0.47
	0.01	0.25	0.21	0.30	0.59	0.21	0.20	0.36	0.77	0.19
2λ	0.05	2.95	2.61	3.82	7.08	2.44	2.66	4.57	9.71	2.23
	0.04	2.13	1.83	2.69	5.14	1.75	1.83	3.20	7.01	1.59
	0.03	1.46	1.23	1.81	3.54	1.20	1.21	2.15	4.81	1.09
	0.02	0.89	0.73	1.08	2.16	0.73	0.71	1.28	2.92	0.66
	0.01	0.35	0.29	0.43	0.86	0.29	0.27	0.50	1.16	0.26
Neumann										
0.5λ	0.05	2.38	3.51	2.66	2.22	1.98	4.67	3.08	2.10	1.86
	0.04	1.70	2.47	1.90	1.59	1.39	3.27	2.19	1.50	1.30
	0.03	1.16	1.66	1.29	1.08	0.92	2.19	1.49	1.01	0.86
	0.02	0.71	0.99	0.78	0.65	0.54	1.30	0.89	0.61	0.51
	0.01	0.28	0.39	0.31	0.26	0.21	0.51	0.35	0.24	0.19
λ	0.05	2.40	2.67	2.40	2.30	2.16	2.86	2.63	2.30	2.11
	0.04	1.70	1.84	1.67	1.60	1.50	1.97	1.84	1.61	1.46
	0.03	1.14	1.21	1.11	1.07	0.99	1.30	1.22	1.07	0.96
	0.02	0.67	0.71	0.65	0.63	0.58	0.76	0.72	0.63	0.56
	0.01	0.26	0.27	0.25	0.24	0.22	0.29	0.28	0.24	0.21
2λ	0.05	3.22	4.16	3.41	3.23	3.13	4.44	3.71	3.23	3.11
	0.04	2.25	2.80	2.36	2.25	2.15	3.04	2.59	2.25	2.12
	0.03	1.50	1.79	1.55	1.48	1.40	1.96	1.71	1.49	1.37
	0.02	0.88	1.01	0.90	0.86	0.81	1.11	0.99	0.87	0.78
	0.01	0.33	0.37	0.34	0.33	0.30	0.41	0.38	0.33	0.29
Impedance, $Z = 1 + i$										
0.5λ	0.05	1.40	1.27	1.63	1.51	1.29	1.27	1.73	1.60	1.25
	0.04	1.08	0.98	1.25	1.16	1.00	0.98	1.33	1.23	0.97
	0.03	0.81	0.73	0.93	0.86	0.75	0.74	0.99	0.91	0.73
	0.02	0.55	0.50	0.63	0.58	0.51	0.51	0.67	0.62	0.50
	0.01	0.27	0.25	0.32	0.29	0.26	0.26	0.33	0.30	0.25
λ	0.05	1.49	1.40	1.93	1.50	1.36	1.44	2.20	1.51	1.27
	0.04	1.13	1.06	1.46	1.14	1.03	1.09	1.66	1.15	0.96
	0.03	0.83	0.78	1.07	0.84	0.76	0.80	1.21	0.84	0.71
	0.02	0.56	0.53	0.72	0.56	0.51	0.54	0.81	0.56	0.48
	0.01	0.27	0.26	0.35	0.27	0.25	0.27	0.40	0.27	0.24
2λ	0.05	1.76	1.70	2.39	1.91	1.59	1.78	2.77	1.99	1.52
	0.04	1.32	1.25	1.77	1.43	1.19	1.29	2.04	1.50	1.13
	0.03	0.95	0.89	1.26	1.04	0.86	0.92	1.46	1.09	0.82
	0.02	0.63	0.59	0.83	0.68	0.57	0.60	0.95	0.71	0.54
	0.01	0.30	0.28	0.39	0.32	0.27	0.29	0.45	0.34	0.26

Table F.4: Relative L^∞ norm differences (%) (F.2), for squares with different radii of curvature, ρ . Scatterer diameter is $2a$ and separation distance, d , for incidence angle $\theta_0 = 0$.

$2a$	ρ	Single Diamond	2 Diamonds				4 Diamonds			
			$d=0.1\lambda$	$d=0.25\lambda$	$d=0.5\lambda$	$d=\lambda$	$d=0.1\lambda$	$d=0.25\lambda$	$d=0.5\lambda$	$d=\lambda$
Dirichlet										
0.5λ	0.05	1.24	1.06	1.21	2.36	1.26	1.10	1.27	2.51	1.34
	0.04	0.89	0.76	0.86	1.70	0.91	0.79	0.90	1.81	0.96
	0.03	0.61	0.52	0.59	1.16	0.62	0.54	0.61	1.24	0.66
	0.02	0.37	0.31	0.36	0.71	0.38	0.33	0.37	0.76	0.40
	0.01	0.15	0.12	0.14	0.28	0.15	0.13	0.15	0.30	0.16
λ	0.05	2.41	2.55	2.99	4.05	2.65	2.60	3.38	4.44	2.72
	0.04	1.73	1.83	2.13	2.93	1.90	1.86	2.41	3.21	1.96
	0.03	1.18	1.25	1.44	2.02	1.30	1.27	1.63	2.21	1.34
	0.02	0.71	0.76	0.87	1.23	0.79	0.77	0.98	1.35	0.81
	0.01	0.28	0.30	0.34	0.49	0.31	0.31	0.39	0.54	0.32
2λ	0.05	4.93	3.99	6.12	7.87	3.97	3.76	6.93	8.77	4.07
	0.04	3.53	2.83	4.22	5.76	2.82	2.65	4.78	6.43	2.89
	0.03	2.41	1.92	2.80	3.99	1.91	1.78	3.16	4.47	1.96
	0.02	1.46	1.15	1.65	2.45	1.15	1.06	1.87	2.74	1.17
	0.01	0.58	0.46	0.64	0.99	0.45	0.42	0.72	1.10	0.46
Neumann										
0.5λ	0.05	1.29	2.31	1.63	1.38	1.38	3.19	2.07	1.32	1.36
	0.04	0.92	1.67	1.17	0.99	0.99	2.32	1.50	0.95	0.98
	0.03	0.63	1.15	0.80	0.68	0.68	1.60	1.03	0.65	0.67
	0.02	0.38	0.70	0.49	0.41	0.41	0.98	0.63	0.39	0.41
	0.01	0.15	0.28	0.19	0.16	0.17	0.39	0.26	0.16	0.17
λ	0.05	2.58	5.04	3.37	2.47	3.33	5.35	3.57	2.73	3.09
	0.04	1.85	3.66	2.44	1.79	2.43	3.90	2.58	1.98	2.24
	0.03	1.26	2.52	1.68	1.23	1.68	2.70	1.77	1.37	1.54
	0.02	0.76	1.54	1.02	0.75	1.04	1.65	1.08	0.84	0.94
	0.01	0.30	0.62	0.41	0.30	0.42	0.66	0.43	0.34	0.38
2λ	0.05	4.51	6.96	5.73	5.68	5.71	7.67	6.92	4.72	5.83
	0.04	3.23	5.16	4.15	4.17	4.11	5.67	5.02	3.42	4.15
	0.03	2.20	3.61	2.85	2.91	2.83	3.97	3.45	2.37	2.82
	0.02	1.33	2.23	1.73	1.79	1.73	2.45	2.10	1.45	1.71
	0.01	0.53	0.90	0.69	0.73	0.70	0.99	0.84	0.58	0.68
Impedance, $Z = 1 + i$										
0.5λ	0.05	1.68	1.42	2.03	2.30	1.50	1.42	2.19	2.50	1.52
	0.04	1.28	1.09	1.56	1.77	1.14	1.09	1.68	1.92	1.16
	0.03	0.95	0.80	1.15	1.32	0.84	0.80	1.25	1.43	0.86
	0.02	0.64	0.54	0.78	0.89	0.57	0.54	0.84	0.97	0.58
	0.01	0.31	0.26	0.38	0.44	0.28	0.26	0.42	0.48	0.28
λ	0.05	2.68	3.14	3.63	3.01	2.85	3.33	3.97	3.20	2.88
	0.04	2.03	2.36	2.74	2.29	2.16	2.51	3.00	2.44	2.18
	0.03	1.48	1.72	2.00	1.69	1.57	1.82	2.18	1.79	1.59
	0.02	0.99	1.14	1.33	1.13	1.05	1.21	1.45	1.20	1.06
	0.01	0.48	0.55	0.64	0.55	0.51	0.58	0.70	0.59	0.51
2λ	0.05	4.97	5.18	6.76	5.81	4.10	5.30	7.52	6.25	4.06
	0.04	3.70	3.82	5.03	4.36	3.04	3.88	5.60	4.70	3.00
	0.03	2.65	2.71	3.60	3.15	2.17	2.75	4.02	3.40	2.13
	0.02	1.73	1.76	2.35	2.07	1.41	1.78	2.63	2.24	1.38
	0.01	0.81	0.82	1.10	0.98	0.66	0.82	1.23	1.06	0.64

Table F.5: Relative L^1 norm differences (%) (F.1), for diamonds with different radii of curvature, ρ . Scatterer diameter is $2a$ and separation distance, d , for incidence angle $\theta_0 = 0$.

		Single	2 Diamonds				4 Diamonds			
$2a$	ρ	Diamond	$d=0.1\lambda$	$d=0.25\lambda$	$d=0.5\lambda$	$d=\lambda$	$d=0.1\lambda$	$d=0.25\lambda$	$d=0.5\lambda$	$d=\lambda$
Dirichlet										
0.5λ	0.05	1.05	0.96	0.60	1.74	1.30	1.22	0.80	2.12	1.63
	0.04	0.75	0.69	0.43	1.26	0.93	0.87	0.57	1.53	1.17
	0.03	0.52	0.47	0.29	0.87	0.64	0.59	0.38	1.05	0.80
	0.02	0.31	0.28	0.18	0.53	0.39	0.36	0.23	0.64	0.49
	0.01	0.12	0.11	0.07	0.21	0.15	0.14	0.09	0.26	0.19
λ	0.05	1.87	2.05	2.66	2.27	2.16	2.44	3.31	3.01	2.39
	0.04	1.35	1.46	1.87	1.65	1.55	1.74	2.33	2.18	1.71
	0.03	0.93	0.99	1.26	1.13	1.07	1.19	1.57	1.50	1.17
	0.02	0.56	0.60	0.75	0.69	0.65	0.72	0.94	0.92	0.71
	0.01	0.23	0.24	0.29	0.28	0.26	0.28	0.37	0.37	0.28
2λ	0.05	2.53	1.67	2.38	5.56	2.29	1.32	2.66	7.16	2.57
	0.04	1.80	1.19	1.62	4.12	1.58	0.94	1.80	5.31	1.79
	0.03	1.22	0.81	1.07	2.89	1.05	0.64	1.16	3.72	1.18
	0.02	0.73	0.48	0.62	1.79	0.62	0.38	0.67	2.30	0.70
	0.01	0.29	0.19	0.24	0.72	0.24	0.15	0.26	0.93	0.27
Neumann										
0.5λ	0.05	2.85	4.05	3.36	2.28	3.26	5.33	3.62	2.01	2.64
	0.04	2.04	2.88	2.38	1.62	2.32	3.77	2.54	1.44	1.89
	0.03	1.38	1.94	1.60	1.10	1.57	2.53	1.70	0.98	1.29
	0.02	0.83	1.16	0.95	0.66	0.94	1.51	1.01	0.59	0.78
	0.01	0.33	0.45	0.37	0.27	0.38	0.58	0.39	0.24	0.31
λ	0.05	3.20	3.81	3.59	2.63	4.29	5.21	3.56	2.44	4.81
	0.04	2.32	2.73	2.59	1.92	3.17	3.73	2.55	1.76	3.42
	0.03	1.60	1.85	1.76	1.33	2.22	2.54	1.72	1.21	2.32
	0.02	0.97	1.13	1.06	0.81	1.38	1.53	1.03	0.73	1.39
	0.01	0.39	0.47	0.41	0.32	0.56	0.60	0.40	0.28	0.56
2λ	0.05	3.53	4.40	3.26	3.33	5.35	4.83	3.87	2.25	5.13
	0.04	2.52	3.07	2.26	2.47	3.71	3.33	2.62	1.61	3.51
	0.03	1.69	2.02	1.47	1.72	2.44	2.16	1.67	1.11	2.27
	0.02	1.00	1.17	0.84	1.06	1.40	1.23	0.92	0.70	1.29
	0.01	0.38	0.44	0.30	0.42	0.52	0.45	0.32	0.28	0.47
Impedance, $Z = 1 + i$										
0.5λ	0.05	1.27	0.67	1.02	1.63	0.83	0.58	1.33	1.94	0.90
	0.04	0.98	0.52	0.77	1.25	0.63	0.43	1.01	1.49	0.68
	0.03	0.73	0.38	0.57	0.92	0.46	0.31	0.74	1.10	0.49
	0.02	0.49	0.26	0.38	0.62	0.30	0.20	0.49	0.74	0.33
	0.01	0.24	0.13	0.18	0.30	0.15	0.09	0.24	0.36	0.16
λ	0.05	1.43	1.09	1.51	1.47	1.50	1.37	1.80	1.46	1.52
	0.04	1.09	0.82	1.13	1.12	1.14	1.03	1.35	1.11	1.15
	0.03	0.79	0.60	0.81	0.82	0.83	0.75	0.98	0.81	0.85
	0.02	0.53	0.40	0.53	0.55	0.56	0.50	0.65	0.54	0.57
	0.01	0.26	0.20	0.25	0.26	0.27	0.25	0.33	0.26	0.28
2λ	0.05	1.61	1.37	2.16	2.63	1.10	1.53	2.54	3.17	1.06
	0.04	1.24	1.00	1.60	2.01	0.81	1.11	1.88	2.42	0.78
	0.03	0.91	0.70	1.14	1.48	0.58	0.77	1.34	1.78	0.55
	0.02	0.60	0.44	0.73	0.98	0.37	0.49	0.86	1.18	0.35
	0.01	0.28	0.19	0.34	0.47	0.17	0.21	0.40	0.56	0.16

Table F.6: Relative L^∞ norm differences (%) (F.2), for diamonds with different radii of curvature, ρ . Scatterer diameter is $2a$ and separation distance, d , for incidence angle $\theta_0 = 0$.

F.2 Far-field Differences

This section contains the numerical results for the scatterer array configurations consisting of two or four scatterers described in Section 7.1, measuring the quantity

$$\sqrt{k} \|u_0^\infty - u_\rho^\infty\|_\infty, \quad (\text{F.5})$$

where u_0^∞ is the far-field of the cornered scatterers and u_ρ^∞ is the far-field of the rounded scatterers with radius of curvature ρ , as ρ approaches 0. The \sqrt{k} factor correctly non-dimensionalises the far-field quantities.

We want to establish whether the following relationship

$$\sqrt{k} \|u_0^\infty - u_\rho^\infty\|_\infty \approx C(k\rho)^m, \quad (\text{F.6})$$

for some constant C holds. The constants C and m were estimated by using a least squares linear fit to the logarithm of the quantity (F.6).

	θ_0	$d = 0.1\lambda$		$d = 0.25\lambda$		$d = 0.5\lambda$		$d = \lambda$	
		C	m	C	m	C	m	C	m
Square	0	1	1.33	2	1.33	4	1.35	2	1.33
	$\pi/8$	1	1.34	2	1.34	4	1.36	3	1.35
	$\pi/4$	1	1.35	2	1.35	3	1.37	3	1.36
	$3\pi/8$	1	1.34	1	1.34	2	1.36	2	1.36
Diamond	0	1	1.33	2	1.36	2	1.35	1	1.32
	$\pi/8$	1	1.33	1	1.34	2	1.34	1	1.34
	$\pi/4$	1	1.33	1	1.33	1	1.34	1	1.34
	$3\pi/8$	1	1.33	1	1.34	1	1.34	1	1.34
Lemniscates									
$\beta = \pi/2$	0	3	1.33	3	1.33	3	1.33	2	1.33
	$\pi/8$	3	1.33	3	1.33	3	1.33	2	1.33
	$\pi/4$	2	1.33	2	1.33	3	1.33	3	1.33
	$3\pi/8$	2	1.33	2	1.33	2	1.33	2	1.33
$\beta = \pi/3$	0	10	1.20	8	1.19	8	1.20	9	1.20
	$\pi/8$	9	1.20	8	1.20	8	1.20	7	1.20
	$\pi/4$	7	1.20	7	1.20	8	1.20	8	1.20
	$3\pi/8$	5	1.20	5	1.20	5	1.20	6	1.20
$\beta = \pi/4$	0	15	1.14	16	1.14	15	1.15	14	1.14
	$\pi/8$	16	1.15	16	1.14	13	1.14	13	1.14
	$\pi/4$	13	1.15	13	1.14	14	1.15	14	1.14
	$3\pi/8$	10	1.15	10	1.15	11	1.15	11	1.15
$\beta = \pi/6$	0	35	1.09	38	1.09	31	1.09	34	1.09
	$\pi/8$	31	1.09	34	1.09	31	1.09	29	1.09
	$\pi/4$	26	1.09	29	1.09	30	1.09	33	1.09
	$3\pi/8$	22	1.09	23	1.09	21	1.09	23	1.09
$\beta = \pi/12$	0	127	1.05	170	1.05	84	1.03	124	1.05
	$\pi/8$	110	1.05	152	1.05	102	1.04	115	1.04
	$\pi/4$	96	1.05	123	1.05	117	1.05	120	1.04
	$3\pi/8$	74	1.05	83	1.05	77	1.05	88	1.05
$\beta = \pi/18$	0	267	1.03	241	1.02	307	1.03	233	1.03
	$\pi/8$	239	1.03	272	1.03	284	1.03	278	1.03
	$\pi/4$	218	1.03	228	1.03	233	1.03	249	1.03
	$3\pi/8$	160	1.03	171	1.03	160	1.03	188	1.03
$\beta = \pi/36$	0	1016	1.03	1261	1.02	1373	1.02	842	1.02
	$\pi/8$	956	1.03	1251	1.02	1241	1.02	1054	1.03
	$\pi/4$	809	1.03	1011	1.02	956	1.03	990	1.02
	$3\pi/8$	623	1.03	696	1.02	639	1.03	754	1.02

Table F.7: Far-field differences as $k\rho \rightarrow 0$ for two scatterers with Dirichlet boundary condition for different separation distances d and different incident angles θ_0 .

	θ_0	$d = 0.1\lambda$		$d = 0.25\lambda$		$d = 0.5\lambda$		$d = \lambda$	
		C	m	C	m	C	m	C	m
Square	0	2.44	1.34	4.67	1.34	11.67	1.36	2.85	1.33
	$\pi/8$	2.25	1.34	4.13	1.34	10.36	1.38	7.88	1.36
	$\pi/4$	1.85	1.36	3.09	1.35	6.93	1.38	8.09	1.39
	$3\pi/8$	1.23	1.37	1.82	1.37	3.49	1.37	4.28	1.37
Diamond	0	3.16	1.33	5.05	1.37	8.11	1.35	3.63	1.35
	$\pi/8$	2.69	1.34	3.42	1.34	6.25	1.35	6.20	1.36
	$\pi/4$	2.79	1.35	2.79	1.34	3.06	1.31	3.41	1.30
	$3\pi/8$	2.38	1.38	2.31	1.36	2.37	1.34	2.31	1.31
Lemniscates									
$\beta = \pi/2$	0	4.9	1.33	7.0	1.33	5.4	1.33	4.2	1.33
	$\pi/8$	6.9	1.33	6.2	1.34	5.0	1.33	4.7	1.33
	$\pi/4$	5.0	1.33	4.9	1.33	5.9	1.33	5.6	1.33
	$3\pi/8$	2.9	1.33	3.3	1.33	3.6	1.33	4.2	1.33
$\beta = \pi/3$	0	22.5	1.20	16.3	1.20	17.4	1.21	20.0	1.20
	$\pi/8$	19.3	1.20	14.9	1.20	16.5	1.21	15.7	1.20
	$\pi/4$	12.6	1.20	14.8	1.20	18.2	1.21	17.3	1.21
	$3\pi/8$	10.0	1.21	10.0	1.21	10.6	1.20	11.9	1.20
$\beta = \pi/4$	0	33.0	1.14	32.1	1.14	34.8	1.15	31.9	1.14
	$\pi/8$	34.3	1.15	35.7	1.14	27.5	1.15	26.8	1.14
	$\pi/4$	27.4	1.15	28.1	1.15	29.4	1.15	27.0	1.15
	$3\pi/8$	18.4	1.15	19.4	1.15	21.1	1.15	22.6	1.15
$\beta = \pi/6$	0	76.6	1.09	84.3	1.10	68.0	1.09	71.5	1.09
	$\pi/8$	64.2	1.09	72.8	1.10	67.0	1.09	61.5	1.09
	$\pi/4$	50.0	1.09	60.0	1.09	58.5	1.09	69.4	1.09
	$3\pi/8$	35.6	1.09	39.9	1.09	37.2	1.09	44.2	1.09
$\beta = \pi/12$	0	257.7	1.04	385.9	1.04	256.1	1.05	232.4	1.04
	$\pi/8$	220.2	1.05	329.0	1.05	212.4	1.04	299.1	1.04
	$\pi/4$	143.6	1.04	243.7	1.04	224.9	1.04	249.9	1.04
	$3\pi/8$	116.3	1.05	134.7	1.05	120.2	1.05	158.1	1.04
$\beta = \pi/18$	0	586.1	1.03	539.6	1.02	723.4	1.03	457.4	1.03
	$\pi/8$	491.3	1.03	590.4	1.03	648.3	1.03	622.1	1.03
	$\pi/4$	415.0	1.04	438.8	1.03	450.7	1.03	562.2	1.03
	$3\pi/8$	252.8	1.03	275.1	1.03	265.2	1.03	359.7	1.03
$\beta = \pi/36$	0	2120.5	1.03	2946.7	1.02	3059.6	1.02	1622.4	1.02
	$\pi/8$	1871.8	1.03	2872.6	1.02	2628.8	1.02	2004.5	1.03
	$\pi/4$	1459.7	1.03	2012.9	1.02	2073.8	1.03	1911.1	1.02
	$3\pi/8$	927.1	1.03	1095.2	1.03	1029.8	1.03	1432.2	1.03

Table F.8: Far-field differences as $k\rho \rightarrow 0$ for four scatterers with Dirichlet boundary condition for different separation distances d and different incident angles θ_0 .

	θ_0	$d = 0.1\lambda$		$d = 0.25\lambda$		$d = 0.5\lambda$		$d = \lambda$	
		C	m	C	m	C	m	C	m
Square	0	2	1.34	2	1.32	1	1.32	1	1.38
	$\pi/8$	2	1.34	2	1.34	2	1.34	2	1.32
	$\pi/4$	2	1.37	2	1.35	2	1.36	2	1.34
	$3\pi/8$	2	1.36	2	1.35	2	1.37	2	1.35
Diamond	0	2	1.34	2	1.33	2	1.34	2	1.35
	$\pi/8$	2	1.35	2	1.36	2	1.33	2	1.35
	$\pi/4$	2	1.33	2	1.32	1	1.31	1	1.32
	$3\pi/8$	1	1.30	1	1.29	1	1.30	1	1.31
Lemniscates									
$\beta = \pi/2$	0	1	1.36	1	1.34	1	1.34	1	1.37
	$\pi/8$	1	1.33	1	1.34	1	1.34	1	1.33
	$\pi/4$	1	1.33	1	1.33	1	1.33	1	1.34
	$3\pi/8$	1	1.33	1	1.33	2	1.32	2	1.32
$\beta = \pi/3$	0	2	1.20	2	1.20	1	1.23	2	1.22
	$\pi/8$	3	1.19	3	1.20	3	1.20	2	1.20
	$\pi/4$	4	1.19	4	1.20	3	1.19	4	1.20
	$3\pi/8$	4	1.18	5	1.20	3	1.19	4	1.20
$\beta = \pi/4$	0	4	1.16	2	1.15	2	1.14	2	1.15
	$\pi/8$	7	1.15	5	1.14	6	1.14	5	1.15
	$\pi/4$	8	1.15	7	1.14	6	1.14	6	1.14
	$3\pi/8$	11	1.15	8	1.15	7	1.14	7	1.14
$\beta = \pi/6$	0	7	1.09	4	1.09	3	1.10	4	1.09
	$\pi/8$	13	1.10	9	1.09	10	1.09	9	1.11
	$\pi/4$	15	1.10	14	1.09	15	1.09	21	1.09
	$3\pi/8$	24	1.09	19	1.09	16	1.09	16	1.08
$\beta = \pi/12$	0	15	1.04	8	1.03	4	1.04	5	1.05
	$\pi/8$	29	1.04	23	1.03	37	1.05	29	1.04
	$\pi/4$	62	1.04	32	1.03	69	1.05	57	1.04
	$3\pi/8$	76	1.04	44	1.03	63	1.04	54	1.04
$\beta = \pi/18$	0	21	1.02	12	1.01	6	1.02	7	1.03
	$\pi/8$	53	1.03	60	1.03	62	1.03	61	1.03
	$\pi/4$	122	1.03	114	1.02	98	1.03	122	1.03
	$3\pi/8$	153	1.02	152	1.02	90	1.02	133	1.03
$\beta = \pi/36$	0	57	1.00	26	1.00	14	1.00	14	1.00
	$\pi/8$	177	1.01	178	1.00	210	1.01	181	1.01
	$\pi/4$	396	1.01	355	1.00	316	1.01	409	1.01
	$3\pi/8$	667	1.01	482	1.01	361	1.01	597	1.00

Table F.9: Far-field differences as $k\rho \rightarrow 0$ for two scatterers with Neumann boundary condition for different separation distances d and different incident angles θ_0 .

	θ_0	$d = 0.1\lambda$		$d = 0.25\lambda$		$d = 0.5\lambda$		$d = \lambda$	
		C	m	C	m	C	m	C	m
Square	0	3.9	1.34	3.2	1.33	2.9	1.34	2.8	1.39
	$\pi/8$	4.8	1.35	3.2	1.34	2.6	1.36	3.0	1.33
	$\pi/4$	4.9	1.38	3.3	1.35	2.1	1.34	3.0	1.32
	$3\pi/8$	4.9	1.41	3.3	1.36	2.2	1.34	2.7	1.33
Diamond	0	5.6	1.36	4.6	1.37	3.6	1.34	5.2	1.38
	$\pi/8$	6.5	1.40	4.8	1.38	4.6	1.35	4.2	1.35
	$\pi/4$	3.1	1.33	4.1	1.35	2.2	1.28	3.0	1.30
	$3\pi/8$	2.7	1.29	2.4	1.28	2.0	1.28	2.3	1.30
Lemniscates									
$\beta = \pi/2$	0	1.8	1.37	1.3	1.39	1.3	1.33	2.3	1.44
	$\pi/8$	2.1	1.34	2.5	1.35	2.5	1.37	2.6	1.36
	$\pi/4$	2.9	1.36	2.9	1.35	2.8	1.33	3.1	1.35
	$3\pi/8$	2.9	1.33	2.5	1.33	3.2	1.32	3.5	1.32
$\beta = \pi/3$	0	1.9	1.21	2.7	1.21	2.2	1.24	2.8	1.23
	$\pi/8$	7.0	1.22	8.0	1.23	6.6	1.21	4.7	1.21
	$\pi/4$	8.3	1.22	9.3	1.20	7.3	1.22	8.9	1.21
	$3\pi/8$	9.8	1.21	14.7	1.21	4.7	1.21	6.2	1.20
$\beta = \pi/4$	0	3.9	1.16	3.7	1.17	3.4	1.18	3.6	1.15
	$\pi/8$	10.3	1.14	8.7	1.16	17.6	1.15	8.1	1.15
	$\pi/4$	14.2	1.14	11.7	1.15	9.9	1.14	12.8	1.14
	$3\pi/8$	13.4	1.12	14.2	1.12	11.0	1.14	15.7	1.16
$\beta = \pi/6$	0	4.8	1.09	5.8	1.09	6.5	1.16	7.4	1.09
	$\pi/8$	41.7	1.15	32.0	1.13	30.0	1.11	34.5	1.12
	$\pi/4$	39.7	1.12	55.3	1.13	26.4	1.10	74.3	1.12
	$3\pi/8$	41.0	1.10	40.5	1.09	44.6	1.13	33.3	1.10
$\beta = \pi/12$	0	12.6	1.03	8.2	1.03	6.2	1.04	8.6	1.04
	$\pi/8$	50.2	1.05	45.4	1.04	76.6	1.04	61.6	1.04
	$\pi/4$	108.7	1.06	73.8	1.03	115.4	1.04	117.0	1.04
	$3\pi/8$	118.9	1.05	87.2	1.03	101.3	1.04	83.8	1.04
$\beta = \pi/18$	0	20.1	1.01	12.2	1.01	6.0	1.02	13.0	1.02
	$\pi/8$	61.4	1.02	87.5	1.02	107.3	1.02	111.7	1.02
	$\pi/4$	148.5	1.03	223.6	1.02	199.1	1.03	312.0	1.03
	$3\pi/8$	198.7	1.02	247.7	1.02	126.7	1.02	203.7	1.02
$\beta = \pi/36$	0	59.5	1.00	26.1	1.01	15.2	1.01	34.3	1.00
	$\pi/8$	215.2	1.02	301.0	1.02	451.4	1.01	421.2	1.01
	$\pi/4$	575.6	1.02	657.3	1.02	765.9	1.01	1069.7	1.01
	$3\pi/8$	813.9	1.01	851.8	1.02	624.8	1.01	881.1	1.01

Table F.10: Far-field differences as $k\rho \rightarrow 0$ for four scatterers with Neumann boundary condition for different separation distances d and different incident angles θ_0 .

	θ_0	$d = 0.1\lambda$		$d = 0.25\lambda$		$d = 0.5\lambda$		$d = \lambda$	
		C	m	C	m	C	m	C	m
Square	0	0.5	1.00	0.7	1.01	0.7	1.02	0.5	1.00
	$\pi/8$	0.5	1.00	0.7	1.01	0.6	1.02	0.6	1.02
	$\pi/4$	0.5	1.02	0.6	1.03	0.5	1.02	0.6	1.03
	$3\pi/8$	0.4	1.03	0.5	1.04	0.3	1.01	0.4	1.02
Diamond	0	0.5	1.03	0.8	1.06	0.7	1.04	0.5	1.03
	$\pi/8$	0.5	1.01	0.6	1.03	0.7	1.03	0.7	1.04
	$\pi/4$	0.5	1.01	0.5	0.99	0.5	1.00	0.5	0.99
	$3\pi/8$	0.4	1.02	0.4	1.00	0.4	1.00	0.4	0.99
Lemniscates									
$\beta = \pi/2$	0	0.6	1.01	0.6	1.01	0.6	1.01	0.6	1.01
	$\pi/8$	0.6	1.01	0.6	1.02	0.6	1.01	0.5	1.01
	$\pi/4$	0.5	1.01	0.6	1.01	0.6	1.01	0.6	1.01
	$3\pi/8$	0.4	1.01	0.5	1.01	0.5	1.01	0.5	1.01
$\beta = \pi/3$	0	2.2	1.01	2.1	1.00	2.0	1.01	2.4	1.01
	$\pi/8$	2.1	1.01	2.0	1.00	2.2	1.01	2.1	1.02
	$\pi/4$	2.1	1.02	2.3	1.02	2.2	1.02	2.3	1.02
	$3\pi/8$	1.9	1.02	1.9	1.02	1.9	1.02	1.9	1.02
$\beta = \pi/4$	0	4.2	1.00	4.4	1.01	3.6	1.00	4.0	1.00
	$\pi/8$	4.3	1.00	4.6	1.01	4.1	1.01	3.7	1.01
	$\pi/4$	3.9	1.00	4.0	1.00	4.3	1.01	4.5	1.01
	$3\pi/8$	3.5	1.01	3.4	1.01	3.7	1.01	3.8	1.01
$\beta = \pi/6$	0	10.6	1.00	11.5	1.00	8.7	1.00	9.6	1.00
	$\pi/8$	9.9	1.00	11.2	1.00	9.5	1.00	9.3	1.00
	$\pi/4$	9.6	1.00	10.8	1.01	10.3	1.01	10.6	1.01
	$3\pi/8$	9.1	1.01	8.8	1.01	9.9	1.02	10.3	1.02
$\beta = \pi/12$	0	44.2	1.00	49.0	1.00	36.7	1.00	39.2	1.00
	$\pi/8$	42.2	1.00	46.0	1.00	39.7	1.00	37.3	1.00
	$\pi/4$	38.9	1.00	42.2	1.00	41.1	1.00	43.0	1.00
	$3\pi/8$	34.0	1.00	35.1	1.00	37.8	1.01	41.6	1.01
$\beta = \pi/18$	0	92.5	1.00	103.8	1.00	86.0	1.00	88.9	1.00
	$\pi/8$	94.6	1.00	108.1	1.00	96.1	1.00	92.7	1.00
	$\pi/4$	93.0	1.01	101.7	1.01	107.5	1.01	109.0	1.01
	$3\pi/8$	81.0	1.01	87.8	1.01	92.8	1.01	101.3	1.01
$\beta = \pi/36$	0	347.6	1.00	429.0	1.00	363.0	1.00	334.8	1.00
	$\pi/8$	355.5	1.00	425.4	1.00	366.4	1.00	360.4	1.00
	$\pi/4$	329.4	1.00	373.3	1.00	380.1	1.00	412.3	1.00
	$3\pi/8$	282.6	1.00	300.9	1.00	324.3	1.00	359.1	1.00

Table F.11: Far-field differences as $k\rho \rightarrow 0$ for two scatterers with Impedance boundary condition, $Z = 1 + i$, for different separation distances d and different incident angles θ_0 .

	θ_0	$d = 0.1\lambda$		$d = 0.25\lambda$		$d = 0.5\lambda$		$d = \lambda$	
		C	m	C	m	C	m	C	m
Square	0	1.01	1.00	1.75	1.02	1.46	1.02	1.07	1.00
	$\pi/8$	0.97	1.00	1.60	1.02	1.26	1.03	1.33	1.03
	$\pi/4$	0.86	1.02	1.29	1.03	0.89	1.02	1.19	1.03
	$3\pi/8$	0.62	1.05	0.87	1.06	0.54	1.03	0.72	1.01
Diamond	0	1.26	1.08	2.01	1.07	1.83	1.05	1.12	1.05
	$\pi/8$	0.91	1.03	1.41	1.03	1.62	1.03	1.56	1.04
	$\pi/4$	0.84	1.02	0.94	1.00	0.96	1.02	1.12	1.00
	$3\pi/8$	0.83	1.04	0.80	1.01	0.83	1.03	0.87	1.01
Lemniscates									
$\beta = \pi/2$	0	1.27	1.01	1.40	1.01	1.19	1.01	1.05	1.01
	$\pi/8$	1.31	1.01	1.22	1.02	1.25	1.02	1.04	1.01
	$\pi/4$	1.11	1.01	1.17	1.01	1.29	1.01	1.30	1.01
	$3\pi/8$	0.82	1.01	0.89	1.01	0.94	1.01	1.04	1.01
$\beta = \pi/3$	0	4.18	1.00	4.20	1.00	3.70	1.01	4.73	1.00
	$\pi/8$	3.89	1.00	3.88	1.00	4.09	1.01	3.89	1.01
	$\pi/4$	3.75	1.00	4.08	1.00	4.47	1.01	4.51	1.01
	$3\pi/8$	3.38	1.02	3.34	1.02	3.40	1.01	3.71	1.01
$\beta = \pi/4$	0	8.86	1.00	7.94	1.00	7.35	1.01	8.21	1.00
	$\pi/8$	9.52	1.00	9.10	1.00	8.09	1.01	7.51	1.01
	$\pi/4$	8.00	1.01	8.56	1.01	10.25	1.01	10.05	1.02
	$3\pi/8$	6.66	1.01	6.86	1.02	7.40	1.01	8.40	1.01
$\beta = \pi/6$	0	24	1.00	24	1.00	17	1.00	21	1.00
	$\pi/8$	21	1.00	24	1.00	19	1.00	18	1.00
	$\pi/4$	19	1.00	22	1.00	22	1.01	22	1.01
	$3\pi/8$	15	1.01	15	1.01	18	1.02	20	1.01
$\beta = \pi/12$	0	92.40	1.00	105.34	1.00	77.26	1.00	77.85	1.00
	$\pi/8$	84.61	1.00	97.30	1.00	77.23	1.00	76.68	1.00
	$\pi/4$	74.53	1.00	88.74	1.00	81.36	1.00	84.04	1.00
	$3\pi/8$	58.32	1.00	61.72	1.00	66.31	1.01	78.53	1.01
$\beta = \pi/18$	0	201.73	1.00	216.86	1.00	174.28	1.00	180.75	1.00
	$\pi/8$	200.84	1.00	224.70	1.00	190.47	1.00	183.99	1.00
	$\pi/4$	183.52	1.01	198.79	1.01	221.93	1.01	211.80	1.00
	$3\pi/8$	132.13	1.01	145.11	1.01	159.55	1.01	188.76	1.01
$\beta = \pi/36$	0	746.58	1.00	932.17	1.00	756.27	1.00	656.26	1.00
	$\pi/8$	753.48	1.00	922.66	1.00	747.18	1.00	729.86	1.00
	$\pi/4$	629.68	1.00	748.10	1.00	787.80	1.00	847.78	1.00
	$3\pi/8$	440.57	1.00	483.11	1.00	545.47	1.00	678.15	1.00

Table F.12: Far-field differences as $k\rho \rightarrow 0$ for four scatterers with Impedance boundary condition, $Z = 1 + i$, for different separation distances d and different incident angles θ_0 .

Appendix G

TMATROM Numerical Results

This chapter contains the detailed numerical results from using the TMATROM package to verify the far-field solutions produced by our original MATLAB programs used for all the work presented in Chapters 3 and 7.

The TMATROM package reports the following quantity (see (8.4)),

$$\max_{l,m=-n,\dots,n} |(T_n + T_n^* + 2T_n T_n^*)_{l,m}|, \quad (\text{G.1})$$

as a measure of the truncation error. This error is dependent on the solver used and the order n chosen for the series truncation. This quantity is labelled T-mat Error in the results.

The quantities L^2 Diff and L^∞ Diff represent the differences in the far-fields by our original code, $u_0^\infty(\hat{\mathbf{x}})$, where $\hat{\mathbf{x}} = \hat{\mathbf{x}}(\hat{\theta}) = (\cos \hat{\theta}, \sin \hat{\theta})$, with $\hat{\theta}$ being the angle of observation of the far-field, and that produced by TMATROM, $u_{TM}^\infty(\hat{\mathbf{x}})$, for these configurations using the L^2 norm

$$\|u_0^\infty - u_{TM}^\infty\|_2 = \left(\int_0^{2\pi} |u_0^\infty(\hat{\mathbf{x}}) - u_{TM}^\infty(\hat{\mathbf{x}})|^2 d\hat{\mathbf{x}} \right)^{\frac{1}{2}}, \quad (\text{G.2})$$

and L^∞ norm

$$\|u_0^\infty - u_{TM}^\infty\|_\infty = \max_{\hat{\mathbf{x}} \in [0, 2\pi]} |u_0^\infty(\hat{\mathbf{x}}) - u_{TM}^\infty(\hat{\mathbf{x}})|, \quad (\text{G.3})$$

as measures of the difference, for all three boundary conditions.

ka	Tmat Error	L^2 Diff	L^∞ Diff	ka	Tmat Error	L^2 Diff	L^∞ Diff
Lemniscate $\beta = \pi/2$				Square, MPSPack, $\theta_0 = 0$, $N = 80$			
$\pi/2$	1.82e-15	8.16e-15	9.36e-15	$\pi/2$	3.73e-11	1.87e-10	1.20e-10
π	1.53e-15	1.00e-14	1.26e-14	π	2.97e-12	1.87e-11	1.33e-11
2π	1.58e-15	1.20e-14	1.64e-14	2π	6.68e-12	2.92e-11	2.26e-11
4π	2.92e-15	2.42e-14	3.29e-14	4π	3.58e-11	8.29e-11	8.62e-11
8π	8.49e-14	5.24e-13	4.50e-13	8π	3.04e-10	8.65e-10	7.79e-10
16π	2.38e-12	7.95e-12	7.05e-12	16π	8.91e-03	1.88e-02	3.16e-02
Lemniscate $\beta = \pi/3$				Square, MPSPack, $\theta_0 = 0$, $N = 100$			
$\pi/2$	1.47e-15	7.29e-15	9.04e-15	$\pi/2$	1.28e-09	3.60e-09	2.67e-09
π	1.44e-15	8.62e-15	9.73e-15	π	3.81e-09	6.10e-09	4.45e-09
2π	1.56e-15	1.15e-14	1.22e-14	2π	8.59e-10	4.02e-09	3.59e-09
4π	4.19e-15	1.25e-13	1.05e-13	4π	1.52e-09	4.26e-09	3.45e-09
8π	2.82e-13	5.09e-12	4.11e-12	8π	1.88e-10	7.59e-10	6.41e-10
16π	1.02e-11	1.15e-10	8.88e-11	16π	4.65e-09	1.83e-08	2.28e-08
Lemniscate $\beta = \pi/4$				Square, MPSPack, $\theta_0 = \pi/4$, $N = 80$			
$\pi/2$	1.61e-15	7.39e-15	1.24e-14	$\pi/2$	3.73e-11	1.41e-10	1.01e-10
π	1.16e-15	8.17e-15	1.23e-14	π	2.97e-12	2.72e-11	1.93e-11
2π	1.39e-15	1.07e-14	1.05e-14	2π	6.68e-12	5.12e-11	3.96e-11
4π	4.05e-15	1.29e-13	1.05e-13	4π	3.58e-11	7.23e-11	5.75e-11
8π	2.88e-13	5.20e-12	4.11e-12	8π	3.04e-10	7.56e-10	5.76e-10
16π	1.02e-11	1.15e-10	8.66e-11	16π	8.91e-03	5.35e-03	6.25e-03
Lemniscate $\beta = \pi/6$				Square, MPSPack, $\theta_0 = \pi/4$, $N = 100$			
$\pi/2$	1.44e-15	6.68e-15	1.04e-14	$\pi/2$	1.28e-09	4.17e-09	2.76e-09
π	1.23e-15	7.46e-15	1.06e-14	π	3.81e-09	1.26e-08	9.42e-09
2π	1.61e-15	1.10e-14	1.04e-14	2π	8.59e-10	5.78e-09	4.59e-09
4π	5.96e-15	1.35e-13	1.06e-13	4π	1.52e-09	7.41e-09	5.41e-09
8π	4.54e-13	5.37e-12	4.08e-12	8π	1.88e-10	9.74e-10	8.68e-10
16π	1.64e-11	1.16e-10	8.41e-11	16π	4.65e-09	1.21e-08	9.58e-09
Lemniscate $\beta = \pi/12$				Square, Our solver, $\theta_0 = 0$			
$\pi/2$	1.66e-15	5.74e-15	7.54e-15	$\pi/2$	1.77e-11	2.40e-11	1.36e-11
π	1.18e-15	7.15e-15	1.01e-14	π	1.72e-11	1.33e-11	8.27e-12
2π	1.73e-15	1.16e-14	1.21e-14	2π	1.69e-11	1.73e-11	1.06e-11
4π	8.50e-15	1.53e-13	1.06e-13	4π	1.40e-11	2.08e-11	1.29e-11
8π	6.47e-13	5.79e-12	4.19e-12	8π	1.91e-11	2.94e-11	2.66e-11
16π	2.32e-11	1.23e-10	9.10e-11	16π	1.05e-10	4.63e-10	4.01e-10
Lemniscate $\beta = \pi/18$				Square, Our solver, $\theta_0 = \pi/4$			
$\pi/2$	2.60e-14	6.13e-15	8.28e-15	$\pi/2$	1.77e-11	2.52e-11	1.62e-11
π	5.00e-14	7.09e-15	1.04e-14	π	1.72e-11	2.71e-11	1.79e-11
2π	9.96e-14	1.18e-14	1.11e-14	2π	1.69e-11	3.53e-11	2.44e-11
4π	1.80e-13	1.59e-13	1.03e-13	4π	1.40e-11	3.72e-11	2.49e-11
8π	6.49e-13	6.12e-12	4.27e-12	8π	1.91e-11	5.22e-11	4.45e-11
16π	2.33e-11	1.27e-10	8.97e-11	16π	1.05e-10	4.95e-10	5.33e-10

Table G.1: Comparison of far-field produced using TMATROM with our Nyström corner solver or MPSPack and the far-field produced by our original MATLAB programs. Incident wave direction for lemniscates, $\theta_0 = 0$, Dirichlet boundary condition.

ka	Tmat Error	L^2 Diff	L^∞ Diff	ka	Tmat Error	L^2 Diff	L^∞ Diff
Lemniscate $\beta = \pi/2$				Square, MPSPack, $\theta_0 = 0$, $N = 80$			
$\pi/2$	4.39e-10	6.70e-15	8.03e-15	$\pi/2$	1.18e-10	5.14e-10	4.29e-10
π	7.98e-10	7.31e-15	1.01e-14	π	1.32e-11	1.29e-10	1.16e-10
2π	1.55e-09	1.21e-14	1.15e-14	2π	5.26e-11	1.75e-10	1.61e-10
4π	2.69e-09	1.62e-13	1.02e-13	4π	1.30e-10	2.30e-10	2.28e-10
8π	4.72e-09	6.39e-12	4.59e-12	8π	1.03e-09	1.83e-09	1.69e-09
16π	7.98e-09	1.33e-10	9.55e-11	16π	8.61e-03	1.85e-02	3.20e-02
Lemniscate $\beta = \pi/3$				Square, MPSPack, $\theta_0 = 0$, $N = 100$			
$\pi/2$	9.48e-11	3.83e-15	4.46e-15	$\pi/2$	1.72e-09	7.20e-09	4.82e-09
π	1.12e-10	6.51e-15	8.87e-15	π	1.70e-08	7.16e-08	4.46e-08
2π	1.47e-10	2.89e-14	2.69e-14	2π	4.72e-09	2.05e-08	1.51e-08
4π	1.20e-10	2.94e-14	2.39e-14	4π	1.01e-08	1.79e-08	1.45e-08
8π	1.19e-10	1.47e-12	1.18e-12	8π	2.88e-09	8.67e-09	6.71e-09
16π	1.14e-10	4.06e-11	3.11e-11	16π	9.03e-09	1.81e-08	1.46e-08
Lemniscate $\beta = \pi/4$				Square, MPSPack, $\theta_0 = \pi/4$, $N = 80$			
$\pi/2$	2.64e-10	3.98e-15	3.52e-15	$\pi/2$	1.18e-10	4.14e-10	2.49e-10
π	2.88e-10	5.19e-15	6.62e-15	π	1.32e-11	1.76e-10	1.44e-10
2π	3.98e-10	1.77e-14	2.23e-14	2π	5.26e-11	2.27e-10	1.67e-10
4π	2.96e-10	2.29e-14	1.81e-14	4π	1.30e-10	2.90e-10	2.30e-10
8π	3.05e-10	1.11e-12	8.21e-13	8π	1.03e-09	2.38e-09	1.93e-09
16π	2.69e-10	3.05e-11	2.11e-11	16π	8.61e-03	4.70e-03	4.92e-03
Lemniscate $\beta = \pi/6$				Square, MPSPack, $\theta_0 = \pi/4$, $N = 100$			
$\pi/2$	7.13e-10	5.35e-15	6.40e-15	$\pi/2$	1.72e-09	4.33e-09	2.86e-09
π	7.87e-10	5.72e-15	7.12e-15	π	1.70e-08	7.22e-08	5.19e-08
2π	9.13e-10	6.73e-15	6.28e-15	2π	4.72e-09	3.86e-08	2.64e-08
4π	7.92e-10	4.48e-14	4.07e-14	4π	1.01e-08	1.52e-08	1.24e-08
8π	6.41e-10	1.93e-12	1.55e-12	8π	2.88e-09	6.06e-09	4.56e-09
16π	6.03e-10	3.78e-11	3.19e-11	16π	9.03e-09	1.99e-08	1.49e-08
Lemniscate $\beta = \pi/12$				Square, Our solver, $\theta_0 = 0$			
$\pi/2$	7.12e-08	1.13e-14	1.17e-14	$\pi/2$	3.81e-11	7.59e-15	8.56e-15
π	7.74e-08	9.96e-15	1.18e-14	π	5.03e-11	1.04e-14	1.31e-14
2π	6.12e-08	8.06e-15	8.45e-15	2π	6.59e-11	2.66e-14	2.38e-14
4π	5.50e-08	6.61e-14	5.07e-14	4π	8.21e-11	2.55e-12	2.25e-12
8π	4.92e-08	2.52e-12	1.85e-12	8π	8.78e-11	2.46e-11	2.18e-11
16π	4.09e-08	5.84e-11	3.99e-11	16π	1.09e-10	4.48e-10	3.85e-10
Lemniscate $\beta = \pi/18$				Square, Our solver, $\theta_0 = \pi/4$			
$\pi/2$	1.23e-07	1.64e-14	1.68e-14	$\pi/2$	3.81e-11	6.03e-15	6.54e-15
π	1.34e-07	1.21e-14	1.22e-14	π	5.03e-11	8.64e-15	1.11e-14
2π	9.42e-08	1.11e-14	1.25e-14	2π	6.59e-11	1.73e-14	1.71e-14
4π	8.37e-08	4.98e-14	4.12e-14	4π	8.21e-11	3.13e-12	3.11e-12
8π	7.52e-08	2.23e-12	1.69e-12	8π	8.78e-11	1.85e-11	1.83e-11
16π	6.46e-08	5.61e-11	4.24e-11	16π	1.09e-10	4.05e-10	4.89e-10

Table G.2: Comparison of far-field produced using TMatROM with our Nyström corner solver or MPSPack and the far-field produced by our original MATLAB programs. Incident wave direction for lemniscates, $\theta_0 = 0$, Neumann boundary condition.

ka	Tmat Error	L^2 Diff	L^∞ Diff	ka	Tmat Error	L^2 Diff	L^∞ Diff
Lemniscate $\beta = \pi/2$				Lemniscate $\beta = \pi/12$			
$\pi/2$	3.53e-01	5.54e-15	7.65e-15	$\pi/2$	3.33e-01	5.45e-15	6.83e-15
π	3.73e-01	7.39e-15	1.20e-14	π	3.36e-01	6.47e-15	7.59e-15
2π	3.82e-01	8.98e-15	1.34e-14	2π	3.39e-01	6.41e-15	6.66e-15
4π	3.88e-01	1.65e-14	2.18e-14	4π	3.39e-01	5.54e-14	4.32e-14
8π	3.91e-01	3.29e-13	2.65e-13	8π	3.37e-01	2.53e-12	1.98e-12
16π	3.92e-01	5.20e-12	4.52e-12	16π	3.35e-01	5.73e-11	4.84e-11
Lemniscate $\beta = \pi/3$				Lemniscate $\beta = \pi/18$			
$\pi/2$	3.43e-01	5.08e-15	5.89e-15	$\pi/2$	3.32e-01	8.08e-15	7.79e-15
π	3.63e-01	6.79e-15	1.02e-14	π	3.33e-01	6.33e-15	6.17e-15
2π	3.73e-01	1.78e-14	2.02e-14	2π	3.35e-01	6.20e-15	6.23e-15
4π	3.80e-01	4.26e-14	3.47e-14	4π	3.33e-01	5.73e-14	3.96e-14
8π	3.83e-01	2.00e-12	1.45e-12	8π	3.31e-01	2.73e-12	2.15e-12
16π	3.85e-01	5.00e-11	3.54e-11	16π	3.28e-01	6.12e-11	4.89e-11
Lemniscate $\beta = \pi/4$				Square, $\theta_0 = 0$			
$\pi/2$	3.38e-01	4.29e-15	4.86e-15	$\pi/2$	3.64e-01	5.63e-15	7.54e-15
π	3.55e-01	5.87e-15	7.76e-15	π	3.79e-01	1.07e-14	2.00e-14
2π	3.64e-01	1.10e-14	1.11e-14	2π	3.84e-01	1.96e-14	2.46e-14
4π	3.70e-01	4.52e-14	3.32e-14	4π	3.86e-01	7.53e-13	5.57e-13
8π	3.73e-01	2.08e-12	1.53e-12	8π	3.88e-01	9.20e-12	8.95e-12
16π	3.74e-01	5.08e-11	3.67e-11	16π	3.88e-01	2.02e-10	1.77e-10
Lemniscate $\beta = \pi/6$				Square, $\theta_0 = \pi/4$			
$\pi/2$	3.35e-01	4.54e-15	5.96e-15	$\pi/2$	3.64e-01	4.88e-15	5.04e-15
π	3.45e-01	5.50e-15	7.63e-15	π	3.79e-01	7.44e-15	8.11e-15
2π	3.52e-01	6.58e-15	6.79e-15	2π	3.84e-01	1.91e-14	2.30e-14
4π	3.55e-01	5.00e-14	3.68e-14	4π	3.86e-01	9.01e-13	7.30e-13
8π	3.57e-01	2.19e-12	1.76e-12	8π	3.88e-01	2.15e-11	2.39e-11
16π	3.58e-01	5.30e-11	4.37e-11	16π	3.88e-01	2.58e-10	2.92e-10

Table G.3: Comparison of far-field produced using TMATROM with our Nyström corner solver or MPSPack and the far-field produced by our original MATLAB programs. Incident wave direction for lemniscates, $\theta_0 = 0$, impedance boundary condition with $Z = 1 + i$.

		$d = 0.1\lambda$		$d = 0.25\lambda$		$d = 0.5\lambda$		$d = \lambda$	
$2a$	Tmat Error	L^2 Diff	L^∞ Diff	L^2 Diff	L^∞ Diff	L^2 Diff	L^∞ Diff	L^2 Diff	L^∞ Diff
Lemniscate $\beta = \pi/2$									
0.5λ	1.82e-15	2.76e-05	1.99e-05	1.60e-06	1.28e-06	6.06e-09	4.27e-09	1.37e-08	1.27e-08
λ	1.53e-15	4.90e-05	4.25e-05	1.09e-06	7.84e-07	4.48e-08	4.16e-08	2.16e-09	1.68e-09
2λ	1.58e-15	2.26e-05	2.07e-05	4.79e-07	5.71e-07	2.60e-08	2.46e-08	1.83e-09	1.40e-09
Square									
0.5λ	1.77e-11	7.62e-01	5.44e-01	5.68e-04	6.88e-04	6.30e-08	5.00e-08	5.69e-11	4.38e-11
λ	1.72e-11	6.77e-02	5.55e-02	2.87e-02	2.39e-02	5.79e-05	3.54e-05	1.47e-10	1.24e-10
2λ	1.69e-11	7.85e-01	6.89e-01	2.52e-01	2.32e-01	1.87e-01	1.56e-01	5.88e-06	5.13e-06
Square MPSPack									
0.5λ	3.73e-11	3.56e+00	2.20e+00	5.97e-04	4.54e-04	4.14e-08	3.75e-08	2.76e-10	2.64e-10
λ	2.97e-12	6.49e-02	5.28e-02	2.78e-02	2.35e-02	5.86e-05	3.58e-05	1.43e-10	1.21e-10
2λ	6.68e-12	3.65e-01	2.99e-01	2.52e-01	2.26e-01	1.95e-01	1.62e-01	5.88e-06	5.12e-06
Diamond									
0.5λ	1.77e-11	1.83e-04	1.39e-04	2.67e-06	1.84e-06	8.11e-09	6.42e-09	5.19e-11	3.66e-11
λ	1.72e-11	6.29e-05	6.40e-05	1.01e-05	8.61e-06	1.25e-07	1.00e-07	9.55e-09	6.81e-09
2λ	1.69e-11	2.62e-04	2.73e-04	1.37e-04	1.30e-04	5.59e-06	5.14e-06	7.47e-10	5.51e-10
Diamond MPSPack									
0.5λ	3.73e-11	1.62e-04	1.00e-04	2.89e-06	2.07e-06	8.35e-09	8.78e-09	3.09e-10	3.27e-10
λ	2.97e-12	6.19e-05	6.29e-05	9.99e-06	8.50e-06	1.25e-07	1.00e-07	9.54e-09	6.80e-09
2λ	6.68e-12	2.61e-04	2.73e-04	1.37e-04	1.30e-04	5.59e-06	5.14e-06	7.64e-10	5.69e-10

Table G.4: Two scatterers. Comparison of far-field produced using TMatROM with our Nyström corner solver or MPSPack and the far-field produced by our original MATLAB programs. Incident wave direction for lemniscates, $\theta_0 = 0$, Dirichlet boundary condition.

		$d = 0.1\lambda$		$d = 0.25\lambda$		$d = 0.5\lambda$		$d = \lambda$	
$2a$	Tmat Error	L^2 Diff	L^∞ Diff	L^2 Diff	L^∞ Diff	L^2 Diff	L^∞ Diff	L^2 Diff	L^∞ Diff
Lemniscate $\beta = \pi/2$									
0.5λ	7.63e-12	1.41e-04	9.21e-05	1.33e-06	7.06e-07	2.74e-09	1.85e-09	1.40e-08	9.29e-09
λ	9.80e-12	6.71e-05	4.85e-05	2.49e-06	2.21e-06	2.58e-08	1.89e-08	1.32e-08	1.01e-08
2λ	1.19e-11	1.17e-03	9.15e-04	1.54e-06	1.23e-06	2.81e-08	4.08e-08	1.89e-08	1.47e-08
Square									
0.5λ	3.81e-11	2.26e+00	1.42e+00	9.16e-04	5.62e-04	6.87e-08	5.10e-08	6.06e-11	5.85e-11
λ	5.03e-11	2.95e-01	1.56e-01	1.88e-01	9.09e-02	2.17e-05	1.28e-05	2.53e-10	1.54e-10
2λ	6.59e-11	5.85e-01	4.46e-01	2.94e-01	1.56e-01	3.22e-01	2.04e-01	4.51e-06	3.66e-06
Diamond									
0.5λ	3.81e-11	3.04e-04	2.04e-04	2.71e-06	1.70e-06	7.35e-09	5.30e-09	9.24e-11	5.72e-11
λ	5.03e-11	1.21e-03	8.75e-04	1.43e-05	1.12e-05	7.03e-08	6.23e-08	1.53e-10	1.46e-10
2λ	6.59e-11	3.77e-03	2.34e-03	1.01e-04	6.86e-05	1.69e-06	1.34e-06	3.63e-09	3.57e-09

Table G.5: Two scatterers. Comparison of far-field produced using TMAPROM with our Nyström corner solver or MPSPack and the far-field produced by our original MATLAB programs. Incident wave direction for lemniscates, $\theta_0 = 0$, Neumann boundary condition.

		$d = 0.1\lambda$		$d = 0.25\lambda$		$d = 0.5\lambda$		$d = \lambda$	
$2a$	Tmat Error	L^2 Diff	L^∞ Diff	L^2 Diff	L^∞ Diff	L^2 Diff	L^∞ Diff	L^2 Diff	L^∞ Diff
Lemniscate $\beta = \pi/2$									
0.5λ	3.53e-01	7.14e-05	4.67e-05	5.35e-07	3.66e-07	1.18e-09	1.06e-09	8.19e-10	6.17e-10
λ	3.73e-01	2.22e-05	1.95e-05	9.06e-07	7.20e-07	7.85e-09	6.75e-09	1.46e-11	1.32e-11
2λ	3.82e-01	5.92e-06	5.17e-06	7.51e-08	6.16e-08	4.13e-09	3.90e-09	2.22e-08	1.72e-08
Square									
0.5λ	3.64e-01	2.57e-01	1.67e-01	1.52e-04	1.01e-04	1.19e-08	8.89e-09	1.66e-08	1.40e-08
λ	3.79e-01	2.56e-02	1.82e-02	9.60e-03	6.54e-03	3.09e-06	2.68e-06	6.34e-09	4.90e-09
2λ	3.84e-01	9.29e-02	9.53e-02	6.90e-02	6.20e-02	2.72e-02	2.04e-02	9.59e-07	7.72e-07
Diamond									
0.5λ	3.64e-01	1.43e-04	9.10e-05	1.17e-06	8.12e-07	1.51e-09	1.06e-09	5.17e-09	5.44e-09
λ	3.79e-01	9.74e-05	7.18e-05	2.04e-06	1.65e-06	1.03e-08	9.00e-09	3.81e-10	3.03e-10
2λ	3.84e-01	3.98e-04	3.47e-04	2.90e-05	2.73e-05	3.31e-07	3.30e-07	8.02e-09	6.67e-09

Table G.6: Two scatterers. Comparison of far-field produced using TMatROM with our Nyström corner solver or MPSPack and the far-field produced by our original MATLAB programs. Incident wave direction for lemniscates, $\theta_0 = 0$, Impedance boundary condition with $Z = 1 + i$.

		$d = 0.1\lambda$		$d = 0.25\lambda$		$d = 0.5\lambda$		$d = \lambda$	
$2a$	Tmat Err	L^2 Diff	L^∞ Diff	L^2 Diff	L^∞ Diff	L^2 Diff	L^∞ Diff	L^2 Diff	L^∞ Diff
Lemniscate $\beta = \pi/2$									
0.5λ	1.82e-15	3.10e-05	2.18e-05	3.15e-06	4.40e-06	2.12e-08	1.79e-08	2.56e-09	1.65e-09
λ	1.53e-15	7.29e-05	6.64e-05	2.39e-06	3.14e-06	9.38e-08	1.41e-07	9.34e-10	8.90e-10
2λ	1.58e-15	2.76e-05	4.00e-05	6.75e-07	1.01e-06	6.63e-08	6.44e-08	6.51e-09	6.22e-09
Square									
0.5λ	1.77e-11	1.50e+00	1.48e+00	1.68e-03	1.91e-03	1.57e-07	1.77e-07	6.32e-10	5.85e-10
λ	1.72e-11	1.40e-01	1.85e-01	4.15e-02	4.27e-02	9.09e-05	9.49e-05	2.09e-08	1.88e-08
2λ	1.69e-11	8.63e-01	8.34e-01	4.64e-01	6.84e-01	2.66e-01	3.02e-01	9.15e-06	1.21e-05
Square MPSPack									
0.5λ	3.73e-11	1.53e+00	1.24e+00	8.19e-04	7.66e-04	8.33e-08	8.04e-08	6.47e-10	5.80e-10
λ	2.97e-12	1.49e-01	1.91e-01	4.21e-02	4.35e-02	9.29e-05	9.73e-05	2.09e-08	1.88e-08
2λ	6.68e-12	3.60e+00	3.21e+00	4.65e-01	6.77e-01	2.69e-01	3.13e-01	9.15e-06	1.21e-05
Diamond									
0.5λ	1.77e-11	2.67e-04	3.03e-04	5.27e-06	6.60e-06	4.90e-08	3.97e-08	3.42e-08	3.13e-08
λ	1.72e-11	1.03e-04	1.64e-04	1.47e-05	2.21e-05	1.73e-07	2.45e-07	1.69e-09	1.65e-09
2λ	1.69e-11	4.63e-04	7.80e-04	2.55e-04	4.09e-04	1.07e-05	1.69e-05	4.74e-08	4.82e-08
Diamond MPSPack									
0.5λ	3.73e-11	2.26e-04	2.39e-04	4.11e-06	4.63e-06	4.54e-08	3.35e-08	3.43e-08	3.15e-08
λ	2.97e-12	1.02e-04	1.63e-04	1.46e-05	2.20e-05	1.76e-07	2.50e-07	1.68e-09	1.66e-09
2λ	6.68e-12	4.62e-04	7.78e-04	2.55e-04	4.09e-04	1.07e-05	1.69e-05	4.74e-08	4.81e-08

Table G.7: Four scatterers. Comparison of far-field produced using TMATROM with our Nyström corner solver or MPSPack and the far-field produced by our original MATLAB programs. Incident wave direction for lemniscates, $\theta_0 = 0$, Dirichlet boundary condition.

		$d = 0.1\lambda$		$d = 0.25\lambda$		$d = 0.5\lambda$		$d = \lambda$	
$2a$	Tmat Err	L^2 Diff	L^∞ Diff	L^2 Diff	L^∞ Diff	L^2 Diff	L^∞ Diff	L^2 Diff	L^∞ Diff
Lemniscate $\beta = \pi/2$									
0.5λ	7.63e-12	2.63e-04	3.17e-04	2.44e-06	2.68e-06	4.43e-09	5.04e-09	1.31e-09	1.35e-09
λ	9.80e-12	9.83e-05	9.12e-05	4.15e-06	5.16e-06	4.05e-08	5.46e-08	1.70e-09	1.28e-09
2λ	1.19e-11	3.22e-03	3.34e-03	2.39e-06	3.21e-06	6.44e-08	1.25e-07	9.20e-09	1.25e-08
Square									
0.5λ	3.81e-11	4.29e+00	3.26e+00	9.83e-04	8.14e-04	1.54e-07	1.35e-07	1.61e-09	1.74e-09
λ	5.03e-11	4.92e-01	3.27e-01	4.14e-01	3.25e-01	3.99e-05	3.98e-05	5.23e-09	3.94e-09
2λ	6.59e-11	5.85e+00	4.53e+00	4.67e-01	3.54e-01	4.91e-01	4.99e-01	8.61e-06	1.08e-05
Diamond									
0.5λ	3.81e-11	6.59e-04	6.46e-04	6.57e-06	5.80e-06	1.28e-08	1.48e-08	3.17e-09	3.64e-09
λ	5.03e-11	2.37e-03	3.01e-03	2.89e-05	3.93e-05	1.33e-07	1.75e-07	3.87e-08	3.24e-08
2λ	6.59e-11	6.00e-03	6.64e-03	1.88e-04	2.22e-04	2.66e-06	3.49e-06	7.37e-09	1.27e-08

Table G.8: Four scatterers. Comparison of far-field produced using TMatTROM with our Nyström corner solver or MPSPack and the far-field produced by our original MATLAB programs. Incident wave direction for lemniscates, $\theta_0 = 0$, Neumann boundary condition.

		$d = 0.1\lambda$		$d = 0.25\lambda$		$d = 0.5\lambda$		$d = \lambda$	
$2a$	Tmat Err	L^2 Diff	L^∞ Diff	L^2 Diff	L^∞ Diff	L^2 Diff	L^∞ Diff	L^2 Diff	L^∞ Diff
Lemniscate $\beta = \pi/2$									
0.5λ	7.63e-12	2.63e-04	3.17e-04	2.44e-06	2.68e-06	4.43e-09	5.04e-09	1.31e-09	1.35e-09
λ	9.80e-12	9.83e-05	9.12e-05	4.15e-06	5.16e-06	4.05e-08	5.46e-08	1.70e-09	1.28e-09
2λ	1.19e-11	3.22e-03	3.34e-03	2.39e-06	3.21e-06	6.44e-08	1.25e-07	9.20e-09	1.25e-08
Square									
0.5λ	3.81e-11	4.29e+00	3.26e+00	9.83e-04	8.14e-04	1.54e-07	1.35e-07	1.61e-09	1.74e-09
λ	5.03e-11	4.92e-01	3.27e-01	4.14e-01	3.25e-01	3.99e-05	3.98e-05	5.23e-09	3.94e-09
2λ	6.59e-11	5.85e+00	4.53e+00	4.67e-01	3.54e-01	4.91e-01	4.99e-01	8.61e-06	1.08e-05
Diamond									
0.5λ	3.81e-11	6.59e-04	6.46e-04	6.57e-06	5.80e-06	1.28e-08	1.48e-08	3.17e-09	3.64e-09
λ	5.03e-11	2.37e-03	3.01e-03	2.89e-05	3.93e-05	1.33e-07	1.75e-07	3.87e-08	3.24e-08
2λ	6.59e-11	6.00e-03	6.64e-03	1.88e-04	2.22e-04	2.66e-06	3.49e-06	7.37e-09	1.27e-08

Table G.9: Four scatterers. Comparison of far-field produced using TMatROM with our Nyström corner solver or MPSPack and the far-field produced by our original MATLAB programs. Incident wave direction for lemniscates, $\theta_0 = 0$, Impedance boundary condition with $Z = 1 + i$.

Appendix H

Large Arrays Supporting Material

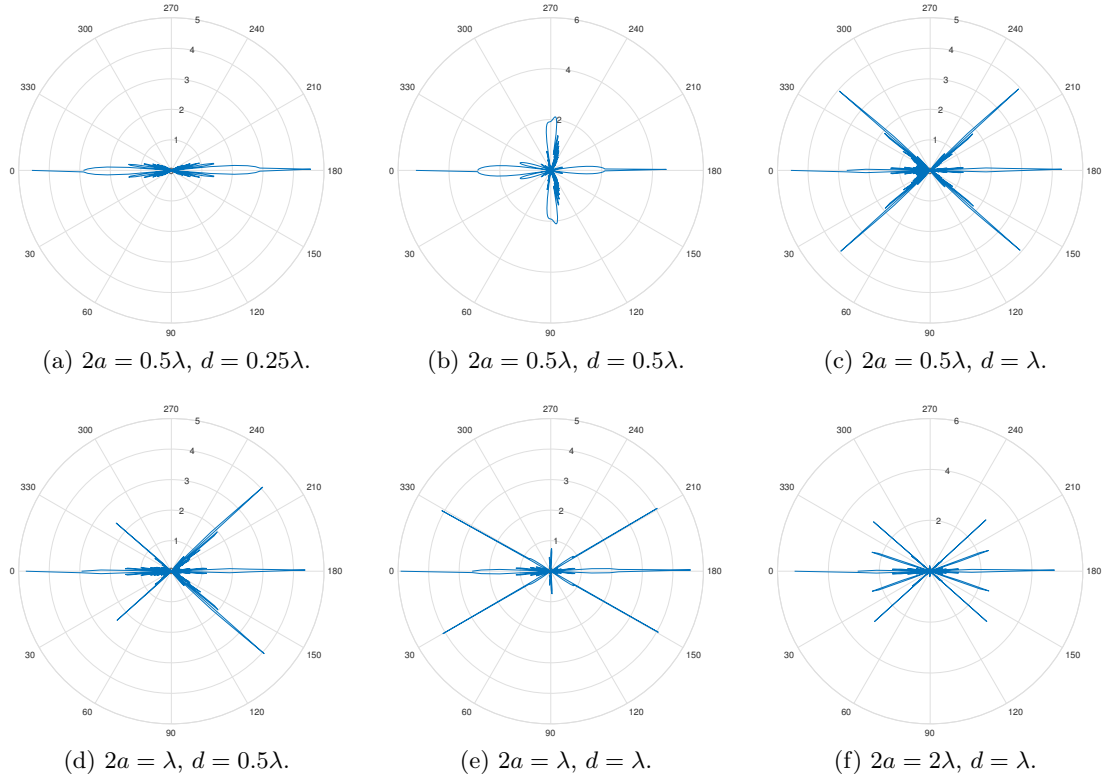


Figure H.1: Logarithmic plot of the far-field $|u^\infty|$, for a single array of squares with differing diameters $2a$, and separation d , all with Dirichlet boundary condition. Number of scatterers $N = 64$ in the array; incident wave direction $\theta_0 = 0$.

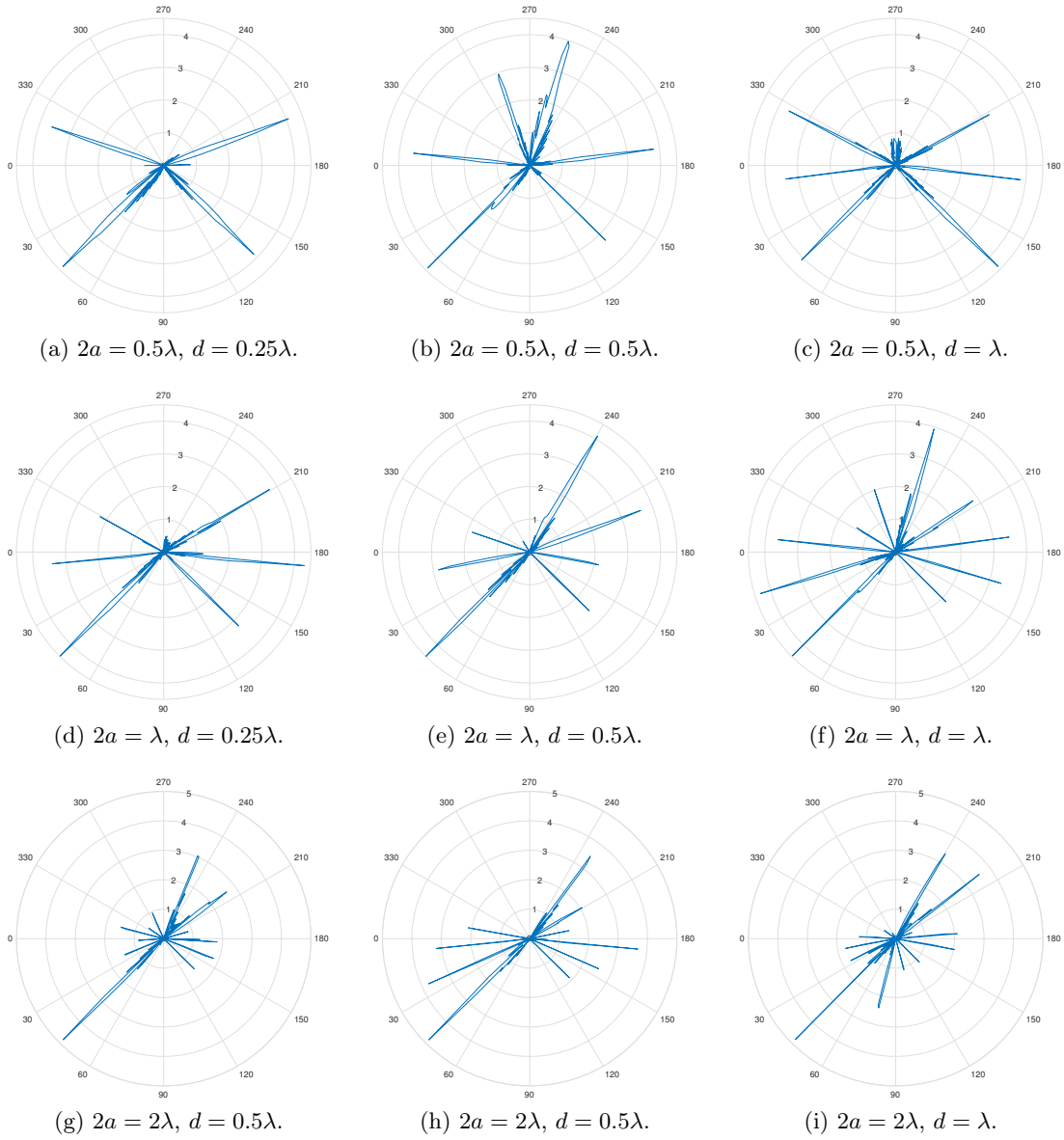


Figure H.2: Logarithmic plot of the far-field $|u^\infty|$, for a single array of diamonds with differing diameters $2a$, and separation d , all with Neumann boundary condition. Number of scatterers $N = 64$ in the array; incident wave direction $\theta_0 = \pi/4$.

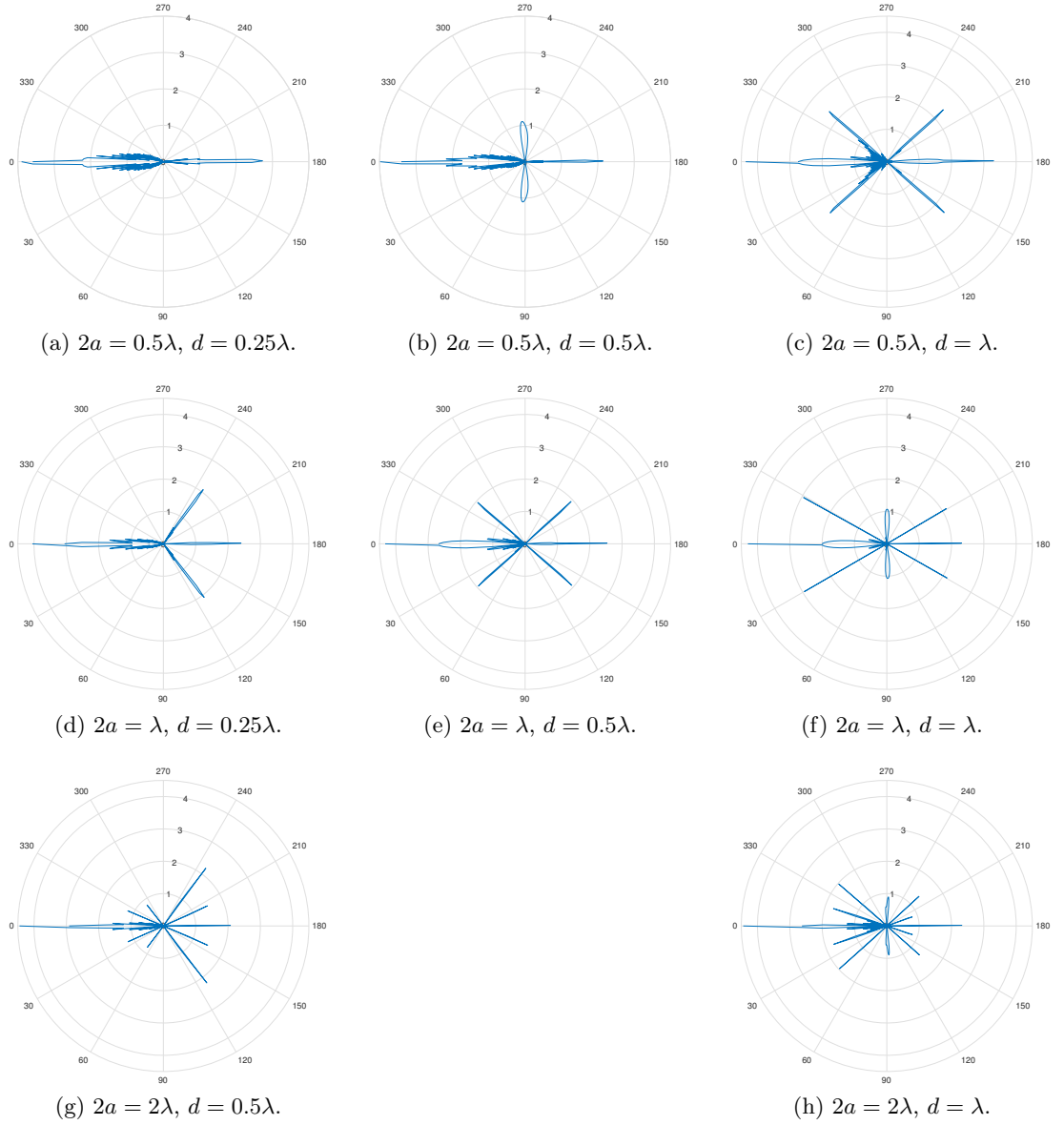


Figure H.3: Logarithmic plot of the far-field $|u^\infty|$, for a double array of lemniscates with differing diameters $2a$, and separation d , all with Neumann boundary condition. Number of scatterers $N = 64$ in the array; incident wave direction $\theta_0 = 0$.

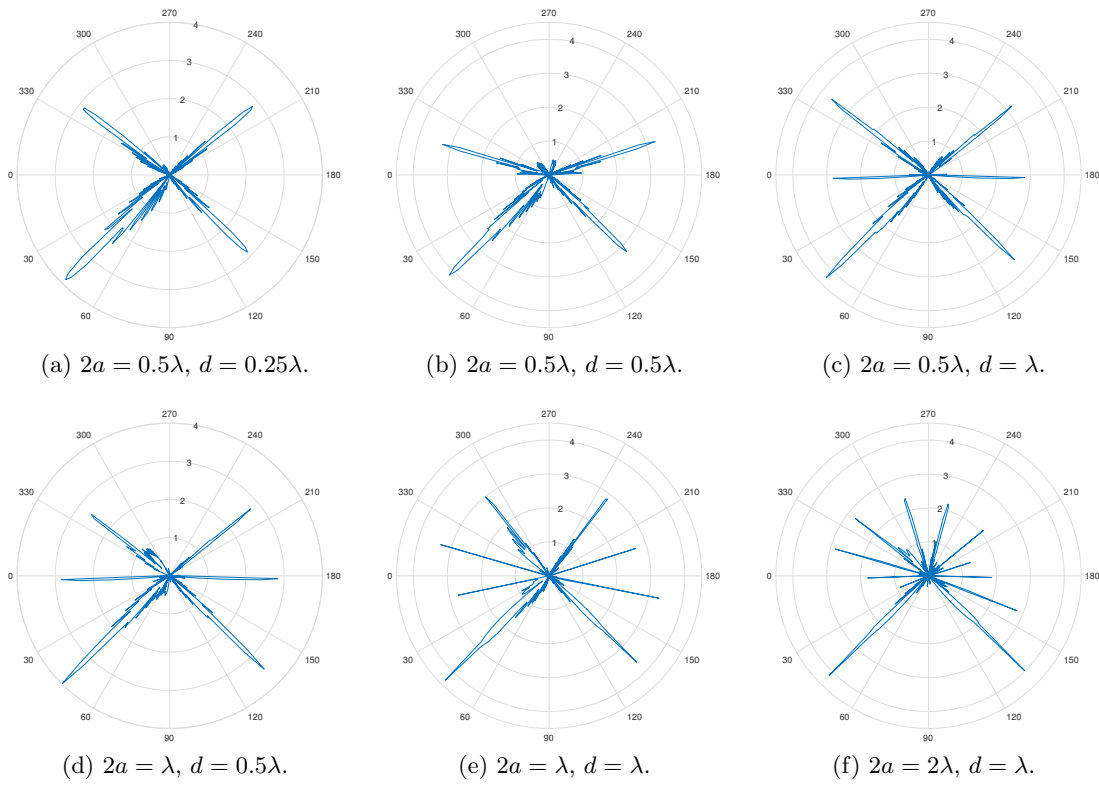


Figure H.4: Logarithmic plot of the far-field $|u^\infty|$, for a double array of squares with differing diameters $2a$, and separation d , all with Neumann boundary condition. Number of scatterers $N = 64$ in the array; incident wave direction $\theta_0 = \pi/4$.

Bibliography

- [1] J. Bowman, T. Senior, and P. Uslenghi, *Electromagnetic and acoustic scattering by simple shapes (Revised edition)*, vol. 1. Hemisphere Publishing Corp., New York, 1987.
- [2] A. Sommerfeld, “Mathematische theorie der diffraction,” *Mathematische Annalen*, vol. 47, no. 2-3, pp. 317–374, 1896.
- [3] A. Sommerfeld, “Mathematical theory of diffraction,” in *Mathematical Theory of Diffraction. Progress in Mathematical Physics*, vol. 35, pp. 9–68, Springer, 2004.
- [4] H. M. Macdonald, *Electric waves*. Cambridge University Press, 2013.
- [5] A. Wiegrefe, “Über einige mehrwertige Lösungen der Wellengleichung $\Delta u + k^2 u = 0$ und ihre Anwendung in der Beugungstheorie,” *Annalen der Physik*, vol. 344, no. 12, pp. 449–484, 1912.
- [6] H. S. Carslaw, “Diffraction of waves by a wedge of any angle,” *Proceedings of the London Mathematical Society*, vol. 2, no. 1, pp. 291–306, 1920.
- [7] D. L. Colton and R. Kress, *Inverse acoustic and electromagnetic scattering theory*. Applied mathematical sciences, New York: Springer, 3rd ed., 2013.
- [8] T. Johansson and B. D. Sleeman, “Reconstruction of an acoustically sound-soft obstacle from one incident field and the far-field pattern,” *IMA Journal of Applied Mathematics*, vol. 72, no. 1, pp. 96–112, 2007.
- [9] J. C. Engineer, J. R. King, and R. H. Tew, “Diffraction by slender bodies,” *European Journal of Applied Mathematics*, vol. 9, no. 2, pp. 129–158, 1998.

- [10] C. L. Epstein and M. O'Neil, "Smoothed corners and scattered waves," *SIAM Journal on Scientific Computing*, vol. 38, no. 5, pp. A2665–A2698, 2016.
- [11] P. D. Smith, A. Markowskei, and A. D. Rawlins, "Two-dimensional diffraction by impedance loaded structures with corners," in *Electromagnetics in Advanced Applications (ICEAA), 2014 International Conference on*, pp. 644–647, 2014.
- [12] P. D. Smith and A. J. Markowskei, "The diffractive effect of rounding the corners of scattering structures," in *Electromagnetics in Advanced Applications (ICEAA), 2015 International Conference on*, pp. 1592–1595, 2015.
- [13] P. D. Smith and A. J. Markowskei, "What effect does rounding the corners have on diffraction from structures with corners?," in *Advanced Electromagnetic Waves* (S. Bashir, ed.), ch. 1, pp. 1–28, Croatia: InTech, 2015.
- [14] P. D. Smith and A. J. Markowskei, "The effect of rounding vertices on the diffraction from polygons and other scatterers," in *2016 URSI International Symposium on Electromagnetic Theory (EMTS)*, pp. 236–239, 2016.
- [15] J. Helsing and A. Karlsson, "An accurate boundary value problem solver applied to scattering from cylinders with corners," *Antennas and Propagation, IEEE Transactions on*, vol. 61, no. 7, pp. 3693–3700, 2013.
- [16] S. N. Chandler-Wilde, S. Langdon, and M. Mokgolele, "A high frequency boundary element method for scattering by convex polygons with impedance boundary conditions," *Communications in Computational Physics*, vol. 11, pp. 573–593, 2012.
- [17] D. P. Hewett, S. Langdon, and J. M. Melenk, "A high frequency hp boundary element method for scattering by convex polygons," *SIAM Journal on Numerical Analysis*, vol. 51, no. 1, pp. 629–653, 2013.
- [18] S. Arden, S. N. Chandler-Wilde, and S. Langdon, "A collocation method for high-frequency scattering by convex polygons," *Journal of Computational and Applied Mathematics*, vol. 204, no. 2, pp. 334–343, 2007.

- [19] S. Chandler-Wilde and S. Langdon, “A Galerkin boundary element method for high frequency scattering by convex polygons,” *SIAM Journal on Numerical Analysis*, vol. 45, no. 2, pp. 610–640, 2007.
- [20] A. H. Barnett and T. Betcke, “An exponentially convergent non-polynomial finite element method for time-harmonic scattering from polygons,” *SIAM Journal on Scientific Computing*, vol. 32, no. 3, pp. 1417–1441, 2010.
- [21] A. J. Markowskei and P. D. Smith, “Scattering from structures with acute, obtuse and reflex corners,” in *Electromagnetics in Advanced Applications (ICEAA), 2016 International Conference on*, pp. 882–885, 2016.
- [22] A. J. Markowskei and P. D. Smith, “Changes in the far-field pattern induced by rounding the corners of a scatterer: dependence upon curvature,” in *2017 International Conference on Electromagnetics in Advanced Applications (ICEAA)*, pp. 1272–1275, 2017.
- [23] A. J. Markowskei and P. D. Smith, “Measuring the effect of rounding the corners of scattering structures,” *Radio Science*, vol. 52, no. 5, pp. 693–708, 2017.
- [24] P. D. Smith and A. J. Markowskei, “The effect of rounding the corners of scattering structures: E-polarisation case,” in *2017 XXXIInd General Assembly and Scientific Symposium of the International Union of Radio Science (URSI GASS)*, pp. 1–4, 2017.
- [25] P. Smith and A. Markowskei, “Surface distribution and field dependency upon the radius of curvature at smoothed corners of a scatterer,” in *2018 International Conference on Electromagnetics in Advanced Applications (ICEAA)*, pp. 311–314, 2018.
- [26] R. Kress, “Boundary integral equations in time-harmonic acoustic scattering,” *Mathematical and Computer Modelling*, vol. 15, no. 3–5, pp. 229–243, 1991.
- [27] M. Ganesh and S. C. Hawkins, “Algorithm 975: TMATROM - A T-Matrix Reduced Order Model Software,” *ACM Transactions on Mathematical Software*, vol. 44, no. 1, pp. 1–18, 2017.

-
- [28] G. A. Chandler, "Galerkin's method for boundary integral equations on polygonal domains," *ANZIAM Journal*, vol. 26, no. 1, pp. 1–13, 1984.
- [29] M. Costabel and E. Stephan, "A direct boundary integral equation method for transmission problems," *Journal of Mathematical Analysis and Applications*, vol. 106, no. 2, pp. 367–413, 1985.
- [30] Y. Yan and I. H. Sloan, "On integral equations of the first kind with logarithmic kernels," *The Journal of Integral Equations and Applications*, pp. 549–579, 1988.
- [31] Y. Yan, "The collocation method for first-kind boundary integral equations on polygonal regions," *Mathematics of Computation*, vol. 54, no. 189, pp. 139–154, 1990.
- [32] Y. Jeon, "A Nyström method for boundary integral equations in domains with a piecewise smooth boundary," *Journal of Integral Equations and Applications*, vol. 5, pp. 221–242, 1993.
- [33] J. Elschner and I. G. Graham, "Numerical methods for integral equations of Mellin type," *Journal of Computational and Applied Mathematics*, vol. 125, no. 1–2, pp. 423–437, 2000.
- [34] K. E. Atkinson, "The numerical solution of boundary integral equations," in *Institute Of Mathematics And Its Applications Conference Series*, vol. 63, pp. 223–260, Oxford University Press, 1997.
- [35] W. L. Wendland, "Boundary element methods for elliptic problems," *Mathematical Theory of Finite and Boundary Element Methods, Birkhäuser, Basel*, pp. 219–276, 1990.
- [36] I. H. Sloan, "Error analysis of boundary integral methods," *Acta Numerica*, vol. 1, pp. 287–339, 1992.
- [37] V. K. Varadan, V. V. Varadan, S. J. Tsao, and W. G. Neubauer, "Scattering of acoustic waves by rigid cylindrical objects with sharp corners," *The Journal of the Acoustical Society of America*, vol. 72, no. 6, pp. 1957–1964, 1982.

- [38] Y. Yan, "A fast boundary element method for the two-dimensional Helmholtz equation," *Computer Methods in Applied Mechanics and Engineering*, vol. 110, no. 3, pp. 285–299, 1993.
- [39] F. X. Canning, "Sparse matrix approximation to an integral equation of scattering," *Communications in Applied Numerical Methods*, vol. 6, no. 7, pp. 543–548, 1990.
- [40] F. Canning, "Sparse approximation for solving integral equations with oscillatory kernels," *SIAM Journal on Scientific and Statistical Computing*, vol. 13, no. 1, pp. 71–87, 1992.
- [41] V. Rokhlin, "Rapid solution of integral equations of classical potential theory," *Journal of Computational Physics*, vol. 60, no. 2, pp. 187–207, 1985.
- [42] V. Rokhlin, "Rapid solution of integral equations of scattering theory in two dimensions," *Journal of Computational Physics*, vol. 86, no. 2, pp. 414–439, 1990.
- [43] S. A. Yang, "A boundary integral equation method for two-dimensional acoustic scattering problems," *The Journal of the Acoustical Society of America*, vol. 105, no. 1, pp. 93–105, 1999.
- [44] K. E. Atkinson, *User's guide to a boundary element package for solving integral equations on piecewise smooth surfaces*. University of Iowa, 1993.
- [45] P. Kolm and V. Rokhlin, "Numerical quadratures for singular and hypersingular integrals," *Computers and Mathematics with Applications*, vol. 41, no. 3-4, pp. 327–352, 2001.
- [46] S. Engleder and O. Steinbach, "Modified boundary integral formulations for the Helmholtz equation," *Journal of Mathematical Analysis and Applications*, vol. 331, no. 1, pp. 396–407, 2007.
- [47] T. A. Nieminen, H. Rubinsztein-Dunlop, and N. R. Heckenberg, "Calculation of the T-matrix: general considerations and application of the point-matching method," *Journal of Quantitative Spectroscopy and Radiative Transfer*, vol. 79-80, pp. 1019–1029, 2003.

-
- [48] R. Kress, "A Nyström method for boundary integral equations in domains with corners," *Numerische Mathematik*, vol. 58, no. 1, pp. 145–161, 1990.
- [49] K. E. Atkinson and I. G. Graham, "An iterative variant of the Nyström method for boundary integral equations on nonsmooth boundaries," in *The Mathematics of Finite Elements and Applications, VI*, pp. 297–303, 1988.
- [50] I. Graham and G. Chandler, "High-order methods for linear functionals of solutions of second kind integral equations," *SIAM Journal on Numerical Analysis*, vol. 25, no. 5, pp. 1118–1137, 1988.
- [51] Y. Yan and I. H. Sloan, "Mesh grading for integral equations of the first kind with logarithmic kernel," *SIAM Journal on Numerical Analysis*, vol. 26, no. 3, pp. 574–587, 1989.
- [52] R. Kress and I. Sloan, "On the numerical solution of a logarithmic integral equation of the first kind for the Helmholtz equation," *Numerische Mathematik*, vol. 66, no. 1, pp. 199–214, 1993.
- [53] C. W. Cryer, *Numerical functional analysis*, vol. 1. Oxford University Press, USA, 1982.
- [54] M. Costabel and E. Stephan, "Boundary integral equations for mixed boundary value problems in polygonal domains and Galerkin approximation," *Banach Center Publications*, vol. 1, no. 15, pp. 175–251, 1985.
- [55] M. Costabel and E. P. Stephan, "On the convergence of collocation methods for boundary integral equations on polygons," *Mathematics of Computation*, vol. 49, no. 180, pp. 461–478, 1987.
- [56] D. L. Colton and R. Kress, *Integral equation methods in scattering theory*. Pure and applied mathematics, New York: Wiley, 1st ed., 1983.
- [57] A. J. Burton and G. F. Miller, "The application of integral equation methods to the numerical solution of some exterior boundary-value problems," *Proceedings of the Royal Society of London A: Mathematical, Physical and Engineering Sciences*, vol. 323, no. 1553, pp. 201–210, 1971.

-
- [58] E. Martensen, *Potentialtheorie*. Stuttgart: Teubner, 1968.
- [59] R. Kussmaul, “A numerical method for the exterior Neumann problem for the reduced wave equation,” *Computing*, vol. 4, no. 3, pp. 246–273, 1969.
- [60] R. Kress, “On the numerical solution of a hypersingular integral equation in scattering theory,” *Journal of Computational and Applied Mathematics*, vol. 61, no. 3, pp. 345–360, 1995.
- [61] R. Kress, “A collocation method for a hypersingular boundary integral equation via trigonometric differentiation,” *Journal of Integral Equations and Applications*, vol. 26, no. 2, pp. 197–213, 2014.
- [62] A. Anand, J. Owall, and C. Turc, “Well-conditioned boundary integral equations for two-dimensional sound-hard scattering problems in domains with corners,” *Journal of Integral Equations and Applications*, vol. 24, no. 3, pp. 321–358, 2012.
- [63] S. N. Chandler-Wilde, I. G. Graham, S. Langdon, and M. Lindner, “Condition number estimates for combined potential boundary integral operators in acoustic scattering,” *Journal of Integral Equations and Applications*, vol. 21, no. 2, pp. 229–279, 2009.
- [64] T. Betcke, S. N. Chandler-Wilde, I. G. Graham, S. Langdon, and M. Lindner, “Condition number estimates for combined potential integral operators in acoustics and their boundary element discretisation,” *Numerical Methods for Partial Differential Equations*, vol. 27, no. 1, pp. 31–69, 2011.
- [65] Y. Boubendir and C. Turc, “Wave-number estimates for regularized combined field boundary integral operators in acoustic scattering problems with Neumann boundary conditions,” *IMA Journal of Numerical Analysis*, vol. 33, no. 4, pp. 1176–1225, 2013.
- [66] C. Turc, Y. Boubendir, and M. K. Riahi, “Well-conditioned boundary integral equation formulations and Nyström discretizations for the solution of Helmholtz problems with impedance boundary conditions in two-dimensional Lipschitz do-

- mains,” *Journal of Integral Equations and Applications*, vol. 29, no. 3, pp. 441–472, 2017.
- [67] O. P. Bruno, J. S. Owall, and C. Turc, “A high-order integral algorithm for highly singular PDE solutions in Lipschitz domains,” *Computing*, vol. 84, no. 3-4, pp. 149–181, 2009.
- [68] I. Akduman and R. Kress, “Direct and inverse scattering problems for inhomogeneous impedance cylinders of arbitrary shape,” *Radio Science*, vol. 38, no. 3, 2003.
- [69] S. N. Chandler-Wilde and D. C. Hothersall, “Efficient calculation of the Green function for acoustic propagation above a homogeneous impedance plane,” *Journal of Sound and Vibration*, vol. 180, no. 5, pp. 705–724, 1995.
- [70] S. N. Chandler-Wilde, “The impedance boundary value problem for the Helmholtz equation in a half-plane,” *Mathematical Methods in the Applied Sciences*, vol. 20, no. 10, pp. 813–840, 1997.
- [71] S. Langdon and S. N. Chandler-Wilde, “A Galerkin boundary element method for an acoustic scattering problem, with convergence rate independent of frequency,” in *4th UK Conference on Boundary Integral Methods*, pp. 67–76, Salford University Press, 2003.
- [72] S. N. Chandler-Wilde, S. Langdon, and L. Ritter, “A high-wavenumber boundary element method for an acoustic scattering problem,” *Philosophical Transactions of the Royal Society of London A: Mathematical, Physical and Engineering Sciences*, vol. 362, no. 1816, pp. 647–671, 2004.
- [73] S. N. Chandler-Wilde and A. T. Peplow, “A boundary integral equation formulation for the Helmholtz equation in a locally perturbed half-plane,” *ZAMM - Journal of Applied Mathematics and Mechanics / Zeitschrift für Angewandte Mathematik und Mechanik*, vol. 85, no. 2, pp. 79–88, 2005.

- [74] S. Langdon and S. Chandler-Wilde, “A wavenumber independent boundary element method for an acoustic scattering problem,” *SIAM Journal on Numerical Analysis*, vol. 43, no. 6, pp. 2450–2477, 2006.
- [75] S. Langdon and S. Chandler-Wilde, “Implementation of a boundary element method for high frequency scattering by convex polygons,” in *Proc. 5th UK Conf. on Boundary Integral Methods, Liverpool*, pp. 2–11, Citeseer, 2005.
- [76] S. N. Chandler-Wilde and S. Langdon, “A Galerkin boundary element method for high frequency scattering by convex polygons,” *SIAM Journal on Numerical Analysis*, vol. 45, no. 2, pp. 610–640, 2007.
- [77] S. Langdon, M. Mokgolele, and S. N. Chandler-Wilde, “High frequency scattering by convex curvilinear polygons,” *Journal of Computational and Applied Mathematics*, vol. 234, no. 6, pp. 2020–2026, 2010.
- [78] S. N. Chandler-Wilde, I. G. Graham, S. Langdon, and E. A. Spence, “Numerical-asymptotic boundary integral methods in high-frequency acoustic scattering,” *Acta Numerica*, vol. 21, pp. 89–305, 2012.
- [79] S. N. Chandler-Wilde, D. P. Hewett, S. Langdon, and A. Twigger, “A high frequency boundary element method for scattering by a class of nonconvex obstacles,” *Numerische Mathematik*, vol. 129, no. 4, pp. 647–689, 2015.
- [80] L. Greengard and V. Rokhlin, “A fast algorithm for particle simulations,” *Journal of Computational Physics*, vol. 73, no. 2, pp. 325–348, 1987.
- [81] V. Rokhlin, “Diagonal forms of translation operators for the Helmholtz equation in three dimensions,” *Applied and Computational Harmonic Analysis*, vol. 1, no. 1, pp. 82–93, 1993.
- [82] L. Greengard, J. Huang, V. Rokhlin, and S. Wandzura, “Accelerating fast multipole methods for the Helmholtz equation at low frequencies,” *IEEE Computational Science and Engineering*, vol. 5, no. 3, pp. 32–38, 1998.

- [83] J. Bremer, V. Rokhlin, and I. Sammis, “Universal quadratures for boundary integral equations on two-dimensional domains with corners,” *Journal of Computational Physics*, vol. 229, no. 22, pp. 8259–8280, 2010.
- [84] J. Bremer and V. Rokhlin, “Efficient discretization of Laplace boundary integral equations on polygonal domains,” *Journal of Computational Physics*, vol. 229, no. 7, pp. 2507–2525, 2010.
- [85] J. Bremer, Z. Gimbutas, and V. Rokhlin, “A nonlinear optimization procedure for generalized Gaussian quadratures,” *SIAM Journal on Scientific Computing*, vol. 32, no. 4, pp. 1761–1788, 2010.
- [86] J. Bremer, “On the Nyström discretization of integral equations on planar curves with corners,” *Applied and Computational Harmonic Analysis*, vol. 32, no. 1, pp. 45–64, 2012.
- [87] J. Bremer, “A fast direct solver for the integral equations of scattering theory on planar curves with corners,” *Journal of Computational Physics*, vol. 231, no. 4, pp. 1879–1899, 2012.
- [88] E. Deckers, B. Bergen, B. Van Genechten, D. Vandepitte, and W. Desmet, “An efficient wave based method for 2D acoustic problems containing corner singularities,” *Computer Methods in Applied Mechanics and Engineering*, vol. 241–244, pp. 286–301, 2012.
- [89] Q. Sun, E. Klaseboer, B. C. Khoo, and D. Y. C. Chan, “A robust and non-singular formulation of the boundary integral method for the potential problem,” *Engineering Analysis with Boundary Elements*, vol. 43, no. 0, pp. 117–123, 2014.
- [90] Q. Sun, E. Klaseboer, B. C. Khoo, and D. Y. C. Chan, “Boundary regularized integral equation formulation of the Helmholtz equation in acoustics,” *Royal Society Open Science*, vol. 2, no. 1, 2015.
- [91] S. Hao, A. H. Barnett, P. G. Martinsson, and P. Young, “High-order accurate methods for Nyström discretization of integral equations on smooth curves in the plane,” *Advances in Computational Mathematics*, vol. 40, no. 1, pp. 245–272, 2014.

- [92] S. Kapur and V. Rokhlin, “High-order corrected trapezoidal quadrature rules for singular functions,” *SIAM Journal on Numerical Analysis*, vol. 34, no. 4, pp. 1331–1356, 1997.
- [93] B. K. Alpert, “Hybrid Gauss-trapezoidal quadrature rules,” *SIAM Journal on Scientific Computing*, vol. 20, no. 5, pp. 1551–1584, 1999.
- [94] L. Hamilton, M. Stalzer, R. S. Turley, J. Visser, and S. Wandzura, “FastScatTM: An object-oriented program for fast scattering computation,” *Scientific Programming*, vol. 2, no. 4, pp. 171–178, 1993.
- [95] L. Canino, L. Hamilton, J. J. Ottusch, R. Ross, J. Visser, and S. Wandzura, “FastScat performance on EMCC benchmark cases,” in *Presentations of Electromagnetic Code Consortium Annual Meeting*, (Rome, NY), 1996.
- [96] V. C. Henriquez and P. M. Juhl, “OpenBEM - An open source boundary element method software in acoustics,” *Internoise 2010*, pp. 13–16, 2010.
- [97] B. Thierry, X. Antoine, C. Chniti, and H. Alzubaidi, “ μ -diff: An open-source Matlab toolbox for computing multiple scattering problems by disks,” *Computer Physics Communications*, vol. 192, pp. 348–362, 2015.
- [98] A. Barnett and T. Betcke, “MPSPack Google code archive,” 2014. Retrieved from <https://code.google.com/archive/p/mpspack/>.
- [99] A. Barnett and T. Betcke, “MPSPack user manual,” 2013.
- [100] M. Ganesh and S. C. Hawkins, “TMATROM Code,” 2017. Retrieved from <http://www.romapp.org>.
- [101] A. H. Barnett and T. Betcke, “Stability and convergence of the method of fundamental solutions for Helmholtz problems on analytic domains,” *Journal of Computational Physics*, vol. 227, no. 14, pp. 7003–7026, 2008.
- [102] M. Ganesh and S. C. Hawkins, “TMATROM: object-oriented T-matrix reduced order model software for efficient simulation of multi-parameter acoustic scattering,” 2016. Retrieved from http://inside.mines.edu/mganesh/2016_tmatrom_manual.pdf.

- [103] M. Ganesh and S. C. Hawkins, “A far-field based T-matrix method for three dimensional acoustic scattering,” *ANZIAM Journal*, vol. 50, pp. 121–136, Oct. 2008.
- [104] M. Ganesh and S. C. Hawkins, “A stochastic pseudospectral and T-matrix algorithm for acoustic scattering by a class of multiple particle configurations,” *Journal of Quantitative Spectroscopy and Radiative Transfer*, vol. 123, pp. 41–52, 2013.
- [105] D. C. Tzarouchis, P. Ylä-Oijala, and A. Sihvola, “Plasmonic modes on rounded hexahedral and octahedral nano-antennas,” in *2016 URSI International Symposium on Electromagnetic Theory (EMTS)*, pp. 767–770.
- [106] D. C. Tzarouchis, P. Ylä-Oijala, and A. Sihvola, “Study of plasmonic resonances on platonic solids,” *Radio Science*, vol. 52, no. 12, pp. 1450–1457, 2017.
- [107] S. Onaka, “A simple equation giving shapes between a circle and a regular N-sided polygon,” *Philosophical Magazine Letters*, vol. 85, no. 7, pp. 359–365, 2005.
- [108] R. Kress, “Minimizing the condition number of boundary integral operators in acoustic and electromagnetic scattering,” *The Quarterly Journal of Mechanics and Applied Mathematics*, vol. 38, no. 2, pp. 323–341, 1985.
- [109] R. Kress, *Linear Integral Equations*, vol. 82. Springer Science & Business Media, 3rd ed., 2013.
- [110] A. Rawlins, “High-frequency diffraction of a electromagnetic plane wave by an imperfectly conducting rectangular cylinder,” *Journal of Engineering Mathematics*, vol. 76, no. 1, pp. 157–180, 2012.
- [111] P. D. Smith and A. D. Rawlins, “Diffraction from structures with an impedance boundary,” in *Electromagnetics in Advanced Applications (ICEAA), 2013 International Conference on*, pp. 1297–1300, 2013.
- [112] A. Clebsch, “Ueber die reflexion an einer kugelfläche.,” *Journal für die reine und angewandte Mathematik*, vol. 61, pp. 195–262, 1863.
- [113] L. Lorenz, H. Valentiner, and Carlsbergfondet, *Œuvres scientifiques de L. Lorenz: Revues et annotées par Valentiner. Publiés aux frais de la fondation Carlsberg.* Lehmann & Stage, 1898.

- [114] N. A. Logan, “Early history of the Mie solution,” *Journal of the Optical Society of America*, vol. 52, no. 3, pp. 342–343, 1962.
- [115] N. A. Logan, “Survey of some early studies of the scattering of plane waves by a sphere,” *Proceedings of the IEEE*, vol. 53, no. 8, pp. 773–785, 1965.
- [116] M. Kerker, “Lorenz–Mie scattering by spheres: Some newly recognized phenomena,” *Aerosol Science and Technology*, vol. 1, no. 3, pp. 275–291, 1982.
- [117] M. Kerker, *The Scattering of Light and other Electromagnetic Radiation: Physical Chemistry: A Series of Monographs*, vol. 16. Academic press, 2013.
- [118] M. Ganesh, S. C. Hawkins, and R. Hiptmair, “Convergence analysis with parameter estimates for a reduced basis acoustic scattering T-matrix method,” *IMA Journal of Numerical Analysis*, vol. 32, no. 4, pp. 1348–1374, 2012.
- [119] A. S. Ilyinsky, G. I. Slepüŷääiŷān, G. Y. Slepyan, and A. Y. Slepyan, *Propagation, scattering and dissipation of electromagnetic waves*. IET, 1993.
- [120] F. W. Olver, D. W. Lozier, R. F. Boisvert, and C. W. Clark, *NIST handbook of mathematical functions*. Cambridge University Press, 2010.
- [121] M. Abramowitz and I. A. Stegun, *Handbook of Mathematical Functions: with Formulas, Graphs, and Mathematical Tables*, vol. 55. Courier Corporation, 1964.
- [122] T. Roy, T. K. Sarkar, A. R. Djordjevic, and M. Salazar-Palma, “Time-domain analysis of TM scattering from conducting cylinders using a hybrid method,” *IEEE Transactions on Microwave Theory and Techniques*, vol. 46, no. 10, pp. 1471–1477, 1998.
- [123] P. C. Waterman, “Matrix formulation of electromagnetic scattering,” *Proceedings of the IEEE*, vol. 53, no. 8, pp. 805–812, 1965.
- [124] P. C. Waterman, “New formulation of acoustic scattering,” *The Journal of the Acoustical Society of America*, vol. 45, no. 6, pp. 1417–1429, 1969.
- [125] B. Peterson and S. Ström, “T-matrix for electromagnetic scattering from an arbitrary number of scatterers and representations of $E(3)$,” *Physical Review D*, vol. 8, no. 10, pp. 3661–3678, 1973.

-
- [126] M. I. Mishchenko, L. D. Travis, and D. W. Mackowski, "T-matrix computations of light scattering by nonspherical particles: a review," *Journal of Quantitative Spectroscopy and Radiative Transfer*, vol. 55, no. 5, pp. 535–575, 1996.
- [127] W. R. C. Somerville, B. Auguié, and E. C. Le Ru, "Severe loss of precision in calculations of T-matrix integrals," *Journal of Quantitative Spectroscopy and Radiative Transfer*, vol. 113, no. 7, pp. 524–535, 2012.
- [128] A. G. Dallas, "On the convergence and numerical stability of the second Waterman scheme for approximation of the acoustic field scattered by a hard object," tech. rep., University of Delaware, Department of Mathematical Sciences, 2000.
- [129] S. Havemann and A. J. Baran, "Calculation of the phase matrix elements of elongated hexagonal ice columns using the T-matrix method," *Journal of Quantitative Spectroscopy and Radiative Transfer*, vol. 89, no. 1, pp. 87–96, 2004.
- [130] M. I. Mishchenko and L. D. Travis, "Capabilities and limitations of a current FORTRAN implementation of the T-matrix method for randomly oriented, rotationally symmetric scatterers," *Journal of Quantitative Spectroscopy and Radiative Transfer*, vol. 60, no. 3, pp. 309–324, 1998.
- [131] S. Havemann and A. J. Baran, "Extension of T-matrix to scattering of electromagnetic plane waves by non-axisymmetric dielectric particles: application to hexagonal ice cylinders," *Journal of Quantitative Spectroscopy and Radiative Transfer*, vol. 70, no. 2, pp. 139–158, 2001.
- [132] D. Petrov, Y. Shkuratov, and G. Videen, "Optimized matrix inversion technique for the T-matrix method," *Optics Letters*, vol. 32, no. 9, pp. 1168–1170, 2007.
- [133] L. Bi, P. Yang, G. W. Kattawar, and M. I. Mishchenko, "Efficient implementation of the invariant imbedding T-matrix method and the separation of variables method applied to large nonspherical inhomogeneous particles," *Journal of Quantitative Spectroscopy and Radiative Transfer*, vol. 116, pp. 169–183, 2013.
- [134] T. Rother and J. Wauer, "Case study about the accuracy behavior of three different T-matrix methods," *Applied Optics*, vol. 49, no. 30, pp. 5746–5756, 2010.

-
- [135] M. Ganesh and S. Hawkins, “Three dimensional electromagnetic scattering T-matrix computations,” *Journal of Computational and Applied Mathematics*, vol. 234, no. 6, pp. 1702 – 1709, 2010.
- [136] M. Ganesh and S. C. Hawkins, “A far-field based T-matrix method for two dimensional obstacle scattering,” *ANZIAM Journal*, vol. 51, pp. 215–230, 2010.
- [137] A. Gibbs, S. Langdon, and A. Moiola, “Numerically stable computation of embedding formulae for scattering by polygons,” *arXiv preprint arXiv:1805.08988*, 2018.
- [138] T. J. Dufva, J. Sarvas, and J. C. E. Sten, “Unified derivation of the translational addition theorems for the spherical scalar and vector wave functions,” *Progress In Electromagnetics Research B*, vol. 4, pp. 79–99, 2008.
- [139] W. J. Wiscombe, “Improved Mie scattering algorithms,” *Applied Optics*, vol. 19, no. 9, pp. 1505–1509, 1980.
- [140] C. W. Clenshaw and A. R. Curtis, “A method for numerical integration on an automatic computer,” *Numerische Mathematik*, vol. 2, no. 1, pp. 197–205, 1960.
- [141] M. Born and E. Wolf, *Principles of Optics, 7th (expanded) ed.* Cambridge, UK: Cambridge University Press, 1999.
- [142] K. E. Atkinson, *The Numerical Solution of Integral Equations of the Second Kind.* Cambridge Monographs on Applied and Computational Mathematics, Cambridge: Cambridge University Press, 1997.